INFORMATION TO USERS

This manuscript has been reproduced from the microfilm master. UMI films the text directly from the original or copy submitted. Thus, some thesis and dissertation copies are in typewriter face, while others may be from any type of computer printer.

The quality of this reproduction is dependent upon the quality of the copy submitted. Broken or indistinct print, colored or poor quality illustrations and photographs, print bleedthrough, substandard margins, and improper alignment can adversely affect reproduction.

In the unlikely event that the author did not send UMI a complete manuscript and there are missing pages, these will be noted. Also, if unauthorized copyright material had to be removed, a note will indicate the deletion.

Oversize materials (e.g., maps, drawings, charts) are reproduced by sectioning the original, beginning at the upper left-hand corner and continuing from left to right in equal sections with small overlaps.

ProQuest Information and Learning
300 North Zeeb Road, Ann Arbor, MI 48106-1346 USA
800-521-0600

Design, Construction and Optimization of a Femtosecond Laser Spectrometer to Study Excited State Processes

by

Karen A.W.Y. Cheng

Submitted in partial fulfillment of the requirements
for the degree of Doctor of Philosophy

at

Dalhousie University
Halifax, Nova Scotia
April 2005

DALHOUSIE UNIVERSITY

To comply with the Canadian Privacy Act the National Library of Canada has requested that the following pages be removed from this copy of the thesis:

Preliminary Pages

Examiners Signature Page (pii)

Dalhousie Library Copyright Agreement (piii)

Appendices

Copyright Releases (if applicable)

This thesis is dedicated to all those
who helped me learn how to smile again
when I forgot how.

I know that You can do all things,
And that no purpose of Yours can be hindered.
I have dealt with great things that I do not understand;
Things too wonderful for me, which I cannot know.
I had heard of You by word of mouth,
But now my eye has seen You.

-Job 42:2-5

Table of Contents

List of Figures

List of Tables

Abstract

On the femtosecond (10^{-15} s) and picosecond (10^{-12} s) time scales, seemingly instantaneous chemical processes can be observed and studied. In order to study these phenomena, the design, construction and optimization of a femtosecond laser spectrometer were undertaken. The spectrometer is composed of the transient absorption spectrometer, and the streak camera system. The transient absorption spectrometer is based upon the pump-probe technique and collects time-resolved full absorption spectra from 395 to 750 nm, with resolution down to 305 fs. Complementary to the transient absorption spectrometer is the streak camera system, which measures time-resolved emission decays at specific wavelengths. This system boasts 3.3 ps resolution with a maximum time window of 90 ns.

One of the ultrafast phenomena that has been investigated with the streak camera system is the placement and movement of pyrene and 9,10-dicyanoanthracene (DCA) molecules within the framework of faujasite X and Y zeolites. Up to two of these molecules can reside in each supercage. In the literature, there has been significant debate as to whether pyrene molecules in doubly occupied supercages exist as ground state dimers or have a dissociative ground state. In this thesis work, the rise time of pyrene excimer emission has been shown to range from 7 to 16 ps, indicating that the latter is true. DCA also exhibits an excimer emission rise time when adsorbed into Y zeolites; however, their behaviour differs from the pyrene molecules in that their rise times increase as a function of decreasing loading level. The placement of the DCA molecules and their intracavity movement have been studied by the analysis of picosecond and nanosecond fluorescence data.

Finally, the femtosecond laser spectrometer was used to study the effect of short excitation wavelength on the ultrafast photophysical behaviour of tris-(2,2'-bipyridine)ruthenium(II) derivatives. Fluorescence studies of five complexes showed that substituted bipyridine ligands exhibited an instrument response limited emission as well as a longer nanosecond emission. Transient absorption studies could not identify the species emitting the longer emission but did detect decay kinetics that were within the instrument response time of the spectrometer (< 300 fs). These results are compared to the literature and discussed.

List of Abbreviations and Symbols Used

t	time
k	rate constant
τ	time constant
[M]	concentration of M
ΔE	energy difference
λ	wavelength
h	Planck's constant
v	frequency
EM	electromagnetic
μ	electric dipole moment operator
ψ	wavefunction
S_n	spin-paired singlet state
IC	internal conversion
ISC	intersystem crossing
T_n	triplet state
MO	molecular orbital
HOMO	highest occupied molecular orbital
LUMO	lowest unoccupied molecular orbital
π	type of orbital
d	type of orbital
t_{2g} and e_g	metal centered d orbitals
MC	metal centered
MLCT	metal to ligand charge transfer
LMCT	ligand to metal charge transfer
GVD	group velocity dispersion
IRF	instrument response function
FWHM	full width at half maximum
χ^2	goodness of fit value
DCA	9,10-dicyanoanthracene
CPA	chirped pulse amplification
SHG	second harmonic generator
THG	third harmonic generator
OPA	optical parametric amplification
KDP	potassium dihydrogen phosphate
VI	virtual instrument
GPIB	general purpose interface bus
BC	Berek's compensator
BBAR	broadband antireflective
PDA	photodiode array
PCA	principal components analysis
USRP	Unchirped Spectral Reconstruction Program
CFnP	Convoluted Fitting of Non-Regularly Spaced Data Program

ManCon	Manual Convolution Program
CCD	charge-coupled device
pix	pixel
IC	Image Correct
MV^{2+}	methyl viologen cation
MeOH	methanol
Φ	quantum yield
bpy	2,2'-bipyridine
dfmb	4,4'-di(trifluoromethyl)-2,2'-bipyridine
dmb	4,4'-dimethyl-2,2'-bipyridine
dmeob	4,4'-dimethoxy-2,2'-bipyridine
dttb	4,4'-di(*tert*-butyl)-2,2'-bipyridine

Acknowledgements

First and foremost, I would like to thank my supervisor, Dr. Frances Cozens, for giving me the tremendous opportunity to build the femtosecond spectrometer, and for believing in me through all these years. Thanks. Thanks also to Dr. Norm Schepp for all his help and support.

I would like to acknowledge the tremendous contributions of Brian Millier for his electronics expertise, Jeurgen Müeller for the production of countless quartz cells and other specialized glass equipment, the Machine Shop and all the office staff, particularly Giselle Andrews. This degree would not have been possible without you.

The support and friendship offered by the 4th floor has been invaluable, notably, the past and present members of the Cozens and Schepp group: Dr. Mel O'Neill, Dr. Wendy Monk, Dr. Sandy Lancelot, Amy Keirstead, Reinaldo Moya, Geniece Hallett, Dr. Sherri McFarland and Dr. Felix Lee. I also need to acknowledge the following people and groups for their love and support: Dr. Fiona Harper, Ricky Mah, Craig Larsh, Matt Clay, Judi Beagan, Stéphanie Simard, Jen Rudolph, Fr. John Fletcher, C.C. and all my brothers in the Companions of the Cross, Fr. Con Mulvihill, S.J., Fr. James Mallon, Sr. Maureen Currie, RSCJ, Dr. Ray Syvitski, St. Thomas Aquinas Parish, St. Joseph's Newman Centre, and the Dalhousie Music Department—you have all touched my life very deeply.

Thanks to my parents for letting me go and spread my wings as far as I needed to. You have sacrificed so much so that I could have every opportunity to learn. Thanks also to my sister for being her wacky self, and my Aunt Cecilia and Uncle Johnny for all their love and prayers and a place to stay every time I came to Toronto on conferences.

Praise be the Lord for making the world so incredibly cool, and letting me stand on Your hand and peek at a timescale that only You can truly see. Thanks for the grace and perseverance to see this crazy time through, the Eucharist for strength, Your holy mother for intercession (especially for fixing the Q-switch of the laser), the wisdom of Your Church, the gift of incredible faith, Your incredible love that spilled over into creation and for choosing me to be Your own. *Gloria tibi, O Sanctissima Trinitas!*

Chapter 1: Introduction

1.1 Kinetics

1.1.1 Chemical Kinetics

Every chemical reaction or process, no matter how fast, takes place over time. From the unimaginably short timescale of electron movement or photon absorption, to the unperceivably slow changes of geologic processes, the studying and understanding of these reactions involves the measurement of changes. The field of chemical kinetics measures and quantifies the rates of reactions, and uses this information to support or refute proposed mechanisms for the reactions studied.

For an unimolecular reaction, whereby the substrate of interest, A, undergoes some process to change into another species, P:

$$A \longrightarrow P, \tag{1.1}$$

the rate of reaction v can be measured as the change in concentration of A or P over time:

$$v = -\frac{d[A]}{dt} = \frac{d[P]}{dt}. \tag{1.2}$$

This can be extended to a more complex reaction

$$aA + bB \longrightarrow cC + dD \tag{1.3}$$

in the following general form:

$$v = \frac{1}{j}\frac{d[J]}{dt}, \tag{1.4}$$

where j is the stoichiometric coefficient of species J, and is negative for reactants and positive for products. Empirically, the rate of reaction for simple processes can be determined to be:

$$v = k[A]^{\alpha}[B]^{\beta}\cdots \tag{1.5}$$

where the values of k, α and β are constants. Equation (1.5) embodies two significant pieces of terminology that are used in describing chemical kinetics: order of reaction, and rate constant. The overall order of a given reaction, n, is an experimental quantity and is defined as the sum $n = \alpha + \beta + \cdots$. Orders are not necessarily integer values. A reaction

can also be defined with respect to one reactant, known as a partial order. For the following reaction

$$A + B \longrightarrow C, \tag{1.6}$$

the empirical rate law may be determined to be

$$v = k[A]^2[B]. \tag{1.7}$$

The overall order of this reaction is n=3, and the reaction is said to be first order with respect to reactant B and second order with respect to reactant A. Experimental measurement of the rate law, especially when the partial orders do not match the stoichiometric coefficients of the reaction, can lend strong support to one proposed mechanism over another.

The rate constant, k, is also an empirically determined quantity. Rate constants are temperature dependent quantities that relate the concentration of the reactant to the overall rate observed for the reaction. Because observed reactions are the statistical averages of events occurring on the molecular level, the probability of an event decreases if the number of reactant molecules available decreases. Thus, as the concentration of a reactant decreases, the overall rate of the reaction also decreases. The determination of the rate constant can give much information about the thermodynamics of a reaction, such as the free energy, enthalpy and entropy governing the system. Often, in ultrafast (femtosecond and picosecond) processes, the rate constant for first order processes is reported by its time constant τ:

$$\tau = k^{-1}. \tag{1.8}$$

Even though the rate law is empirically determined, measuring the rate of change of concentration of a reactant over time is difficult to do experimentally. Most experimental techniques measure the concentration of a species at a given time. In order to translate the experimental data into the rate law, let us begin with the rate law itself as a combination of equations (1.4) and (1.5) for the unimolecular process described by (1.1):

$$\frac{d[A]}{dt} = -k[A]. \tag{1.9}$$

Equation (1.9) is a differential equation. Integration of (1.9) results in an equation that describes the concentration of species A at any given time t:

$$[A]_t = [A]_0 e^{-kt}. \tag{1.10}$$

Equation (1.10) is known as the integrated rate law for any first order reaction. Analytical solutions for basic rate laws are given in Table 1.1, and integrated rate laws can be obtained numerically for the more complex rate laws.

Integrated rate laws allow for experimental data to be used to determine whether a rate law describes a system. In the laboratory setting, the concentrations of either a reactant or a product are measured over time, until the reaction has come to completion. The proposed rate law is then fit to all of the data. Concentrations predicted by the proposed rate law are compared to the actual data collected to determine whether the proposed rate law adequately describes the observed kinetics of the reaction. It is imperative that data throughout the reaction is used so that for complex reactions, *i.e.* reactions in which the products also participate in the reaction and affect the rate, an accurate description of the rate law can be determined.

Table 1.1 Analytical solutions for basic rate laws.[1]

Order	Reaction	Rate Law	Integrated Rate Law
0	$A \rightarrow P$	$v = k$	$[A]_t = [A]_0 - kt$
1	$A \rightarrow P$	$v = k[A]$	$[A]_t = [A]_0 e^{-kt}$
2	$A \rightarrow P$	$v = k[A]^2$	$[A]_t = \dfrac{[A]_0}{1 + kt[A]_0}$
2	$A + B \rightarrow P$	$v = k[A][B]$	$kt = \dfrac{1}{[B]_0 - [A]_0} \ln \dfrac{[A]_0[B]_t}{[B]_0[A]_t}$
2	$A + 2B \rightarrow P$	$v = k[A][B]$	$kt = \dfrac{1}{[B]_0 - [A]_0} \ln \dfrac{[A]_0[B]_t}{[B]_0[A]_t}$
3	$A + 2B \rightarrow P$	$v = k[A][B]^2$	$kt = \dfrac{[B]_t - [B]_0}{(2[A]_0 - [B]_0)[B]_t[B]_0} + \dfrac{1}{(2[A]_0 - [B]_0)^2} \ln \dfrac{[A]_0[B]_t}{[B]_0[A]_t}$

An extension of the basic rate laws can be made to systems where several different processes proceed from a single reactant. For example, a molecule in its first excited singlet state may return to the ground state via fluorescence or vibrational relaxation, or it may undergo intersystem crossing to a triplet state, or it may fragment into ground state molecules. Such a system of parallel intramolecular processes may be described as follows:

$$^1A^* \xrightarrow{k_f} A + h\nu \text{ (fluorescence)} \quad (1.11)$$

$$^1A^* \xrightarrow{k_{VR}} A \text{ (internal conversion, then vibrational relaxation)} \quad (1.12)$$

$$^1A^* \xrightarrow{k_{ISC}} {}^3A \text{ (intersystem crossing)} \quad (1.13)$$

$$^1A^* \xrightarrow{k_{frag}} B^\bullet + C^\bullet \text{ (homolytic cleavage)} \quad (1.14)$$

The rate law describing equations (1.11) to (1.14) is

$$v = k_f[^1A^*] + k_{VR}[^1A^*] + k_{ISC}[^1A^*] + k_{frag}[^1A^*]. \quad (1.15)$$

The rate law can be simplified to

$$v = (k_f + k_{VR} + k_{ISC} + k_{frag})[^1A^*] = k_t[^1A^*], \quad (1.16)$$

where all the rate constants are gathered together into one observable rate constant, k_t. When observing the change in $[^1A^*]$ over time, a first order decay will be observed. In order to separate the components of k_t, measurements observing the production of $B^\bullet, C^\bullet$, ^3A, or A need to be made.

Another experimental system that may arise is the observation of multiple simultaneous reactions all giving rise to the same measurable signal. For example, the unimolecular process $A \rightarrow P$ taking place in a heterogeneous microenvironment would result in two or more rate constants for the same reaction. Perhaps different mechanisms are even at work in these different environments. If the concentration of P is being measured, then truly several different reactions are occurring:

$$A \xrightarrow{k_1} P \text{ (environment 1)} \quad (1.17)$$

$$A \xrightarrow{k_2} P \text{ (environment 2)} \quad (1.18)$$

$$\vdots$$

The observed $[P]$ is a superposition of all the different reaction products:

$$[P] = [P]_{env.1} + [P]_{env.2} + \cdots \quad (1.19)$$

And thus the observed integrated rate law would also be a superposition of the individual rate laws:

$$[P]_t = [A]_1 e^{-k_1 t} + [A]_2 e^{-k_2 t} + \cdots \quad (1.20)$$

Fitting data obeying equation (1.20) involves iterative non-linear fitting routines, such as the Levenberg-Marquardt algorithm.[2] For the purpose of this thesis, proposed rate law models with several first order components are referred to as multiexponential fits, with the most common being double exponential and triple exponential fits.

For the multiexponential model where one or more rate constants are very small compared to the other rate constants in the model, (*i.e.* $k_{n\geq 3} << k_1, k_2$) the equation:

$$[P]_t = [A]_1 e^{-k_1 t} + [A]_2 e^{-k_2 t} + [A]_3 e^{-k_3 t} + [A]_4 e^{-k_4 t} + \cdots \quad (1.21)$$

would become:

$$[P]_t = [A]_1 e^{-k_1 t} + [A]_2 e^{-k_2 t} + M, \quad (1.22)$$

where the small terms have been approximated by the addition of a single constant. When fitting the very fast components of reactions that may have much slower processes, the use of equation (1.22) will yield accurate values for k_1 and k_2, provided that the use of M is justified within $0 > t_{obs} > t$.

Another specific case in possible reaction processes involves the production and reaction of an intermediate happening simultaneously:

$$A \xrightarrow{k_1} I \xrightarrow{k_2} P \quad (1.23)$$

This is known as a consecutive mechanism. The net formation of I is:

$$\frac{d[I]}{dt} = k_1[A] - k_2[I] \quad (1.24)$$

The concentration of $[A]$ at any time t has already been determined in equation (1.10) to be:

$$[A]_t = [A]_0 e^{-k_1 t} \quad (1.10)$$

and thus equation (1.24) becomes:

$$\frac{d[I]}{dt} = k_1[A]_0 e^{-k_1 t} - k_2[I]. \quad (1.25)$$

The integration of equation (1.25) gives[3]:

$$[I] = [A]_0 \frac{k_1}{k_2 - k_1}(e^{-k_1 t} - e^{-k_2 t}). \quad (1.26)$$

When measuring and fitting $[I]$ to a rate equation, equation (1.26) is essentially a double exponential equation. A graphical representation of the time evolution of $[A]$, $[I]$, and $[P]$ is shown in Figure 1.1.

There are two limiting cases to reaction (1.23). In the first case, $k_1 >> k_2$, the reaction A is quickly converted to I, which slowly forms P. The formation of I has a rapid rise and its decline is slow. The formation of P is approximately first order. The second case, where $k_1 << k_2$, is much more interesting. The formation of I is slow, while its

conversion to P is rapid. After a short while, it is found that the change in $[I]$ is approximately zero, and this is the basis of the steady state approximation. As none of the systems studied in this thesis use the steady state approximation, a further discussion of this case will not be pursued here.

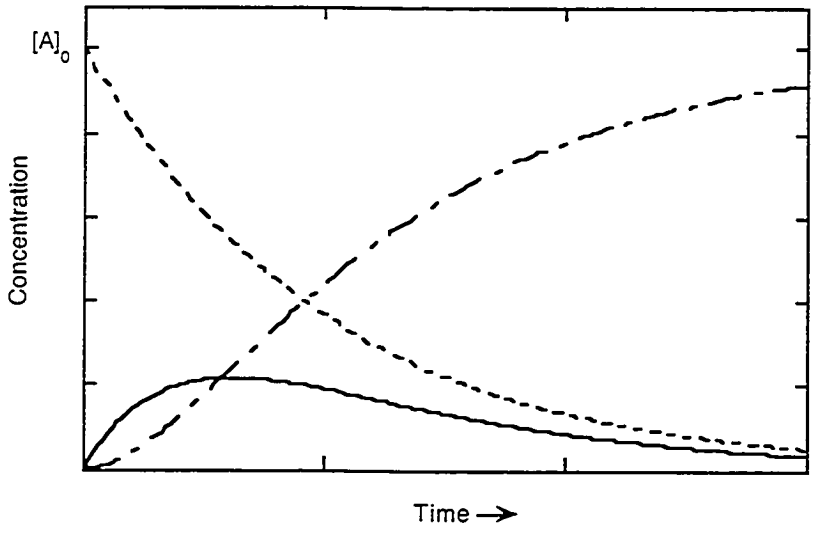

Figure 1.1 A graphical representation of the consecutive reaction $A \rightarrow I \rightarrow P$, with $[A]$ (---), $[I]$ (—) and $[P]$ (—·—). Notice that the concentration of I goes through a maximum.

The integrated rate laws that have been discussed embody the bulk of the kinetic models necessary to describe the systems studied in this thesis. The challenge is to propose rate laws which describe very complex systems, some of which are superpositions of reactions taking place simultaneously. However, before one can analyze kinetic data, the data must be measured well. The following sections discuss techniques of experimental design and data collection, which are imperative to being able to characterize processes accurately.

1.1.2 Techniques of Kinetic Data Collection

With the advent of the Arrhenius equation in 1889, the study of the rates of reactions as a probe for chemical information has always been dependent upon

measurable rates. Time-resolved data collection is a field that is continually under development in the pursuit of shorter and shorter time resolution. There are two major instrumental challenges in achieving shorter time scales: accurately determining time zero, and being able to make a concentration measurement more and more quickly. The following brief survey of techniques developed in the past century will highlight how these two challenges were met to eventually achieve resolution on the femtosecond time scale.

In order to collect time-resolved data, there needs to be some way of measuring the concentrations of species at a given time during the reaction. The quenching method allows the reaction to proceed for a measured amount of time, then the reaction is stopped, and the composition of the mixture is then analyzed at leisure. Repetition of the experiment with varying quenching times allows the rate of the reaction to be measured. Quenching can be achieved by such methods as rapid cooling, or addition of a quenching agent. However, this method is only accurate if the reaction makes insignificant progress during the quenching process, and thus is only useful for reactions that take place over minutes or hours.

Real-time analysis of the reaction composition takes place during the course of the reaction, either by withdrawal of a small sample, or analysis of the bulk reaction. Any standard analytical technique may be used to determine reactant, intermediate and product concentrations, including mass spectrometry, magnetic resonance, conductivity, fluorescence, and spectrophotometry. Spectrophotometry, or absorbance measurements, is widely used due to the ability to make quantitative measurements in extremely short amounts of time, right down to the current limits of time resolution. In the present work, two detection methods are employed that make use of the absorbance and fluorescence techniques.

The first breakthrough to recording data at sub-second rates was reported in 1923 using the flow tube method to study reactions in solution.[4] In the flow tube method, the reactants are injected into a mixing chamber at a constant rate. Past the mixing chamber, the reacting solution flows through a tube where the components are analyzed spectrophotometrically. The distance along the tube from the mixing chamber is proportional to the elapsed time of the reaction.

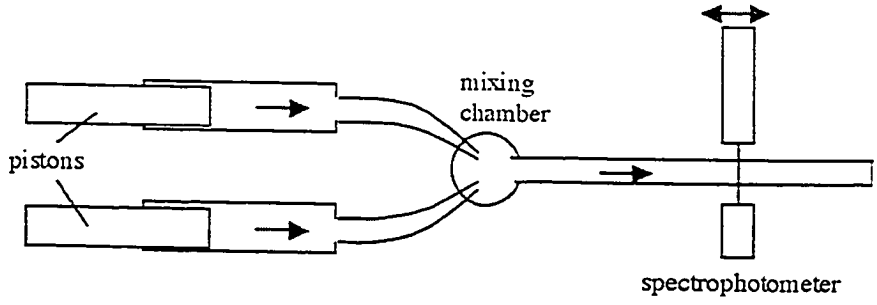

Figure 1.2 Schematic of a flow setup. Figure reproduced from reference 1.

One of the major disadvantages of the flow tube method is the large volume of reactant solution necessary, especially for high flow rates. Faster reactions require high flow rates to achieve better time resolution along the tube length. The stopped-flow and accelerated flow technique[5,6] address this disadvantage by replacing the flow tube with an observation chamber equipped with a stopping piston. Reactant solutions are injected rapidly into the mixing chamber, moving the stopping piston back until the maximum volume (about 1 mL) has been injected. The reaction continues in the observation chamber, where it is monitored by a stationary spectrophotometer. The stopped-flow technique reached the millisecond timescale in the 1940s and continues to be used today to study biochemical reactions due to its ability to study small samples.

World War II fueled the development of electronics that were used in 1950 to access the microsecond time scale, for which Manfred Eigen, R. G. W. Norrish, and George Porter shared the 1967 Nobel Prize. Eigen developed a technique called "the relaxation method,"[7] which involves perturbing a system originally at equilibrium, and observing the subsequent return of the system to equilibrium. Two methods are possible for disturbing the equilibrium: a sudden temperature jump, and a sudden change in pressure. For very small volumes, both temperature and pressure changes can be produced very quickly and thus shorter time scales could be accessed by making time zero very short and precise. In his Nobel lecture, Eigen refers to the reaction kinetics measurable at the microsecond time scale as being "immeasurably fast."[8].

Norrish and Porter developed the first flash photolysis system, which is the basis of the ultrafast techniques that have been subsequently developed.[9] A sample is exposed to a brief, high intensity flash of light and then the contents of the reaction chamber are monitored spectrophotometrically. After the invention of the laser[10] in 1960, the advent of high powered, short laser pulses and their subsequent development has allowed for the study of reaction kinetics using flash photolysis on time scales that are difficult to comprehend. The nanosecond (10^{-9} s) time scale was made possible by Q-switched lasers, and picoseconds (10^{-12} s) became accessible by employing mode-locked methods.[11] Subpicosecond pulses[12] were achieved in 1974 and the subsequent development of solid state Ti:sapphire lasers[13] has made femtosecond (10^{-15} s) pulse generation a standard laboratory technique. Whereas before one had to build and maintain a femtosecond laser in order to use it as part of a spectrometer, commercially available ultrafast lasers are now compact turn-key units.

Faster and faster time scales have been accessible using shorter and shorter pulses because the length (in time) of the pulse defines the precision of the zero time of the reaction. For a reaction to be observable, the length of the pulse must be shorter than the time that it takes for the reaction to be completed. The second challenge is the time resolution of the concentration measurement. Although the time response of electronics has improved dramatically, the precision of electronics reaches its limits at the sub-nanosecond time scale. On shorter time scales, it is necessary to use techniques such as pump-probe and upconversion techniques, or special instrumentation such as streak cameras to accurately monitor the reaction as it evolves. The spectrometer constructed as part of this thesis project uses the pump-probe technique and streak camera instrumentation, both of which will be described in detail in Section 1.3.

One of the challenges of studying kinetic reactions is being able to study the reaction of interest. Often, as will be highlighted in the Chapter 4 of the thesis, it is difficult to have all the instrumentation necessary to study a particular reaction. Instruments are designed with flexibility in mind; however, it is impossible to build a spectrometer to measure reactions in all three phases of matter, at all temperatures, with ultrafast resolution and yet have the capability to measure millisecond experiments as

well. By definition, instruments are limited. It is the responsibility of the researcher to design the experiment to be within the capability of the instrument.

Because the femtosecond spectrometer is based upon a flash photolysis system, all the experiments designed require an unreactive precursor molecule that is activated in some form by a pulse of light to form an active species. The photophysics of these molecules need to be understood in order for the subsequent chemical processes that result to be interpreted.

1.2 Molecular Photophysics

1.2.1 Photon-Molecule Interactions

Photons with wavelengths between 200 and 700 nm possess sufficient energy to excite a molecule from a lower electronic energy state to a higher one. By applying the law of conservation of energy, a photon of light will be be absorbed by a molecule if the energy of the photon, $h\nu$, is equal to the energy difference between two electronic states of the molecule, ΔE, where h is Planck's constant, and ν is the frequency of light. Light is an electromagnetic (EM) wave composed of oscillating electric and magnetic fields that may exert forces on charged particles, such as electrons and nuclei, or on particles with magnetic dipoles. The electric field component of an EM wave, oscillating at some frequency ν, will cause a point charge to oscillate at the same frequency, provided that both wave and particle are sufficiently close. In the case of molecules, it is the oscillating dipole with which the EM field can interact. If both the wave and dipole are oscillating at the same frequency, even for an instant, they are said to be in resonance. This resonance allows the energy of the photon to be transferred to the oscillating dipole of the molecule. The probability of transition is proportional to the square of the transition dipole moment,

$$\mu_{fi} = \int \psi_f^* \mu \psi_i d\tau \qquad (1.27)$$

where μ is the electric dipole moment operator, and ψ_i and ψ_f are the wavefunctions describing the initial and final states.

1.2.2 Selection Rules for Electronic Transitions

Transitions between electronic states are classified as either "allowed" or "forbidden." The probability of transition is governed by three selection rules: electronic, Franck-Condon, and spin factors. Electronic factors refer to the spatial overlap and symmetry matching of the two orbitals involved in the electronic transition. For a transition to be allowed, the two orbitals must be overlapped spatially, and possess symmetries that can transform onto one another with a non-zero transition dipole moment. The Franck-Condon factor involves the geometry of the nuclei of the initial electronic state compared to the final electronic state. According to the Franck-Condon principle, the nuclei do not change position while the electronic transition takes place. Transitions are thus governed by the size of the overlap integral between the initial and final vibrational wavefunctions at a given geometry. Finally, the spin factor compares the structure and motion of spins in ψ_i and ψ_f. For transitions in which total spin is conserved, the transition is allowed, and for systems that do not conserve total spin, the transition is spin-forbidden and its probability depends upon the amount of spin-orbit coupling.

The terms "allowed" and "forbidden" are not absolute terms. When calculating the transition probability given a set of idealized geometries and quantum numbers, absolute transition probabilities of zero may be obtained, and yet experimentally the transition may be observed. This is due to an insufficient level of theory being used to describe the entire system in question. In real systems, factors such as vibrational motion and spin-orbit coupling results in mixing of the molecular orbitals involved in the transition, such that the orbitals now have some of the character necessary to couple the initial and final wavefunctions. In some cases, the breakdown of selection rules is so severe that forbidden transitions can occur with the same probability as allowed transitions.

1.2.3 Radiative and Non-Radiative Processes

Upon photoexcitation, an electron is promoted from its spin-paired singlet ground state (S_0) to an empty orbital, forming a singlet excited state molecule with an unpaired

electron in each of two orbitals. Due to spin selection rules, the electron being promoted must maintain the same spin state in both orbitals, and thus the resulting unpaired electrons are of opposite spins, and the initially excited state is a singlet state (S_n). Excitation generally occurs to a vibrationally excited state of S_n, which relaxes by internal conversion (IC) to the lowest vibrational energy level of S_1. Internal conversion is a non-radiative process involving thermal and vibrational relaxation. From the S_1 state, the excited molecule can undergo a series of photophysical processes. Relaxation to S_0 by the emission of a photon is called fluorescence. Non-radiative decay to the ground state through IC is also possible. A third photophysical pathway is intersystem crossing (ISC) to the triplet state (T_n). ISC is a spin-forbidden pathway resulting in the spin flip of one of the unpaired electrons resulting in both unpaired electrons having parallel spins. After an ISC process to reach the T_1 state, relaxation from T_1 to S_0 is possible through phosphorescence and ISC. These processes, along with approximate times scales for organic molecules, are shown schematically on the Jablonski diagram in Figure 1.3.

The femtosecond and picosecond time scales, collectively referred to as being ultrafast, encompass the fastest of these photophysical processes. The absorption of a photon is a subfemtosecond process, estimated[14] to be $\sim 10^{-16}$ s. On the ultrafast time scale, electronic motion, electron transfer, vibrational relaxation, fast fluorescence, and intersystem crossing of very strongly spin-orbit coupled systems are observable. The slower processes, such as phosphorescence, and delayed fluorescence are too slow to be detected. When studying solution samples, molecular tumbling of small molecules becomes significant.

Transitions between states are best described as being transitions between potential energy surfaces. Radiative transitions are governed by the Franck-Condon principle; that is, the electronic transition occurs with minimal change in nuclear geometry. However, the equilibrium nuclear distances of the S_0 geometry are in general shorter than that of the excited states due to an increase in antibonding character of the excited state. On a potential energy diagram, the transition is depicted as vertical. Absorption and emission transitions occur in highest probability from the lowest vibrational level of the initial state to all the vibrational levels in the final electronic state. The intensity of the transition to each vibrational level depends upon the size of the square of the vibrational overlap

integral (Franck-Condon factor). For potential energy surfaces where the equilibrium distances of the nuclei are similar, the 0-0 transition will be most intense. When the nuclear geometries differ, however, the overlap integral of the initial state with that of a vibrationally excited state will be largest, with the integrals getting successively smaller with upper and lower vibrational states. This is illustrated in Figure 1.4. Vibrational structure of both absorption and emission spectra is most easily resolved for molecules in the gaseous state. Molecules in solution will have these spectra broadened due to solvent-molecule interactions to give the characteristic broad-band shape of the absorption or emission spectra.

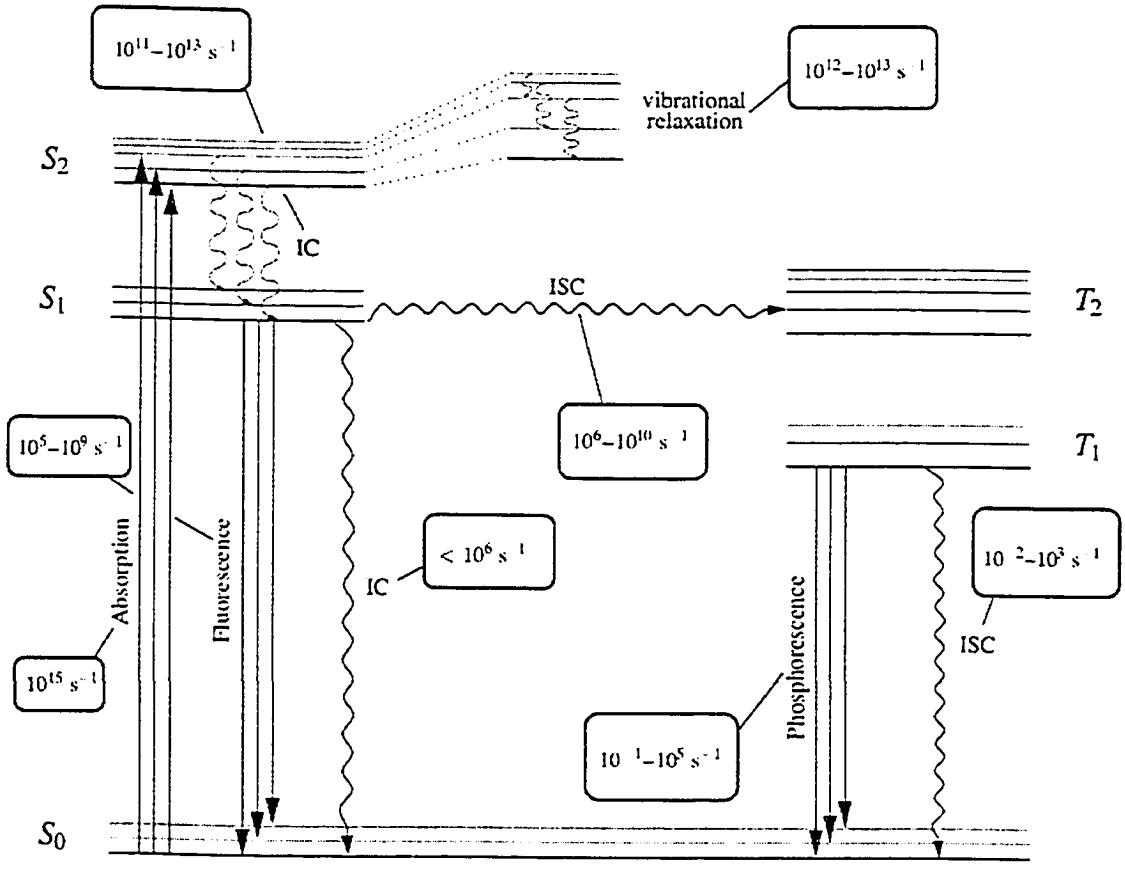

Figure 1.3 Jablonski diagram detailing basic photophysical processes. Energy is increasing in the vertical direction. Figure is reproduced from reference 15.

Non-radiative relaxation pathways between electronic states transform potential energy into kinetic energy. In a classical picture, there is a critical nuclear geometry at which a radiationless transition occurs. At this point, the potential energy surfaces of the initial and final state come close together and electronic coupling can occur between the two potential energy surfaces which make it probable that the molecule can travel from one potential energy surface to another. The molecule moves along the upper surface until it reaches this critical geometry, jumps to the lower surface, and then moves upon the lower surface until it reaches a stable minimum on the lower state surface (Figure 1.5). Molecules that have a large amount of vibrational energy and are non-rigid are more likely to relax along non-radiative pathways.

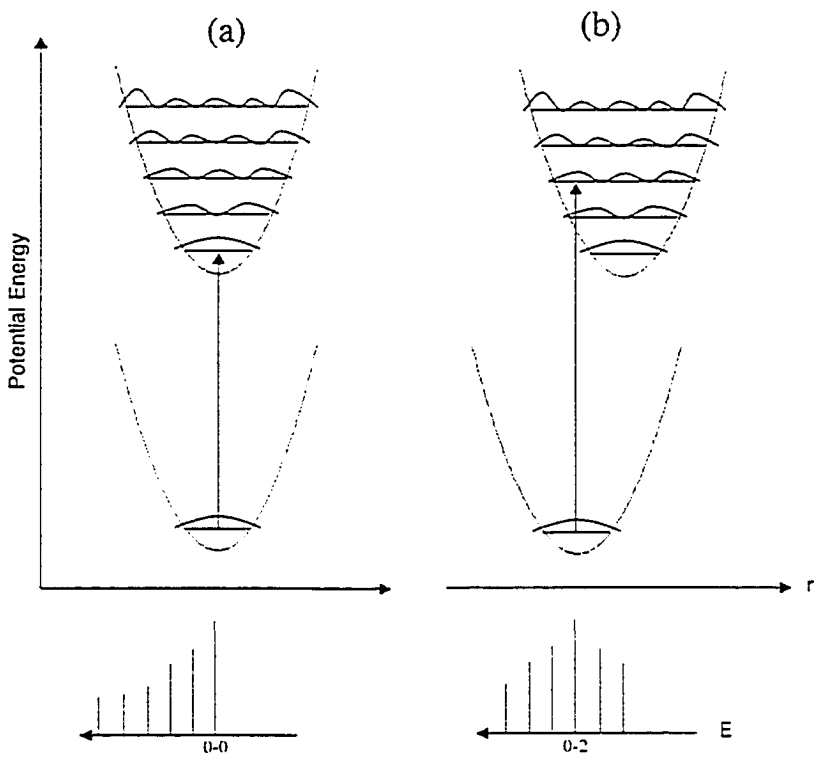

Figure 1.4 Potential energy diagrams illustrating vertical transitions from one electronic state to another. The intensity of the transition is related to the size of the overlap integral. The vibrational structure of the electronic absorption spectra are shown schematically below. (a) Internuclear distances remain the same between the ground and excited state. (b) The upper potential energy curve is displaced to longer bond lengths.

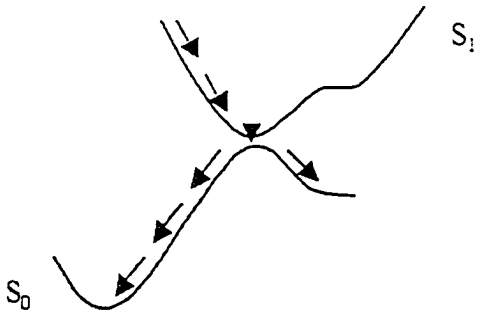

Figure 1.5 Photophysical radiationless transition from an upper potential energy surface to a lower potential energy surface at a critical nuclear geometry.

1.2.4 Excimers and Exciplexes

An electronically excited molecule M^* with two half filled orbitals can participate in charge-transfer interactions with other ground state molecules (M or N) to produce an excited state charge-transfer complex.

$$M \xrightarrow{h\nu} M^* \tag{1.28}$$

$$M^* + N \longrightarrow (M^* N) \tag{1.29}$$

Complexes comprised of two molecules of the same species ($M = N$) are called excimers, while complexes of differing molecules ($M \neq N$) are known as exciplexes. Excimers and exciplexes are stabilized relative to the energy level of the excited monomer. In the ground state, the collision complex between these molecules is only weakly attractive or completely dissociative due to a lack of significant stabilization. Thus, excimers and exciplexes have longer lifetimes than the corresponding ground state complex.

Excimers and exciplexes can relax to the ground state by emission of a photon. Excited complex emission is generally of longer wavelength than fluorescence from the monomer, and because the ground state potential energy surface is dissociative, the emission spectra are completely void of vibrational structure. Ground state absorbance spectra of the monomers do not show a new absorption band for the excimers and exiplexes being produced. The absence of a new absorption band indicates that the

excimer is formed in a two step process detailed in (1.28) and (1.29) above, rather than from a ground state complex of any appreciable lifetime.

Enhanced stabilization of the excited state complex in comparison to the ground state complex can be explained using basic molecular orbital (MO) theory. For a ground state complex, the highest occupied molecular orbitals (HOMO) and the lowest unoccupied molecular orbitals (LUMO) of both molecules will interact with each other to form the MOs of the complex. For the ground state complex, both monomer HOMOs are filled and thus both the bonding and antibonding MOs of the complex are also filled, with no net stabilization of the complex. However, for the excited state complex, the excited state monomer has one electron in each of the HOMO and LUMO, and the ground state monomer has a full HOMO and an empty LUMO. Thus, in the MOs of the excited state complex, the mixed orbitals have three stabilized electrons and only one destabilized electron, resulting in a net stabilization of the complex.

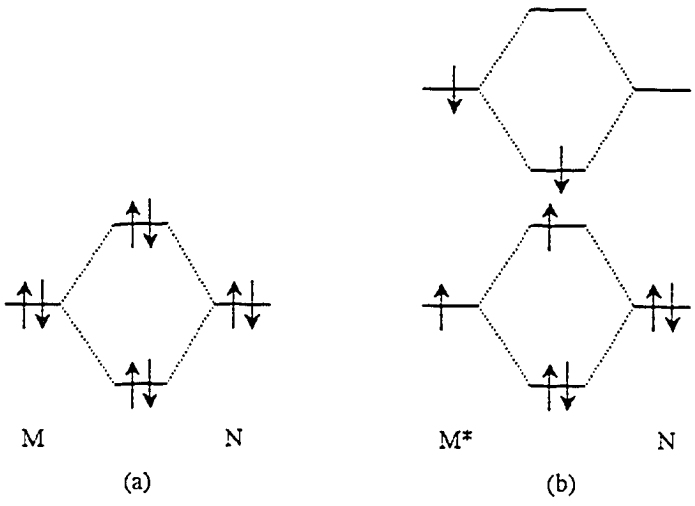

Figure 1.6 Molecular orbital interactions of (a) a ground state complex and (b) an excimer or exciplex.

Excimers and exciplexes most commonly arise from species that are planar aromatic hydrocarbons capable of π-stacking. Pyrene is the classic example of a species capable of excimer formation and emisison.[16] The fluorescence spectra of pyrene in

solution are concentration dependent: at low concentrations, only monomer fluorescence is observed, while at higher concentrations, a broad structureless emission band appears at longer wavelengths at the expense of the monomer emission intensity. Time-resolved emission studies[17] provide confirmation of the dynamic excimer formation process. Directly after the excitation pulse, the excited species is primarily monomer. The excimer band is observed to grow in on the nanosecond timescale at the expense of the monomer band intensity. After ~100 ns, the emission spectrum is identical to that observed under steady state conditions.

For species in which excited state complex formation is a process in competition with other photochemical processes, decreasing the entropic factor involved in bringing two molecules together can encourage complex formation. The tethering of two organic fluorophores by either a molecular chain or by embedding within solid host materials can lead to the preferential production of excimer or exciplex. An elegant demonstration of induced anthracene excimer formation in glasses was reported by Ferguson et. al. in 1973.[18] Anthracene forms a reversible photodimer when excited, and the photoreaction proceeds through the excimer as an intermediate. However, the excimer is too short-lived to be detected in solution. When anthracene dimer is embedded into a soft glass matrix and photolysed, the cross bonds between the anthracene molecules are broken but the face-to-face configuration of the anthracene monomers are retained. The emission spectrum of this anthracene-glass matrix shows clearly an emission band that has all the characteristics of excimer emission, thereby indicating the presence of the anthracene excimer.

1.2.5 Electronic Transitions of Transition Metal Complexes

For transition metal complexes, three different types of photoexcitation are possible: metal centered (MC), ligand centered (LC), and metal-to-ligand charge transfer (MLCT) transitions. Ligand centered transitions involve only the orbitals on the ligand. These are similar to those for free organic molecules, and are comprised of $n \rightarrow \pi^*$ and $\pi \rightarrow \pi^*$ transitions. Metal centered transitions are transitions between the t_{2g} and e_g levels of the d orbitals. For most transition metal complexes, the energy difference

between the t_{2g} and e_g levels corresponds to the visible region of the electromagnetic spectrum, and hence these complexes are often coloured.

A MLCT transition promotes an electron from the *d* orbital on the metal center to a ligand centered π^* orbital. This transition effectively oxidizes the metal center to a higher oxidation state, and thus this transition is strongly affected by the oxidation and reduction potentials of the metal and ligands, respectively. The charge transfer nature of the MLCT state makes it sensitive to solvent polarity. Interaction of the metal *d* orbitals and the ligand π orbital can produce a large spin-orbit coupling, enabling mixing between the singlet and triplet states and facilitating intersystem crossing. For $Ru(bpy)_3^{2+}$ complexes, intersystem crossing from the ^{1}MLCT to ^{3}MLCT surface happens with almost unit efficiency. Luminescence can arise from either MLCT state. From the MLCT state, a ligand-to-metal charge transfer (LMCT) transition may also arise, where an electron can be donated from a neutral ligand back onto the metal center.

1.3 Ultrafast Time-Resolved Spectroscopy as a Means of Studying Photophysical Processes

1.3.1 Ultrafast Pulses

Ultrafast pulses exhibit all the properties of regular, continuous wave light radiation; however, the extreme brevity of the pulse duration causes some properties to seem different. As the pulse duration becomes increasingly short, the frequency bandwidth of the pulse becomes increasingly large. This is a direct consequence of Heisenberg's uncertainty principle, and the principle upon which mode-locking techniques are based. A mode-locked laser requires that a bandwidth of frequencies lase such that their relative phases are locked, thereby producing a pulse where the frequencies overlap constructively.

If the pulse is modeled as being Gaussian in shape, the bandwidth of a laser pulse is related to its pulse length (defined as the full width at half maximum or FWHM) by:[19]

$$\Delta\nu\Delta t = 0.44 \qquad (1.30)$$

where $\Delta\nu$ is the bandwidth in frequency and Δt is the length in time. Because the frequency scale is inversely related to wavelength, the bandwidth in wavelength units is dependent on the central wavelength of the pulse. In the visible range, a red light pulse with a central wavelength of 775 nm and FWHM of 150 fs has a bandwidth of 4.6 nm. The same pulse in the x-ray region would have a much narrower bandwidth, around 0.1 nm. In order to study chemical processes using spectroscopic techniques, an adequate frequency resolution is necessary to use the specified technique. Exceeding a bandwidth of about 5 nm degrades spectroscopic signals past the point of useful information, even for techniques with wide bandwidth tolerance such as absorbance. Hence, for visible light spectroscopy, pulse lengths of 10-100 fs will be the shortest pulses that are practical for studying ultrafast chemical processes. This property of ultrafast processes will likely be the ultimate limit for time-resolved techniques to study chemical systems via pump-probe spectroscopy. However, it is necessary to note that most chemical processes do not require accessing shorter time scales and there is much scope for research on the ultrafast time scale!

Ultrashort pulses are difficult to maintain in length and spectral properties when directed about a laser table. A light pulse travels only 0.33 μm in 1 fs. Hence, when an ultrashort pulse is reflected off a turning mirror, any deviations in surface flatness of greater than 0.33 μm will broaden a 150 fs pulse in time by 1%. When the pulse is directed off many mirrors and through different optical components, the spreading of the pulse in time will lower the time resolution of the experimental data. The rate of pulse spreading can be quantified by a group velocity dispersion (GVD) parameter, which is defined as the derivative of the pulse center velocity with respect to the wavelength.[19] Qualitatively, GVD is a measurement of the difference in light speed from one wavelength to another. A large GVD indicates that the photon velocity has large frequency dependence. Subsequently, the rate of dephasing is high, which leads to the pulse dispersing quickly. Pulse spreading can also be achieved by changes to its spectral shape.

A pulse can have a characteristic spectral shape that is coupled to its temporal shape. Ultrashort pulses can be designed to acquire any shape that is desired for the application at hand. An unchirped pulse is a pulse that is Gaussian in both time and

spectral bandwidth.[19] At all points in time at this pulse, the spectral distribution of bandwidths is equal. Chirped pulses describe pulses that have different spectral distributions throughout the pulse in time. If the front of the pulse is of higher frequency than the end of the pulse, then the pulse is considered down-chirped. An up-chirped pulse has the opposite characteristic. A pulse can develop chirp by traveling through a dispersive medium, in which different frequencies travel at different velocities. In pump-probe experiments, an unchirped pulse is desired because time zero is then equivalent for all wavelengths. This is especially important if entire spectra are being collected at each time delay. Without this characteristic, the spectra collected are not representative of one particular time after excitation. Correction of the data must take place to produce consistent time spectra.

Ultrafast pulses have peak powers in the terawatt to gigawatt range, so focusing the beam must be done with extreme care to avoid the possible production of plasmas or the damage of objects placed at or near the focal point. While the fundamentals of continuous wave optics can be used to describe the behaviour of Gaussian beams, it is important to remember the peak power intensity when designing optical systems to ensure that reflected light does not result in unintentional focal points.

1.3.2 Pump-Probe Spectroscopy

Pump-probe spectroscopy[20,21] is a technique that uses the speed of light as the clock of the spectrometer. At the heart of the spectrometer, a pulsed laser generates ultrafast pulses. Each pulse generated by the laser is split *via* a beam-splitter into two concurrent pulses. Both pulses are directed towards the same target; however, the paths that the pulses follow are different. The speed of light and the path length difference govern the time difference between the incidence of the two pulses on the target sample. This technique becomes chemically useful when one pulse of light is frequency tuned to form an excitation pulse; this becomes the pump pulse and generally reaches the target first to initiate the photoinduced reaction. The remaining pulse, known as the probe, is modified to produce the desired frequency for monitoring the reaction progress. It is

directed along a path of variable length before reaching the target and probing the reaction via a spectroscopic measurement, such as laser-induced fluorescence or absorption. By changing the path length that the probe pulse travels, the time between the initiation of the reaction and the spectroscopic measurement is changed. Measurements taken at each path length are used to build a kinetic trace of the reaction. For each measurement, the chemical process is begun anew by the pump pulse. This technique has the major assumption that the same reaction occurs every time the reaction is initiated. Care must be taken to ensure that the experimental conditions are constant for every measurement to guarantee this assumption.

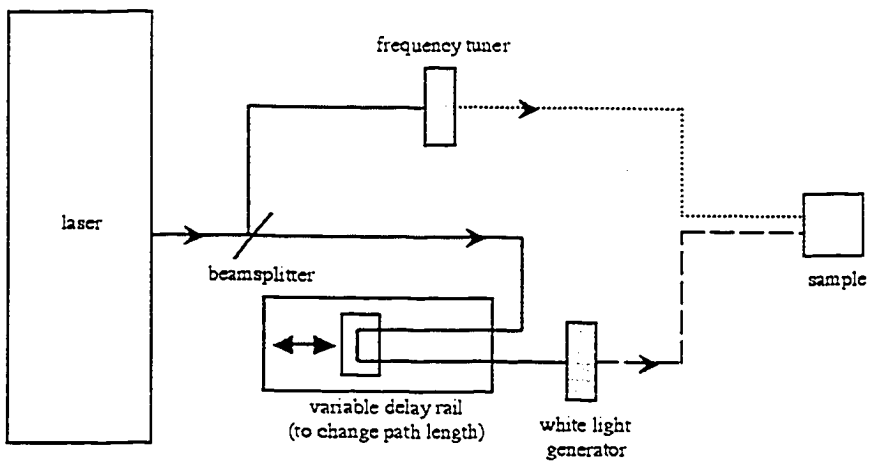

Figure 1.7 Schematic layout of a pump-probe spectrometer. Detection is accomplished after the sample cell.

The speed of light is a physical constant and is unimaginably fast: c = $2.99792458 \times 10^{8} ms^{-1}$. In a familiar time interval of a second, light travels ~300 000 km! Obviously the pump-probe experiment would not be useful for these sorts of time scales as the delay rail needed would be impractically long. The longest practical delay rail is no more than several meters in length, which corresponds to ~10 ns. Thus the pump-probe setup is only applicable for the picosecond and femtosecond time scales. The minimum time interval available is determined by the finest mechanical step size possible that is accurately measurable. Currently, it is common to be able to step down to 3 μm increments, which corresponds to 10 fs steps. However, the actual resolution of the

spectrometer is determined by a combination of step size, and pump and probe pulse length. Temporal resolution is generally determined experimentally using cross-correlation measurements.

Pump-probe spectroscopy is used to study many different reactions in the liquid and gas phase. Most notably, this technique has been developed and demonstrated by Ahmed H. Zewail, whose study of reactions in the gas phase has been coupled with theory to experimentally determine potential energy surfaces.[22-25] Zewail's work highlights the power of careful experimental design and the application of known spectroscopic techniques to probe systems for information on the ultrafast time scale. Adaptation of pump-probe techniques to study liquid-phase reactions yields information of ultrafast photophysical processes, such as vibrational-relaxation[26] and intersystem crossing.[27] The continued development of pump-probe spectroscopy is an essential tool for the study of fundamental chemical processes.

1.3.3 Fluorescence Techniques

Two main techniques exist for the measurement of ultrafast emissions: fluorescence up-conversion, and streak camera measurements. Fluorescence up-conversion uses a pump-probe-like setup to excite the sample. The emission from the sample is recombined with the probe beam in a non-linear crystal, resulting in amplification of the emission, which is then detected. Changing the delay of the probe beam allows for the intensity of emission to be measured as a function of time, thereby allowing for the determination of a fluorescence decay rate. Fluorescence up-conversion has several advantages. The first advantage is its time resolution, which can be in the low femtoseconds. Secondly, up-conversion techniques are only sensitive to high emission flux rates, which allow it to be selective to only the ultrafast emissions. Thus, if a sample fluoresces weakly and phosphoresces strongly with overlapping spectral widths, conventional techniques would be unable to detect the fluorescence signal underneath the overwhelming phosphorescence emission. However, because phosphorescence occurs on much slower time scales compared to fluorescence, its emission flux is too low to be

detectable by upconversion and the detected signal is pure fluorescence. Thus, fluorescence upconversion is a powerful tool in studying ultrafast emissions.

One of the major disadvantages of the fluorescence upconversion technique is its difficulty in setup and use. An alternative to the upconversion technique is streak camera technology, which enables the time-resolved collection of emission without the use of delay rails. The sample is excited by the excitation pulse, and the resulting emission is incident upon the front of the streak camera, where a photocathode transforms the photon train into a proportional electron train retaining the time information of the emission. The electron train is then accelerated through parallel plates that apply a voltage ramp to the electrons, deflecting the electrons proportionally to their position in the train so that the time information of the electron train has been translated into the vertical dimension of space. Finally, the electrons are incident upon a phosphor screen, which luminescences. Each image of the phosphor screen captured has all the decay information of the emission.

While streak camera technology is lauded for its ease of setup and use, it has several major disadvantages in comparison to the upconversion technique. The first is the significant cost of the instrument. As well, streak cameras are fairly insensitive and intense emissions are necessary for detection. This is due to the deflection step where the electrons are spread out vertically. The higher the resolution, the greater the spread of electrons and the thinner the resultant electron density, which results in a lower intensity signal being detected. At low intensities, the signal-to-noise ratio becomes too low for the streak camera data to be interpreted. Finally, the resolution of the streak camera is limited by the reproducibility of the voltage ramps, rendering the femtosecond time scale inaccessible. Despite these difficulties, however, the streak camera is still widely used as an efficient method of collecting time-resolved emission data.

1.3.4 Time Resolution and Deconvolution

Instrumental detection of a time-resolved signal always results in a convolved signal of the true signal $f(t)$ with the instrument response function (IRF) $g(t)$:

$$F(t) = \int_{-\infty}^{t} g(t')f(t-t')dt'. \qquad (1.31)$$

In the cases where the influence of IRF convolution is negligible, Eqn (1.31) simplifies to

$$F(t) = f(t), \qquad (1.32)$$

which can then be analyzed directly. However, in the cases where IRF convolution is significant, the analysis is much more complex.

The instrument response function is defined as being the signal detected when the input signal is infinitely short. In practice, the IRF is measured experimentally and generally has a Gaussian shape. The full width at half maximum (FWHM) of the IRF is a good measure of the resolution of the instrument. Convolution of *f(t)* with the IRF becomes significant when the time constant τ of the signal being measured is less than two orders of magnitude larger than the FWHM of the IRF. In these cases, it is necessary to deconvolute the measured signal in order to recover *f(t)*. However, convolution is essentially a "smearing" of *f(t)* in time and results in overall degradation of the signal resolution, which may be impossible to recover.

While convolution is a well-defined function in the time domain, deconvolution is not. Once the data is transformed into frequency domain via the fast Fourier transform,[2,28-31] however, deconvolution is a simple division operation as long as the IRF is known. Although the method seems feasible in theory, in practice, deconvolution in the Fourier domain is highly sensitive to noise[32] and requires the application of a Fourier cutoff filter to remove high frequency white noise in the original data before the deconvolution can take place. The difficulty with using the high frequency cutoff filter is the removal of all noise from the deconvoluted data. Thus, no mechanism is available for evaluating the goodness of the calculated fit. As well, the artificial application of the filter can lead to artifacts in the recovered signal *f(t)*.

The standard method of analyzing convoluted kinetic data is not the expected two step process involving first the deconvolution of *F(t)* to recover *f(t)* and then the subsequent fitting of *f(t)* to a proposed kinetic model. Rather, *F(t)* is fit via convoluted fitting procedures where convolution of the proposed kinetic model with the measured IRF is then evaluated against *F(t)*. Convoluted fitting is easily incorporated into the standard iterative Levenberg-Marquardt algorithm of non-linear fitting as a final step

before the evaluation of the goodness of fit χ^2 between the collected data and the calculated fit. Figure 1.8 shows a schematic layout of the Levenberg-Marquardt algorithm modified for convoluted fitting.

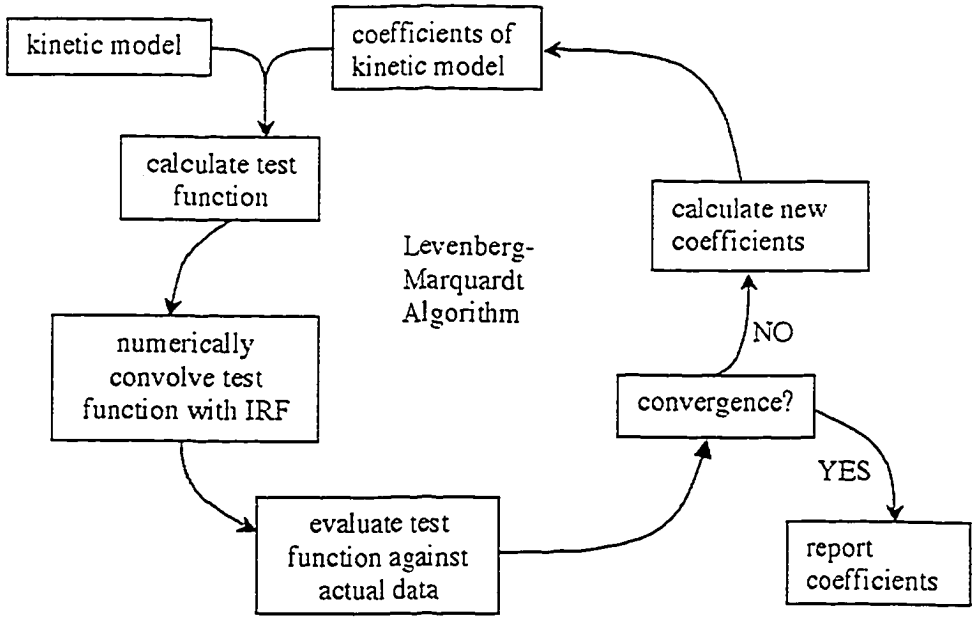

Figure 1.8 Schematic representation of the Levenberg-Marquardt algorithm. Addition of a numerical convolution step allows for convoluted fitting.

Convoluted fitting reduces the robust nature of the Levenberg-Marquardt algorithm, making it highly sensitive to the initial trial coefficients and the overlap position of the IRF with $F(t)$. Translation of the IRF forwards or backwards in time with respect to $F(t)$ results in a calculated fit that is also translated in time relative to the actual data, rendering a good fit impossible. Thus, the positioning of the IRF relative to $F(t)$ must either be determined experimentally or a new variable must be taken into account in the convoluted fitting.

1.4 Nature and Scope of Thesis

1.4.1 Design, Construction and Optimization of a Femtosecond Laser Spectrometer

The instrumentation necessary to study ultrafast processes is only beginning to become commercially available. However, commercial instruments generally lack the flexibility of instruments that are designed and constructed by the user. The challenge is to construct an instrument that is capable of making multiple measurements that are complementary to one another. Such an instrument can then be used to study a chemical system most thoroughly and produce the most representative picture.

Development of laser systems is an iterative process that begins with a proposed design. In this thesis project, the goal was to develop a femtosecond laser spectrometer to accomplish both transient absorption and emission spectroscopy. Once the basic spectrometer is built, it must be tested, improved, and expanded to have greater flexibility. The main challenges are to continually improve the time resolution and the signal-to-noise ratio of the spectrometer while minimizing spectral chirp. Secondary challenges include the development of convoluted fitting software with numerous kinetic models and range expansion of the excitation wavelength and detection wavelengths. Further improvements to the spectrometer include expansion of the spectrometer to accommodate samples in solution, solid and heterogeneous media, reliable automated data collection software and variable temperature capabilities. The second chapter describes the current iteration of the femtosecond spectrometer, which has a transient absorption line and utilizes a streak camera to study ultrafast emission. The transient absorption setup boasts 305 fs resolution, and its time scale traverses the entire picosecond domain up to 5 ns. Streak camera measurements have a minimum resolution of 3.3 ps and are capable of capturing emission data out to 90 ns.

1.4.2 Exploring Dynamic Excimer Formation in Zeolite Host Materials

Zeolites as host materials are interesting because their open framework structure allows for the incorporation of guest molecules into environments that are difficult to

achieve in solution. These environments can considerably alter the behaviour of guest molecules. Spectroscopic techniques can penetrate the zeolite sufficiently to study the physics and chemistry of molecules that have been fully incorporated into the zeolite interior. Chapter 3 uses streak camera measurements to study the physical behaviour of two polyaromatic hydrocarbons, pyrene and 9,10-dicyanoanthracene (DCA), in the zeolite host environment.

Pyrene excimer formation in faujasite zeolite supercages has been inferred by the observation of excimer emission from pyrene embedded zeolite samples. While it is well established that the ground state collision complex of two pyrene molecules travels along a dissociative potential energy surface, the potential energy surface of two pyrene molecules within the same zeolite supercage has been postulated to have an energy minimum due to the strong electrostatic nature of the supercage interior. Thus pyrene excimer formation could be a static process rather than a dynamic process, as excitation of a pyrene ground state dimer would lead directly to excimer formation.

Up until now, pyrene excimer emisison has had an unresolved rise time, although there are some indications that the emission has a non-instantaneous rise time. On the ultrafast time scale, the observation and resolution of pyrene excimer emission rise time is possible. The first section of Chapter 3 explores the dependence of the rise time upon factors such as zeolite counterbalancing cation, zeolite structure, and the presence of co-incorporated solvents.

Excimer emission of DCA in solution is difficult to detect. However, the incorporation of DCA into Y zeolites produces pale yellow samples that exhibit both fluorescence and excimer emission when excited. Analysis of nanosecond streak camera measurements of both emissions indicates that DCA is absorbed to several absorption sites within the zeolite interior. The central section of Chapter 3 studies the photophysical behaviour of DCA/zeolite as a function of loading level and cation dependence.

A combination of ultrafast time-resolved and steady-state methods to study behaviour of DCA in zeolites shows that the excimer emission rise time can be resolved in zeolites. While this dynamic formation of excimer is similar to that of pyrene, the rise times for DCA are loading level dependent, indicating that intercavity movement of

excited state molecules is necessary for excimer formation. The final section of Chapter 3 develops a model based on occupancy probabilities to predict a maximum number of intercavity jumps that an excited DCA molecule can make.

1.4.3 Detection of Non-Thermalized States in $Ru(bpy)_3^{2+}$ Derivatives

$Ru(dcbpy)_2(NCS)_2$, or "RuN_3" dye, is one of the most efficient sensitizers for use in solar cells. Current measurements for electron injection from RuN_3 to semiconductor nanoparticles range from ~20 fs to 50 ps. It is well established that a higher efficiency solar cell results from faster electron injection. Electron injection proceeds extremely rapidly from the initially populated, vibronically non-thermalized, singlet excited state. In order to understand the ultrafast photophysics of RuN_3 and to develop better solar cell materials, a prototype of RuN_3, $Ru(bpy)_3^{2+}$, is intensely studied.

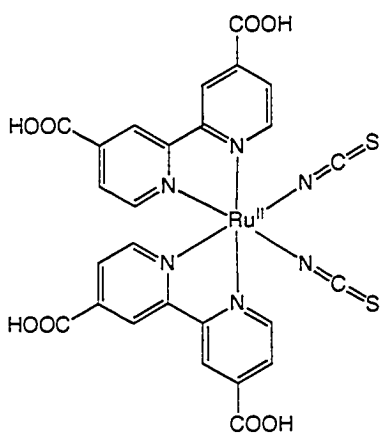

$Ru(dcbpy)_2(NCS)_2$ or "RuN_3" dye

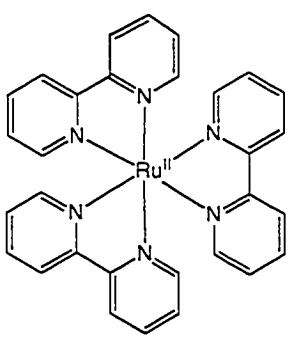

$Ru(bpy)_3^{2+}$

Figure 1.9 Chemical structures of $Ru(dcbpy)_2(NCS)_2$ and $Ru(bpy)_3^{2+}$.

Excitation into MLCT band of $Ru(bpy)_3^{2+}$ produces a vibrationally hot ^{1}MLCT state that is heavily spin-orbit coupled to the triplet manifold. Intersystem crossing[33] from the ^{1}MLCT state to the ^{3}MLCT potential energy surface occurs with nearly unit efficiency in 40 ± 15 fs, and phosphorescence from the ^{3}MLCT state occurs around 600 nm. Although the fluorescence from the ^{1}MLCT state is weak and has a lifetime of 40 fs, it is

detectable on the streak camera as an IRF limited peak. The first section of Chapter 4 explores differences in the fluorescence traces as a function of 4,4'-derivatization of the $Ru(bpy)_3^{2+}$ compound. In order to draw a more comprehensive picture of the origins of the long lived fluorescence tail observed for $Ru(bpy)_3^{2+}$ derivatives, transient absorption spectroscopy is employed. The remainder of Chapter 4 examines the absorption characteristics of $Ru(bpy)_3^{2+}$ derivatives both on the femtosecond and the short nanosecond time scales.

Chapter 2: The Femtosecond Laser System

Building a laser spectrometer is not entirely unlike composing a symphony. The composer has the possibility of using string instruments, brass and woodwind instruments, percussion instruments, harps, etc. However, it is the specific way in which he prescribes the use of these instruments that produces his unique symphony. Similarly, laser spectrometers are constructed from modular components that are similar in every set: laser tables, lasers, mirrors, lenses, detection systems, non-linear optical crystals, etc. It is the specific layout of these components upon the laser table that produces the desired spectrometer. The work involved in producing a spectrometer is iterative, involving trial designs, construction, evaluation, and improved designs, which require further reconstruction. In the end, a spectrometer should be produced that can collect accurate data with a high signal-to-noise ratio and the desired time resolution.

This chapter describes the results of five years of iterative spectrometer building. Housed in room 440 of the Dalhousie Chemistry building is a working laser spectrometer that boasts both femtosecond transient absorption and picosecond time-resolved emission capabilities on the same laser table. The transient absorption system is a pump-probe setup that has two excitation wavelengths and collects time-resolved absorption spectra over the visible region. Time-resolved emission is collected *via* a streak camera with user selected wavelength excitation and single variable wavelength detection. These two systems provide complementary data when studying ultrafast chemical processes.

2.1 Femtosecond Technology

2.1.1 The Laser

The heart of the spectrometer is a compact, turn-key CPA-2001 laser built by Clark-MXR, Inc. Completely contained within the laser housing are the three integrated lasers and all pulse amplification procedures to produce the final laser output. A solid state, fiber-coupled diode laser, at approximately 980 nm output, pumps a self-modelocked fiber ring SErF™ oscillator that uses Erbium doped fiber as the gain

medium. The output of the SErF™ laser is centered at 775 nm with a 25 MHz repetition rate. This provides the seeding for the Ti:sapphire regenerative amplifier *via* a fast photodiode and a Pockels cell system. A timing circuitry board filters and amplifies the photodiode signal to form the basic clock rate, which is then internally divided by 2000 and then a user-defined integer to determine the output repetition rate. This divided clock signal drives the Pockels cell assembly, which determines the timing of the seed injection into the regenerative amplifier. The Ti:sapphire regenerative amplifier is pumped by the frequency doubled output of the ORC-1000 Nd:YAG laser (532 nm). The CPA-2001 laser system is optimized at 1 kHz repetition rate with the output beam centered at 775 nm, and 150 fs pulse width (FWHM). The laser setup is shown schematically in Figure 2.1.

Although the output of the SErF™ laser is an ultrashort pulse centered at 775 nm, the power in the generated pulses must be amplified before usable in a spectrometer. The Ti:sapphire regenerative amplifier is based upon the technique known as chirped pulse amplification (CPA), which allows short pulses to be amplified while high peak powers are avoided during the amplification process.[34] Because the pulses are so short, an amplified pulse will have its peak power in the terawatt region. During any amplification process, the pulse will need to pass through an amplification medium many times. If the pulse were to reach its maximum peak intensity during the amplification process, the medium would be severely damaged. CPA is an amplification technique that allows for this situation to be avoided by stretching the pulse reversibly. The pulse lengthening is accomplished by introducing chirp into the pulse through the use of a diffraction grating or an optical fibre. The peak power, now decreased by three orders of magnitude, is then amplified six to nine orders of magnitude. The highly energetic pulse is then recompressed by a second grating pair, which counteracts the originally introduced chirp to produce a transform limited, femtosecond pulse. The CPA-2001 laser produces transform limited pulses *via* CPA with an average pulse energy of 815 μJ.

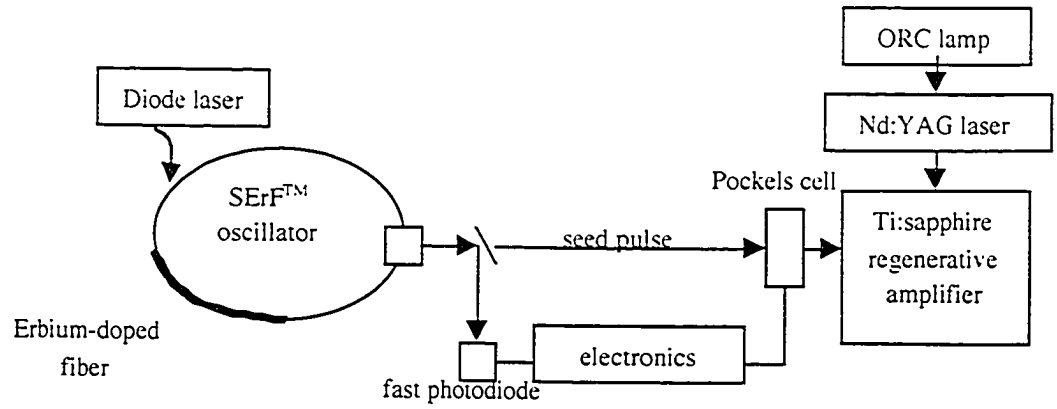

Figure 2.1 A schematic overview of the CPA-2001 laser components. Arrows represent output laser pulses and solid wires represent electronic connections.

2.1.2 The STORC-2001™ Unit

Amplified pulses from the CPA-2001 laser are directed into the STORC-2001™ unit, which is also supplied by Clark-MXR, Inc. The output of the STORC unit is two beams: 1. fundamental (775 nm) pulses, and 2. frequency doubled (388 nm) or frequency tripled (258 nm) pulses. Upon entering the STORC unit, the CPA-2001 output beam is split *via* a beam-splitter. One of the beams from the splitter emerges unaltered as the fundamental beam. The other beam produced by the splitter is directed through the second harmonic generator (SHG) crystal to form the 388 nm radiation with some residual fundamental beam. If frequency doubled radiation is desired, this beam is directed out of the STORC cavity by a 388 nm dichroic thin film mirror. The 388 nm pulse energy, when optimized, is 76.5 μJ. If frequency tripled radiation is required, the second harmonic beam is separated from the fundamental *via* a beam splitter, and both beams are sent through respective delay lines before being overlapped in the third harmonic generation (THG) crystal. The output of this crystal consists of the 258 nm, 388 nm and fundamental beams. By directing the output with 258 nm specific mirrors, the third harmonic is preferentially directed out of the STORC, with an optimized pulse energy of 15 μJ. A schematic of the STORC unit is shown in Figure 2.2.

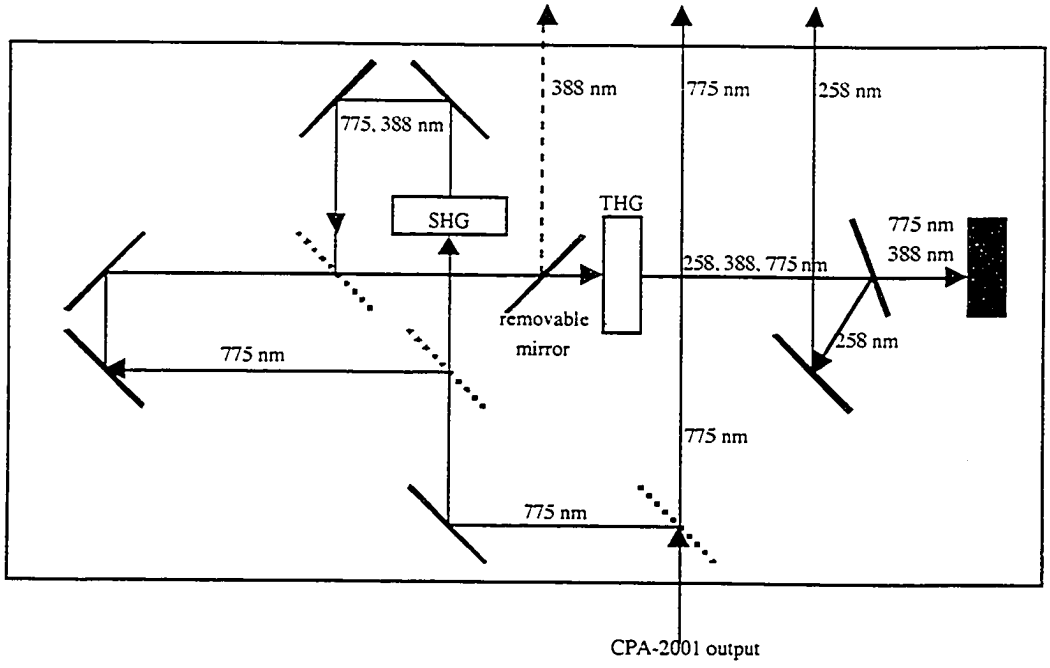

Figure 2.2 The schematic view of the STORC-2001™ unit. The presence of the removable mirror chooses 388 nm output, while the removal of the mirror chooses 258 nm output.

In the STORC unit, the second harmonic generation is produced *via* a phase matched non-linear crystal. A non-linear optical crystal interacts with light non-linearly; that is, the interaction of the crystal with the first photon changes the crystal such that it interacts differently with a second photon.[35] In order for a crystal to exhibit second harmonic generation, it must have electrons that respond to a local electric field with a strong second-order molecular non-linear optical susceptibility term.[36] For high conversion efficiency, the phase of the second harmonic frequency generated must match the phase of the input frequency, a property known as phase matching.[37] An example of a crystal that exhibits these behaviours is potassium dihydrogen phosphate (KDP), which is used for frequency doubling of Nd:YAG lasers.[21]

The third harmonic generation is accomplished *via* frequency mixing of two separate frequencies in the THG. In order for frequency addition to occur, the two beams must overlap spatially and temporally in the THG crystal. The STORC unit overlaps the second harmonic with the fundamental to generate the third harmonic frequency.

2.1.3 The Optical Parametric Amplification (OPA) Unit

Optical parametric amplification uses non-linear crystals and basic optics to modify the fundamental frequency of the laser to produce a low powered beam of femtosecond pulses with wavelengths tunable throughout the visible region. This is accomplished *via* the Vis-OPA unit, built by Clark-MXR, Inc. The basic premise of the OPA is as follows: Upon entering the OPA unit, the fundamental 775 nm pulse from the CPA-2001 is split into two pulses. The first pulse is transformed into chirped white light, generating all wavelengths, while the second pulse is frequency doubled into a high energy pulse, providing the energy for the amplification processes. Overlap of the high energy pulse with the chirped white light in a non-linear OPA crystal results in amplification of the specific wavelength of the white light that is phase matched and both spatially and temporally overlapped with the high energy pulse. Changing the time delay of the white light pulse and rotating the OPA crystal thus chooses a different wavelength to be amplified. The resultant wavelength is amplified again to produce the final output. The OPA process is described schematically in Figure 2.3.

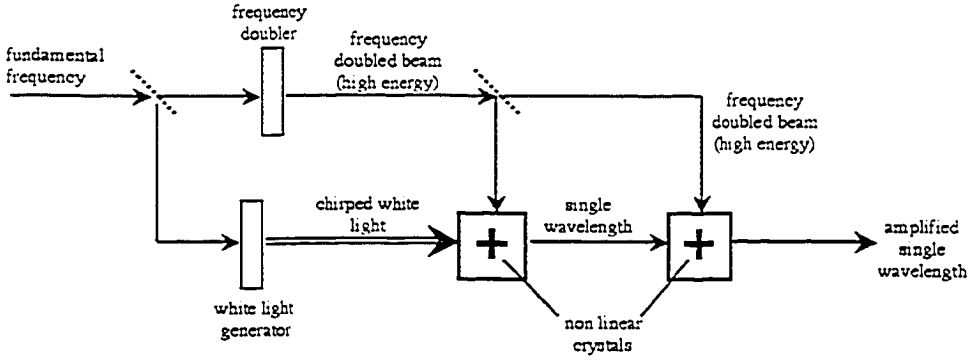

Figure 2.3 A schematic of optical parametric amplification.

The Vis-OPA unit is arranged in a double pass geometry that results in parametric amplification. The fundamental frequency of the CPA-2001 (through the STORC unit) is split *via* a beamsplitter. One of the resultant beams is directed through a variable delay rail before transformation into a chirped white light continuum by focusing upon a

sapphire flat. The second beam is directed through a SHG crystal to produce the second harmonic frequency (SHF), ω_1. The chirped white light continuum and the SHF are then mixed in an OPA crystal. A difference frequency interaction occurs between the SHF and the frequency of the white light (the seed frequency) that is overlapped with the SHF.[37] In such an interaction, the seed frequency, ω_2, extracts another pulse of the same frequency, ω_2, from the SHF. This is known as parametric gain. By conservation of energy, a new pulse of frequency $\omega_3=(\omega_1 - \omega_2)$ is also formed from the interaction. Thus from the mixing of two frequencies ω_1 and ω_2, the high frequency pulse is split into two pulses: a pulse of frequency ω_2, thereby amplifying ω_2, and a new low energy pulse ω_1, which is essentially leftover energy. The amplified frequency, ω_2, is commonly referred to as the signal, and ω_1 is referred to as the idler. Care is taken to remove the idler from the output of the OPA. Parametric gain is achieved for only the narrow band of frequencies of the continuum that satisfy phase matching and temporal overlap. Different frequencies will satisfy the phase matching criterion depending on the angle of the OPA crystal, and hence the output frequency of the Vis-OPA unit is continuously tunable over the 400-700 nm wavelength range by rotation of this crystal. The variable delay rail of the continuum beam is adjusted to maximize the temporal overlap of the desired frequency with the SHG frequency.

In practice, the output beam of the Vis-OPA unit is of very low energy and requires extremely high alignment maintenance to maintain stability. The practical wavelength range of the output beam extends down to only 460 nm, with extreme degradation in both beam energy and stability once the wavelengths are shorter than 490 nm. This particular Vis-OPA design has been acknowledged by Clark-MXR to have a design flaw that results in premature burning of the OPA crystal. Use of the OPA unit is thus minimal in the overall design of the spectrometer.

2.1.4 Mirrors

Directing laser beams about the laser table is accomplished by the use of mirrors. Mirrors for femtosecond applications must be especially flat to prevent pulse spreading. A surface variation of 0.33 μm will cause a 150 fs pulse to spread by 1%.

Two types of mirrors are used in the femtosecond lab: thin film and silver mirrors. Thin film mirrors are composed of a thin (nanometer) film surface on a base. These mirrors are incident angle, polarization and wavelength specific, and their efficiency can be as high as 99%. Thin film mirrors are used as turning mirrors (45° incidence) on the laser table for fundamental (775 nm), SHF (388 nm) and THF (258 nm) beams. Silver mirrors are a thin layer of silver upon a base. These mirrors have lower efficiencies, but are not wavelength, polarization or incident angle specific. The majority of mirrors utilized on the laser table are thin film mirrors to maximize reflective efficiency, with silver mirrors used only when absolutely necessary.

2.1.5 Lenses

Lenses are made of transparent materials that transmit light and change the propagation properties of the incident beam. Beams can be focused or diverged and their shapes can be changed. Lenses are commonly made of materials such as BK7, MgF_2, CaF_2 or quartz glass. Quartz glass will transmit wavelengths that extend into the UV, whereas the BK7 lenses only transmit in the visible region. However, the quartz glass tends to distort the pulse shape more than the BK7 glass. The addition of specific coatings to the lenses can minimize back reflections and maximize the transmission wavelength range of a particular lens.

One of the unfortunate properties of lenses is their ability to introduce chirp into the pulse. For ultrafast applications, chirp becomes extremely significant. The current tendency is to use off-axis parabolic mirrors to accomplish the same function as lenses while minimizing the introduction of chirp. Unfortunately, this introduces complexity into any optics line because the optics can no longer be set up linearly. The current setup of the femtosecond spectrometer uses lenses rather than off-axis parabolic mirrors.

2.1.6 Computer Interfacing and Control

The entire femtosecond lab is controlled by a G4 Macintosh computer. Interfacing between the computer and each instrument is accomplished by standard GPIB and RS-232 protocols. Individual controller boxes, if not available commercially, were built in-house by Brian Millier, who also built the basic drivers for the controllers. The remainder of the instruments either came with drivers or were directly handled using standard GPIB communication virtual instruments (VIs). All other software was written by the author as part of this thesis project.

The programming language used to produce all the data acquisition and analysis software is LabVIEW 5.1, a visual programming language produced by National Instruments. Each program designed by the programmer has a front panel with control and indicator objects, which allow the user to interact with the program, as well as a block diagram panel, which contains the code to run the program. In contrast to text-based programming languages, LabVIEW is completely based upon data-flow pathways that link functions together. This difference is evident visually as the block diagram consists of icons representing functions, wired together in a flowchart style. The availability of all the necessary input functions determines when a function will execute, unlike a text-based language, which is sequential in execution.

There are many advantages to developing an application program in LabVIEW. First of all, the end product has a pleasing user interface, which allows users to view collected data and make decisions on the status of experiments, without the programmer needing any experience in graphical programming. Secondly, LabVIEW is fully integrated for easy communication with instrumental hardware through GPIB and RS-232 interfaces. Finally, the number of available functions in LabVIEW for data processing and manipulation make it a comprehensive package, such that the programmer can be relatively inexperienced and still produce the desired application. These functions are also largely accessible to the programmer so that they can be modified to become more efficient or to suit a particular need.

2.2 The Transient Absorption Spectrometer

2.2.1 Basic Layout and Design

UV-visible absorption spectra are distinctive characteristics of molecules that have chromophores in the ultraviolet and visible regions. The intensity, shapes and positions of absorption peaks are all useful indicators of the presence or absence of molecular species. By monitoring the changes in absorption spectra as a function of time, the growth and decay of specific bands allow the researcher to determine the sequence of reactions that are taking place over the time window of the experiment. The absorbance system is designed to allow the user to monitor time-resolved visible absorption spectra on an ultrafast time scale.

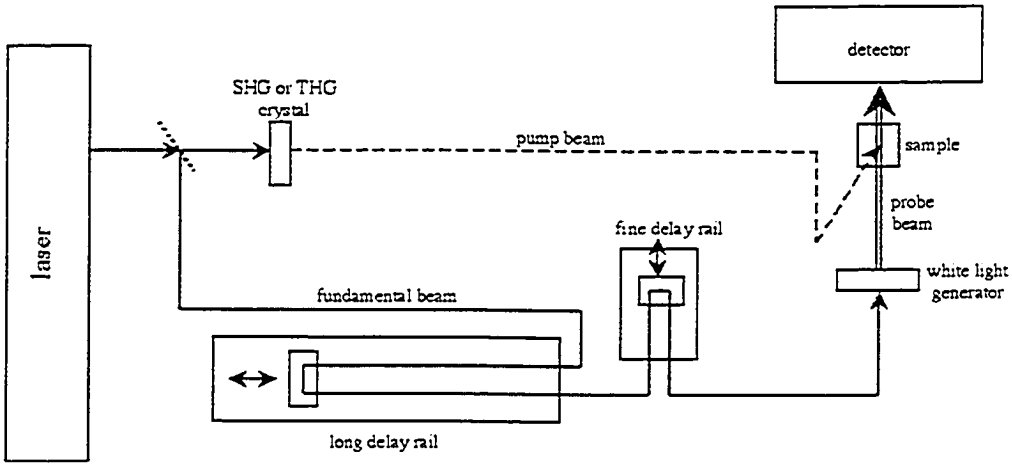

Figure 2.4 The schematic layout of the transient absorption spectrometer.

The layout of the transient absorption spectrometer is shown schematically in Figure 2.4. A basic pump-probe design is used, with the pump beam being the second and third harmonic frequencies of the laser output, 388 nm and 258 nm, respectively. This beam is incident upon the sample cell with front face excitation. The probe beam is composed of broadband femtosecond pulses generated by the fundamental frequency

(775 nm) by focusing the beam into a transparent medium just prior to incidence upon the front face of the sample cell. Two delay rails, a fine stepping rail and a longer, coarser rail, are used to change the path length of the probe beam. After passing through the sample, the intensity of the broadband probe pulse as a function of wavelength is measured both with and without the pump beam. Calculation of the absorption spectrum of the transients generated is accomplished by the standard equation:

$$A(\lambda) = \log \frac{I(\lambda)}{I_0(\lambda)}. \qquad (2.1)$$

Only two fundamental components, the CPA-2001 laser and the STORC-2001™, are used for the absorbance system. In the pump-probe setup of the absorbance system, the beam-splitter that splits each pulse into the pump and probe pulses is contained in the STORC unit. Both the pump and probe beams always travel exactly parallel to the table, at a height of 108 mm, measured to the center of the beam. The second or third harmonic frequency that emerges from the STORC unit is directed to the sample cell holder using thin-film mirrors. This beam is sufficiently well collimated to not require further optical adjustment, and travels throughout the table as a circular beam with a 7 mm diameter until it is focused upon the sample cell. The incident angle of the pump beam is 15 ° from normal through a plano-convex lens with 50 mm focal length. At the focal point, the energy of the pump beam is sufficient that, where the beam waist is less than 1 mm, the beam is capable of etching high quality quartz. Thus extreme care must be used in alignment of this beam to prevent damage to the sample cell. A soft focus of beam waist ~1.5 mm is desired at the sample cell, and the beam is allowed to pass through its focal point and begin expansion before striking the sample cell. This has a three-fold purpose. Firstly, the focal point is not at the center of the sample cell and hence diminishes the accidental etching of the sample cell surface. In addition, the sample cell itself is recessed in both its casing and the sample cell holder, and the focal point of the beam allows it to narrowly miss the sample cell holder, as shown in Figure 2.5. Finally, avoiding a focal point in the sample will avoid most two-photon processes of the sample.

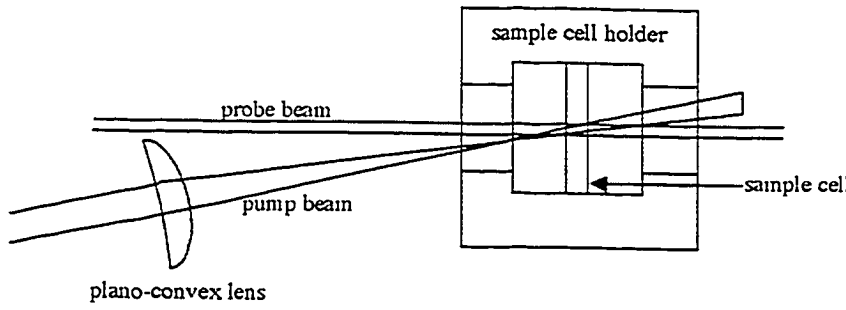

Figure 2.5 Focus of the pump beam onto the sample cell chamber (top view). The focal point of the pump beam occurs before the sample cell and allows the beam to narrowly avoid the wall of the sample cell holder.

Once the pump beam is aligned, it is not adjusted for the remainder of the experiment. This is to ensure the consistent excitation of the sample every time the experiment is repeated, independent of the time delay. The consistency this produces allows the magnitude of peaks from one time delay to be compared quantitatively to another.

The probe, or monitoring, beam emerges from the STORC unit as the unchanged, fundamental beam. It is directed about the table by thin film mirrors. Like the pump beam, the probe beam is well collimated upon exiting the STORC unit and has a circular beam diameter of 8 mm. The probe beam is directed through two variable delay rails: the Parker Rail Table and the NanoStepper. The Parker Rail table allows the user to choose work with time delays up to 7 ns, with resolution down to 188.3 fs. The NanoStepper allows the user to probe the first 500 fs of the experiment with a fine resolution of 33.36 fs. Both rails are fully automated and can be controlled either manually or by computer. Alignment of the beam through the delay rails must be perfect so that movement of the rails to change the path length of the probe beam does not affect the alignment of the subsequent optics. Once the fundamental 775 nm beam passes through the second delay rail, it is directed into the sequence of optics that generates, collimates and focuses the white light monitoring beam through the sample.

The optics that generate the monitoring beam, and direct it through the sample cell and into the spectrograph are arranged linearly. This design is not only space efficient but also facilitates ease of alignment, whether the alignment needs to be slightly adjusted or all the optics removed and the line rebuilt. The first component of the optical line is the Berek's Compensator (New Focus), the alignment and retardance of which are set such that the Berek's Compensator (BC) acts as a half wavelength waveplate for 775 nm radiation. A half wavelength (1/2 λ) waveplate rotates the polarization of plane-polarized light. This waveplate, together with the Glan-laser polarizer (Thorlabs) that directly follows it, forms a variable attenuator with the output polarization determined by the orientation of the Glan-laser polarizer. The Glan-laser polarizer is a polarizer that is capable of withstanding high power radiation, including the terawatt power of the femtosecond pulse peaks. Orientation of the Glan-laser polarizer is set such that the output radiation is polarized in the desired direction, usually 55° from the polarization direction of the excitation beam. The fundamental beam is then focused by a 100 mm focal length BK7 broadband antireflective (BBAR) coated planoconvex lens into the white light generator. The white light generator is either a 1 mm thick sapphire flat or water contained in a 30 mm cell with quartz windows. The broadband radiation generated immediately begins to spread and is collimated by an achromatic MgF_2 lens with a focal length of 50.8 mm. If the water cell is used, a Schott colour glass filter (S8612) is inserted to selectively attenuate the red wavelengths, and an iris is used to selectively choose the stable center of the broadband beam. Finally, the probe beam is focused using an achromatic lens (150 mm focal length) through the sample cell directly onto the fibre optic cable, which directs the light into the spectrograph and photodiode array (PDA) detector. A neutral density filter wheel attenuates the probe beam just prior to the fibre optic holder. A schematic of the optics line is shown in Figure 2.6.

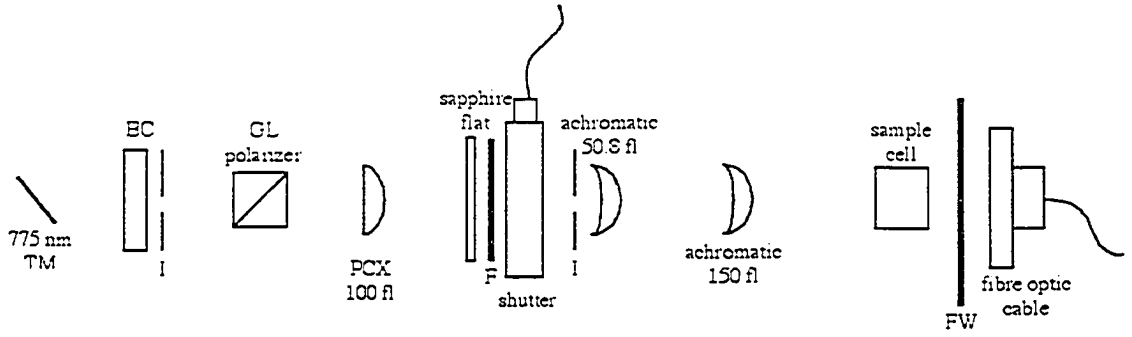

Figure 2.6 The optics line that generates and focuses the probe beam. The fundamental beam enters on the left and is directed through the center of all the optics from left to right. Substitution of the sapphire flat by the water cell produces the other configuration of the optics line. Two irises are necessary for alignment purposes; the second plays a dual purpose in selecting the central section of the continuum. TM: turning mirror, BC: Berek's compensator, I: iris, GL: Glan-laser, PCX: planoconvex, fl: focal length (mm), F: filter (optional), FW: filter wheel (optional).

The generation of ultrafast broadband pulses by focusing ultrafast pulses into transparent condensed media is a widely used technique but a poorly understood phenomenon.[38] It is largely proposed that self-focusing of the beam occurs once a critical power level is exceeded. Once self-focusing occurs, continuum generation with both Stokes and anti-Stokes wings is produced. For the purposes of the probe beam, only the anti-Stokes wing is necessary. The intensity of the anti-Stokes wing falls off quickly, rendering the intensity in the blue wavelengths very small. Several properties of the generated continuum are of note, namely, that the spectral width is dependent upon the generation medium, its polarization is the same as the input polarization, and the pulse produced is up-chirped. The final emission consists of a central white section with low divergence, surrounded by a rainbow like conical emission. The second iris selectively removes the conical emission, which has much lower spectral and shot-to-shot stability than the central portion.

While the water cell introduces considerably more chirp and pulse spreading into the probe beam, it has several advantages over the use of the sapphire flat. The white light produced has a much more consistent shot-to-shot stability that is independent of the specific portion of the solution cell being used and the input power of the fundamental beam. Conversely, the sapphire flat has the potential to produce extremely high shot-to-

shot stability but is inconsistent from one day to the next and is highly dependent on the exact alignment of the beam upon the flat. Because extremely low input powers are necessary to produce stable white light, alignment of the sapphire flat is challenging. The low input power upon the flat results in low output power, which can degrade the signal-to-noise ratio of the resulting spectra. The much higher intensity white light produced by the water cell requires attenuation, but is more consistent in the signal-to-noise ratio. Finally, the water cell produces a longer anti-Stokes tail, and spectra are reliable down to 400 nm, while the low intensity of the high frequency radiation produced by the sapphire flat measures accurate absorption spectra only down to 450 nm. Figure 2.7 compares representative spectral profiles of continuum generated by both methods.

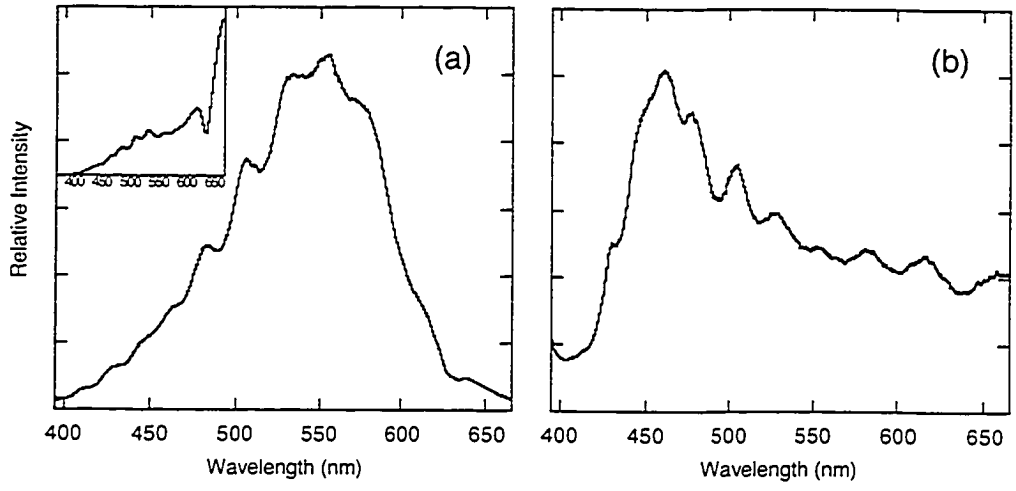

Figure 2.7 Spectral profiles of continuum generated by focusing the 775 nm fundamental beam into (a) the water cell, and (b) the sapphire flat. The inset of (a) shows the continuum before filtering by S8612.

Both methods of continuum generation are sensitive to heat generation as a by-product of self-focusing. This is most noticeable in the water cell, where the focused beam path traveling through the solution produces a trail of tiny bubbles, presumably due to localized boiling of the water. In order to ensure that the white light generator equilibrates at a constant temperature, the fundamental beam is focused upon the flat or

cell for at least thirty minutes before data is collected. The shutter that blocks the probe beam from the sample cell is placed after the white light generator so that no temperature differences are introduced into the white light continuum during the course of an experiment.

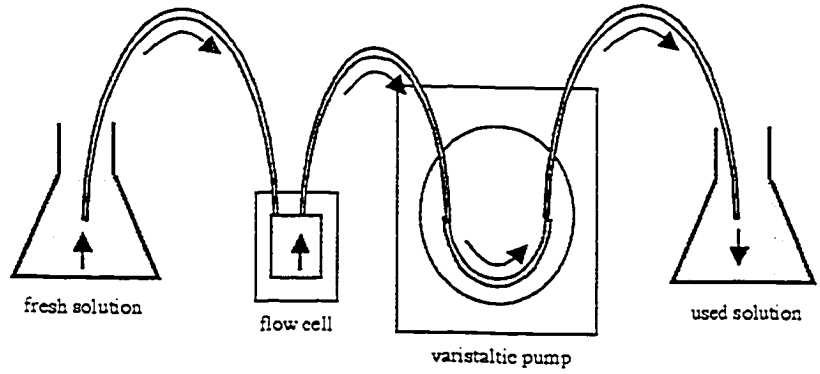

Figure 2.8 A schematic diagram of the pumped solution. The arrows indicate direction of flow. Solutions are shown separately for clarity.

The sample cell is a 1 mm path length quartz flow cell made by Hellma. All samples must be in solution to be studied with the absorbance system. The cell has a width of 1 cm and flow direction always introduces fresh solution from the bottom to the top of the sample cell. The entrance of the flow cell is directly connected to fresh solution. A varistaltic pump, connected to the cell's exit, drives the flow of solution towards the collection container (Figure 2.8). Masterflex precision Tygon 2000 tubing is used to connect the flow cell to the solution and in the drive belt of the varistaltic pump. Constant flow of the solution is necessary to renew the concentration of the starting material, as well as to remove any photoproducts and to prevent secondary photochemistry from interfering. The flow rate used in the absorbance setup is 116.5 mL / min, corresponding to fresh solution every 8 laser shots. The minimum amount of solution necessary to run an experiment is 50 mL, and in practice, the solution is recycled through the flow cell until the buildup of photoproducts or depletion of starting material renders the measurements unreliable. The absorbance of the solution at the chosen

excitation wavelength should be between 0.4 and 0.6 (1 mm path length). In order to minimize concentration changes by evaporation of the solvent, the solution flask is sealed with laboratory sealing film and small openings are used for the insertion of tubing. A portable fumehood vent is located just above the sample flask for user safety.

Once the monitoring beam has passed through the sample cell, it is attenuated by a neutral density filter wheel before being collected by a fiber optic cable and directed into the SpectroPro-300i Imaging Spectrograph (focal length 0.300 m), built by Acton Research Corporation. The entrance slit is set at 290 μm and the fiber optic aligned such that its exit slit is aligned with the entrance slit. The central wavelength of the spectrograph is user defined and set from the computer *via* a GPIB interface with the spectrograph. Aligned on the exit of the spectrograph is the ST-116 PDA by Princeton Instruments, Inc. The PDA is evacuated and thermoelectrically cooled to -20°C. Both units were calibrated together using a mercury lamp as a discrete line source. The spectral resolution of the fiber optic-spectrograph-PDA setup was determined to be 2.7 nm (FWHM). The minimum electronic data transfer time of the PDA data is 6 ms; thus, it is impossible to trigger the PDA to collect discrete experiments (one laser shot at a time) because of the kilohertz repetition rate of the laser. The PDA's controller box independently clocks the collection of data for a user-defined amount of time, which corresponds to an approximate number of shots. Due to the saturation of the diodes on the PDA, it was found that 50 ms is an appropriate amount of time to collect data and does not require large amounts of external filter attenuation. Partial saturation of the PDA is characterized by blooming of individual diodes to share charge with neighbouring diodes, decreasing spectral resolution of the instrument. Full saturation is recognized by a maximum intensity reading, beyond which the PDA is no longer sensitive. In order to maximize the number of individual laser experiments measured while minimizing data transfer time, the data are accumulated on a chip in the controller box, and then transferred to the computer *via* a GPIB interface. This is repeated as specified by the user and the data combined through software averaging.

2.2.2 Current Experimental Capabilities

The pump-probe spectrometer offers great flexibility to the user. At present, it is capable of studying systems in solution by transmission transient absorption spectroscopy with the choice of two excitation wavelengths: a soft UV wavelength at 388 nm, and a higher frequency excitation wavelength of 258 nm.

The results of the pump-probe experiments are time-resolved absorption spectra. Spectra can be corrected for sample fluorescence and background counts. Each spectrum has a wavelength width of 270 nm, and the wavelengths can range from 395 nm to 750 nm, depending upon the broadband source and the choice of cutoff filters used. Table 2.1 summarizes the wavelength ranges for each setup.

Table 2.1 Wavelength ranges for combinations of white light generators and filters.

White Light Generator	Filter(s)	Wavelength Range
sapphire plate	none	450 - 750 nm
water cell	S8621 (colour glass filter)	395 - 665 nm
water cell	650 nm cutoff filter	410 - 700 nm

By the collection of a series of time-resolved absorption spectra, a two-dimensional data set can be collected that describes the change in absorption spectra as a function of time. Slicing the data set to remove a narrow wavelength region provides kinetic data for a specific absorption band. More sophisticated techniques of chemometric analysis, such as multivariate analysis or principle components analysis (PCA), can be used to separate species components and their kinetic information provided that the data set collected has uniformly spaced time intervals and chirp is insignificant. Kinetic data can be collected using either the NanoStepper or the Parker Delay Rail, but not both simultaneously. Table 2.2 summarizes the time ranges available to the user.

Table 2.2 Time ranges available for pump-probe experiments.

Delay Rail	Smallest Step Size	Time Range
NanoStepper	33.36 fs	-100 to 500 ps
Parker Delay Rail	188.3 fs	-0.5 to 5 ns

Because the pump and probe beams are both polarized, the transient absorption spectrometer has the capability of making anisotropy measurements by changing the polarization direction of the probe beam with respect to the pump beam. These measurements are possible for molecules in solution only on the femtosecond timescale before molecular tumbling, which proceeds on the picosecond timescale, destroys the coherence of the excited molecules. By exciting the sample with a polarized pulse, only those molecules whose transition dipole moment vector components are parallel to the excitation polarization will be promoted into their excited state. The coherence that this generates in the excited state can be measured by a polarized probe pulse, which interacts with the transition dipole moments of the excited state.

Anisotropy is defined[39-41] as the difference in the number of excited state molecules with transition dipole orientations parallel ($I_{\parallel}$) and perpendicular ($I_{\perp}$) to the excitation polarization,

$$r = \frac{I_{\parallel} - I_{\perp}}{I_{\parallel} + 2I_{\perp}}, \tag{2.2}$$

where the denominator acts as a normalization term and represents the total number of excited state molecules. The overall anisotropy is dependent upon the orientations of the excited state transition moment being probed, $\mu(t)$, relative to the ground state transition moment that was initially excited, $\mu(0)$, as a function of time, Eqn. (2.3). τ is the lifetime of the excited state species being observed.

$$r(t) = \frac{2}{5}\int_0^{\infty} \left\langle P_2[\mu(0)\mu(t)] \right\rangle \exp\left(-\frac{t}{\tau}\right) d\left(\frac{t}{\tau}\right) \tag{2.3}$$

Time-resolved anisotropy measurements are useful for measuring changes in the transition dipole directions of excited states, which can be interpreted as changes in symmetry and structure of the excited state. These processes must be carefully

determined to be different from rotational diffusion of the molecules into random orientations, which is the main process that degrades the size of *r(t)*.

It is often of interest to study only the population kinetics of the system without anisotropy effects. Anisotropy equals zero when the Laplace transform in Eqn 2.3 is equal to zero:

$$P_2(\cos\theta) = 3\cos^2\theta - 1 = 0 \qquad (2.4)$$

The resultant angle, 54.7 °, is often referred to as the magic angle. When the absorption measurement is carried out with the polarization of the probe beam oriented at the magic angle with respect to the pump beam, the intensity of the signal recorded is $I_{\parallel} + 2I_{\perp}$ and represents the population kinetics of the system. The pump-probe spectrometer is most commonly used in this mode. Because the two pump wavelengths have different polarizations, the orientation of the probe beam must be adjusted accordingly by adjusting the orientation of the Glan-laser polarizer that directly precedes broadband generation.

2.2.3 Data Consistency

There are several factors to consider when optimizing the absorbance system for maximum consistency. The first is laser stability, both in shot-to-shot reproducibility as well as long time consistency. Laser stability is crucial to this experiment because the white light probe used is assumed to be constant throughout the time it is collected as the reference continuum and the time it is collected as a transient probe. In order to make the experiment less sensitive to laser stability, a large number of accumulations are performed, as well as a large number of averages of collected data. The absorbance spectra collected are also averaged to produce the most representative data possible.

When collecting a series of time-resolved measurements, the user has the option of evaluating each spectrum individually as it is collected, or allowing the instrument to collect the data completely without requiring the user's presence. While the latter seems appealing to the experimentalist, it is unadvisable to collect experimental data this way. An automatic data collection is useful, however, to determine the parameters of the kinetic data to be used for high quality collection. Despite its time-consuming and

tedious nature, continual spectrum evaluation produces high quality data and allows the user to remove misfired shots or to correct any instrumental problems immediately. Instrumental problems may include malfunctions of the laser, most commonly loss of modelock, or sample setup problems, such as leaks and bubbles. All of the data presented in this thesis have been collected with individual spectrum evaluation.

One of the challenges of evaluating every spectrum is to evaluate each one objectively, without choosing spectra that "fit" with the user's preconceived notion of what the kinetic data should show. In order to combat this, the data can be collected either in the forwards or backwards chronological order. Further randomization by the user is encouraged. Collecting all the data chronologically is discouraged so that gradual systematic errors, such as dropping of laser power or changes in the solution being studied can be detected and minimized.

A large consideration in pump-probe experimental data consistency is reproducible overlap of the pump and probe beams on the sample cell as the path length of the probe beam is changed. Any change in overlap is normally due to imperfections in alignment of the delay rail optics. Ideally, the flux of pump photons at the sample cell should be constant throughout the beam diameter. However, in practice, this is not the case and hence any movement of the probe beam within the pump excitation area will be sensitive to the changing number of excitation photons. This is illustrated in Figure 2.9, with decreasing photon flux from the center of the beam diameter to the perimeter. The probe beam area is always smaller than the pump beam area. This is to maximize the absorbance signal, because it is a comparison of a reference signal to a transient signal. If there is no transient generation in part of the area being probed, then the difference between the reference and transient signals become much smaller and the experiment is less sensitive overall. In practice, the pump pulse is only marginally larger than the probe pulse.

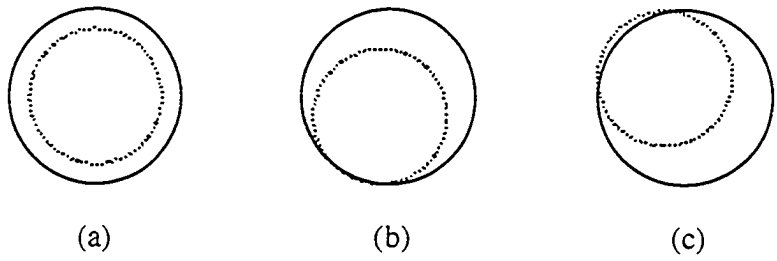

Figure 2.9 The effects of changing pump-probe overlap, with the flux represented by shading and the dotted circles representing the probe overlap area. Movement and flux are exaggerated for clarity. (a) The monitoring beam probes the area of highest flux, and will detect the highest intensity of transient species. (b) The probe covers an area with lower flux and will detect fewer transients. (c) The probe covers a small area where the flux is zero and will detect the fewest transients. If peak heights are compared for these three experimental measurements, false changes in transient concentrations may be implied.

The effects of inconsistent pump-probe overlap are illustrated by Figure 2.10. Figure 2.10 shows the detection of the chloranil triplet in dichloromethane measured at three different time delays. Because the lifetime of the chloranil triplet is known to extend into the microseconds,[27,42-44] the intensity of the chloranil triplet should appear to remain constant over the first nanosecond.

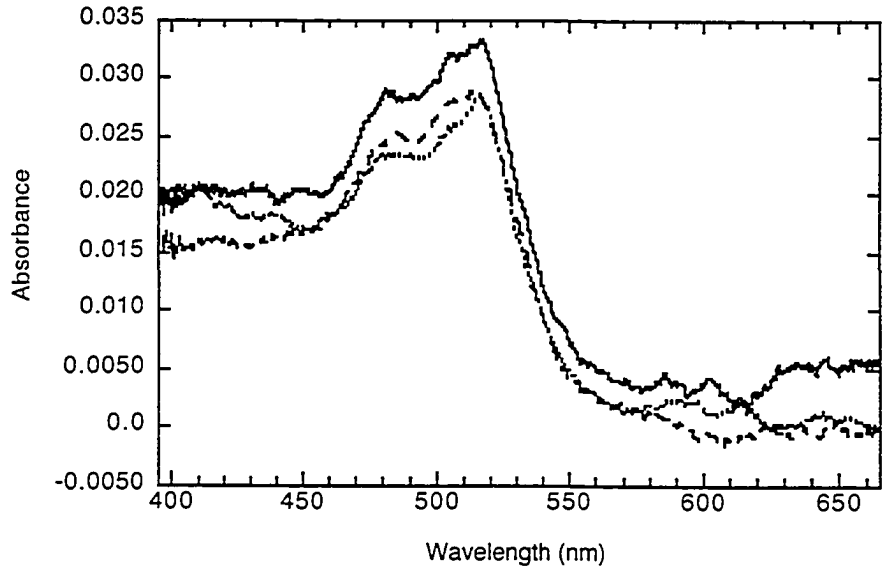

Figure 2.10 The spectra of the chloranil triplet measured at 200 ps (– –), 400 ps (···) and 500 ps (—). Differences in height are due to changes in pump-probe beam overlap.

In order to have consistent pump-probe overlap at the sample cell, the probe beam position is adjusted minutely using the last mirror of the fundamental beam. This mirror directs the 775 nm radiation into the broadband generation optics and allows for very fine adjustment of the probe beam position. Alignment by eye is not always accurate; hence, a technique was developed to increase the accuracy of the process. This technique involves the use of a mock sample cell case with a piece of business card replacing the quartz faces of the cell itself. Because the pump beam causes the card to fluoresce blue, the excitation beam is visible to the eye and also causes a blemish on the card. The blemish can then be marked using a fine permanent marker of blue or black, which fluoresces red when placed in the pump beam, so the pump beam area can be compared to the mark area. It is important that the mark is placed correctly and checked. The probe beam area is then compared to the mark without the pump beam on. Because the probe radiation is white, the area of the probe beam best corresponds to that of the pump beam when the probe light is most quenched by the dark mark on the card. By following this procedure at the beginning of each new time delay, very reproducible results can be produced, as shown in Figure 2.11.

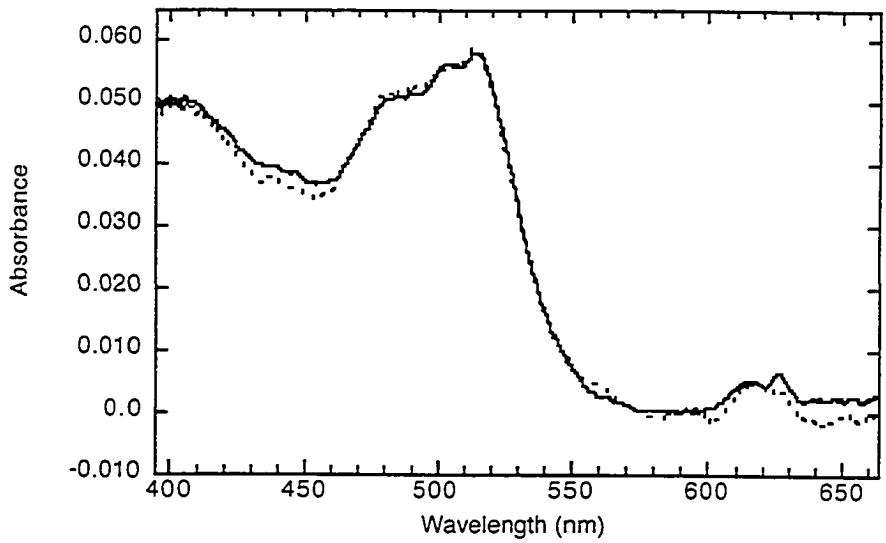

Figure 2.11 Measurement of the chloranil triplet 300 ps (---) and 500 ps (—) after excitation with 388 nm radiation, using the consistent pump-probe beam overlap technique.

In practice, overlap adjustment is only necessary when using the Parker Rail table. This may be due to the increased difficulty of having perfect alignment over the distance of the longer rail, or the rail table itself may not be completely flat. As well, the pump-probe overlap can only be adjusted if the adjustment process does not significantly change the path length of the probe beam. When collecting time-resolved spectra with very fine temporal steps, adjustment of pump-probe overlap will introduce significant error into the time delay of the measurement. This point is illustrated in Figure 2.12, where the two-photon absorption spectra of 2-methylnapthalene are shown, with each spectrum measured 100 fs apart. The wavelength of the peak varies systematically with the time delay; over this short region, the relationship is almost linear. Figure 2.12 (a) shows the spectra when the pump-probe overlap is not adjusted and the time-delays are accurate. Contrast this with Figure 2.12 (b), where pump-probe overlap has been adjusted for each spectrum. The linear relationship is no longer measured because overlap adjustment has changed the probe beam time delay by up to ± 60 fs; *i.e.* the path length of the probe beam has been changed by up to ± 18 μm. This difference is highly significant when using a step size of 100 fs.

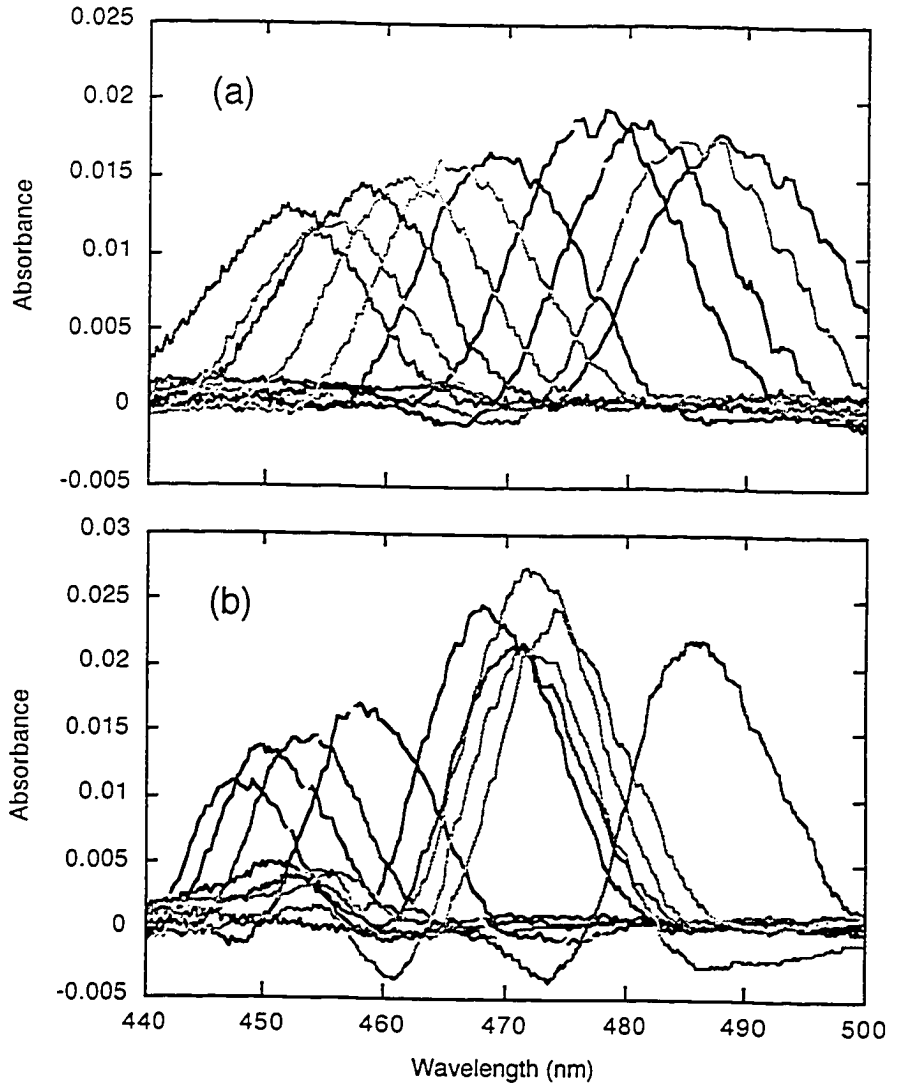

Figure 2.12 The effect of adjusting pump-probe overlap when the step size is very fine (100 fs). (a) The variation of the peak wavelength varies linearly with each successive 100 fs time delay without pump-probe overlap adjustment. (b) Pump-probe overlap adjustment introduces changes in the probe beam path length that are long enough to introduce significant error into the time delay.

2.2.4 Software

Software is a necessary component of every instrumental system, and consists of two main types. The first variety of software acts as an interface between the user and the hardware components of the instrument to facilitate data collection. The second category

of software is used for analysis of the data collected. While some of this software is commercially available, such as Kaleidagraph and Matlab, it is necessary to write specialized data fitting software that allows for convoluted fitting. All the software is designed with user ease in mind, so that subsequent users of the femtosecond transient absorption system can focus on chemical research.

2.2.4.1 The Absorbance Program

The main goal of the absorbance program is to facilitate data collection. It is designed to maximize flexibility for the user while maintaining automation. The user can choose to collect a spectrum at a single time delay, or run a series of up to 50 spectra sequentially at different time delays. Once a series of data is collected, whether in separate stints or all at once, this program has the capability of analyzing the data to extract kinetic information at specific wavelengths. All the spectra and kinetic data collected can be saved in text files that can then be plotted and analysed for kinetic information. Although care has been taken to make the absorbance program comprehensive, the user of the absorbance system must understand the limits of the instrumental setup in order to collect the best data possible.

The data acquisition computer is a Macintosh G4 that communicates with the PDA, the spectrograph, Uniblitz shutters, and both variable delay rails. The former two use the GPIB interface, while the later are controlled through RS-232 linkage. Brian Millier is responsible for the RS-232 electronics and the VIs that function as drivers for the shutters and delay rail. No drivers were available for the PDA or spectrograph; these were directly handled using standard GPIB communication VIs.

There are four core sections to the absorbance program, each of which is composed of many sub-VIs and stands alone. Each section has its own front panel that is displayed when the user chooses to use it. The four sections and their specific functions are given in Table 2.3.

Table 2.3 Subsections of the absorbance program highlighting user capabilities.

Settings	Check Experiments
• Set delay rail zero manually or automatically • Choose delay rail to use • Choose number of time delays to collect data • Choose time delays • Choose corrections to implement and how often: fluorescence, dark counts • Set center wavelength on spectrograph • Choose whether data collection is automatic or requires individual spectral evaluation	• Change the center wavelength on spectrograph • Change the time delay • Collect a probe beam spectrum (check for saturation) • Collect a fluorescence spectrum • Collect a dark counts spectrum • Check reproducibility of any of the above spectra • Save any collected spectra to a text file
Go: Acquire Data	**Extract Kinetic Information**
• Set time of PDA exposure, number of accumulations, and number of computer averages • Set number of spectral averages, if necessary • Evaluate spectra as they are collected; choose whether or not to continue experiment on current setup • Save data to text file • Abort data collection if necessary	• Combine data from several different files • Choose different central wavelengths and ranges over which to average data for kinetic information • Save kinetic data to text files for further analysis

The Settings menu allows the user to choose parameters under which the experiment is performed. For example, an experiment determining sub-picosecond rise times of intermediates will require short time steps and will use the NanoStepper delay rail, while an experiment measuring longer decays (tenths of nanoseconds) will require the length available from the Parker Rail Table. For consistency, the data from each experiment are all collected using only one rail table, so that systematic errors in positioning associated with each table are consistent throughout. Another parameter that must be chosen is the types of corrections to be applied to the data. Dark count corrections, also known as background corrections, are always necessary, while

fluorescence corrections are optional. However, collecting fluorescence and dark counts can add a significant amount of time to data collection time. If these corrections are small and invariable over collection time, then to save time, these corrections can be collected only once for each time delay and used in all the spectral calculations. This saves up to 50 % of the collection time, which becomes significant when considering the need to conserve the reactive material and collect data from many time delays over the course of one day. Other parameters that can be adjusted in the Settings menu include the central wavelength setting of the spectrograph, number of time delays to collect (specific times entered either manually or calculated automatically by the program), and delay rail zero positions.

In order to determine the parameters to be set on the Settings menu, another panel is available to the user, called Check Experiments. The Check Experiments panel was originally designed for determining the stability of the continuum signal; however, its function has now expanded to determining stability of fluorescence and dark counts spectra, checking PDA saturation by the probe, and experimenting with changing wavelength and time delay settings. Data collected from this panel can be written to text files for future use. By looking at the raw fluorescence and dark count signals, the need for corrections is determined. The Check Experiments panel provides the user with crucial information for determining the best parameters under which the data are collected.

Once the experiment is set up, the data are collected under the Absorbance panel, which also serves as the main display panel and program housing the other sections as sub-VIs. The Absorbance panel allows the user to monitor the data being collected in real time through four spectral windows at the bottom of the screen (Figure 2.13). This is important because any problems that arise from shutters being manually left open, PDA saturation, or obvious laser instability can be noticed immediately and the affected data discarded. If the data collection needs to be aborted, an emergency abort button is available to stop the run immediately. In this case, the collected data is saved to a text file with a text header that specifies the aborted nature of the data. Figure 2.14 gives a flowchart view of how the data collection sequence is performed. Double lined boxes indicate computer communication with hardware, thick lined boxes indicate required user

input, and thin lined boxes indicate internal if-then decisions made based upon parameters set in the Settings menu. In order to simplify the diagram, all evaluations of the abort button status have been omitted. The status of the abort button is evaluated at each step so that the process can be interrupted as efficiently as possible if the user presses the abort button. Even so, it can take up to one minute to fully abort a data collection run, depending on which part of the flowchart cycle is in use.

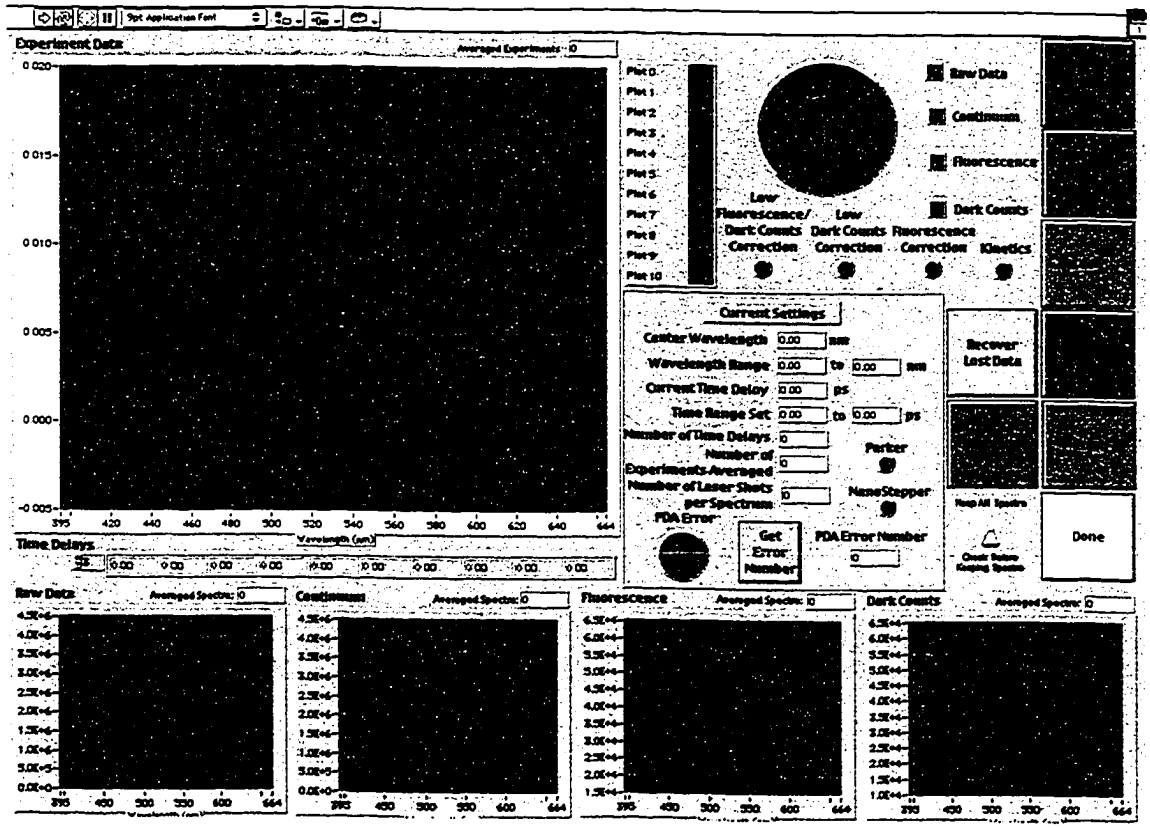

Figure 2.13 The front panel of the Absorbance Program.

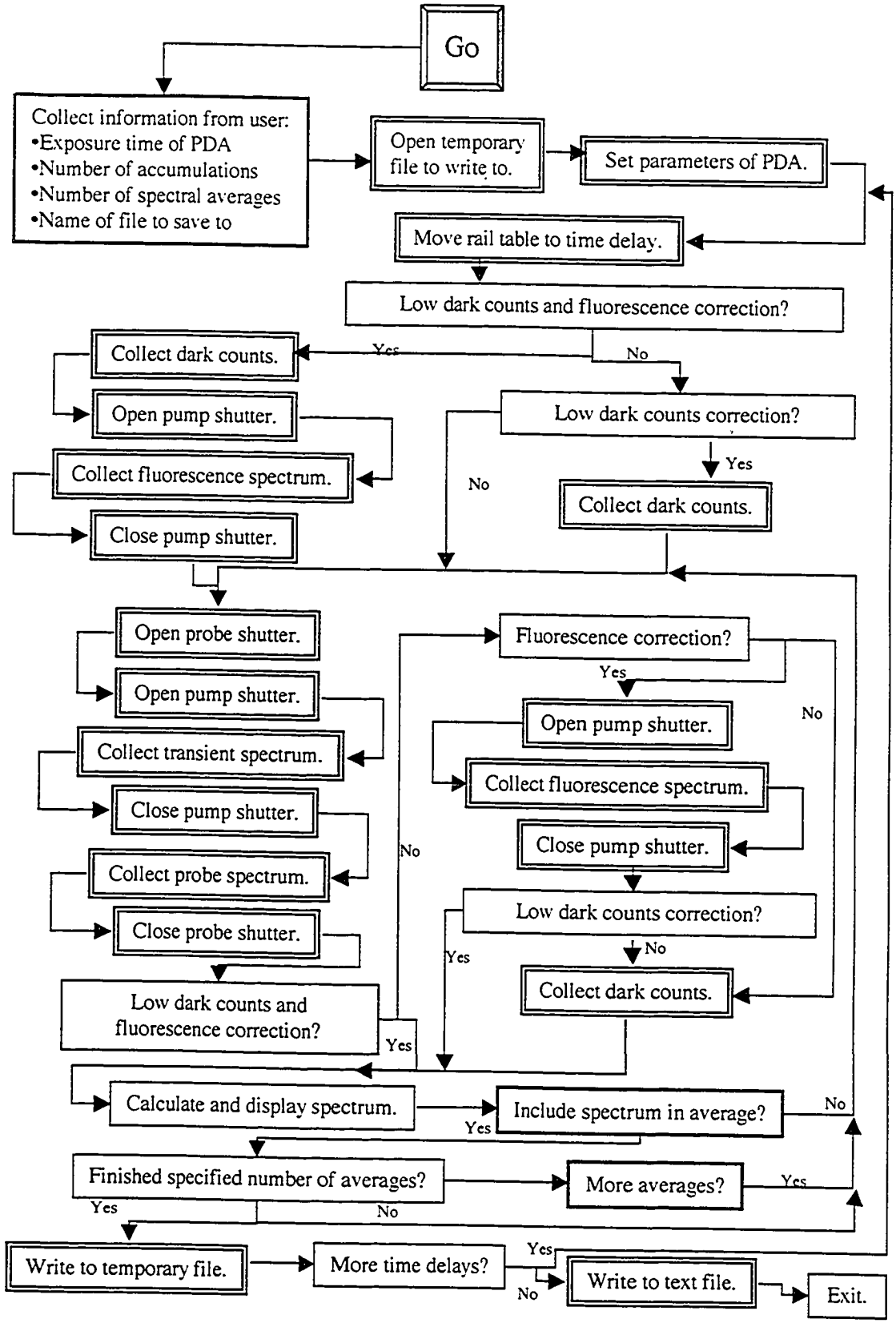

Figure 2.14 A flowchart detailing the data collection sequence of the Absorbance Program.

An absorbance spectrum is calculated for each collected wavelength according to the following equation:

$$A = \log \frac{C_{probe} - D}{R_{pump,probe} - F_{pump}}, \tag{2.5}$$

where A is the calculated absorbance value, C_{probe} is the probe datum in the absence of pump beam, D is dark counts datum, $R_{pump,probe}$ is the probe datum collected while the pump beam is incident on the sample cell, and F_{pump} is fluorescence datum (pump beam only). If no fluorescence corrections are applied, then F_{pump} is replaced with D. Because the wavelength setting of the spectrograph is constant for the duration of an experiment, the evaluation of Eqn (2.5) is performed entirely using vector arithmetic within the program. As each spectrum is 1024 array units long, this increases the speed of calculations.

Intrinsic to the absorbance collection program is the data save routine, which queries the user at the beginning of the collection sequence for a file name to which data will be saved. Data is kept in dynamic memory until the very end of the data collection sequence, at which point it is saved to a final text file; however, for sequences that collect up to 50 time delays, the textual data save sequence may not be performed for hours. In order to protect the user against accidental loss of data, the information is saved to a binary file after every time delay is completed. Saving to a text file is difficult due to the spreadsheet format of the saved data, which requires that data from each new time delay be added as a column. Text files are saved with delineated format, so that the addition of new time delay data requires the insertion of each data piece into the present file, rather than a simple addition of text on the end. Hence, the data collection to a text file is not implemented until all data are available. A binary file is preferred for interim saving because each individual number saved is the same size, so it is simple to replace certain key bytes in a file to enable file translation. In case of text file loss, a translation program has also been written to restore files from the binary format into a text file in spreadsheet format for easy use. All text files produced by the absorbance program have comprehensive text headers giving specific details on the parameters used in the program.

The last section of the Absorbance Program is used to extract kinetic information from the time delay spectra collected over one, or many, data collection sequences. This

part of the program allows the user to load the collected data, combine data from different files, and then look at specific wavelengths for changes in absorbance as a function of time. Because the stability of one specific wavelength is often not high enough for analysis, a narrow range of wavelengths centered about one wavelength is averaged. The user has two ways of specifying the wavelength range: 1. By specifying wavelength limits manually or using interactive cursors on the diagram, or 2. By specifying the central wavelength and then number of points to average about that wavelength. Multiple kinetic data traces generated are displayed in a window on the panel and the user has the flexibility to delete undesired traces or compare traces at different wavelengths. When finished, the data are saved to a text file in spreadsheet format for analysis. It should be emphasized that the kinetic section of the absorbance program can be used to analyze any previously collected data without any of the instrumental hardware running.

The Absorbance Program is designed to give the user maximum flexibility in data collection. A global control program is not necessary to collect the data; each instrumental element can be operated through manual control and the data collected manually. However, the Absorbance Program facilitates data collection efficiency and provides a user-friendly interface so that many users can effectively collect ultrafast data without a thorough instrumental background.

2.2.4.2 The Unchirped Spectral Reconstruction Program (USRP)

A chirped broadband probe pulse has a distribution of wavelengths that vary from the front to the back of the pulse (Figure 2.15). Although the entire pulse may be several picoseconds long, the width of each wavelength can be much shorter.

Because $t = 0$ is defined as the point at which the probe pulse exactly temporally overlaps with the excitation pulse, the result of having a chirped broadband pulse is a variation in the placement of zero for each wavelength. For data sets in which the width of chirp is significant compared to the overall time width of the data collected, the spectra collected will not be representative of a single time delay after excitation. In order to produce unchirped spectra, the spectra must be reconstructed from the original data. Figure 2.16 demonstrates the necessity of unchirped spectral reconstruction.

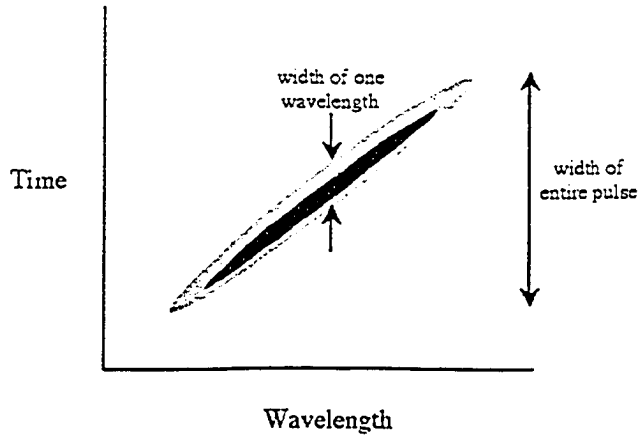

Figure 2.15 A schematic of a linearly chirped broadband pulse. The width of each wavelength is significantly shorter than the length of the entire pulse.

In order to use the USRP software, the temporal-spectral profile of the chirped pulse must be known. This is generally calculated from two-photon absorption spectra of 2-methylnathphalene[45] and has the form of an equation $t = f(\lambda)$. Once this temporal-spectral profile has been measured, it remains invariant[46] as long as the instrumental setup has not been considerably altered, and needs only to be periodically re-measured.

The user must manipulate all the spectral data collected into three spreadsheet files: one containing a vector of wavelengths, one containing a vector of time delays, and one containing a matrix of all the spectral data. These are saved as tab delimited text files and loaded into the USRP program. The user then chooses a wavelength and the absorption kinetics of that wavelength are displayed, allowing the user to choose a time on that kinetic profile to designate as $t = 0$. A time matrix is then calculated for the absorbance matrix based upon the temporal-spectral profile and corrected to place zero as designated. The time between data points remains unchanged; this is established by the time delays during collection. Data for each wavelength is simply shifted along the time axis until the zero time is placed as desired. The user can then choose any wavelength to display the kinetic trace with the corrected time, ensuring that zero is in the correct place for all wavelengths. These traces can be saved if desired.

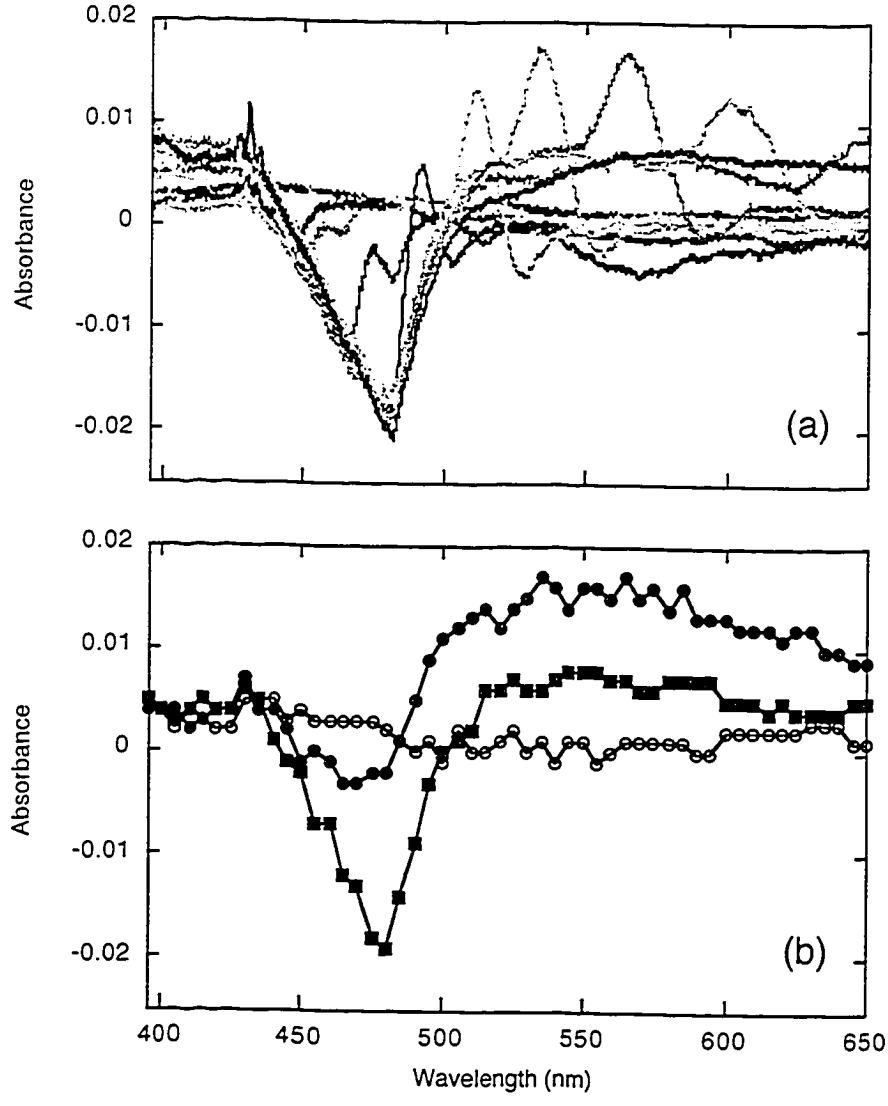

Figure 2.16 Demonstration of unchirped data reconstruction from chirped data of $Ru(dmb)_3^{2+}$ after 388 nm excitation. (a) Raw spectra of $Ru(dmb)_3^{2+}$ collected by the transient absorption spectrometer using the sapphire plate, 0.4 ps apart. The peaks represent a short-lived transient species that exists for < 75 fs. By the time a neighbouring wavelength detects the transient, the time delay of the first wavelength is already past the lifetime of the species. (b) Reconstructed spectra of $Ru(dmb)_3^{2+}$, using raw spectra taken 33 fs apart, including those shown in (a). The true shape of the absorption spectrum of the short-lived transient is a broad band that decays into a long-lived bleach (480 nm) and smaller absorption band. Spectra are shown at -0.5 ps (○), 0.0 ps (●) and 0.3 ps (■) after excitation.

Unchirped spectra are then reconstructed using the absorbance matrix and the corrected time matrix. The user inputs the desired time and a threshold value, and the

program searches the time matrix for data points that fall within the threshold value of the desired time. The coordinates of these points are used with the absorbance matrix to return absorbance values and these are plotted against the corresponding wavelengths to generate the unchirped spectrum. In order to generate unchirped spectra well, the original data set must be very large and have time delays that are very close together; otherwise, there will be insufficient points to generate representative spectra.

2.2.4.3 The Convoluted Fitting of Non-Regularly Spaced Data Program (CFnP)

For those cases in which the kinetic data are significantly altered by convolution with the IRF, convolved fitting is necessary for data analysis. CFnP is a modification of the Deconfit Program (section 2.3.3.2) written to analyze the streak camera data. The goal of CFnP is to iteratively fit the time-resolved data to a proposed kinetic model convoluted with the IRF function and return fitted parameters of the model.

Convolution of the model fit with the IRF is a crucial step in this program. For an analogue function, $f(t)$, convolution with the IRF, $g(t)$, is defined as (from Section 1.3.4):

$$F(t) = \int_{-\infty}^{t} g(t')f(t-t')dt'. \tag{1.31}$$

For discrete, finite length vectors of length N_g and N_f, Eqn (1.31) becomes its numerical analogue:

$$F(n) = \sum_{n'=-\infty}^{\infty} g(n')f(n-n') \tag{2.6}$$

$$g(n) = 0 \quad \text{for} \quad (n < 0) \text{ or } (n > N_g - 1)$$

$$f(n) = 0 \quad \text{for} \quad (n < 0) \text{ or } (n > N_f - 1).$$

The final vector $F(t)$ has a length

$$N_F = N_g + N_f - 1. \tag{2.7}$$

Numerical convolution involves only two vectors, without retaining the time information that may go with each point. Therefore, three of the requirements of numerical convolution are as follows: 1. The data are evenly spaced in time, 2. The time spacing for both vectors is the same, and 3. The time spacing is sufficiently small that the

discrete summation is a reasonable approximation of the analogue integral. One of the challenges of numerical convolution is the production of a vector that is longer than either of the initial vectors without time information attached to the vector components. This time information needs to be reattached to the vector components. As well, in practice, absorption kinetics are not usually collected with evenly spaced data, and it is necessary to exactly overlay the convolved fit with the actual data to calculate the goodness of fit, χ^2. Again, this requires keeping careful track of the time information of the data. In order to deal with these challenges, CFnP has some important modifications from the standard Deconfit Program.

The Deconfit Program requires the user to load the raw data and the experimental IRF as vectors. Both of these are readily measured for streak camera data, and are already evenly spaced in time. CFnP requires the user to load the raw absorption kinetic data for a single wavelength as a matrix of time delay and absorption data. From the time information, a vector, Time4Calc, of 500 evenly spaced time points are generated between the minimum and maximum time. The indices, Ind, of the Time4Calc vector that correspond to the true time points are noted. Rather than inputting an experimental IRF, the IRF is assumed to be Gaussian in shape and is calculated using the Time4Calc vector using a user specified FWHM. The IRF is scaled so that its total area is equal to 1, thus enabling the convoluted function to be compared in height to the experimental data. The user then manually aligns the position of the IRF against the raw kinetic data, chooses a model function and starting parameters. The CFnP program then uses the Levenberg-Marquardt algorithm with convolution to calculate best fit parameters. In the algorithm, the calculation requires comparison of the calculated fit to the raw kinetic data; however, the calculated fit has many more vector elements than the raw data. The Ind indices are used to extract the correct time points and only these are used to calculate the χ^2 value and to generate new coefficients. In this way, the Levenberg-Marquardt algorithm has been modified to allow convoluted fitting of non-evenly spaced data. Figure 2.17 shows schematically the layout of the basic CFnP program.

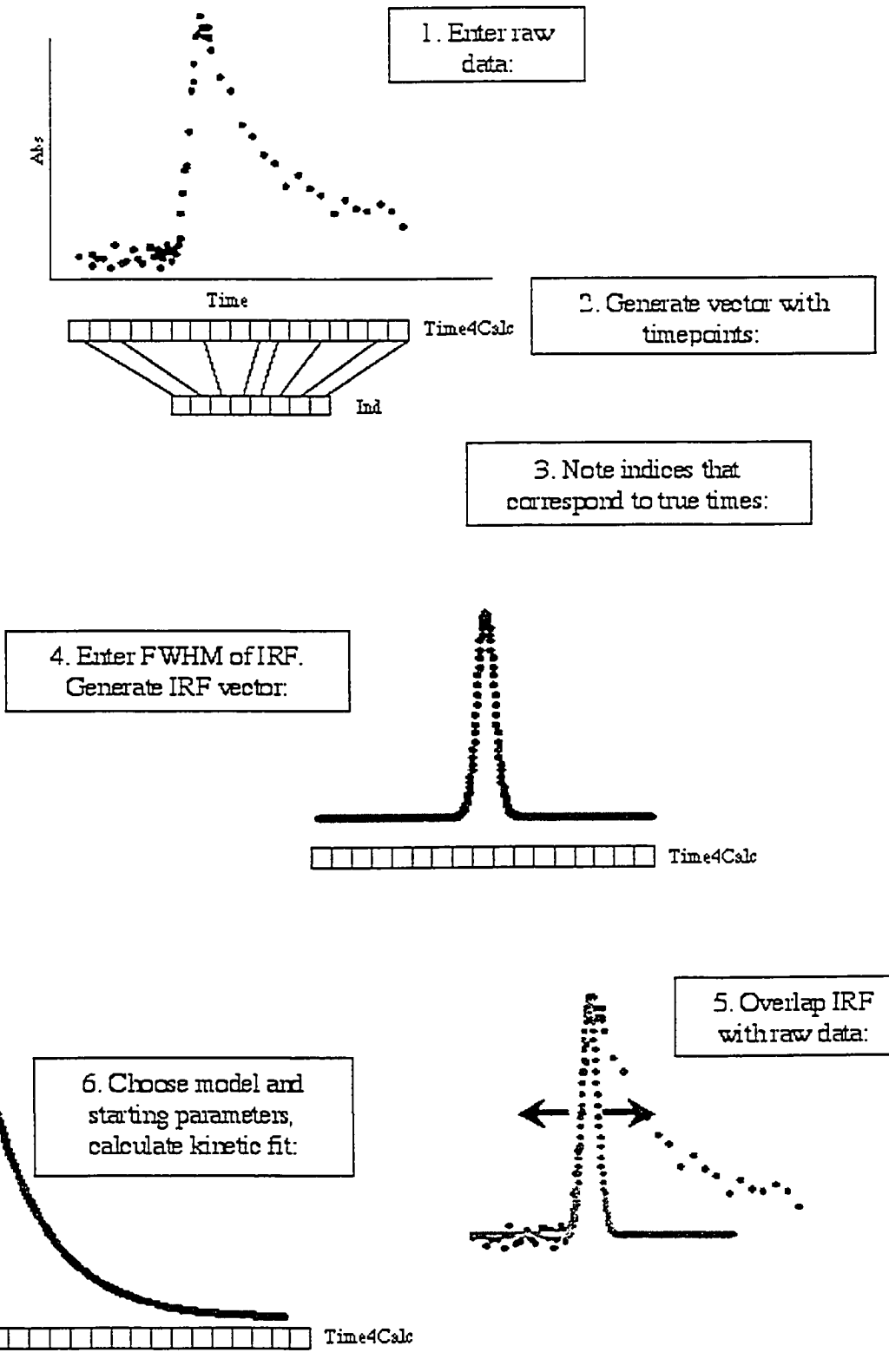
1. Enter raw data:
Abs
Time
Time4Calc
Ind
2. Generate vector with timepoints:
3. Note indices that correspond to true times:
4. Enter FWHM of IRF. Generate IRF vector:
Time4Calc
5. Overlap IRF with raw data:
6. Choose model and starting parameters, calculate kinetic fit:
Time4Calc

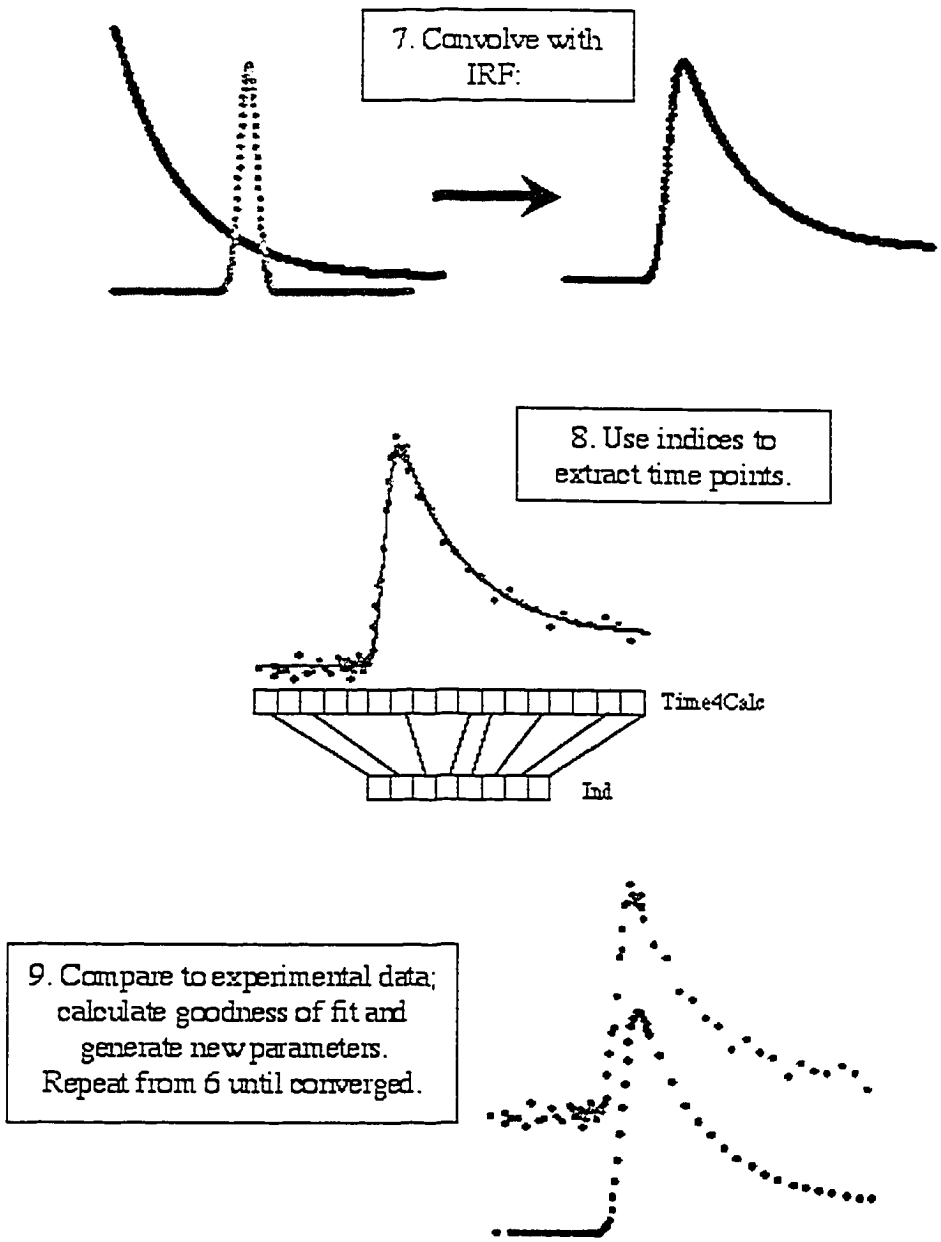

Figure 2.17 Schematic representation of CFnP.

Because the convolved fit does not retain time information, movement of the IRF forwards or backwards in time will result in a convolved fit that is shifted in time and cannot be compared to the raw data. Consequently, the calculation is sensitive to the exact placement of the IRF. In order to decrease this sensitivity, the CFnP program automatically calculates the best fit value for 10 different placements of the IRF with respect to the raw data, centered around the placement chosen by the user. All the fits are presented to the user along with calculated residuals and the user can evaluate each fit visually and choose the best fit. The user interface is shown in Figure 2.18.

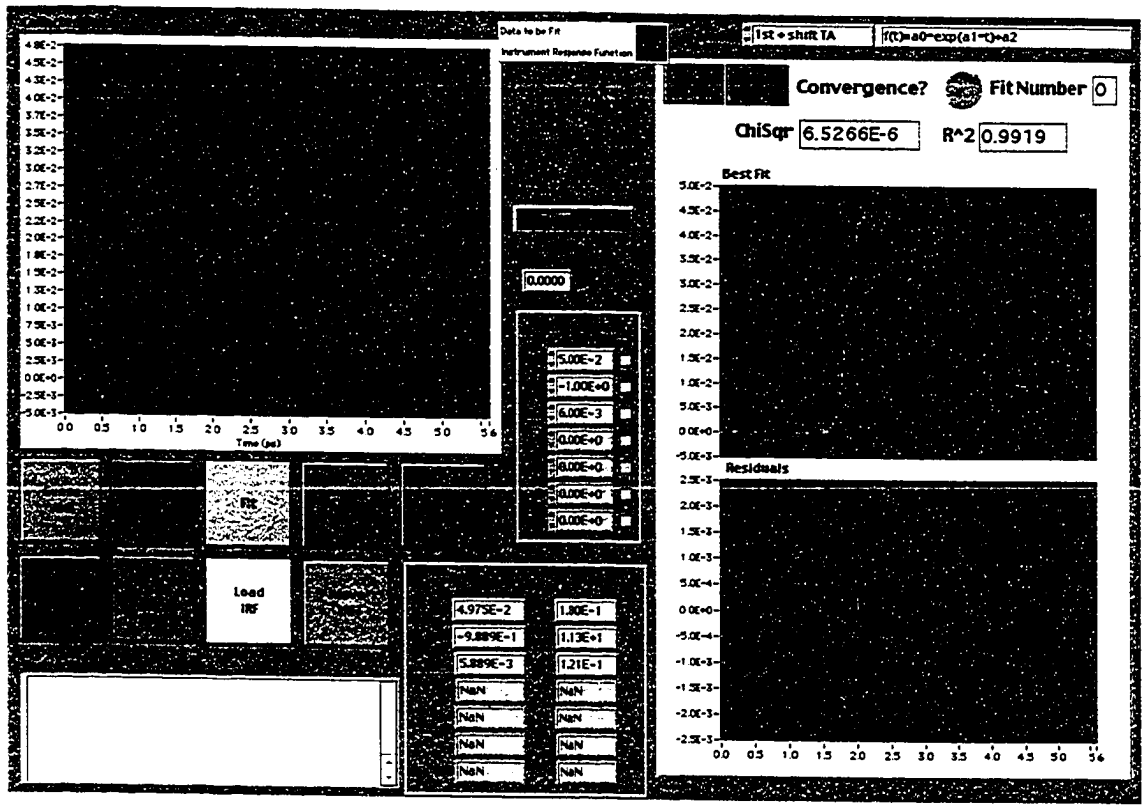

Figure 2.18 User interface of the CFnP program.

2.2.4.4 The Manual Convolution (ManCon) Program

While the CFnP software represents the easiest way of fitting convoluted absorption data, there are some circumstances under which it will not return meaningful results. The presence of excessive noise in the data, and decays that have lifetimes

similar to the FWHM of the IRF, both cause the CFnP program to fail. In order to analyze this type of data, a second convoluted fitting analysis program was developed. At the present time, it only has one model (a single exponential with an offset) available for fitting; however, further expansion of the program is a fairly simple task.

Manual convolution is a process in which the user calculates a convoluted fit using different estimates of the model parameters and visually compares it to the experimental kinetic trace. By changing the rate constant systematically and evaluating whether the fit is acceptable, the user can determine a line of best fit and error boundaries. This method has been used to determine lifetimes of ultrafast fluorescence data.[33]

Although the manual convolution process could be done by hand, the ManCon program was developed both as a teaching tool and to ease analysis. The user is required to load the file containing the experimental data and enter the FWHM of the IRF. A Gaussian IRF is calculated in the same method as in the CFnP program. Initial estimates of the fit parameters are input, and the calculation begins. The program calculates and displays in real time the convoluted fit according to the position of the IRF and the fit parameters that the user inputs. Dragging sliders back and forth or manually entering new fit parameters can change the position of the IRF and the fit parameters. The advantage of using the ManCon program lies in the ability of the user to change each variable and to monitor in real time how this change affects the convoluted function. An accurate estimation of the error, not based on theoretical calculations, can also be determined. When the user has finished using the ManCon program, the values determined can also serve as initial parameter values in the CFnP program for further refinement. An illustration of the ManCon program interface is shown in Figure 2.19.

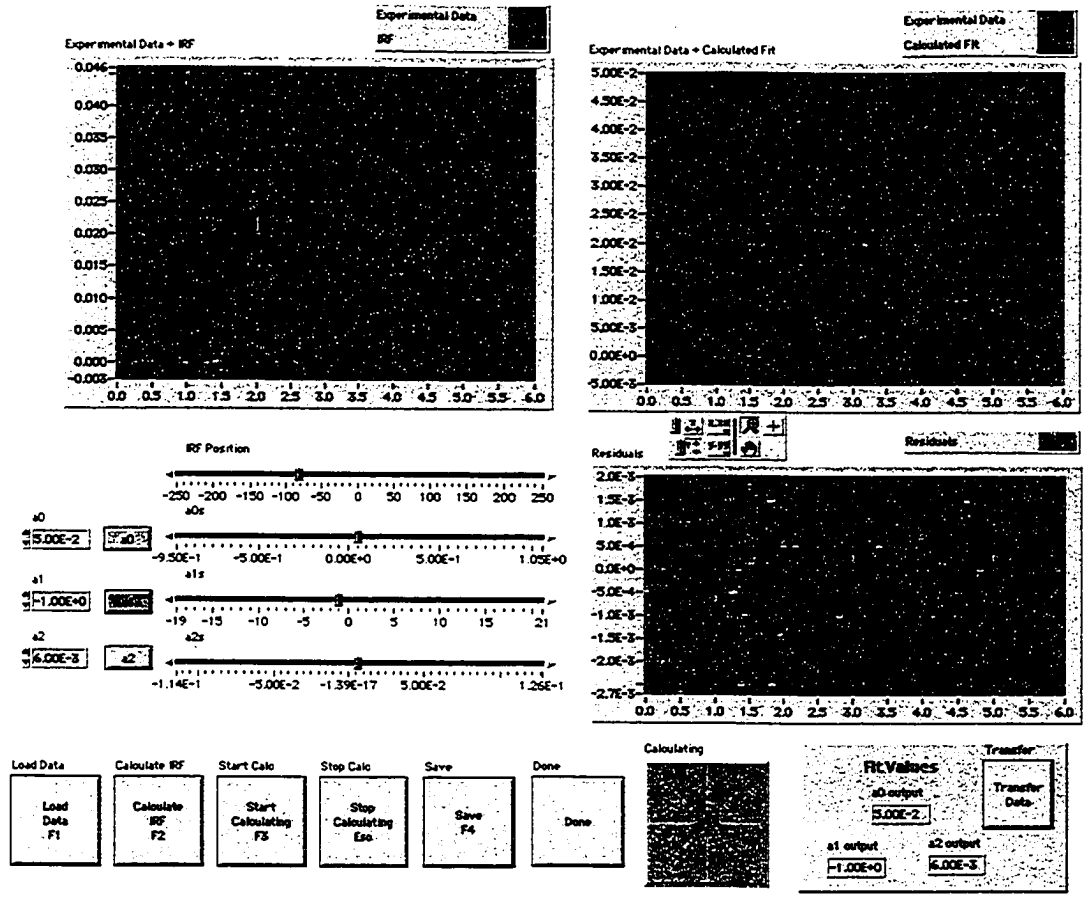

Figure 2.19 User interface of the ManCon program.

2.2.5 Characterizing the Pump-Probe System: The Water Cell as White Light Generator

Newly built instruments need to be tested to demonstrate that the data collected by the instrument are accurate, and that further use of the spectrometer to study new systems will yield meaningful results. It is also necessary to establish characteristics of the pump-probe system under each of its white light generation sources. In order to characterize the water cell as a white light generator, two experiments were performed. The first uses the ultrafast development of a bleach signal of the tris-(2,2'-bipyridine)ruthenium(II) cation to estimate the time resolution of the pump-probe system, and the second measures the rate of intersystem crossing of chloranil singlet to triplet to verify that the kinetic data collected by the ultrafast system are in agreement with published literature results.

2.2.5.1 *Time Resolution: Measuring the Ultrafast Bleach Formation of $Ru(bpy)_3^{2+}$*

Tris-(2,2'-bypridyl)ruthenium (II) cation, $Ru(bpy)_3^{2+}$, is a transition metal complex with a strong absorption in the visible region that makes it a bright orange-red hue in solution. This absorption band is attributed to a metal-to-ligand charge transfer ($^1MLCT \leftarrow {}^1A_1$), in which an electron is transferred from a *d*-orbital on the metal to a π^* orbital on one of the ligands. Upon ultrafast excitation of the $Ru(bpy)_3^{2+}$ cation at 400 and 480 nm, bleach of the MLCT band is observed at 460 nm, with spectral evolution complete in under 300 fs and unchanging to 3 ns and longer.[26,45] Measurement of the bleach formation, which can be considered instantaneous on the time scale of the pump-probe system, should therefore give a good indication of the rise time capabilities of the transient absorbance spectrometer.

$Ru(bpy)_3Cl_2 \cdot 6H_2O$ was obtained from Aldrich and dissolved in water to form a 50 mL solution of approximately 5 mM. Upon excitation with 388 nm radiation, bleach formation at 460 nm was rapid and unchanging on the full time scale of the pump-probe system. Figure 2.20 shows the development of the bleach with significant spectral chirp.

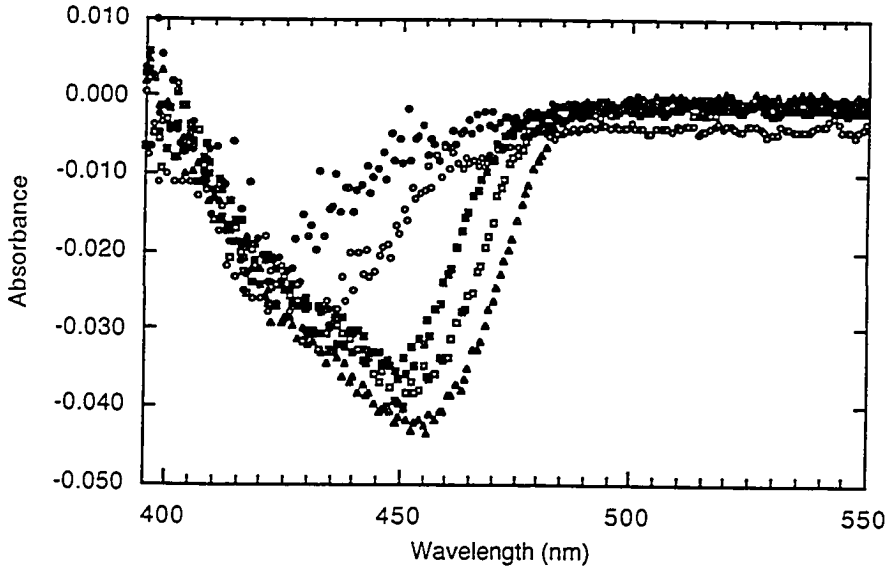

Figure 2.20 Excited state absorption spectrum of $Ru(bpy)_3^{2+}$ in water after 388 nm excitation at various times: -1.0 ps (●), -0.6 ps (○), 0.2 ps (■), 0.5 ps (□) and 0.9 ps (▲).

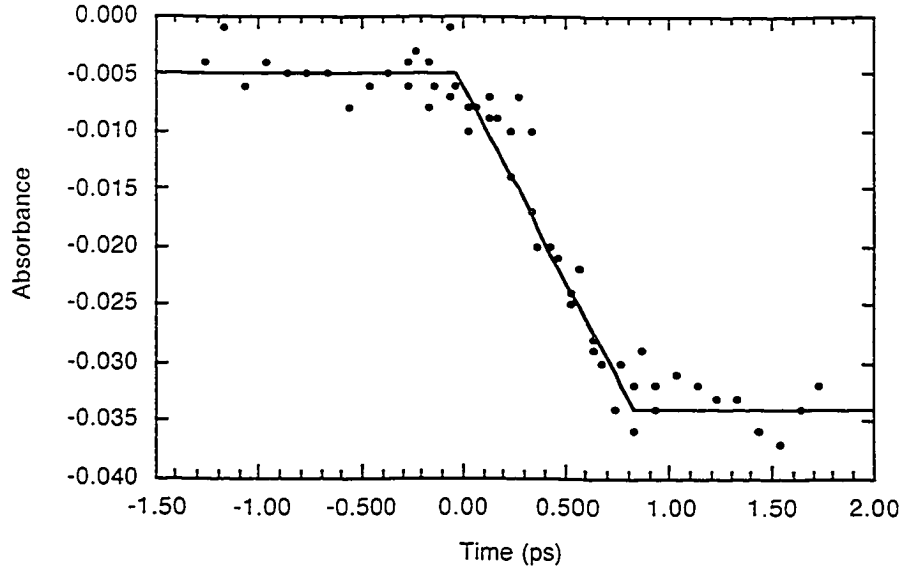

Figure 2.21 Kinetic profile at 465 nm of the bleach of $Ru(bpy)_3^{2+}$ after 388 nm excitation. From the evolution of the bleach, the time resolution of the pump-probe system is estimated to be 800 fs.

Extraction of the absorption measurements over time at 465 nm resulted in the kinetic profile plotted in Figure 2.21. Figure 2.21 shows a low baseline followed by a sharp development of a bleach and subsequent plateau at the bleach level. The development of the bleach is complete in under 1 ps, and the time resolution of the pump-probe system using the water cell as white light generator is estimated to be 800 fs from the plot.

2.2.5.2 Kinetic Accuracy: Measuring the Intersystem Crossing of Chloranil

The molecule chloranil was chosen for study because its excited state behaviour has been well characterized.[27] Upon excitation of chloranil in dichloromethane with 388 nm radiation, the chloranil singlet is generated in less than 700 fs. The singlet undergoes intersystem crossing with a time constant of 8 ps to form the chloranil triplet, Scheme 2.1.

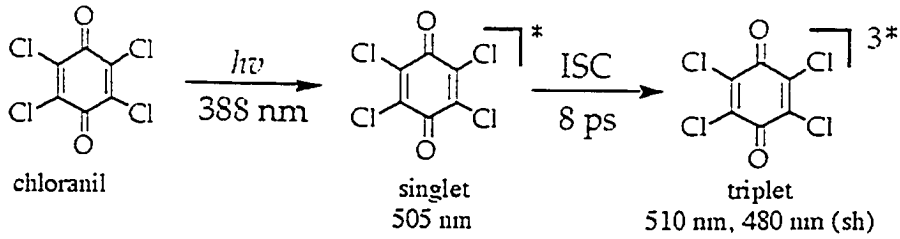

Scheme 2.1

The singlet has been reported[27] to have a symmetrical absorption band with maximum wavelength of 505 nm, while the triplet has a distinctive absorption band with maximum of 510 nm and shoulder at 480 nm. Figure 2.22 shows the shapes of the chloranil singlet and triplet absorptions. Intersystem crossing from the singlet to triplet species is complete in 30 ps.

Chloranil was obtained from Aldrich and recrystallized once from ethanol to yield pale yellow crystals. 5 mM solutions of chloranil were made with spectrophotometric grade dichloromethane (EM Science) and flowed through the 1 mm sample cell continuously during data collection. Figure 2.23 shows the spectra obtained at successive time intervals after excitation.

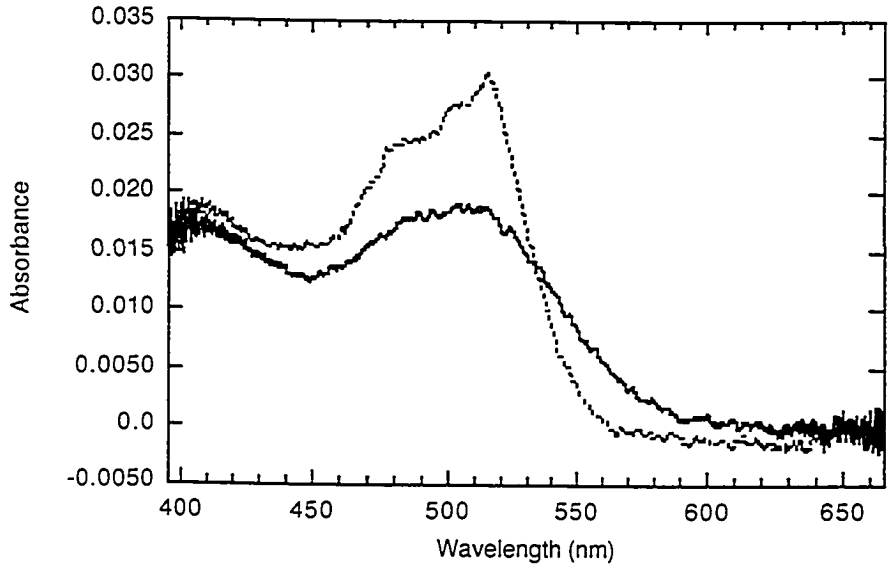

Figure 2.22 Characteristic spectra of the chloranil singlet (solid line) and triplet (dotted line). The absorption band at 400 nm is due to the chloranil radical anion.

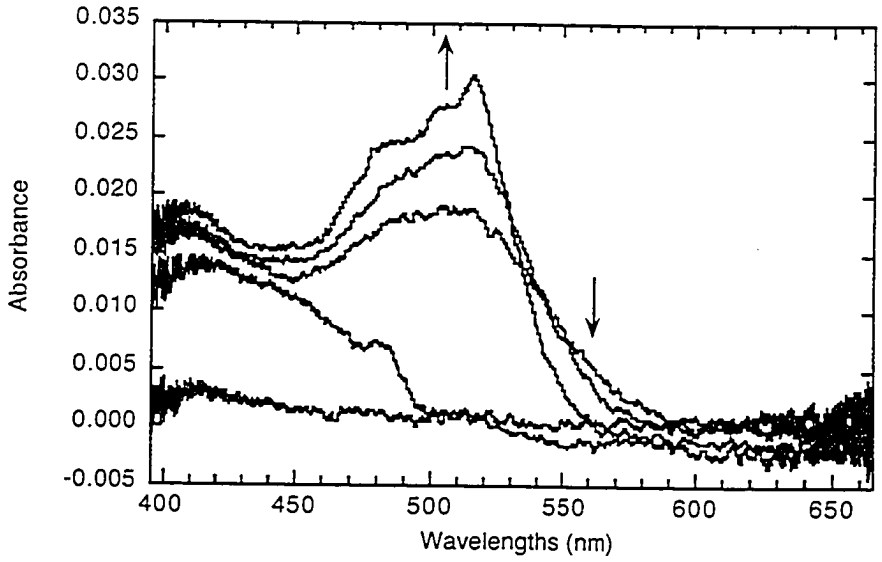

Figure 2.23 Selected traces showing chloranil singlet to triplet evolution. In order from bottom to top, the time delays at 480 nm are as follows: -6.0 ps, 0.0 ps, 5.2 ps, 12.2 ps, and 35.2 ps.

In Figure 2.23, the trace at 0.0 ps appears to have an absorption band in the blue region but not in the red region of the spectrum. This is a demonstration of a band with spectral chirp, where the high frequency part of the spectrum is delayed in time with respect to the lower frequencies. Examination of the kinetic traces at three different wavelengths, 480 nm, 514 nm, and 547 nm, also clearly demonstrate the presence of chirp, Figure 2.24. An estimate of the chirp can be made by comparing the zero times of each trace in Figure 2.24. Time zero is defined as being halfway up the fast rise of each trace. From 480 to 547 nm, a spread of 3 ps is estimated. Assuming linear chirp, the chirp across the entire spectral window of 270 nm is 12 ps.

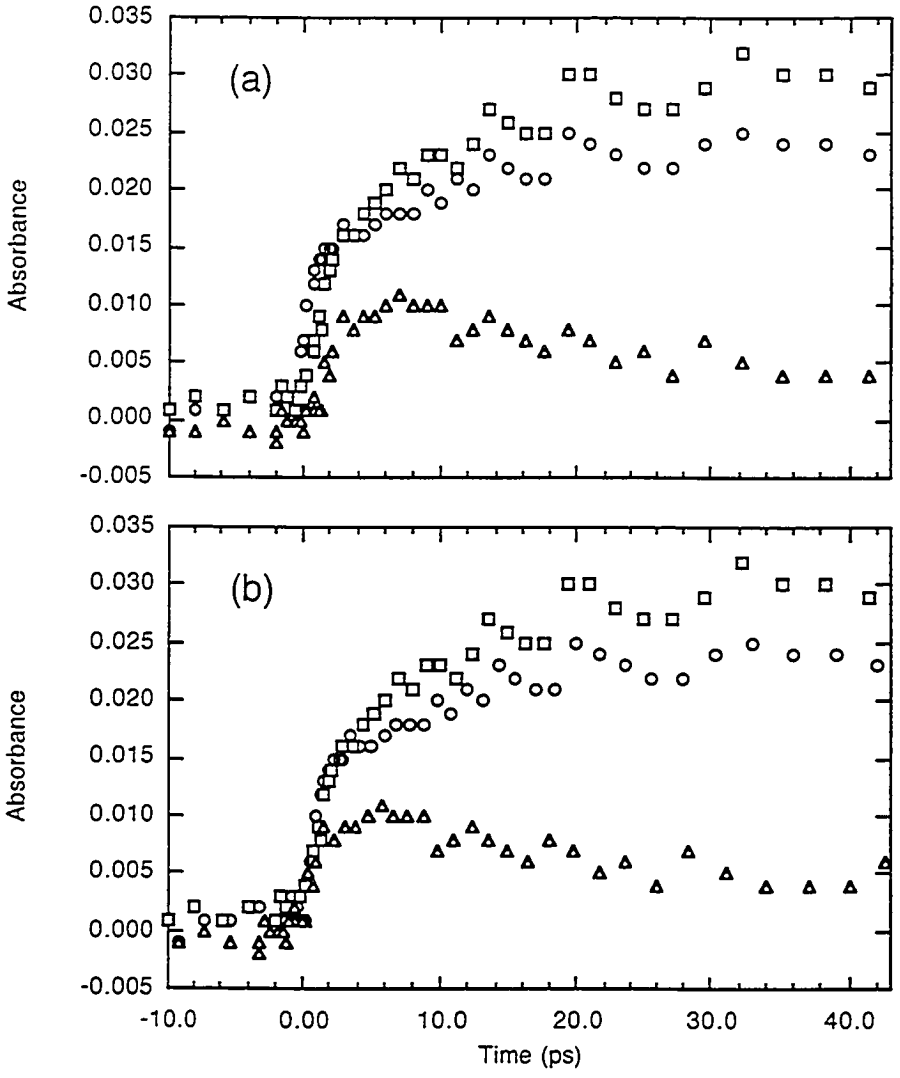

Figure 2.24 Kinetic traces of the chloranil singlet to triplet evolution at 480 nm (○), 514 nm (□), and 547 nm (△) where (a) no time correction has been applied, and (b) manual realignment of the kinetic traces has been performed.

Each of the kinetic traces shows a fast rise component, which is attributed to the rise of the chloranil singlet. The chloranil singlet to triplet transition is then characterized by a slower rise of the triplet peak (475-514 nm). Decay of the singlet absorption is observed at 547 nm, with an isobestic point at 535 nm. The rise time constant of the triplet signal should equal the decay time constant at 547 nm if indeed the triplet arises from the singlet excited state. The CFnP program, using an IRF FWHM of 800 fs, was used to fit each kinetic trace shown in Figure 2.24. Both rise time constants and the

decay constant were found to have the time constant of 8.4 ± 0.7 ps, in excellent agreement with the literature reported value of 8 ps. The fits are shown below in Figure 2.25.

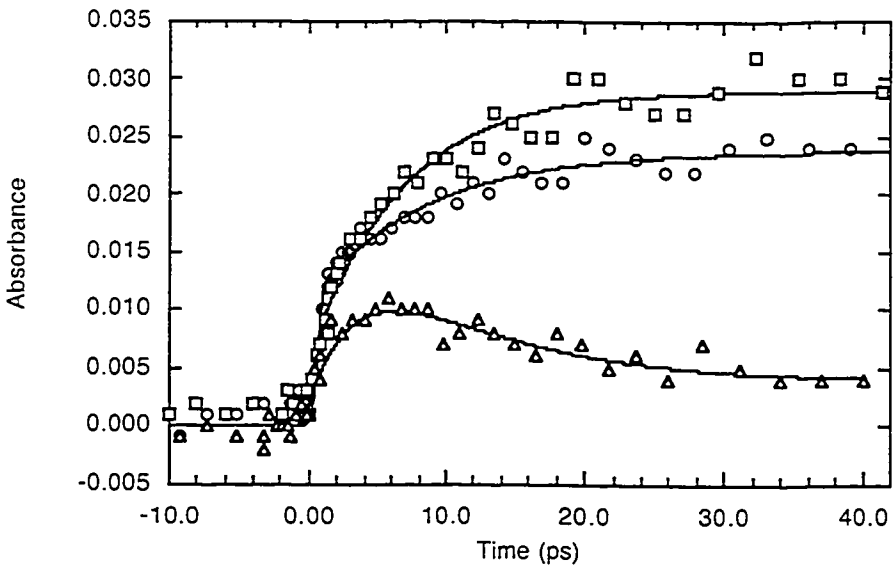

Figure 2.25 Kinetic traces of the chloranil singlet to triplet evolution with best fits calculated by the CFnP program. The fits for absorption changes at 480 nm (○), 514 nm (□), and 547 nm (△) are represented by solid lines.

2.2.6 Characterizing the Pump-Probe System: The Sapphire Plate as White Light Generator

White light generation using the sapphire plate offers a substantial decrease in the FWHM of the IRF, thereby enabling measurements down into the femtosecond region. Determination of the IRF shape and width, as well as quantification of the temporal chirp, was accomplished through two photon absorption cross-correlation measurements of 1-methylnapthalene.[45,47] A 1:4 solution by volume of 1-methylnapthalene (Aldrich, 99%, used as received) in acetonitrile (Spectrograde, Aldrich) was recycled through the 1 mm flow cell. Cross-correlation is a measurement that describes the overlap of two pulses. If any part of the two pulses are overlapping in time, then a signal will be recorded which is

proportional to the amount of overlap. At the peak of the signal, the two pulses are exactly overlapped. This point represents time zero. The temporal profile of the cross-correlation function also represents the IRF. Figure 2.26 shows the cross-correlation measurements as a three-dimensional plot, clearly showing the narrow width of the correlation function at all wavelengths.

A contour plot of Figure 2.26, shown in Figure 2.27, shows some of the characteristics of the probe pulse. Below 450 nm, the intensity of the cross-correlation peak dies away sharply, which indicates there is insufficient light intensity below 450 nm to make measurements. As well, the chirp of the pulse is not linear and spans 3 ps from 450 to 650 nm. The curvature of the chirp can be described by analyzing the time profile of the probe pulse as a function of wavelength. Figure 2.28 shows a line plot of the cross-correlation peak points of Figure 2.26, and best fit analysis of the points yields the following polynomial equation, where λ is in nm and yields t in ps:

$$t(\lambda) = -73.3 + 0.348\lambda - (5.50 \times 10^{-4})\lambda^2 + (2.97 \times 10^{-7})\lambda^3 \qquad (2.10)$$

Equation (2.10) is used in the USRP program to facilitate unchirped spectral reconstruction.

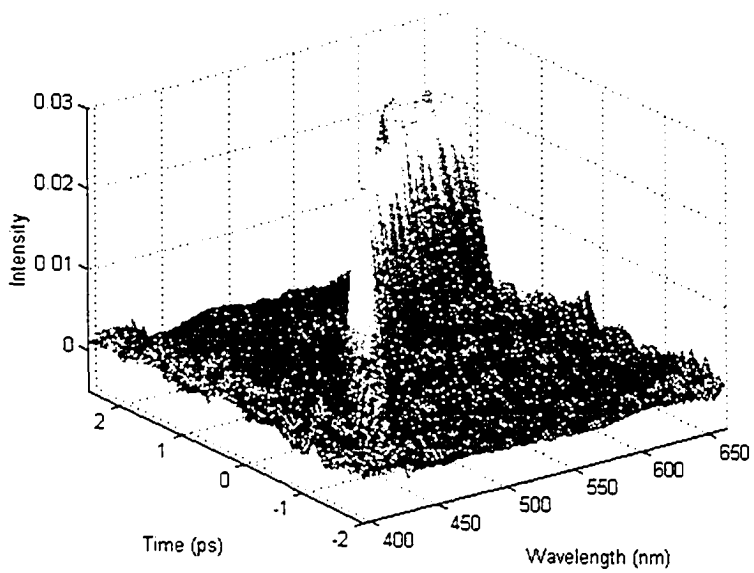

Figure 2.26 Two photon cross-correlation plot of 1-methylnaphthalene measured by the transient pump-probe spectrometer using the sapphire plate as the white light generator. The colour scale is from blue to red, with blue representative of the lowest intensity and red the highest.

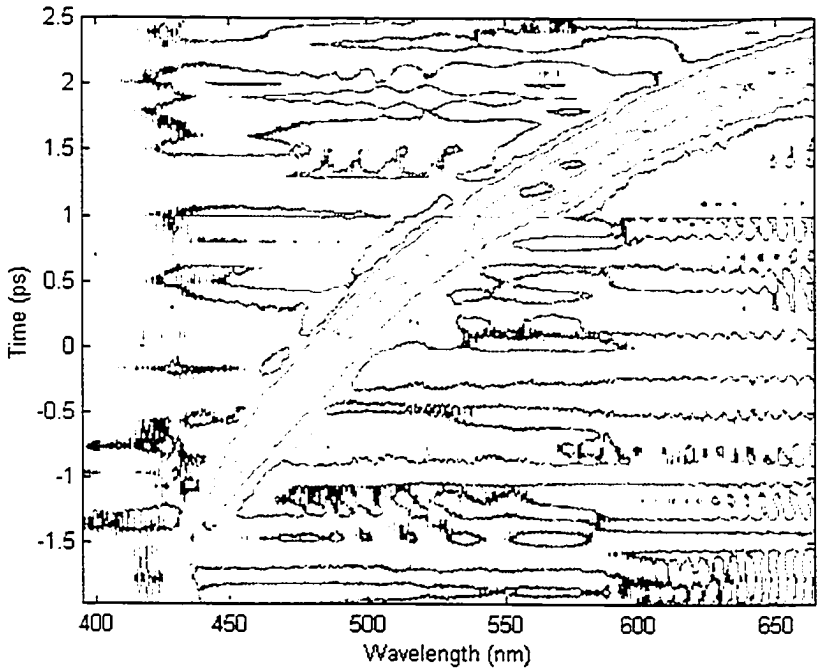

Figure 2.27 A contour plot representing the two photon cross-correlation of 1-methylnaphthalene measured by the transient pump-probe spectrometer using the sapphire plate as the white light generator. The colour scale is from blue to red, with blue representative of the lowest intensity and red the highest.

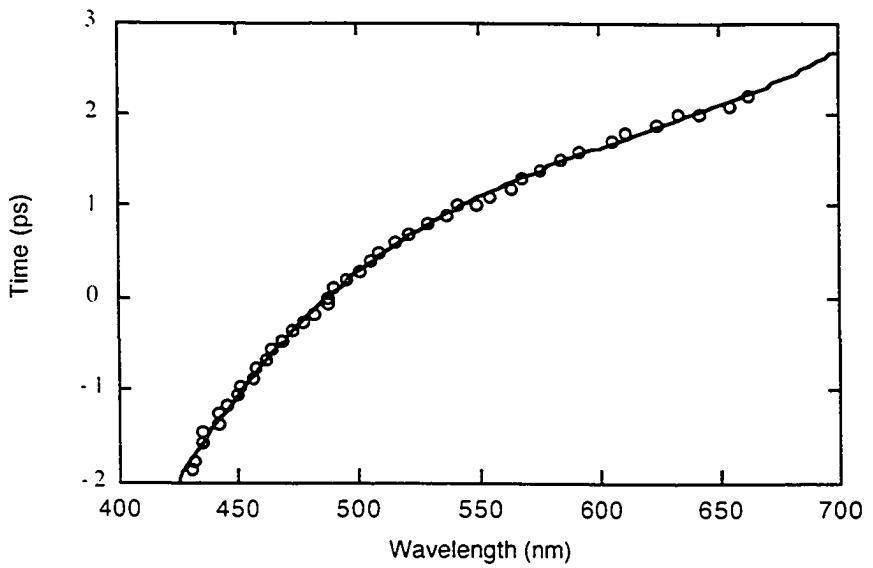

Figure 2.28 Plot of time zero as a function of wavelength. The solid line represents a line of best fit described by equation 2.10.

The time profiles of each wavelength represent the IRF function for that wavelength. Plots of the time profiles at various wavelengths are shown in Figure 2.29 with the FWHM varying from 285 to 387 ps. The FWHM is calculated to be 305 ± 17 fs for the wavelength range 500 to 650 nm. For the high frequency wavelength of 450 nm, a wider pulse is recorded: 387 fs. The larger width is due to the increasing amount of chirp in the shorter wavelengths, as well as the lower intensity. Overall, the pump-probe spectrometer, with a sapphire plate as the WLG, has a resolution of 305 ± 17 fs.

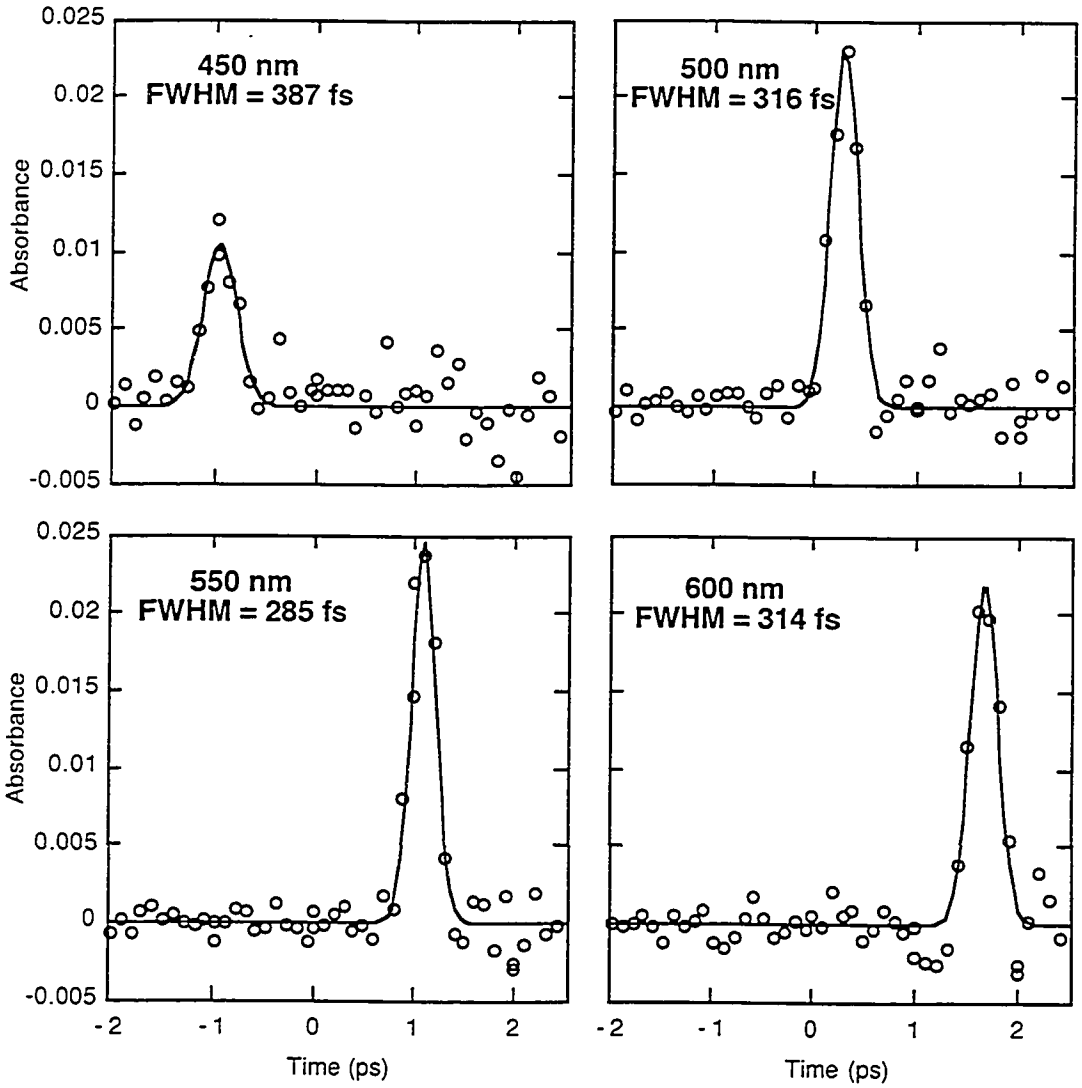

Figure 2.29 Time profiles of the instrument response functions at various wavelengths. Broadband generation is *via* the sapphire plate. Solid lines represent Gaussian fits to the data.

Considering that the pulse produced by the laser is usually between 150 and 200 fs, the instrument response function of the spectrometer at 305 fs represents a small increase of the pulse length. The length of the probe and pump pulses can be estimated at the sample cell considering that the cross-correlation measurement is a convolution of the pump and probe pulses. Assuming that both pulses are the same width and are Gaussian, the cross-correlation function simplifies to an autocorrelation function[19] where the FWHM of the pump pulse is related to the FWHM of the IRF by $FWHM_{IRF}/FWHM_{pulse}$ = 1.414. Thus, the pump and probe pulses at the sample cell have a pulse width of ~216 fs. The majority of this spreading likely takes place as the pulse travels through the optical components on the table rather than by dispersion from the mirror surfaces. The introduction of significant chirp also occurs in the collimation and focusing lenses after white light generation has taken place. The use of off-axis parabolic mirrors rather than lenses would greatly reduce the amount of spectral chirp.[45]

One of the questions that arises from this reported "resolution" of 305 fs is: What is the fastest kinetic decay that can be measured quantitatively? This is a question that can be answered with the help of the ManCon program. Using convoluted fitting techniques, it is possible to resolve kinetic traces that are faster than the IRF of the spectrometer, if the shape and the width of the IRF are well known. For a fast transient that disappears in a first order fashion, convolution of the single exponential decay and the IRF will always result in a signal as long as the initial intensity of the fast transient is sufficiently high to be detected. However, there is a limit to the rate that can be quantified.

Figure 2.30 shows the convolution of first order decays with varying lifetimes varying from 30 to 150 fs with an IRF function, FWHM = 305 fs. As the lifetimes become shorter and shorter, the convoluted decay becomes increasingly similar to the IRF function, with the 30 fs decay virtually indistinguishable from the IRF. In this idealized sense it is possible to distinguish between most of the decays but the presence and magnitude of noise in the data will determine the error limits of the lifetime estimation. As a practical limit, the shortest lifetime that can be determined is 75 ± 25 fs.

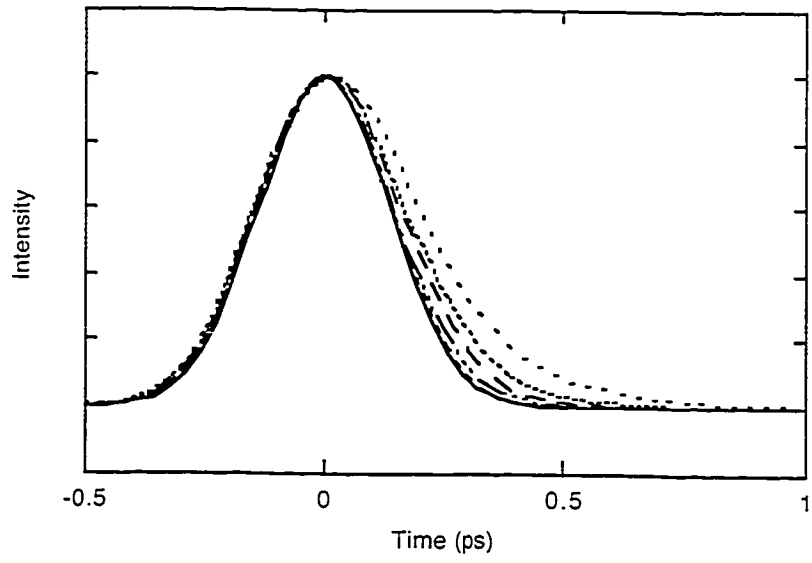

Figure 2.30 Convolution of the IRF (FWHM = 305 fs) with first order decays of varying lifetimes. 30 fs (– –), 50 fs (— ··· —), 75 fs (— —), 100 fs (···), 150 fs (---), IRF (——).

2.2.7 A Summary of the Transient Pump-Probe Spectrometer

Thus far, a working spectrometer has been described that uses the pump-probe technique to study solution samples by absorption measurements. Two materials are available for white light generation: 1. a water cell, and 2. a sapphire plate. The water cell offers wider bandwidth, greater stability, and ease of use, without the time resolution and reduced chirp available from the sapphire plate. With the water cell, subpicosecond resolution (~800 fs) is possible while the sapphire plate extends the time resolution to 305 fs. Both systems have been demonstrated to measure data in good agreement with values reported in the literature.

Software has also been developed to facilitate data collection and analysis. Four programs have been developed: 1. the Absorbance Program, 2. the Unchirped Spectral Reconstruction Program (USRP), 3. the Convoluted Fitting of Non-Regularly Spaced Data Program (CFnP), and 4. the Manual Convolution Program (ManCon). The Absorbance Program is the user-instrument interface. It allows the user to collect a time-resolved set of transient absorption data according to user-defined parameters, and to extract kinetic traces at specified wavelengths for further analysis. All the other programs

are used after the Absorbance Program as data analysis programs and are independent of the instrumentation. If there is significant chirp present in the spectral data, USRP reconstructs the data into unchirped spectra. The two final programs, CFnP, and ManCon, allow the user to fit the kinetic data using convoluted fitting. The former combines convoluted fitting with the Levenberg-Marquardt algorithm to produce parameters of best fit. For cases in which the CFnP program fails, such as in cases with a low signal to noise ratio, the ManCon program can allow the user to manually fit the data with a convolved function by experimenting with each of the parameters. The resulting parameters can be used as starting parameters in the CFnP program.

The resulting transient absorption spectrometer is a complete tool for chemical research. It offers flexibility with ease of use for data collection on a very challenging timescale.

2.3 Time-Resolved Fluorescence: Ultrafast Streak Camera Measurements

2.3.1 Hardware Components

2.3.1.1 Ultrafast Streak Camera

The ultrafast streak camera, designed and built by Axis Photonique, Inc., is an extremely sensitive instrument used to measure the time dependence of weak luminescence signals. The streak camera is a completely passive instrument, and is coupled to an electronic trigger unit and a charge-coupled device (CCD) camera (Photometrics SenSys) to produce images that can be analyzed to provide time-resolved data. In our studies, the streak camera will be used to measure ultra-fast fluorescence rises and decays, acting as a good probe for measuring the extent of chemical events such as electron transfer and intra-cage movement of molecules in zeolite hosts.

The sample of interest is excited by front-face pulsed excitation. Luminescence emitted by the excited sample is collimated by a plano-convex quartz lens of 51.5 mm focal length, and passed through a high-pass cutoff filter of appropriate wavelength to remove any diffuse reflectance of the pump beam. The emission then passes through a

variable number of neutral density filters before being focused onto the photocathode of the streak camera *via* a second plano-convex quartz lens of 51.5 mm focal length. A bandpass filter directly in front of the photocathode allows for wavelength selection.

The streak camera is entirely housed in one unit, which contains the photocathode, vacuum electron tube, streak plates and phosphor screen. Incident photons on the photocathode between 200 and 800 nm cause the photocathode to emit a proportional number of electrons into the tube, such that the emitted electron train is an electron replicate of the incident photon train. The electron train is focused and accelerated by electronic lenses to energy levels of 15 keV, resulting in a velocity that is 25% of the speed of light. While passing between the streak, or deflection, plates, a linear voltage ramp is applied to the electron train, causing the electrons to deflect amounts proportional to their position in the train. The front of the electron train is deflected the least, whereas electrons later in the train are deflected farther, so that when the electrons impact the phosphor screen, they are separated spatially according to their position in time in the electron train. Thus, the streak camera transforms the time information in the electron train (and thus in the incident optical pulse) into spatial information on the phosphor screen. When struck by the electrons, the phosphor screen fluoresces and a CCD camera captures this image after reduction by an imaging lens. Analysis of the image produced by the CCD camera yields time-resolved fluorescence decay data that can be used for studying chemical systems. This process is depicted in Figure 2.31.

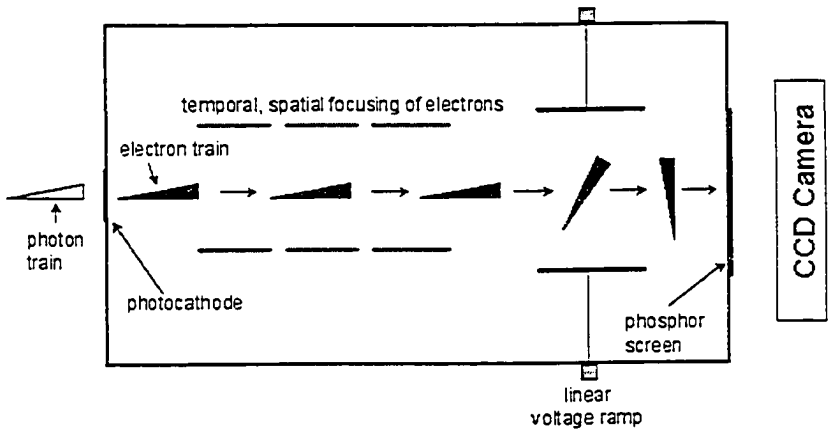

Figure 2.31 Schematic representation of the streak camera.

The linear voltage ramp used to spatially separate the electron train must be temporally correlated with the position of the electron train. Two trigger units, one for ultrafast time resolution and the second for nanosecond measurements, produce the voltage ramps. One of the trigger units is optically triggered by the CPA-2001 fundamental output and the other is electronically triggered. Both units have variable delay units, either optical or electronic, to facilitate the temporal correlation. These units are separate from the streak camera, and transfer the voltage ramp produced directly onto the deflection plates *via* exposed connectors on the streak camera housing.

Once the electronic lenses that focus the electrons between the deflection plates are optimized, the streak camera is a completely passive unit that houses only static electric fields. All elements are sealed within the streak camera unit and cannot be changed without replacing the entire unit. Due to the extreme sensitivity of the photocathode to light, measurements must be taken in the dark and caution is exercised when exposing the photocathode to light, especially when the streak camera is on. Putting an excessive number of photons onto the photocathode at once will irreparably damage it, and because the photocathode cannot be replaced independently, the streak camera will be rendered useless.

The time resolution possible on the streak camera is a function of the physical width of the photocathode multiplied by the sweep speed of the linear voltage ramp applied to the deflection plates. The physical width of the photocathode can be measured by capturing an image of incident light with no deflection ramp or bias voltage applied to the streak plates. This is referred to as a static signal, as no time information is available. The static signal measured on our streak camera is roughly Gaussian in shape with a FWHM as 47 μm (7 pixels). If the streak speed produced by the voltage ramp is 300 fs / pixel, then the best resolution that can be achieved by the streak camera is 2.1 ps. Small amounts of light measured by this method, when spread spatially by deflection at this high resolution, result in extremely weak levels of light being recorded by the CCD camera. Therefore, in order to be able to see a signal, the photon emission and transformation within the streak camera to impact the phosphor screen must be repeated tens of thousands of times in order to capture an image which has a high signal to noise

ratio. However, each time a new electron train passes through the streak camera, the voltage ramp must be applied to the electron train to deflect it. If the voltage ramp has any uncertainty in either slope or timing relative to the electron train, then successive sets of electrons striking the phosphor screen will not overlap spatially. The distribution in spatial overlap will limit the resolution of the streak camera. As a result, the difficulty in achieving a high-resolution streak camera is not so much in the camera technology, but in the voltage ramp production technology. Conventional methods of triggering are based upon electronics, but even the best electronic designs introduce tens of picoseconds of electronic jitter. For streak speeds that do not require ultrafast resolution, electronic triggering, is sufficient to produce the voltage ramps. For ultrafast applications, a method based on photoswitches is necessary to eliminate the electronic jitter.

2.3.1.2 The G2 Jitter-Free Unit

The G2 jitter-free unit, designed and built by Axis-Photonique, Inc., is a prototype voltage ramp generator developed commercially for ultrafast chemical streak camera applications. While conventional electronics govern the voltage ramp's shape and size, the triggering unit for the ramp is based upon semiconductor photoswitch technology. The semiconductor material has infinite impedance when no light is incident upon its surface, and can withstand a high potential difference without breakdown. When exposed to light, electrons are promoted into the conductive band of the photoswitch and the impedance of the switch material drops to zero, allowing current to pass with little to no resistance. Hence, raising the potential of one side of the switch in the absence of incident light and then exposing the switch to light can release a high voltage difference very quickly, while the zero impedance prevents heating produced by resistance to current flow. Using an ultrafast laser as the light source can thereby lower the switching time of the photoswitch to the femtosecond time scale.

Two adjacent square photoswitches, measuring 10 by 10 mm each, are set 10 mm apart from each other on a photoswitch plate. Each photoswitch is connected on one side to charging electronics, which can raise the potential difference across the photoswitch to 1000 V. The other side of each photoswitch is connected to one of the deflection plates

of the streak camera through a simple capacitive circuit. Further electronics put a constant bias potential on the deflection plates of the streak camera, so that any electrons that precede or follow the true signal are deflected off the phosphor screen. This bias also has the effect of changing the start point of the voltage ramp from the center of the phosphor screen to off the screen, so that the voltage ramp deflects the electrons across the entire surface of the phosphor. An electronic trigger signal from the laser triggers the G2 unit to begin building up charge across the photoswitches 200 ns before the fundamental beam of the laser is incident on the photoswitches. When the laser pulse arrives on the photoswitches, the impedance of the switches drops to zero and the rush of current across the photoswitches produces the linear voltage ramp on the deflection plates. The lengths of the excitation and triggering pathways must be set so that the voltage ramp is temporally coincident with the front of the electron train. Because the laser pulse arriving on the photoswitches originates from the same pulse used to excite the sample, there is no jitter between the triggering of the linear voltage ramp and the electron train representing the fluorescence emitted. This allows for reproduction of the experiment hundreds of thousands of times in order to accumulate sufficient signal intensity without loss of time resolution. Slight differences in voltage ramp slope arise from laser instability and shot to shot non-reproducibility.

The design of the optics directing the laser trigger onto the photoswitches was also designed by Axis-Photonique and uses the fundamental beam, 775 nm. The fundamental beam is aligned through the Parker delay rail such that movement of the delay rail does not affect the optical alignment of the fundamental beam on the photoswitches. Movement of the delay rail back and forth changes the temporal overlap of the electron train and the voltage ramp, and requires adjusting so that background noise can be corrected for during data collection. Once the fundamental beam passes through the delay rail, it is directed into the optical line (Figure 2.32) leading to the switches, which is raised horizontally 158 mm from the optical table. The round 3 mm diameter beam is expanded by a Galilean beam expander telescope consisting of a divergent lens (7.5 mm focal length) and a 250 mm focal length convergent lens located 150 mm after the divergent lens. The resulting beam is round and is approximately 10 mm in diameter. A convergent cylindrical lens focuses the beam in the vertical direction through a 0.5 mm

thick, 800 nm, saturable absorber located very close to the focal line. After the focal line, the beam begins to diverge, and a 775 nm thin film turning mirror directs the expanding beam onto the switches. The resulting radiation on the photoswitch plate is approximately 1 cm in width and 3 cm in height, and both square photoswitches are bathed completely in the radiation. Even illumination of the switches is crucial to their proper operation and maintenance.

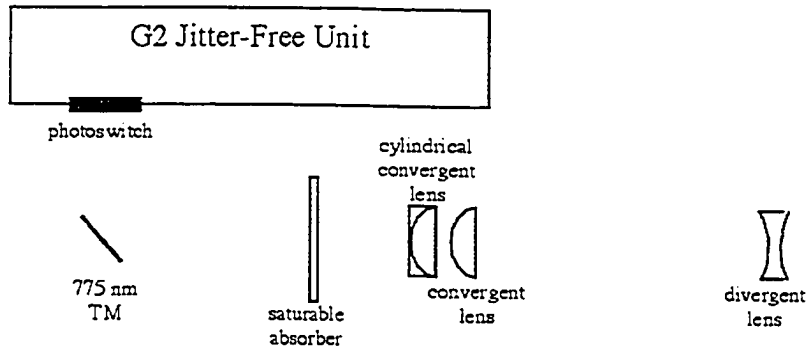

Figure 2.32 Lens setup onto the G2 Unit photoswitches. The beam enters from the bottom right, through the divergent lenses, through to the turning mirror and onto the photoswitches. A focal line is located between the saturable absorber and the turning mirror very close to the absorber.

The purpose of the saturable absorber is to increase the steepness of the rising edge of the laser pulse. The cleaner the rise, the steeper the voltage ramp applied to the deflection plates and the faster the electrons are swept across the screen. Thus, for the shortest resolution possible on the streak camera, the rising edge of the laser pulse must be as clean and steep as possible. A saturable absorber accomplishes this task by absorbing photons up to a threshold incident power, and past that threshold, the absorber allows all photons to pass. As a result, any small pre-pulses are removed and the shape of the pulse is much closer to a true Gaussian shape. The effect of the saturable absorber on the voltage ramp shape is clearly observable on an oscilloscope as a straightening and steepening of the rising edge of the voltage ramp.

The main goal in careful alignment and setup is the production of a linear and steep voltage ramp. Calibration of the streak camera and the jitter-free unit has been accomplished by changing the temporal overlap of the voltage ramp and the electron train produced by measuring the laser pulse directly as an infinitely short pulse. Using the speed of light to determine the difference in triggering time, and comparing this to the deflection of the laser pulse on the captured image, allows the sweep speed and the linearity of the voltage ramp to be evaluated. The linearity of the voltage ramp on the fastest sweep speed of the jitter-free unit is shown in Figure 2.33. Although the ramp has a slight curvature, it has been approximated as linear to facilitate data analysis.

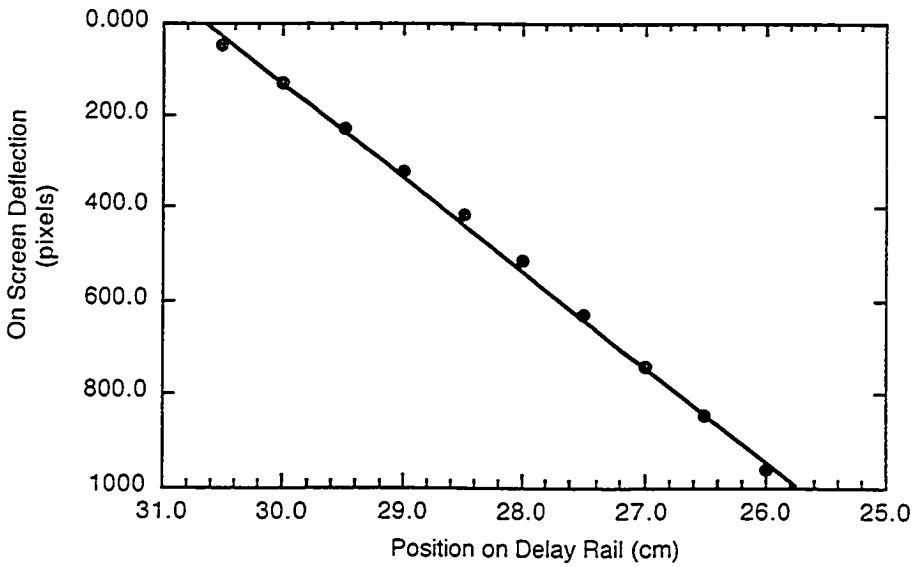

Figure 2.33 The linearity of the voltage ramp produced by the G2 jitter-free unit.

Two measurements are used to determine the time resolution of the streak camera: 1. sweep speed, and 2. FWHM of the IRF. Sweep speed is a measure of how fast the voltage ramp sweeps the electrons across the phosphor screen, and is determined using the slope of the voltage ramp. From Figure 2.33, the sweep speed can be calculated from the slope of the line to be 0.327 ps / pix, and for a 1034 pixel image, the entire image then represents a time window of 340 ps. Sweep speeds are measured every day of data

collection and after every alignment adjustment. Typical sweep speed measurements range from 0.305 to 0.347 ps / pix and are a good gauge of how well the optics leading to the photoswitches are aligned, with smaller measurements being preferred. The second measurement, IRF width, is typically an indication of how well the optics between the sample and the streak camera photocathode are aligned. The IRF of the G2 unit and streak camera have been measured using the shortest possible signal, the femtosecond laser pulse. Figure 2.34 shows the signal of the 387 nm pulse to have a FWHM of 2.2 ps. This is the ultimate resolution of the streak camera. Under conditions with real samples, the time resolution of the streak camera is longer and will be discussed in Section 2.3.2.1.

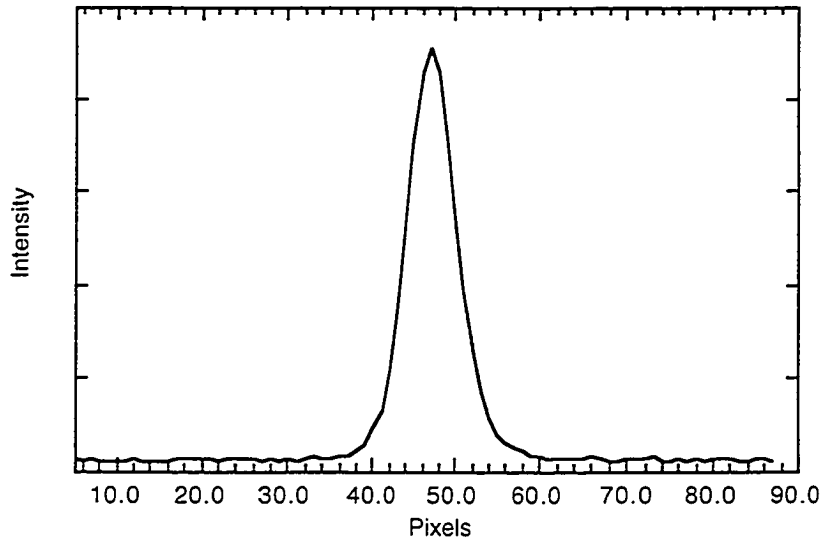

Figure 2.34 Detection of the 388 nm laser pulse using the streak camera and G2 unit. The sweep speed is 0.310 ps/pix, and the FWHM is 7 pixels = 2.2 ps. 10 000 laser pulses have been accumulated.

By measuring the FWHM of the laser pulse at each part of the phosphor screen, any changes in time resolution of the streak camera as a function of screen position can also be detected. Distortions can be caused by imperfections in the imaging lens used to focus the phosphor screen onto the CCD camera, and are indicated by a sharp change in the linearity of the voltage ramp. Analysis of the IRFs collected at varying positions of

the image does not indicate the presence of any distortion in either the vertical or horizontal positions.

In summary, the G2 unit provides a jitter-free, reproducible linear voltage ramp applied to the streak camera deflection plates. The G2 unit is triggered by the pulsed fundamental laser beam incident upon optical photoswitches. Critical alignment of the beam upon the photoswitches provides a fast, clean rising edge to the voltage ramp, which results in typical sweep speeds of 0.327 ps / pix, a full time window of 340 ps and an ultimate resolution of 2.2 ps for the streak camera. The G2 unit facilitates streak camera studies of initial rise and decays of short-lived emission signals, some of which will be presented in Chapters 3 and 4.

2.3.1.3 The Slow Sweep Unit

While the jitter-free unit is impressive in the time resolution that it offers, the short time window limits its usefulness to resolving ultrafast rise times and short fluorescence decays. For measuring slower fluorescence decays, the picosecond time resolution is unnecessary and a much longer time window is necessary in order to capture the entire emission decay. Thus, a slow sweep unit, allowing a longer range of time windows, is necessary to extend the range of chemical systems that can be studied with the streak camera.

The slow sweep unit, designed by Axis Photonique, Inc. and built by Kentech Instruments, is designed to trigger on a TTL signal synchronized to the laser pulse. The unit generates voltage ramps of six different speeds, with full time windows ranging from 1 ns to 135 ns. Like the G2 unit, the output voltage ramps are connected to the deflection plates of the streak camera. Originally, the TTL signal used to trigger the slow sweep unit was the SYNC 3 output of the CPA-2001, which is synchronized to the output pulses; however, the SYNC 3 output has 400 ps of electronic jitter between it and the laser pulse. In order to overcome this jitter, our electronics technician Brian Millier designed and built a circuit whose function is to produce a trigger signal synchronized with the output pulses with a minimum amount of jitter. Essentially, the SYNC 3 signal is used as a gate for choosing one peak of the modelock signal, and this particular peak is

then stretched and amplified until the level is high enough to trigger the slow sweep unit. The output trigger is then sent through a variable delay box of BNC cables, made by ORTEC, which adjusts the time overlap between the voltage ramp production and the electron train in nanosecond increments. Currently, the slowest 4 sweep speeds can be used readily. The fastest two sweep speeds are difficult to use because the time overlap between the voltage ramp production and the electron train requires finer adjustment than nanosecond increments to be properly overlapped. Table 2.4 lists sweep speeds, full time window widths, and typical IRF widths for the first four settings of the slow sweep unit. Sweep speeds of the slow sweep unit are reproducible from day to day and only require infrequent measurement. These four settings, along with the ultrafast window of 340 ps available on the G2 unit, extend the time range of the streak camera over three orders of magnitude.

Table 2.4 Working specifications of the first four settings of the slow sweep unit.

Setting	Sweep Rate (ps / pix)	Full Time Window (ns)	IRF FWHM (ps)
1	89.7	92.6	750
2	27.0	27.9	180
3	11.3	11.7	116
4	4.18	4.3	64

2.3.2 Experimental Setup

2.3.2.1 Solid and Solution Samples

Sample setup and alignment are crucial to being able to collect reliable data. All samples are excited by oblique front face excitation, while the streak camera collects emissions from the front face of the sample. Excitation at an angle allows the direct reflectance of the excitation beam to be avoided. The sample emission is then filtered to remove specular reflectance of the excitation beam and attenuated by neutral density filters if necessary. Emission at desired wavelengths can then be selectively studied by

passing the emission through a bandpass filter before it is incident upon the photocathode of the streak camera.

Solid samples, such as zeolites, are the easiest samples to be studied by the streak camera. The zeolite samples do not introduce much spreading into the IRF because the excitation beam penetrates the surface of the solid only minimally. As well, an accurate IRF is easily obtained by measuring the specular reflectance of the excitation beam of a blank solid sample.

Solution samples present a much greater challenge to streak camera work. Traditionally, solution samples are excited by 90 ° excitation in 10 mm sample cells. For streak camera work, 90 ° excitation produces two problems: 1. weakness of the emission signal and 2. spreading of the IRF. While it is possible to collect nanosecond streak camera data by 90 ° excitation under careful conditions, a wide IRF makes ultrafast work impossible. For all the data collected by the streak camera, a front face excitation configuration has therefore been adopted.

The sample cell for the solution experiments is a 1 mm quartz cell (Hellma) with a teflon stopper. Because solution samples are generally transparent, the excitation beam can penetrate the width of the cell and excite throughout the sample width. This penetration results in degradation of time resolution. Unfortunately, this problem is compounded by the inhomogeneous excitation of the sample. As the beam enters the sample, the photons are absorbed and less light penetrates to the center. As a result, the sample does not fluorescence from all parts of the sample cell evenly, but the front fluoresces most brightly with an exponential decrease towards the back. There are two methods for resolving this problem. The first method involves decreasing the sample concentration such that the intensity of the excitation beam does not change significantly as it penetrates the cell, resulting in homogeneous sample excitation. Samples excited in this manner have poor time resolution (up to 12 ps on the ultrafast system); however, the IRF can be readily obtained by measuring the scatter of the excitation beam by a suspension of an insoluble solid, such as cornstarch, in the blank solvent. For solution samples where low emission intensity is a problem, the second method of resolving the inhomogeneous excitation difficulty is to increase the concentration of the sample. If the sample is sufficiently concentrated, the excitation beam will be entirely absorbed in the

first section of the sample and little intensity will remain to excite the remainder of the sample. Thus, all the emission will be produced in the front of the sample in a manner that is comparable to the solid sample. It has been determined experimentally that a blank zeolite IRF is representative of the IRF of these solution samples for the slow sweep unit, and scatter off the blank cell is sufficient for the IRF on the G2 unit. Throughout this thesis, the solution sample concentrations have been sufficiently high to minimize excitation beam penetration through the sample.

Because the introduction of different types of samples changes the time resolution of the streak camera, it is essential that the IRF be carefully measured for each set of samples. Table 2.5 lists typical FWHM of IRFs for each type of sample measurable on the streak camera.

Table 2.5 Expected IRF FWHM of the streak camera data for varying types of samples.

Sample Type	Voltage Ramp Production	IRF FWHM (ps)
Solid Sample	G2 jitter-free unit	3.3—4.5
Solution Sample (low concentration)	G2 jitter-free unit	7—12
Solution Sample (high concentration)	G2 jitter free unit	5—6
solid and solution	slow sweep unit, 1	750
solid and solution	slow sweep unit, 2	180
solid and solution	slow sweep unit, 3	116
solid and solution	slow sweep unit, 4	64

2.3.2.2 Variable Wavelength Excitation Sources

In order to study luminescent samples, it is necessary to excite the samples with an appropriate wavelength of light. The streak camera setup allows the user to choose from two excitation sources. The first setup involves the use of frequency doubled (388 nm) or tripled (258 nm) radiation produced by the STORC unit. The second setup uses visible light from 460 to 700 nm, produced by the OPA unit. There is a significant amount of setup time necessary to switch between desired excitation sources.

STORC output radiation offers a greater ease of use to the user. Both 388 and 258 nm radiation can be readily used as an excitation source; however, the path length within the STORC unit necessary for producing the higher frequency radiation is longer by 33 cm. Thus, the timing of the voltage ramp production, whether determined electronically using the ORTEC box and SYNC 3 (slow sweep unit) or by delay rail movement (G2 unit) will differ and needs to be determined every time the excitation wavelength is changed.

Both these radiations excite in the UV region, and thus the sample cells used must transmit UV light. For 388 nm radiation, ordinary quartz glass has been found to be sufficient, but for 258 nm radiation, an extremely high quality of quartz glass is necessary. It has been found that ordinary quartz glass fluoresces when exposed to 258 nm radiation and cannot be used to study luminescent samples.

If the excitation wavelength chosen is in the visible region, the OPA unit is required. The OPA unit modifies fundamental frequency pulses into visible light pulses of very low energy, and is situated on the laser table after the STORC unit. In order to use both the OPA unit and the G2 unit, it is necessary to bypass the STORC unit entirely. This is facilitated by a flippable mount housing the beamsplitter within the STORC. By changing the position of this mount, the beamsplitter is removed from the beam path and the entire fundamental beam passes through the STORC unit unchanged. A 50-50 beamsplitter at the exit of the STORC unit allows for half of the photons to be directed into the OPA unit, while the remainder of the beam is directed through the Parker delay rail onto the G2 unit. Because the path length through the OPA unit is much longer than through the STORC unit, it is necessary to increase the path length of the G2 triggering beam to facilitate temporal overlap. Three mirrors need to be added to the pathway before the Parker Rail table to add a meter to the path length. The OPA source with the G2 unit typically has slightly wider IRF widths when compared with IRFs obtained using the STORC unit.

The use of the OPA unit with the slow sweep unit does not require bypassing of the STORC unit, and can simply use the fundamental beam output of the STORC to drive the OPA unit. Large adjustments in timing using the SYNC 3 and ORTEC settings are necessary, and vary with excitation wavelength.

In order to use the OPA unit as an excitation source, the sample must emit brightly. OPA output energies are between one and two orders of magnitude smaller than those produced by the STORC unit and fewer photons are available to excite the sample. Also, the user must use as many bandpass filters as necessary to ensure that the wavelengths being detected by the streak camera are clean of the wavelength being used for excitation.

Table 2.6 below summarizes the various excitation frequency arrangements available for the streak camera system.

Table 2.6 A summary of the various excitation sources available for the streak camera system.

Excitation Source	Wavelength (nm)	Trigger Unit	Bypass STORC?	Path length addition?
STORC	388	G2	no	no
STORC	258	G2	no	no
STORC	388	slow sweep unit	no	no
STORC	258	slow sweep unit	no	no
OPA	460—700	G2	yes	yes
OPA	460—700	slow sweep unit	does not matter	no

2.3.2.3 Background Correction

In many cases, it is necessary to minimize and correct for background signals when collecting streak camera data. Background noise can be sourced to dark counts accumulation of the CCD camera, stray radiation, variations in phosphor screen sensitivity and long-lived luminescent decays of the excited sample. The first source, dark counts accumulation, is minimized by cooling of the CCD camera by a thermoelectric cooling source. Stray radiation is minimized by collecting all data in the dark and using black cloth, tape and cardboard to ensure that the space directly around the photocathode is light tight.

The third cause of background noise, inconsistent phosphor screen sensitivity, is a property of the streak camera that has been discovered by experimental work and requires

user awareness in order to minimize its effect. Because the phosphor screen translates the electrons on its surface into phosphorescence, it continues to be luminescent for some time even after the electrons are no longer being swept across the screen. Accordingly, two images cannot be collected too closely together or a shadow of the first image will be superimposed upon the second image. A period of time (from 1 to 10 minutes) is necessary between each experiment to allow the phosphor screen to relax, and sufficient time has passed when an image taken without exciting the sample does not show a shadow of the previous experiment. Yet it has also been observed that the phosphor screen becomes more sensitive to the parts where electrons have been incident upon the screen, even if a dark image does not show evidence of a shadow. This is most often observed after the measurement of an IRF, where a very concentrated line of electrons is incident upon the phosphor screen. Even after a 20 minute relaxation period, collection of an emission image will have an increased emission artifact in the position of the IRF. To combat this, the user must consider not only the time between image collections, but also the order in which the experiments are performed. If the streak camera setup is consistent from day to day, IRF measurements should be performed at the end of each experimental day to minimize the effects of phosphor screen sensitivity variation.

There exists one type of background signal that can be corrected for, and that is the background signal due to the long-lived luminescence of the excited sample. This signal cannot be avoided and is produced by the reset of the voltage plates upon the streak camera between voltage ramps. Each voltage ramp begins with a bias upon the plates, sweeps the electrons across the phosphor screen from the top down, and then the voltage across the plates is held at an opposite bias for microseconds, which is long enough for the majority of the sample emission to die away. Subsequently the voltage is reversed and the original bias is restored until the next voltage ramp begins. If during the reversal of the voltage ramp there is still some very small luminescent tail emanating from the sample, these electrons will be swept back across the screen slowly and result in a background signal. The background signal usually manifests itself as a tilted baseline underneath the fluorescence decay.

Collecting and subtracting a background image can correct for this residual signal. A background image is generated when the timing of the voltage ramp is set to intersect

the electron train just after the initial sweep across the phosphor screen has been completed. In practice, this is accomplished by moving the rise of the emission signal just off the bottom of the image and capturing an image. The assumption made is that the luminescence decay at long times is sufficiently invariant so that moving along it by the length of one time window will not alter its shape or intensity significantly, Figure 2.35. Subtraction of this image as the background image has shown that the assumption is valid.

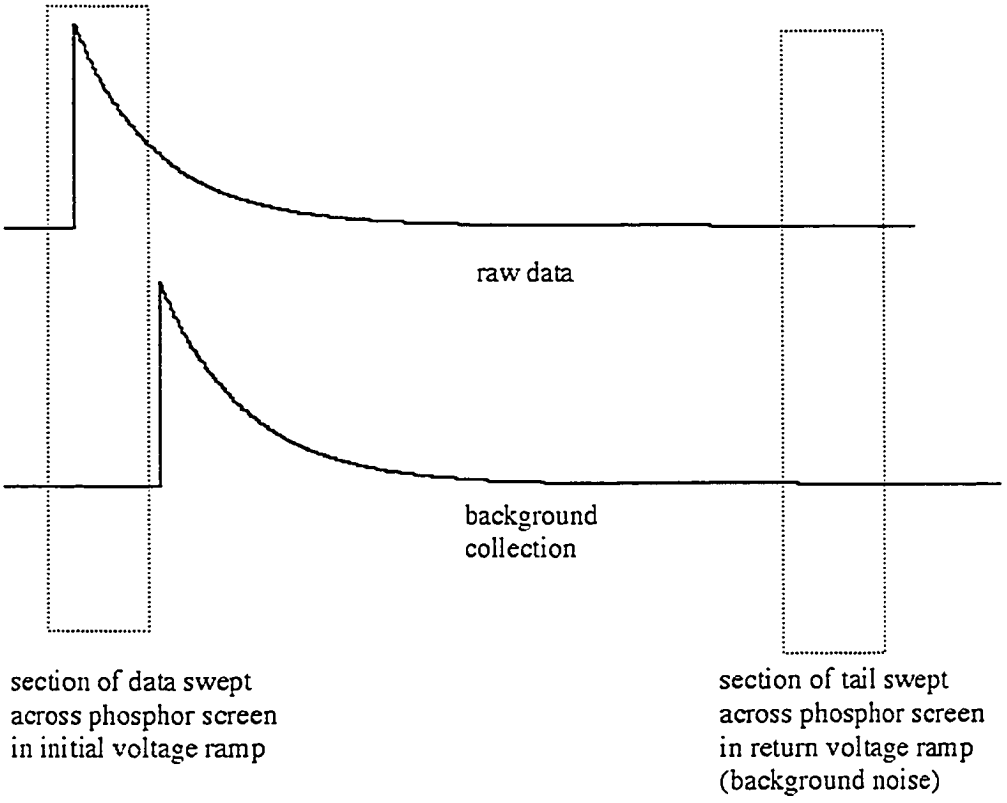

Figure 2.35 Schematic representation of the background collection. Background collection records only the long-lived tail. The tail is changing very slowly so one time window backwards yields the same background signal as that of the true data.

2.3.2.4 Variable Temperature Capabilities

At the current time, the temperature dependent capabilities of the lab are limited to solution samples and only tested within the narrow temperature range of 0 °C to 22 °C. A

sample cell water jacket consisting of a block of brass cooled by chilling solution running through it was machined in house and attached by Tygon tubing to the chiller apparatus and pump using a circulating solution of 50 % ethylene glycol in water. Cooled air is also blown over the front and back of the sample cell to prevent condensation upon the cell surface. The insertion of a thermocouple into the center of the sample cell allows for the monitoring of the sample cell temperature. Further expansion of the temperature range has not been fully developed because the variable temperature apparatus was no longer necessary at the time.

2.3.3 Software

The instrumental interfacing and data collection software is the commercial package IPLab Spectrum (Photometrics). This software allows for the timing of images without synchronization to the laser. When collecting a data image, the streak camera and trigger unit both remain on before, during and after the image collection, and the collection begins when the user prompts the software to do so. In order to preserve the sample being excited, a shutter blocks the excitation beam from the sample until just before the image collection is initiated. It is the user's responsibility to open the shutter and then initiate image collection.

Once the image has been collected, the user closes the shutter. Generally, the remainder of the equipment is left running between data collections, especially if the time between image collections is short. The software displays the image upon the screen for user manipulation. Basic mathematical operations are also available in IPLab Spectrum, such as subtraction of two images (used for background correction) and summation of images into vectors so that the kinetic profile can be quickly viewed before data analysis. Generally, the background corrected images are saved as binary files for further manipulation and analysis using software written in-house as part of this thesis project. Kinetic analysis and deconvolution software was not part of the package purchased from Axis-Photonique, Inc.

Two main programs have been written to manipulate the images and analyze the emission kinetic profiles they represent. The first program, Image Correct, is a program

designed to correct for characteristics of the streak camera manifest in the images. The second program, Deconfit, is a convoluted fitting routine designed specifically to produce kinetic fits for the emission profiles studied by the streak camera system.

2.3.3.1 The Image Correct (IC) Program

In order to translate the images produced by the streak camera into an emission decay trace of emission intensity as a function of time, the images need to manipulated and then summed. The vertical direction of each image contains the time information, while the horizontal direction contains the spatial information of each experiment. In essence, each image is composed of a collection of vertical kinetic traces, which, if summed, can produce a single kinetic trace of high signal to noise ratio. However, horizontal summation can only be performed if every pixel in one row represents the same time. In general, the streak camera, when triggered by the G2 unit, has two factors that introduce a distribution of times across a row of pixels. The IC program allows the user to correct for these factors and return a corrected image, which can then be summed horizontally, Figure 2.36.

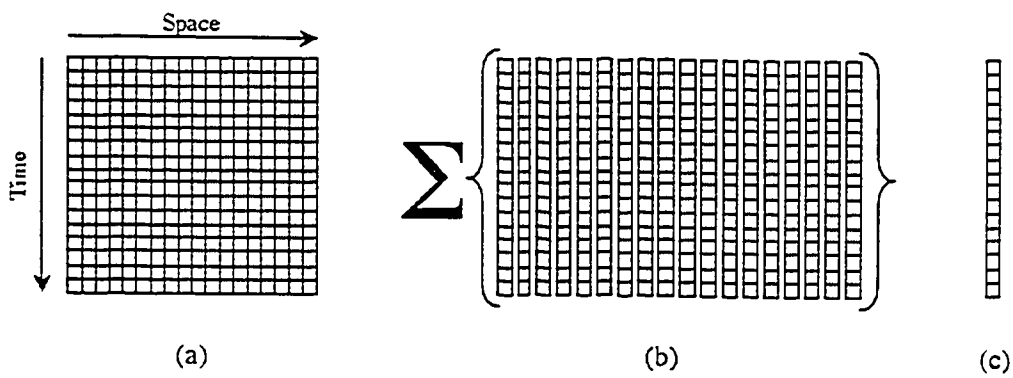

Figure 2.36 A schematic representation of horizontal summation. (a) The original image is a matrix of emission intensities as a function of time and space. (b) As long as the time information across a row is constant, the vertical vectors can be summed across the spatial dimension to produce (c), a single vector representing the emission intensity as a function of time.

The first distribution of time across the horizontal dimension of the photocathode is introduced by the angle of incidence of the excitation beam. Because the excitation beam excites the sample at an angle while the detection of emission is normal to the sample face, the path length difference of excitation from one side of the sample to the other induces emission from one side of the sample several picoseconds before the other side. On the image, this is manifest as a noticeable tilt (Figure 2.37).

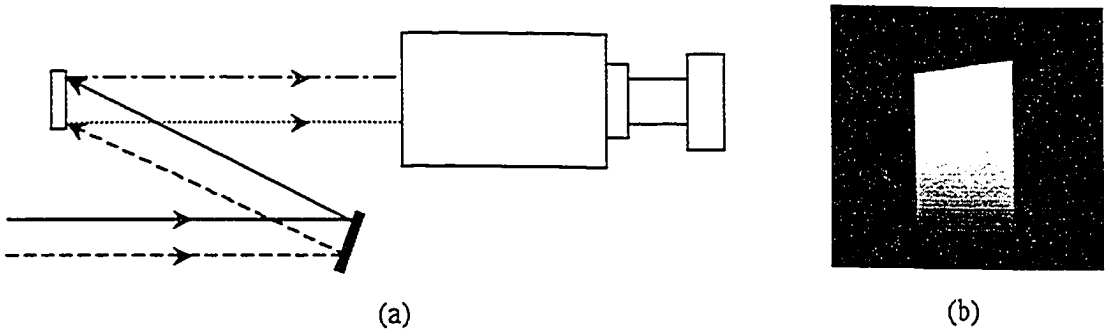

Figure 2.37 A schematic demonstration of the cause of tilt in ultrafast streak camera images. (a) Due to the angle of incidence of the excitation beam upon the sample, one side of the beam (---) travels a shorter distance than the other side of the beam (—). Thus one side of the sample will emit luminescence (···) before the other side (—·—), resulting in an image (b) that is tilted.

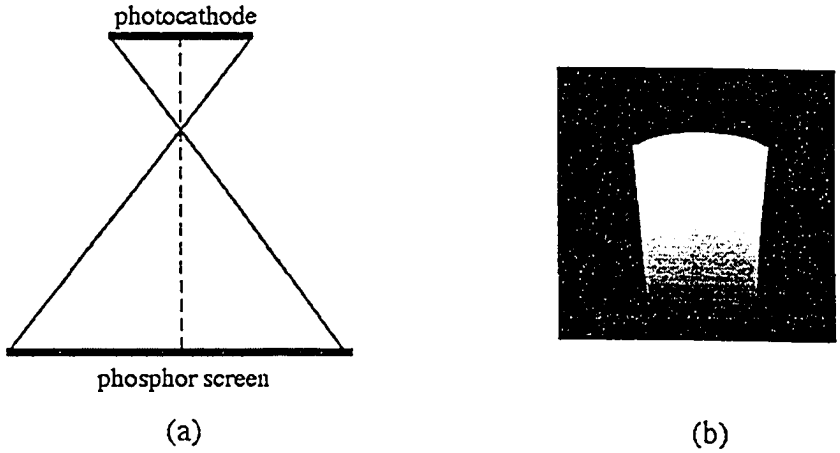

Figure 2.38 A schematic demonstration of the cause of curvature in picosecond streak camera images. (a) The pathway of all the electrons from the photocathode to the phosphor screen is directed through the center of the streak camera, resulting in the electrons from the center of the photocathode traveling a shorter distance than those leaving from the edges, producing (b) an image with curvature.

Another path length difference leading to noticeable image curvature is introduced by the electronic optics inside the streak tube. Because the electrons are focused through a focal point and expanded before reaching the screen, electrons leaving the photocathode from the side will travel a longer path length than the ones leaving from the center. This manifests as curvature in the resulting image (Figure 2.38).

The IC program accepts images collected and saved using IPLab Spectrum software in a binary format. Each image measures 1034 by 1317 pixels and is displayed to the user, who can adjust the brightness and contrast of the image. The IC program cannot read images that have been cropped using the IPLab program. Large square buttons on the right side of the screen allow the user to choose the functions that are to be performed on the image. These include correcting curvature, correcting tilt, cropping the image, and horizontal summation of the picture.

Curvature correction, if necessary, is always the first function to be performed and must be performed on a full image, while the other functions can be performed in any order. The distance in pixels that the image needs to be corrected, $\Delta S(N)$, is a function of pixel distance from the center of the CCD image and the sweep speed. It is defined by Eqns 2.11 and 2.12, with constants for our streak camera listed in Table 2.7.

$$\Delta t(N) = \frac{1}{v_e}\left\{\sqrt{(NM_dC)^2\left(\frac{M_s+1}{M_s}\right)^2 + L^2} - L\right\} \tag{2.11}$$

$$\Delta S(N) = \frac{\Delta t(N)}{SS} \tag{2.12}$$

Table 2.7 Constant parameters used in equation 2.11.

Variable	Definition	Streak Camera Parameter
v_e	velocity of electrons in the streak tube	0.07269 mm/ps
M_d	demagnification of image from phosphor screen to CCD camera	1.9
C	pixel size of the CCD camera	6.8 μm
M_s	magnification of image spatially in streak tube	1.7
L	length of streak tube	262 mm

The remaining parameters are N, the distance in pixels from the center of the image, $\Delta t(N)$, a constant vector that defines the time delay in picoseconds of electrons reaching the phosphor screen relative to the center of the screen, and SS, the sweep speed in picoseconds per pixel, being applied to the electron train by the voltage ramp. Because $\Delta t(N)$ is a constant for the camera, the only parameter the user is required to enter is SS in order to calculate $\Delta S(N)$, the correction in pixels for each column of the image array. For example, for a sweep speed of SS =155 fs / pix at a point N = 385 pixels from the center of the screen, the ΔS = 10 pixels. This means that this column must be moved up by 10 pixels in order to straighten the image.

Tilt correction is accomplished manually for each data set. Because the entire image is tilted linearly, the tilt can be defined as a straight line across the image. Activating the tilt correction function produces a red line displayed across the image with two cursors. The user adjusts the cursors until the line matches the tilt of the image, generally by aligning the line to the beginning of the emission signal. When the line has been set, the program calculates the number of pixels to adjust each column of the image array to produce a corrected matrix.

Both the curvature and tilt corrections are accomplished within the program first by calculating the number of pixels that each column needs to be shifted. Next, each column of the image matrix is rotated by the corresponding number of pixels n, *i.e.* the first n numbers get shifted to the end of the vector and all the remaining numbers shift up n positions. The resulting image is properly corrected in the center but the shifting of the numbers from the top to the bottom of the image in the vector rotations invalidates the bottom section of the matrix. In order to discard these and other parts of the image that are irrelevant, cropping is necessary. Activating the cropping function activates two cursors that can be dragged by the user to define the new borders of the data set. Once these borders have been set, the program returns the smaller image.

Besides discarding irrelevant sections of the image, cropping can also increase the signal to noise ratio of the final summed kinetic profile by discarding the sections of the data that do not contain any emission information. These dark areas, generally on the left and right edges of the image, contain noise. When discarding sections of the matrix, it is important to determine whether the portion of the image being retained will reflect the

true kinetic profile once summed. Built into the IC program is a small function that allows the user to preview the summed emission profile and compare its shape to any one column. This function is most useful in determining whether more of the image needs to be discarded, and confirms when the image is ready to be summed and saved. The summation preview is located on the bottom right corner of the IC user interface, Figure 2.39.

Summation of the image produces a vector that is saved as two ascii files. The first file contains the absolute emission intensities and a second file contains the emission intensities scaled between 0 and 1 for ease of plotting and display purposes. Both text files can be read by any spreadsheet program, as well as used as input files into the convoluted fitting program, Deconfit, which will be described in the next section.

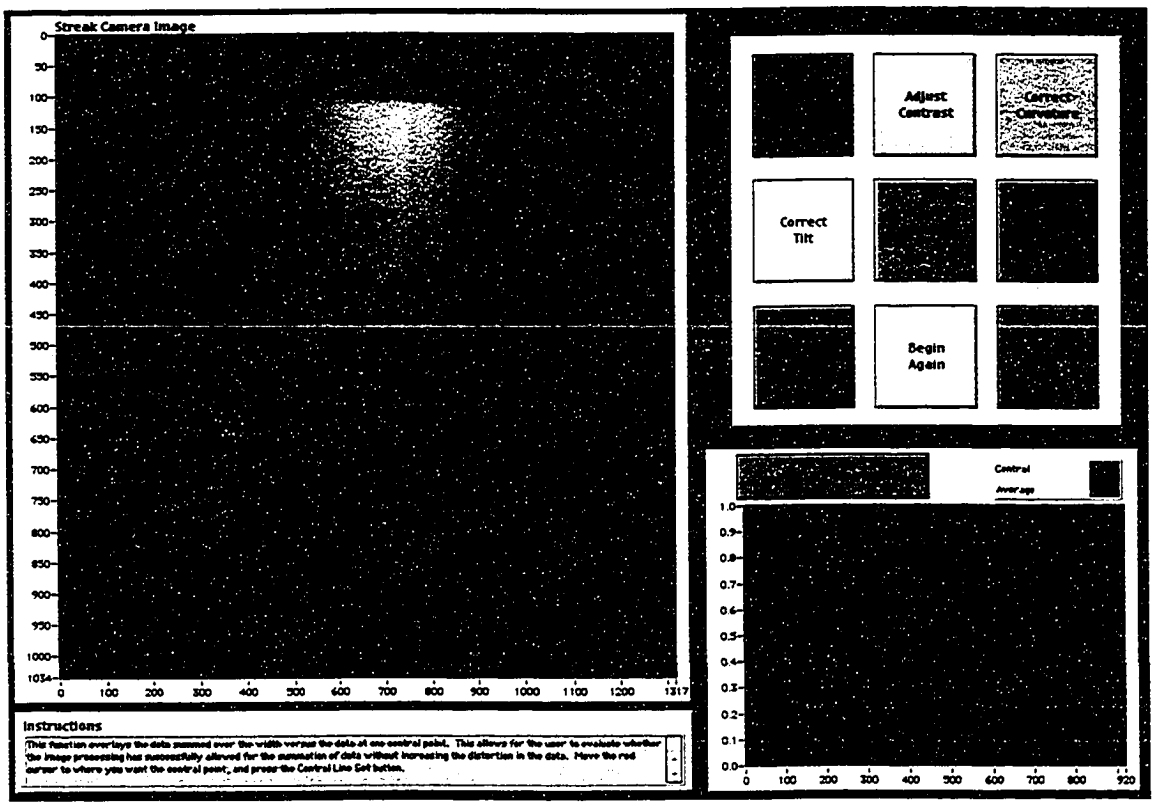

Figure 2.39 The front panel of the Image Correct program.

2.3.3.2 The Deconfit Program

For the emission data where convolution with the instrument response function of the streak camera system is significant, it is generally necessary to analyze the luminescence profiles using convoluted fitting. All of the data collected using the G2 trigger unit, and settings 3 and 4 on the slow sweep unit require convoluted fitting analysis to yield meaningful kinetic rates because the width of the IRF is significant in comparison to the time window. The Deconfit program was written in order to iteratively fit the emission profile to a kinetic model convoluted with the IRF and return the fitted parameters.

The Deconfit program is based upon a modified Levenberg-Marquardt algorithm, where a convolution step has been inserted. Briefly, the basic function of the Deconfit program is to use the starting parameters and kinetic model to calculate a kinetic profile, which is then convoluted with the experimental IRF to generate a calculated fit. The calculated fit is then compared with the experimental emission profile to calculate new starting parameters and the cycle is repeated until convergence between the calculated fit and experimental profile is achieved.

In order to use the Deconfit Program, the user must measure both the decay profile of interest and the corresponding IRF and manipulate them using the IC program. The output files of the IC program are then read directly by the Deconfit program, which then displays the experimental data and the IRF function on the same plot. The display IRF function is scaled to appear the same height as the experimental data while the IRF used for convolution has actually been scaled so that its total area is equal to 1. Both the IRF and the experimental data are regularly spaced in time due to the linear nature of the voltage ramp, and both vectors must have the same spacing in time in order for the program to function, *i.e.* they must both be collected on the same sweep speed. When the vectors are loaded into the Deconfit program, there is no time information attached. The user is asked to enter the sweep speed, and this value is used with the number of data points to generate the time vector beginning at time zero. The time vector is then used with the model and parameters to calculate a kinetic profile. Convolution of this kinetic profile generates a convoluted fit.

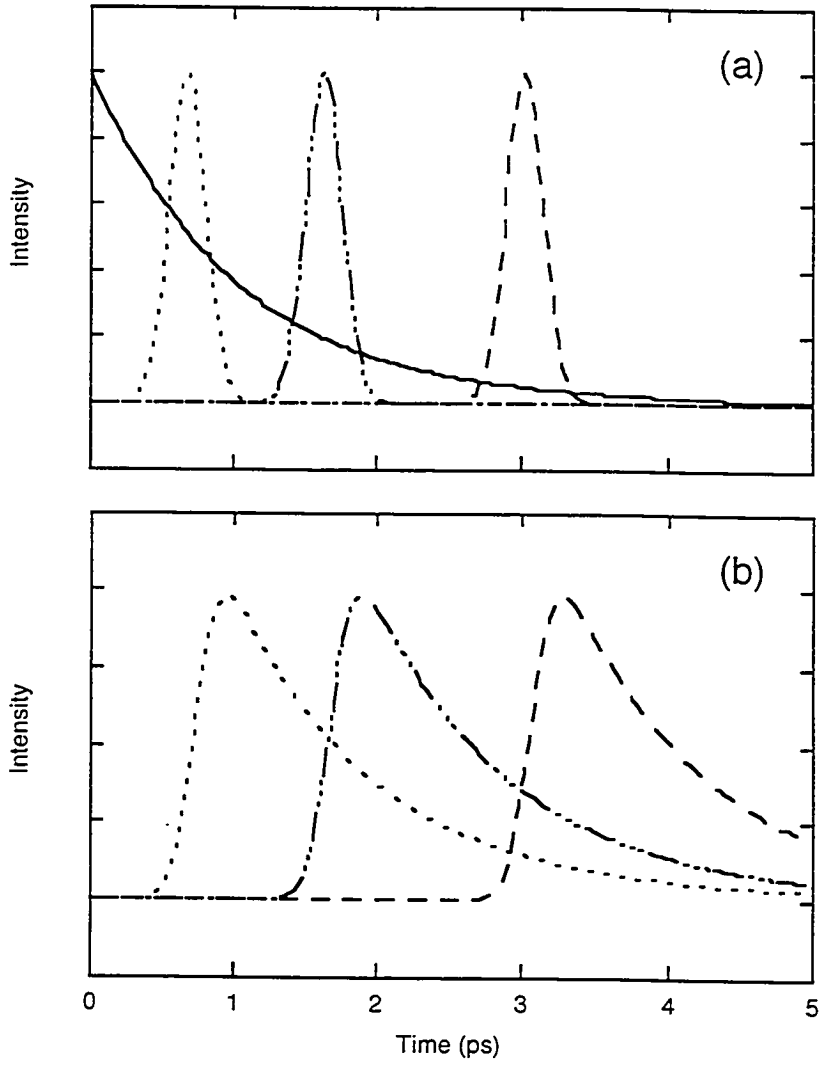

Figure 2.40 A demonstration of the shifting in time of a convoluted vector. (a) The kinetic model (—) is convoluted with Gaussian IRFs that are shifted in time relative to one another. (b) The resulting convoluted vectors are shifted in time relative to one another. The amount of shifting is directly caused by the placement of the IRF.

In order for the convoluted fit to be aligned in time with the experimental data, the IRF must be properly aligned with the experimental data. The user accomplishes this manually and the IRF vector is rotated as its position is adjusted. This is possible because the IRF vector is approximately Gaussian so all points away from the peak center are zero

and can be considered placeholders. Therefore rotating the vector by taking points from the back of the vector and adding them to the front or vice versa changes the position of the IRF peak. When the IRF is then convoluted with the kinetic profile, the position in time of the generated fit is determined by the placement of the IRF. This is illustrated in Figure 2.40.

Numerical convolution, as described in Section 2.2.4.3, is defined as

$$F(n) = \sum_{n'=-\infty}^{\infty} g(n') f(n-n') \tag{2.6}$$

$$g(n) = 0 \quad \text{for} \quad (n < 0) \text{ or } (n > N_g - 1)$$

$$f(n) = 0 \quad \text{for} \quad (n < 0) \text{ or } (n > N_f - 1).$$

for two finite vectors of length N_g and N_f. The resulting vector is of length $N_g + N_f - 1$. In order to compare the convoluted fit to the experimental data, the convoluted fit is truncated to the same length as the experimental data vector by discarding the points at the end of the vector. The remaining calculations to determine new parameters for the model and whether convergence has been reached can now be performed between the convoluted fit and the experimental data. These calculations are standard in the Levenberg-Marquardt algorithm and were performed using the existing packages provided with LabVIEW 5.1, although modifications were introduced to increase the efficiency of the calculations.

Because the time placement of the IRF is critical to the success of the Deconfit program, each fit is automatically performed ten times by the program. Each fit is performed with the IRF in a slightly different position, both before and after the position chosen by the user. The IRF is shifted by single vector units for each fit. All the fits are returned to the user in order of the largest to smallest χ^2 value with residuals so that the user can evaluate each fit and choose the most suitable one. Each fit can be saved as a text file containing all the initial and calculated parameters, as well as the experimental data, fitted data, and residuals for ease of plotting in any standard spreadsheet program.

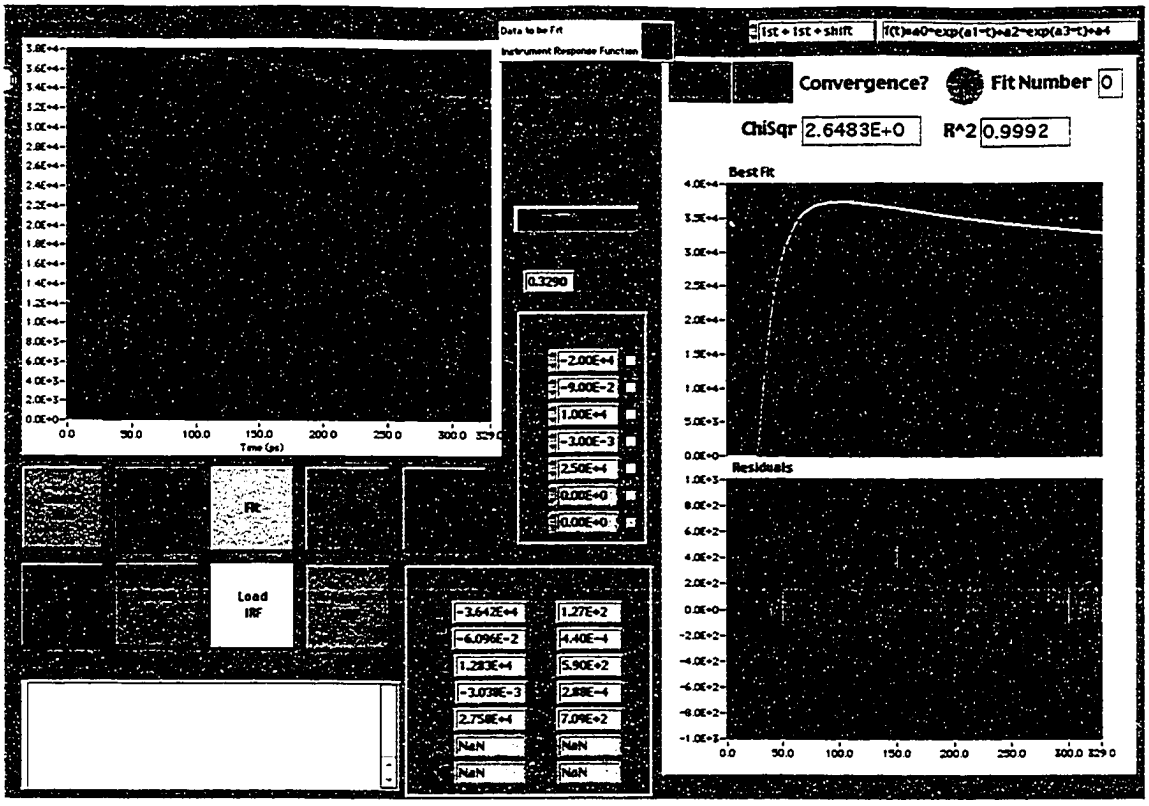

Figure 2.41 The front panel of the Deconfit program.

The Deconfit program and the CFnP program (Section 2.2.4.3) are very closely related as the CFnP program is a revision of the Deconfit program. Although their front panels are essentially identical, there are some major differences between the two programs. First of all, the Deconfit program requires that the user measure the IRF experimentally while the CFnP program generates the IRF based upon the experimental data and the user-defined FWHM. As well, the experimental data for the Deconfit program is always evenly spaced in time, so it is not necessary to generate a time vector to do the calculation and then extract out only the points to be compared to the experimental data. Even with the extra steps, the CFnP program runs much faster than the Deconfit program due to fewer experimental data points.

Use of the Deconfit program to analyze streak camera data is absolutely necessary and requires practice in order to generate good analyses efficiently. Experience produces knowledge of the best placement of the IRF, valid truncation of data, and manipulation of the vectors when first loaded into the program by background subtraction. The use of the

Deconfit program facilitates the extraction of valid and meaningful kinetic information from the vast amount of data that can be collected using streak camera experiments.

2.3.4 A Summary of the Streak Camera System

The streak camera system facilitates the study of time-resolved luminescence emitted from samples after excitation with femtosecond laser irradiation. Using the G2 jitter-free unit as a triggering source for the streak camera, the resolution is 3.3 ps for both solid and solution samples, and the total time window available for capturing luminescence is 340 ps. A second unit, the slow sweep unit, is also available for triggering the streak camera. This unit has four sweep speeds that allow luminescence to be captured for time windows of 4.3, 11.7, 27.9, and 92.6 ns, with IRFs of 64, 116, 180, and 750 ps, respectively. Both solid and solution samples are studied using front face excitation, and the excitation wavelengths available are frequency doubled (388 nm) and frequency tripled (258 nm) radiation, and visible light wavelengths produced by the OPA unit (460 to 700 nm). The luminescence wavelength captured is determined by the use of bandpass filters directly in front of the photocathode of the streak camera.

Streak camera data are captured using a CCD camera, and the resultant images must be processed in order to extract the luminescence decay data. Inherent to the streak camera images are curvature and tilt; these are introduced by the streak camera and must be corrected for when using the G2 unit. All the images require cropping and summation to produce the usable luminescence decay data. Image processing is accomplished using the Image Correct program. For data collected using the G2 unit and the fastest two sweep speeds of the slow sweep unit, convolution of the IRF with the luminescence data must be taken into account when extracting kinetic rate constants from the data. This is accomplished using iterative convoluted fitting through the Deconfit program. Both the Image Correct and Deconfit programs were written in-house as part of this thesis project.

2.4 Integration of the Transient Absorption Spectrometer and Streak Camera System

The beauty of having both the transient absorption spectrometer and the streak camera system on the same laser table is the economy of both funds and space. By running both systems from the same laser, it is only necessary to have one laser, one laser table and many of the elements are usable in both setups and do not require repetition on the laser table. These elements include the STORC, the Parker Rail table and many of the mirrors steering the beams about the table. All of the elements of both streak camera systems fit neatly onto a 4 by 12 foot laser table housed in a small, enclosed room. The temperature and humidity of this small space can be controlled easily by an air conditioner to produce ideal conditions for laser operation. As well, the room light can be darkened for streak camera measurements without disturbing others and all laser light can be contained within the room for laser safety.

In order to facilitate switching between setups with a minimum of effort, flippable mirror mounts (New Focus) were employed. These mirror mounts house a mirror in a very narrow amount of space, and by flipping the mirror mounts up or down, the laser beam can pass over the mount or be redirected by the mirror it contains. The use of these mirrors allows for the setups to both be completely built upon the table at all times, and because the mirrors have excellent alignment reproducibility, the repeated use of the mirrors requires only minor adjustments in the beam alignment. Switching between the streak camera and transient absorption setups only requires the flipping of two mirrors.

Figure 2.42 shows the layout of the femtosecond laser table with all the permanent optics. Figures 2.43 and 2.44 show the beam pathways of the transient absorption spectrometer and streak camera system, respectively. These three figures clearly demonstrate the integration of both systems on one laser table and the ease of switching between one system and another by the adjustment of flippable mirror mounts.

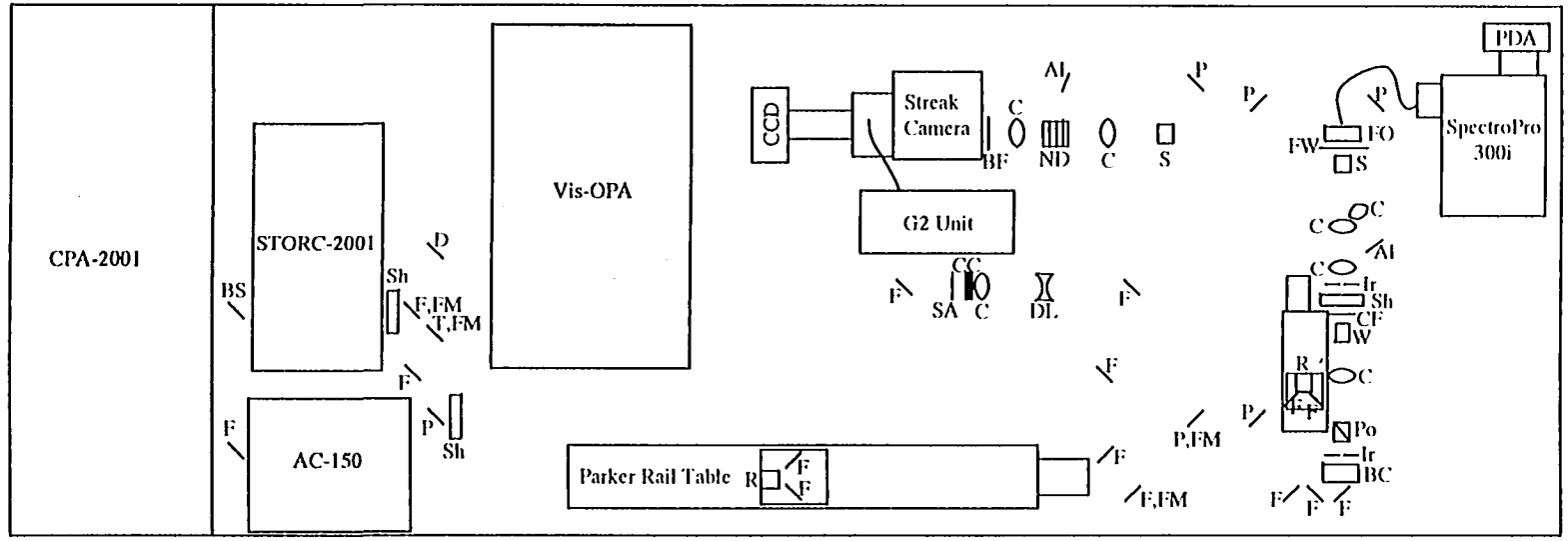

Legend

BS: Beam splitter
F: 775 nm turning mirror
Sh: Uniblitz shutter
D: 388 nm turning mirror
T: 260 nm turning mirror
P: 260/388 nm turning mirror
Al: Aluminum turning mirror
R: Retroreflector
C: Convergent lens
SA: Saturable absorber
S: Sample holder
Ir: Iris
CF: Cutoff filter
FO: Fibre optic
CC: Cylindrical convergent lens
DL: Divergent lens
BF: Bandpass filter
ND: Neutral density filters
FW: Filter wheel
BC: Berek's compensator
Po: Glan-laser polarizer
W: Water cell
FM: Flippable mirror mount

Figure 2.42 The layout of the femtosecond laser table. Non-permanent optics, such as the aluminum mirrors and lenses directing the output of the OPA, have been omitted for clarity.

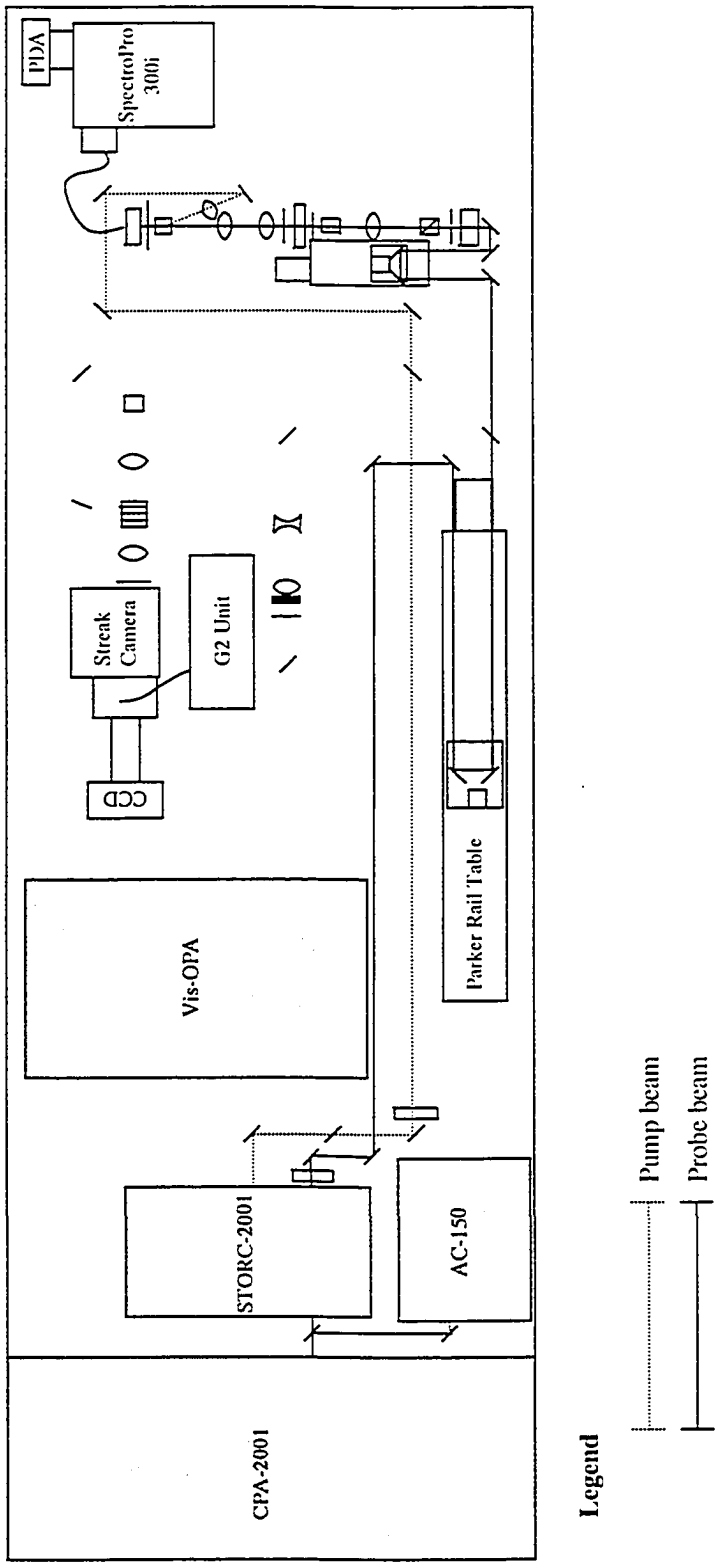

Figure 2.43 The beam pathways of the transient absorption spectrometer, using the water cell and 388 nm excitation.

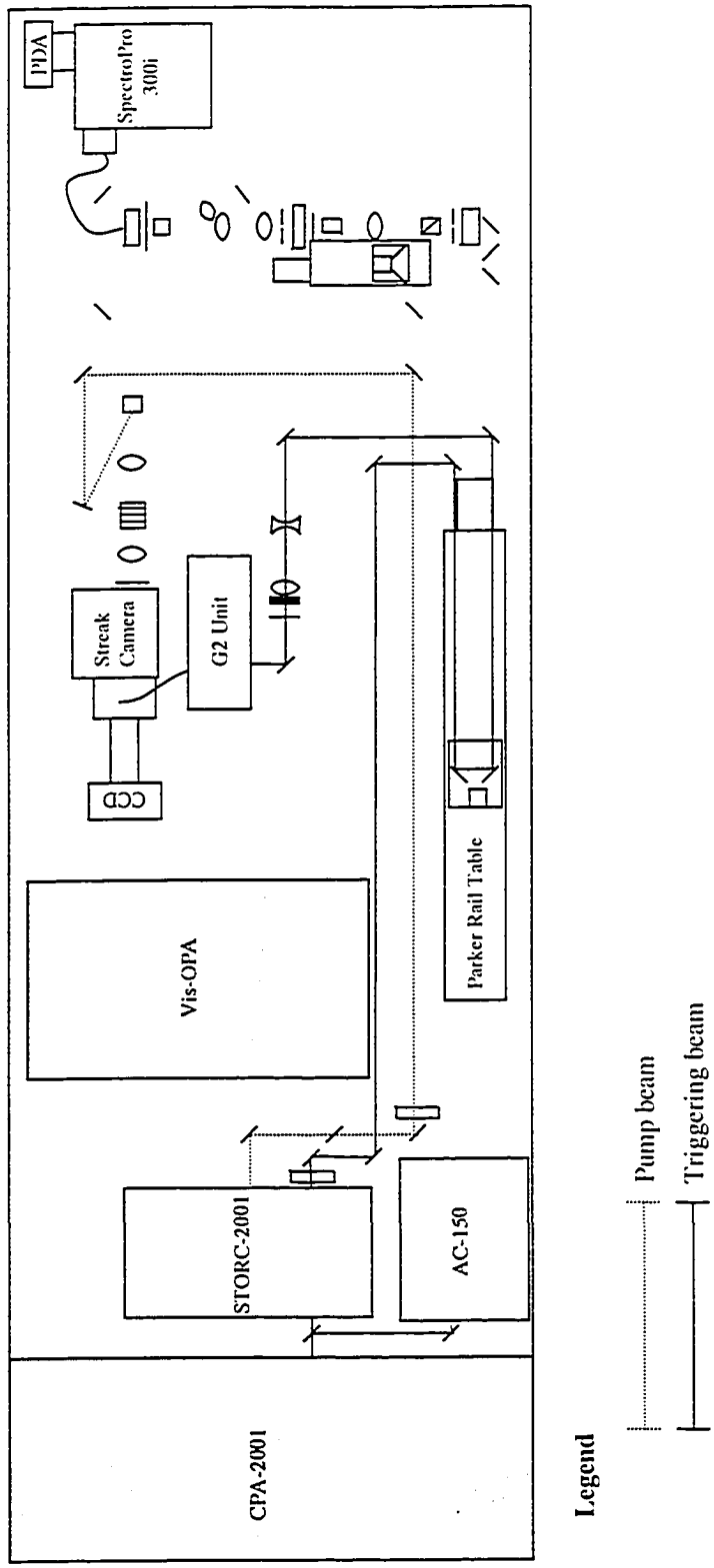

Figure 2.44 The beam pathways of the streak camera system, shown using the G2 Jitter-Free unit as the voltage ramp generator.

Chapter 3: Ultrafast Dynamics of Pyrene and 9,10-Dicyanoanthracene in Faujasite Zeolites

Zeolites are inorganic, naturally occurring minerals with an open framework structure.[48,49] This open structure allows zeolites to act as sponges, adsorbing and incorporating guest molecules into the framework structure. Just as molecules in solution interact with surrounding solvent molecules, the unique structural and physicochemical features of the zeolite affect the molecules they host. Zeolites can have molecular-sized pores, channels and cavities arranged in periodic arrays. This regular structure induces a distribution of guests in spatial arrangements and long range ordering that is unique to the zeolite environment. In addition, the zeolite interior is often a strongly polar environment due to the negatively charged lattice, which is counterbalanced by cations. The study of guest molecules in polar environments, particularly neutral, non-polar organic molecules, is made difficult in solution due to their insolubility, but can be realized using a zeolite host material. These two major factors of structure and environment make the behaviour of molecules incorporated into zeolites interesting.

This chapter describes the study of pyrene and 9,10-dicyanoanthracene (DCA) in cation-exchanged zeolites X and Y by ultrafast fluorescence. Pyrene impregnated zeolites have been a subject of much investigation in the literature.[50-57] It has been postulated that the polar nature of the zeolites can induce a ground state dimer.[57-60] If true, this behaviour contrasts sharply with the dissociative nature of the pyrene dimer in solution. The absence or presence of a ground state dimer can be investigated by examining the rise-time for excimer emssion using the ultrafast streak camera. The first part of this chapter describes the fast dynamics of excimer formation in zeolites, and also explores the influence of the zeolite host on pyrene excimer emission rise times. DCA exhibits dramatically different behaviour in zeolites than in solution. The systematic study of DCA in zeolite Y as a function of counterbalancing cation and loading level is described in the remainder of this chapter. Using nanosecond streak camera studies, both monomer and excimer emission profiles are analyzed in Section 3.3 to determine the distribution of DCA in adsorption sites on the surface of the zeolite interior. As well, the

dynamic motion of DCA through the zeolite upon excitation is explored by ultrafast fluorescence, and a model of the intercavity motion is presented in Section 3.4. Together, these studies demonstrate the utility of the streak camera system to investigate heterogeneous systems and contrast the traditional behaviour of these polyaromatic compounds in solution to their observed behaviour in zeolites.

3.1 Zeolites

3.1.1 X and Y Zeolite Topologies

The description of a zeolite must include both its composition and its framework structure. At the heart of all zeolite topologies are the primary building blocks: SiO_4^{4-} and AlO_4^{5-} tetrahedra.[61-64] Figure 3.1 demonstrates how these tetrahedra are linked *via* shared oxygen atoms to produce substructures such as sodalite and pentasil cages. Each of these substructures can then be arranged in a myriad of topologies to generate different zeolites, some of which are shown in Figure 3.2. The connection of these substructures generates three-dimensional networks of cavities, pores and channels.

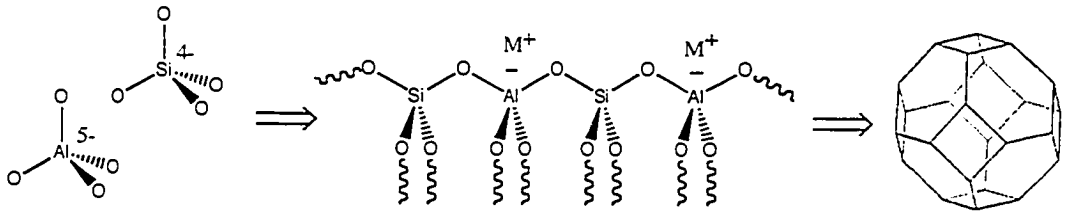

Figure 3.1 Schematic representation of tetrahedral building blocks linked together to form substructures such as the sodalite cage shown.

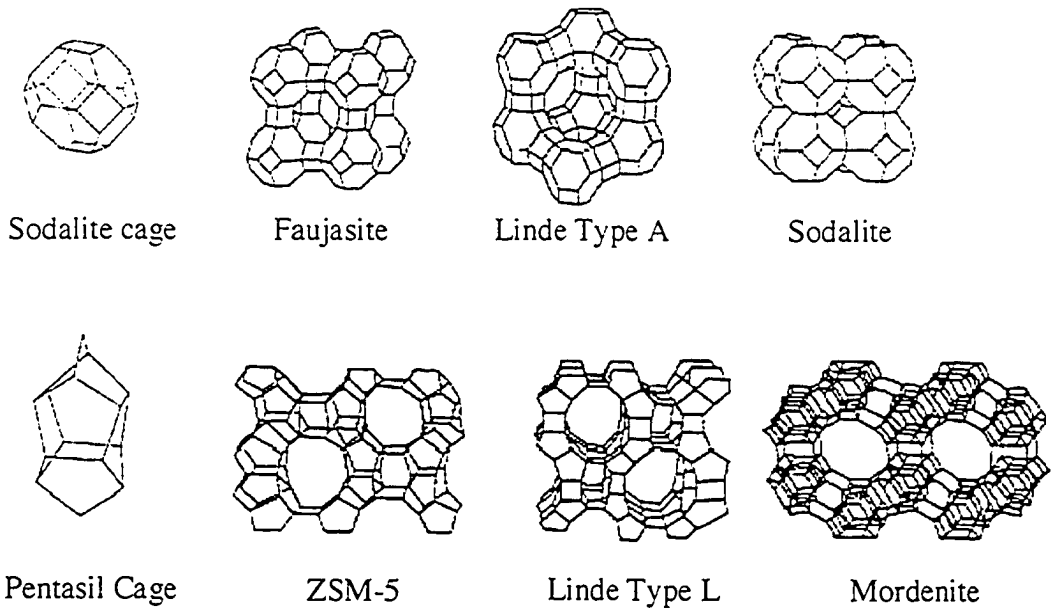

Figure 3.2 Examples of various zeolite topologies generated through spatial arrangement of sodalite and pentasil cages. Figure reproduced from reference 49.

Zeolites[48,49,62,63,65] are often described by their substructure, pore size, channel system and dimensionality. Common systems include channels composed of cages and windows, which can be connected in one, two or three dimensions.[62] In one-dimensional systems, zeolites have tube systems that are isolated from one another. Two-dimensional systems have channels that intersect to form isolated layers, and three-dimensional systems have channels that intersect in three directions. Faujasite zeolites, such as zeolites X and Y, have sodalite cages arranged into three-dimensional channels of large, spherical, void spaces known as supercages. There are eight supercages in a unit cell of zeolites X and Y. These supercages are linked to each other tetrahedrally *via* 7.4 Å pores. Guest molecules can diffuse through the pores to reside within the zeolite framework.[54,56,66,67] Since only small molecules such as water can be present within the sodalite cages of the zeolite framework, organic guest molecules reside preferentially within the supercages.[56,58]

Due to the presence of tetravalent aluminum in the framework, the lattice bears a net negative charge that is balanced by charge balancing cations located throughout the lattice. Cations are typically protons or alkali or alkaline earth metals that are not covalently bound to the framework. As a result, they are mobile and can be readily

exchanged. These cations reside in the lattice either within a sodalite cage (Type I cations) or at specific sites within the supercage walls (Type II or Type III cations).[62,63,65,68] Type I cations are inaccessible to guest molecules located within the supercages. Type II and Type III cations are accessible to guest molecules, where Type II cations are located on the walls of the sodalite cages facing into the supercage and Type III cations are located entirely within the supercage. Type III cations are rare in Y zeolites with only 8 cations per unit cell, but are much more prevalent in X zeolites where there are 38 cations per unit cell. Figure 3.3 shows pictorally the possible positions of the charge-balancing cations about a faujasite supercage.

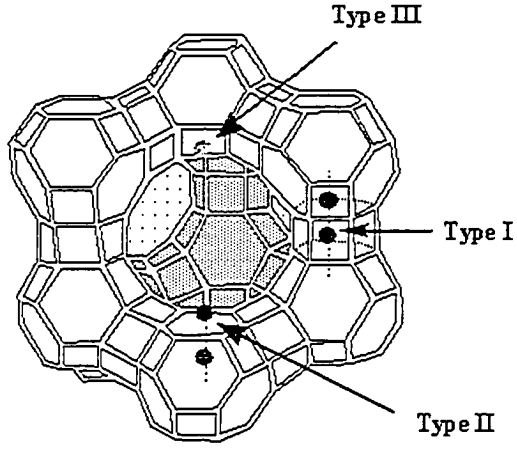

Figure 3.3 Representation of a faujasite supercage demonstrating the locations of Type I, II and III cations. Reproduced from reference 68.

Besides silicon, aluminum, oxygen and counterbalancing cations, zeolites naturally adsorb water into the framework. The typical unit cell compositions of zeolites X and Y are:[62]

$$\text{Zeolite X: } M_{86}(AlO_2)_{86}(SiO_2)_{106} \cdot 264\ H_2O$$

$$\text{Zeolite Y: } M_{56}(AlO_2)_{56}(SiO_2)_{136} \cdot 253\ H_2O$$

where M is a monovalent cation. Zeolites X and Y are topologically identical, and only differ in their morphology. Zeolite X has one of the highest concentrations of framework aluminum of all zeolites, with a Si/Al ratio of approximately 1.5, while zeolite Y has a Si/Al ratio of 2.5. Due to the greater concentration of aluminum in zeolite X, more

cations are necessary to achieve charge neutrality. The presence of these added cations, mostly as Type III cations, drastically changes the interior environment of zeolite X compared to Y with respect to both available volume and polarity.

In addition to the number of cations, the nature of the cation also plays a large role in defining the microenvironment within the zeolite interior. The most commonly exchanged cations are alkali metal cations: Li^+, Na^+, K^+, Rb^+ and Cs^+. By varying the counter-ion, the free space and the polarity within the zeolite interior can be altered.[69] Li^+ and Na^+, being small, hard cations, have tightly held charges that are tightly bound to the framework. The high charge density results in stronger electrostatic fields being present and a greater amount of free volume available for guest molecules. In contrast, the largest two cations, Rb^+ and Cs^+, are considered soft cations due to their diffuse positive charge. These two cations take up the greatest amount of volume within the zeolite cavity. Li^+ and Na^+ are known to be within the supercage walls,[62,70] while K^+, Rb^+ and Cs^+ reside within the supercages.[71] Table 3.1 gives quantitative data for the free volume and electrostatic fields within Y zeolites, while Figure 3.4 demonstrates pictorally the free space within the zeolite interior as a function of counterbalancing cation.

Table 3.1 Cation dependence of supercage free volume and electrostatic field in MY zeolites.[68,72]

Cation (M^+)	Ionic Radius of the Cation (Å)	Vacant Space in Supercage ($Å^3$)	Electrostatic Field within Supercage ($V/Å^3$)
Li	0.76	834	2.1
Na	1.02	827	1.3
K	1.38	807	1.0
Rb	1.52	796	0.8
Cs	1.67	781	0.6

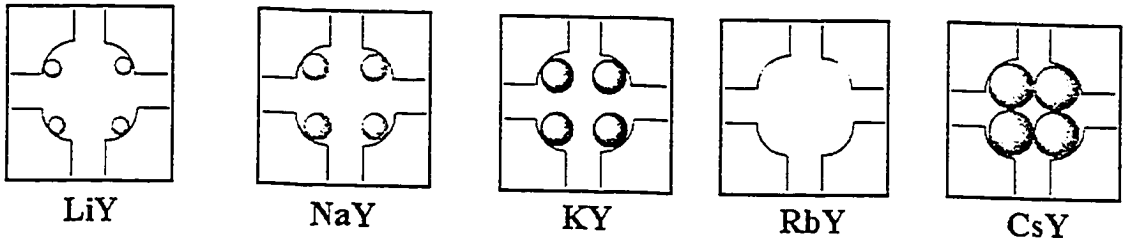

Figure 3.4 A pictoral demonstration of the free space within a faujasite zeolite supercage as a function of counterbalancing cation size. Figure reproduced from reference 73.

3.1.2 The Zeolite as Solvent: Host-Guest Relationships

3.1.2.1 Incorporation of Guest Molecules into Zeolite Hosts

Because of the void space within the faujasite zeolite interior, molecules that are of sufficiently small size and shape can be accommodated within the supercages. These guest molecules can either enter the zeolite by diffusion, provided that their dimensions allow for travel through the pores, or by "ship in a bottle" synthesis,[67,74,75] producing guests that fit only within the supercages but are too large to move between supercages. In order for a guest molecule to be incorporated into a zeolite, the pores and supercages must allow the guest molecule access to the interior. Zeolites that are saturated with water or other solvents will not allow guest molecules to move in or out of the interior.[54,76]

In order to be able to compare data from one experiment to the next, or from one laboratory to another, it is necessary to clearly define a reproducible method of guest molecule inclusion. One of the standard procedures today involves stirring activated zeolite together with the molecule in a carrier solvent, such as *n*-hexane or chloroform.[52,77-79] Zeolite activation is important to remove adsorbed water from the zeolite surface and interior. Carrier solvents need to be inert and volatile, and have a relatively low affinity for the zeolite, so that they are easily removed by drying under vacuum. The use of carrier solvents provides a method of determining the extent of guest molecule adsorption into the zeolite matrix, as the spectrophotometric absorbance of the solvent after stirring allows the amount of the species remaining unadsorbed into the zeolite can be determined. It is assumed that the adsorption process results in inclusion

of the reagent molecules into the zeolite interior as the interior surface area of the zeolite is vastly greater than the external surface area. As well, washing of the impregnated zeolite with an additional amount of pure carrier solvent is assumed to remove any molecules that have been adsorbed on the surface.[80] The time allotted for washing must be short to prohibit the removal of molecules that have diffused into the interior of the zeolite particles. This washing process ensures that guest molecule inclusion is not an outer surface phenomenon. The extent of zeolite impregnation is greatly affected by the type of carrier solvent used, the time allowed for the adsorption process, the temperature at which the adsorption process is carried out, how the carrier solvent is removed, and the introduction of water into the samples during preparation.[81] Because zeolites X and Y are synthetic zeolites, the use of different batches of zeolites can also introduce differences in adsorption. Variations in the aforementioned factors must be minimized to achieve reproducible methods for producing zeolite / guest samples and enable the rational study of intrazeolite processes.

Besides guest molecule inclusion by carrier solvent, zeolites can also be impregnated by the introduction of molecules in the vapour phase. For gaseous species such as xenon and nitrous oxide, the activated sample is exposed to the vapour at a specific temperature and pressure until the pressure drops as a result of adsorption onto the zeolite surface.[79,82-84] Species that are highly volatile, such as methanol and hexane, can be co-adsorbed with an impregnated guest species by gas phase introduction onto the dry zeolite sample,[60,85,86] while another method involves direct addition of the co-solvent onto the impregnated sample to form a slurry, followed by subsequent evaporation by passing dry nitrogen over the sample.[58] The latter method is qualitative and lacks any assurance that co-solvent adsorption has taken place. The procedure developed in our laboratory involves injecting a measured amount of the liquid co-solvent into the sample cell and vapourizing the co-solvent for gas phase adsorption into the zeolite sample.

The loading level, <S>, of a guest molecule in a host zeolite is a quantitative indication of concentration in zeolite/guest composites and is defined as the number of guest molecules per supercage. Typically, these numbers are calculated from the spectrophotometric analysis of the carrier solvent after the adsorption process has occurred, assuming that any molecules that have been adsorbed have been distributed

throughout the zeolite cavities homogeneously. When the assumption of a statistical distribution may not be valid, the loading level is still used as an indication of relative concentrations between samples.

3.1.2.2 Roles of Guest Molecules

Once the sample is prepared, the zeolite/guest composite can be studied by a variety of methods, including NMR,[82,83,87-89] IR,[90,91] ESR,[77,84] diffuse reflectance and emission spectroscopy,[78,86,92] by inducing photochemistry and photophysics,[52] or by neutron diffraction[66,70,93,94] methods. The aims of these studies differ widely. One of the main objectives of introducing molecules into zeolites is to probe the interior properties of the zeolite. The behaviour of probe molecules in known environments, such as solvents of varying polarity, compared to their behaviour in the zeolite helps to characterize the zeolite interior. A classic example of this is the use of the fluorescence spectrum of pyrene.[95,96] The fluorescence spectrum of the pyrene monomer consists of five peaks, numbered I to V from the highest frequency to the lowest frequency. The vibronic band intensities of pyrene solutions are strongly perturbated by the polarity of the surrounding solvent molecules, and the ratio of the third, fourth or fifth peak to the first peak is a good indication of the type and polarity of the solvent. The most sensitive indicator is the III/I ratio. Solvent molecules that are less polar and exhibit little polarizability induce smaller III/I ratios.[96] When put into zeolites, the measured III/I ratio of the pyrene fluorescence has allowed the interior of zeolite supercages to be compared to polar solvents, and the interiors of zeolites X and Y to be compared to each other.[57,59]

Another objective of studying zeolite / guest composites is to study the interaction of the zeolite interior with the guest molecules. Zeolite host materials can act either as passive or active reaction vessels.[67] As passive vessels, the zeolite interior does not participate in the reaction, but influences the chemistry by its very nature and structure. For example, flexible molecules can be forced into frozen conformations by incarceration within channel structures, such as the impregnation of methyl viologen cation (MV^{2+}) within the one-dimensional channel zeolites ZSM-5 and mordenite.[97] In aqueous

solution, MV^{2+} does not fluoresce because bond rotation about its center bond provides an efficient pathway for internal conversion to the ground state; however, when this rotation is physically restricted by the channel boundaries of the zeolite, fluorescence becomes a viable deactivation pathway. In other zeolite / guest composites, the zeolite participates actively in the reaction, either by donating or accepting electrons, or acting as a catalyst. Previous work in our group by M. A. O'Neill has demonstrated that the NaY zeolite can mediate electron and hole transfer over distances of 11 and 18 Å, respectively.[80] The catalytic ability of zeolites is exploited by the petroleum industry to crack hydrocarbons. Methanol and toluene, when co-adsorbed onto an acidic zeolite, are catalyzed by the framework to form *ortho-*, *meta-* and *para-* isomers of xylene.[65] These examples are but two of a plethora of papers studying the active role of zeolites in chemical reactions.

3.1.2.3 Placement of Guest Molecules Within Zeolites

In order to better understand the interaction of guest molecules with their surroundings, it is important to determine the distribution and location of the these substrates. Generally, molecules are adsorbed into the interior of the zeolite, not as a random and mobile fluid, but in specific sites that become increasingly defined with stronger binding interactions between the zeolite surface and the molecule. For strongly interacting molecules such as water, the binding energy is so high that temperatures of 450 °C or higher are necessary to remove the water molecules from the zeolite structure.[63] Organic molecules do not adhere as tightly to the framework, but rather their adsorption sites are less well-defined due to thermal motions.[58,72] A classic example of thermal motion is the aging of pyrene samples. Sealed pyrene / Y zeolite samples exhibit aging over days and weeks, changing from aggregated samples exhibiting excimer fluorescence to homogeneously distributed samples emitting predominately monomer fluorescence.[54] The redistribution of these samples from aggregation to statistical distributions over time is a result of slow diffusion of pyrene through the zeolite particles, indicating that the pyrene molecules are only loosely bound to the zeolite framework. This weak interaction means that the guest molecule position, when adsorbed to a specific site, is less defined and can be described as a statistical distribution of positions about a central location.

The interior of the zeolite is a fixed, crystalline surface. Unlike a fluid solution environment, where the rapid tumbling of molecules produces a homogeneous microenvironment, the rigid nature of the framework structure produces different microenvironments within the same bulk structure. A guest organic molecule can adhere to different adsorption sites within the supercage interior, each of which interact with the guest molecule uniquely. Previous studies have shown that aromatic guest molecules are present at specific adsorption sites such as the window site,[94] the wall site and the cation site.[58,79] Sites available to a guest molecule are specific to the shape and size of the guest molecules. One such example is the benzene molecule, which studies have suggested resides at the window interconnecting two supercages, stabilized by electrostatic interaction with the 12 ring oxygens of the sodalite unit.[94] In contrast, polyaromatic hydrocarbons are not able to achieve the same interaction at the pore due to their larger size and prefer other sites.[60,86] Water molecules, being small and very polar, are very tightly bound to the cations,[60,86] especially those of lower atomic mass. The size and shape of the guest molecule influences the degree of adherence to the adsorption site by determining the interaction distance of the molecule to the zeolite surface. Ramamurthy *et al.* reported an elegant demonstration of this phenomenon by comparing the emission spectroscopy of pyrene, pyrenealdehyde, and *para*-dimethylaminobenzonitrile in alkali cation exchanged zeolites X and Y.[55] All three molecules are qualitative polarity probes,[78,96,98,99] and the expected result was the polarity of the cage would decrease with increasing cation size. While the emission data of pyrenealdehyde and *para*-dimethylaminobenzonitrile was as predicted, the emission data of pyrene did not show much difference in polarity among Li^+, Na^+, and K^+ faujasite zeolites.[55] This is attributed to pyrene's large and flat structure, while both pyrenealdehyde and *para*-dimethylaminobenzonitrile have small moieties which can penetrate into narrow regions and adhere more tightly to these small, buried cations (Figure 3.5).[55] The interactions of these latter two probes are thus significantly different from those of pyrene. Consequently, adsorption sites are determined by not only the zeolite structure and the counterbalancing cations, but also the size and shape of the guest molecule.

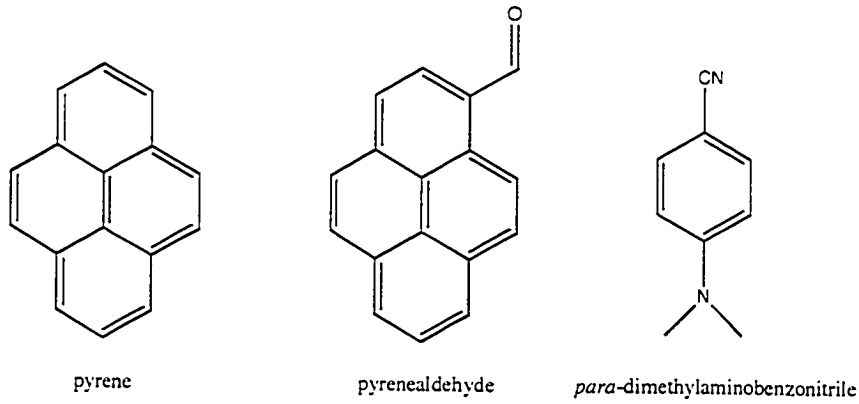

pyrene pyrenealdehyde *para*-dimethylaminobenzonitrile

Figure 3.5 Structures of the three qualitative polarity probes: pyrene, pyrenealdehyde, and *para*-dimethylaminobenzonitrile.

One of the most interesting sites available for adsorption is the cation site. Zeolites are unusual in being able to juxtapose a "naked" cation with an organic molecule. In solution, only the most polar organic molecules or charged species can be dissolved in solvents that are sufficiently polar to dissolve cationic species. In order to study the interaction between a cation and a non-polar polyaromatic hydrocarbon molecule, zeolites are good substrates to bring these two species together. Through experimental and theoretical work, the phenomenon known as the π-cation effect has become recognized in zeolite / guest composites.[68,86,100-108] The π-cation effect describes the strong stabilizing, and yet non-covalent, interaction between the electron-rich face of an aromatic ring and a cation,[109] and was first recognized in gas phase interactions.[107] Table 3.2 lists experimental gas phase binding energies between alkali metal cations and benzene, and notably, these become less exothermic with increasing cation size. The optimal interaction distance between the ion and ring increases with increasing cation size. The π-cation effect has been recognized to play a large role in biological systems, such as the selectivity of ion channels for K^+ over Na^+ being attributed to the role of aromatic residues about the channel pore.[109,110]

Table 3.2 Gas phase binding data of benzene to alkali metal cations.[109]

Ion	Ionic Radius (Å)	ΔE^{bind} (kcal/mol)	r (Å) [a]
Li^+	0.76	-39.5	1.96
Na^+	1.02	-24.4	2.41
K^+	1.38	-19.2	2.88
Rb^+	1.52	-15.8	2.96

[a]Distance from M^+ to the center of the benzene ring.

The electrostatic interaction between cations and guest molecules influences the photophysical behaviour of the guest species in zeolite hosts. As the mass of the cation increases, molecules such as naphthalene exhibit a dramatic decrease in fluorescence intensity accompanied by an increase in the intensity of phosphorescence.[72] This enhancement of intersystem crossing from singlet to triplet excited state has been attributed to the heavy atom effect, coupled with the π-cation effect which ensures a close interaction between the napthalene molecule and the cation. Some measure of control, then, of singlet to triplet reactivities of substrate molecules can be introduced in zeolites by changing the counterbalancing cation.

Interactions between guest molecules and the zeolite interior can also be influenced by the introduction of co-solvent molecules, especially those that bind to the adsorption sites more tightly than the guest molecules. The most persuasive example is the introduction of water molecules, whose affinity for the naked cation displaces the weakly bound organic species and effectively shields the guest molecule from the cation's full charge. Systematic introduction of water into pyrene / NaY samples has been shown to severely decrease the strength of pyrene-cation interactions and increase the III/I ratio of the monomer fluorescence fine structure.[59] This increase indicates that the wet microenvironment about the pyrene probe molecule is significantly less polar than interactions between pyrene and dry zeolite. In general, the introduction of small solvent molecules that are strongly polar can shield guest species from the zeolite surface, while some research suggests that the introduction of non-polar solvent molecules might push the guest molecules towards the zeolite framework.[60] Solvent molecules can only be introduced if the guest molecules already present within the framework do not hinder the movement of the co-solvent molecules. Even so, the strong influence of co-solvent

molecules on the interaction between the guest species and the framework structure make it imperative that the sample preparation must be done with utmost care to ensure that the desired sample properties are achieved.

3.1.2.4 The Zeolite as Organizational Structure

The regular spacing of the zeolite supercage cavities provides a method of inducing periodic organization of the guest molecules without introducing crystallinity. The extent of periodic organization is dependent upon the distribution of molecules throughout the zeolite. For small molecules that are easily carried by the carrier solvent through the zeolite pores, sample preparation can result in a statistical distribution of guest molecules throughout the zeolite structure. However, for large, polyaromatic molecules such as pyrene and anthracene, diffusion through the pores is slow and sample preparation results in inhomogeneous distributions, with high concentrations of guest molecules in supercages close to the surface of the zeolite particle, but low concentrations of guest molecules in the particle interior.[54] Aggregation is also possible, provided that the zeolite supercage can accommodate more than one guest molecule. It has been determined that no more than two pyrene[54,59,92] and anthracene[111,112] molecules can fit within the faujasite zeolite supercage.

The role of the zeolite supercage surrounding guest molecules can be likened to that of encapsulation. For two guest molecules within the supercage, the likelihood of finding another molecule in close proximity is unity. A synthetic analogue of supercage encapsulation is the idea of molecular tethering,[52] where two units tethered together no longer have to overcome entropy factors to interact with each other. Because the supercages are arranged in periodic fashions, the distances between singly occupied supercages are limited to discrete values so that through-space interactions can be studied by concentration measurements and statistical analysis.[80,113] Section 3.4 uses the specific periodic array of zeolite Y supercages to model the ultrafast movement of excited state DCA molecules through the zeolite framework.

3.2 Resolution of Ultrafast Pyrene Excimer Emission Rise Times in Zeolites X and Y

3.2.1 Introduction

Pyrene has been a favourite photophysical probe molecule for zeolite research due to its ability to exhibit both monomer and excimer emission upon excitation,[50-57] Scheme 3.1. Monomer emission (375 - 420 nm) has characteristic vibrational structure that is dependent upon the polarity of the environment,[96] whereas excimer emission (400 - 550 nm) is broad, featureless and centered at longer wavelengths, Figure 3.6[16] Excimer emission is observed upon pyrene inclusion in faujasite zeolites with supercages of sufficient size, *i.e.* X and Y zeolites, at sufficiently high loading levels for double occupancy of supercages to occur.[57-59,76]

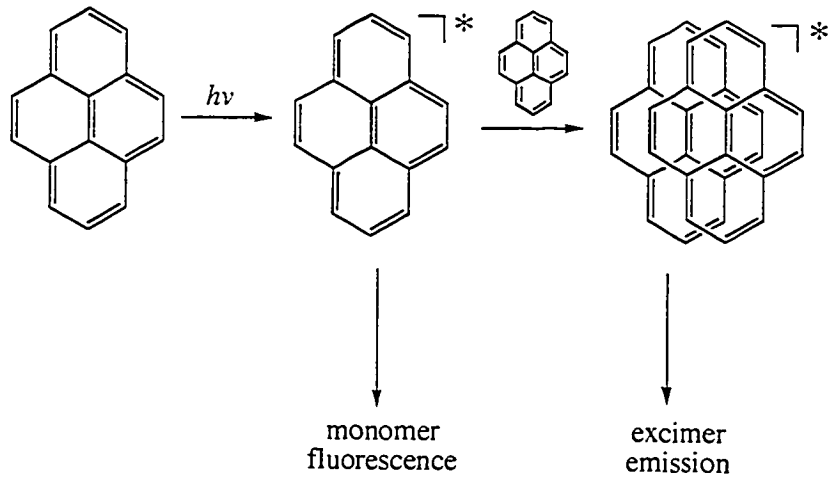

Scheme 3.1 Pyrene monomer and excimer emission.

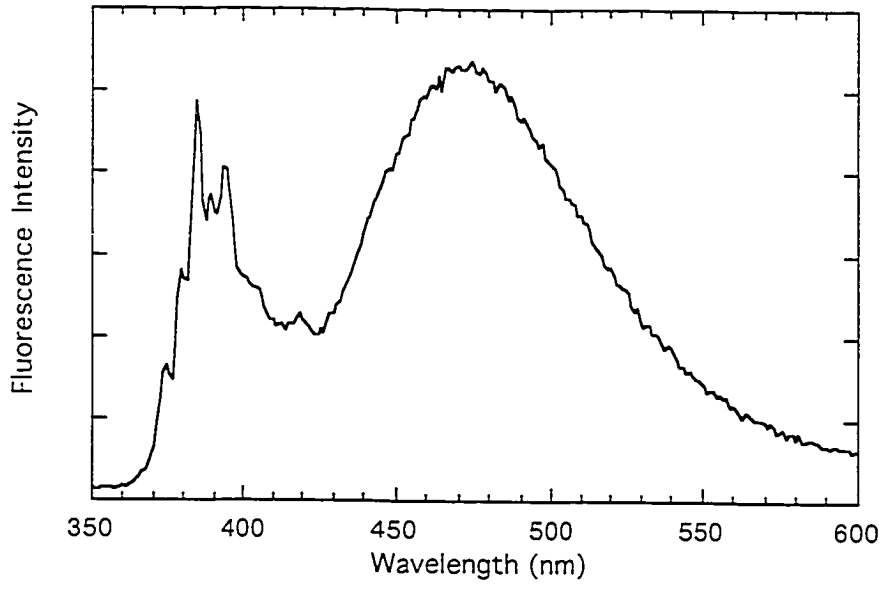

Figure 3.6 The steady state emission spectrum of pyrene in hexane, exhibiting both monomer (375 - 420 nm) and excimer (400 - 550 nm) emission. The excitation wavelength is 315 nm.

While pyrene molecules can be incorporated into X and Y zeolites, its large size makes intercavity hopping through the 7.4 Å pores interconnecting the supercages in NaY very slow, on the order of 100 s.[54] Slow diffusion of pyrene through the cavities results in a non-homogeneous initial distribution of molecules upon incorporation within Y zeolites, where the presence of doubly occupied cavities is readily achieved[54,57,92] and detected by the observation of excimer emission. Upon aging over a period of days in a dry atmosphere, the pyrene molecules redistribute into a statistical distribution, evidenced[54] by the increase of monomer fluorescence and the decrease of excimer emission. Water present within the zeolite framework blocks the intercavity movement of pyrene, preventing both the initial incorporation of pyrene into the zeolite[76] and the rearrangement of incorporated pyrene molecules into a statistical distribution.[54,56,114]

Within a doubly occupied zeolite supercage, the placement of individual pyrene molecules with respect to one another has been a subject of much investigation. There are two views in the literature. The first is that a pair of pyrene molecules within a zeolite cavity retain the dissociative ground state that they exhibit in solution,[16] and hence require some rearrangement for the excimer to form. This view is supported by results from time

resolved picosecond fluorescence spectroscopy studies in which the rise time of excimer emission was unresolvable but not quite complete within the 30 ps excitation pulse.[52-54] The contrary opinion is that pyrene molecules form a ground state dimer when held within the close confines of the zeolite supercage.[57-60] Considerable evidence for this opinion has been cited, including the non-resolvable rise time for excimer emission upon pulsed laser excitation.[57-59] In addition, the excimer excitation spectrum has been found to vary with the intrazeolite concentration of pyrene. At low loading levels, the excimer excitation spectrum has been observed to match the monomer excitation spectrum.[57] At higher loading levels, the excitation spectrum does not match either the monomer or microcrystalline state of pyrene,[58-60] and has been assigned to a possible ground state dimer. Theoretical studies have also suggested that a ground state dimer of benzene stabilized by the presence of a cation is energetically possible, and have suggested that other aromatic molecules may also form ground state dimers in the presence of cations.[60]

The current study provides new data for this argument, and combines the use of ultrafast time-resolved fluorescence spectroscopy with steady-state fluorescence spectroscopy to further the understanding of how pyrene molecules reside in doubly occupied zeolite supercages. The zeolites LiY, NaY, KY and NaX have been chosen to be impregnated with pyrene and the resultant excimer emission rise times of pyrene studied as a function of sealing technique and co-incorporated solvents.

3.2.2 Results

3.2.2.1 Ultrafast Data

For the ultrafast streak camera studies, pyrene was incorporated into dry zeolite samples using hexanes or dichloromethane as the carrier solvent. Typical loading levels achieved were <S> = 0.016 (LiY), 0.031 (NaY), 0.045 (KY) and 0.11 (NaX). These zeolite / pyrene composites were irradiated with 388 nm pulses with a pulse width of 220 fs and an energy of ca. 75 μJ. Emission from these samples was collected using the streak camera, which has an instrument response function (IRF) that varies between 3 and 3.5 ps. The pyrene excimer emission was monitored using a 25 nm bandpass filter

centered at 500 nm. This wavelength region captures only excimer emission, with no overlapping emission from the monomer. The pyrene monomer was studied using a 10 nm bandpass filter centered at 420 nm to avoid scatter from the excitation beam. This wavelength region is not purely monomer fluorescence, but is contaminated by a small amount of excimer emission. Further details about the experimental procedures are given in Chapter 5.

The results obtained upon monitoring excimer emission at 500 nm after 388 nm laser irradiation of alkali-metal cation exchanged zeolites with incorporated pyrene are shown in Figure 3.7. The data clearly show that development of the excimer emission continues for a period of time considerably longer than the IRF, which indicates that formation of the 500 nm emission is not instantaneous within the time scale of the experiment. In contrast, the rise times of the pyrene monomer fluorescence at 420 nm, in all four zeolites, are generally within the time resolution of the streak camera (< 1.5 ps), Figure 3.7. A small amount of time resolved increase in the fluorescence at 420 nm is observed. However, this may be attributed to the weak excimer emission also present at 420 nm.

The decay of the pyrene monomer fluorescence over the first 150 ps did not vary significantly from one zeolite to the next or with the addition of the spectator solvents. Because of the large number of existing literature reports on pyrene monomer fluorescence decay kinetics,[50,52,54,56,58,59,76,79,92,114,115] coupled with our time-resolved data focusing only on the first 150 ps, these results were not analyzed further and are not presented here.

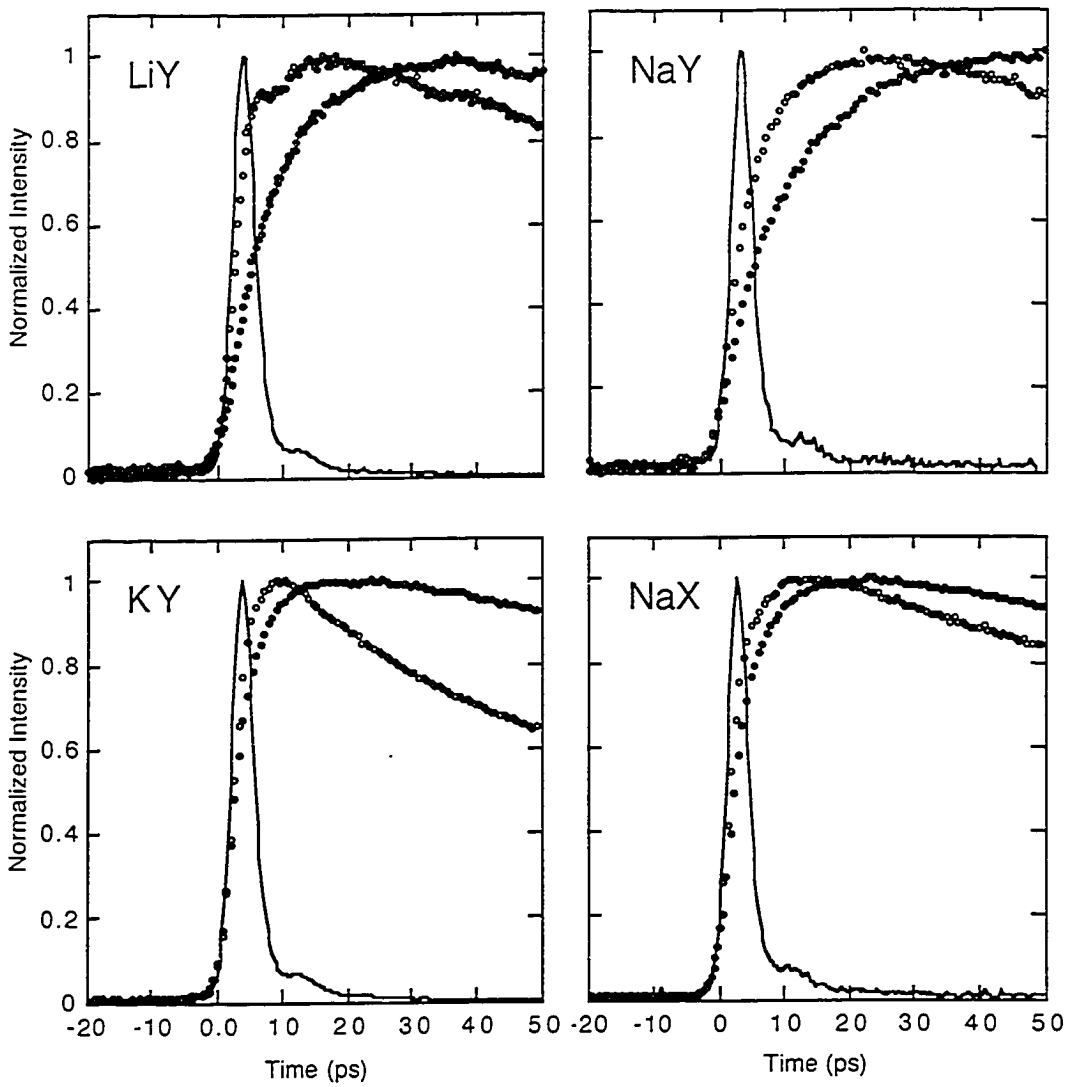

Figure 3.7 Rise-time traces for pyrene monomer emission at 410 nm (○) and excimer emission at 500 nm (●) obtained upon 388 nm femtosecond laser irradiation of pyrene incorporated into faujasite zeolites under vacuum flame sealed conditions. Every second data point is plotted for clarity. Each plot also includes the IRF (—).

3.2.2.2 Excimer Emission Rise Times

In general, the development of pyrene excimer emission at 500 nm is resolvable on the time resolution of the ultrafast streak camera. This indicates that pyrene excimer formation is not instantaneous on the ultrafast time scale of these experiments and therefore must involve some dynamic process. The rise time information can be extracted

from the collected time trace by convoluted non-linear fitting techniques using the Deconfit program (Chapter 2, Section 2.3.3.2), Figure 3.8. The fitting equation used in all cases is an exponential growth plus exponential decay, and the rise time (τ) of the excimer is defined as being the inverse of the growth rate constant.

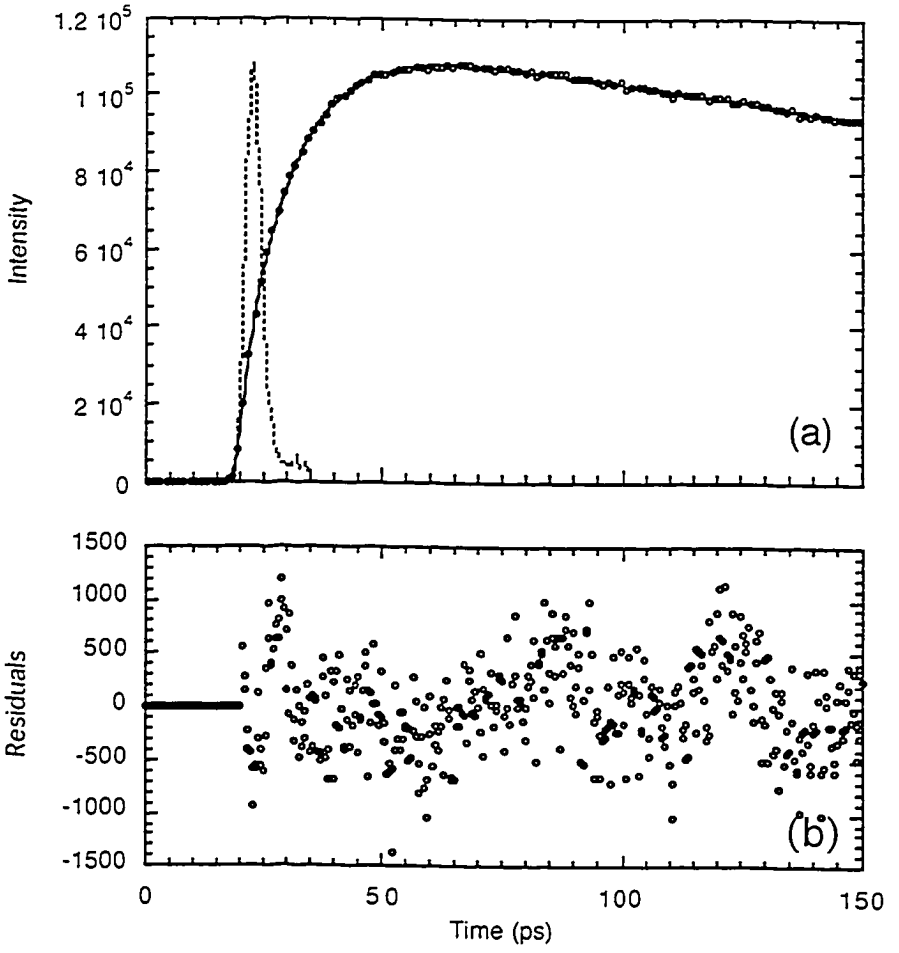

Figure 3.8 Excimer rise time extraction from collected time-resolved fluorescence data using the Levenberg-Marquardt algorithm with convolution. (a) Rise-time trace for pyrene excimer emission at 500 nm (O) (every 5th data point plotted for clarity) obtained upon 388 nm femtosecond laser irradiation of pyrene incorporated into NaY, co-incorporated solvent hexane (7 hexane molecules / cavity). Figure shows best fit line (—) and the IRF (---). (b) Residuals of best fit line from (a).

Table 3.3 presents the excimer rise times for the pyrene impregnated dry zeolite samples employed in this study under vacuum sealed and dry nitrogen conditions. In

each case, excimer formation upon laser irradiation of the pyrene / zeolite sample was resolvable. Under vacuum sealed conditions, the rise time was slowest in NaY with a value of 16 ps and significantly faster in NaX where excimer formation took place with a rise time of 7.6 ps. For the cation-exchanged Y zeolites, excimer formation was fastest in KY with a rise time of 7.0 ps and then slowed dramatically upon going to NaY. In LiY, the rise time was somewhat similar to that in KY and found to be 9.5 ps. The three rise time traces are plotted in Figure 3.9. Although the change in rise times under vacuum sealed conditions upon going from KY to NaY is only 9.0 ps, the difference is significant and represents a greater than two-fold increase from the fastest to slowest rise time.

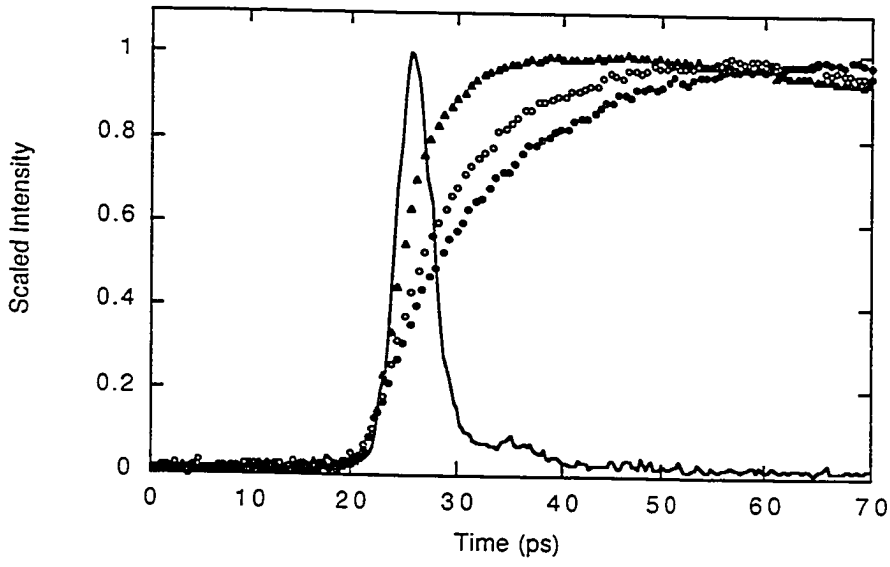

Figure 3.9 Rise-time traces for pyrene excimer emission at 500 nm obtained upon 388 nm femtosecond laser irradiation of pyrene incoporated under vacuum flame-sealed conditions in LiY (○), NaY (●), and KY (▲). Every second data point is plotted. The Figure also includes the IRF (—).

Table 3.3 Pyrene excimer emission rise times, τ (ps), obtained upon 388 nm fs laser irradiation of pyrene within four zeolites under vacuum flame sealed and dry nitrogen conditions.

Zeolite	Vacuum sealed τ (ps)	Dry N_2 septa τ (ps)
LiY	9.5	8.9
NaY	16.0	13.8
KY	7.0	11.0
NaX	7.6	10.1

Three factors contribute to the uncertainty in the excimer emission rise times reported. The first source of error stems from variations between rise times observed for samples made on different days. This variation is estimated to be ±1 ps by comparison between different zeolite / pyrene batches. Another source of uncertainty is differences between rise times from multiple data collections performed using the same sample. (Samples were shaken between data collections to ensure that a fresh zeolite surface was exposed to the laser each time.) Errors from multiple data collections are estimated to be ±0.5 ps. A third source of uncertainty arises from the fitting algorithm itself. Error calculated by the algorithm for each fit are ±0.1 ps, and the error from multiple fits to the same data is ±0.2 ps. Because the major source of rise time error is variations between repeated trials, the error in all the rise times reported is estimated to be ±1 ps.

Previous studies have shown that aging of pyrene / zeolite samples results in a significant change in the pyrene distribution over all zeolite supercages.[54] Under the conditions used for these experiments, the samples showed no significant change in rise time over a period of days; however, as the sample aged, the excimer pyrene emission became much lower in intensity as the number of doubly-occupied supercages decreased. All rise time figures reported here were determined from data collected on fresh samples. There was also no significant variation of rise time for pyrene / NaY samples studied at differing loading levels, indicating that the initial excimer emission arises from doubly-occupied cavities only and that the rise time for excimer formation is independent of loading level variation. These results indicate that the pyrene excimer emission on the early picosecond time scale only probes the doubly occupied supercages and

intrasupercage movement. Intercavity hopping resulting in delayed emission does not need to be taken into account when evaluating the data for this study.

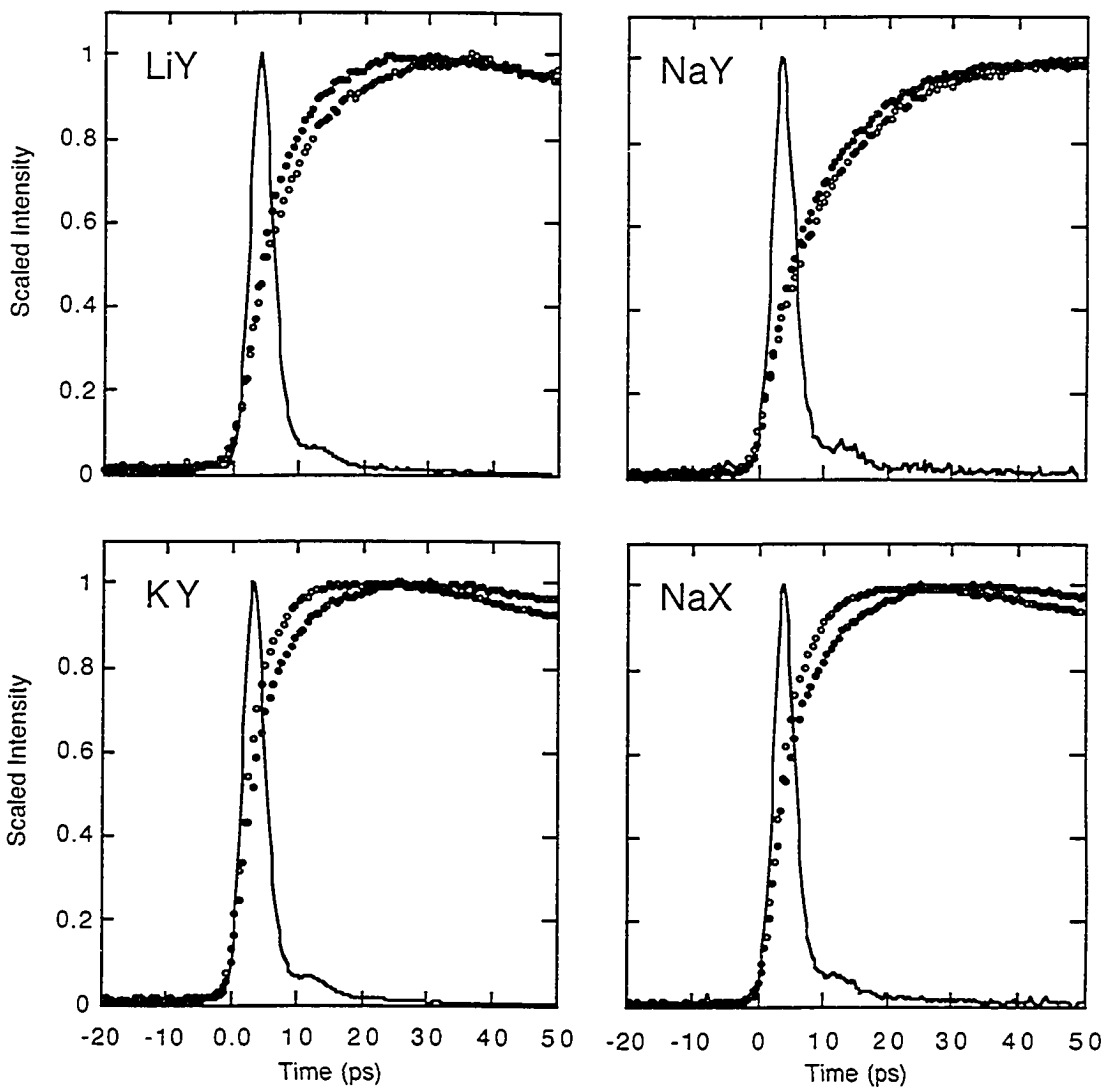

Figure 3.10 Rise-time traces for pyrene excimer emission at 500 nm obtained upon 388 nm femtosecond laser irradiation of pyrene incorporated in various zeolites under vacuum flame sealed (○) and dry nitrogen (●) conditions. Every second data point is plotted. Each plot also includes the IRF (—).

It is interesting to note that there was consistently a significant difference in the rise time of pyrene excimer formation at 500 nm for the vacuum sealed samples when

compared to the dry samples sealed under an atmosphere of dry nitrogen. These rise times are also reported in Table 3.3. For KY and NaX samples, the dry nitrogen conditions resulted in a slower rise time than the samples sealed under vacuum, while the opposite result was observed for NaY zeolite. LiY zeolite showed a small decrease in rise time but this decrease is insignificant within the estimated error of measured rise time data. Figure 3.10 illustrates the measurable difference in rise times under these two sealing atmospheres.

3.2.2.3 Cosolvent Addition

The spectator solvents added to the zeolite / pyrene samples were methanol, water and hexane. These solvents were chosen for both their size and polarity. Water molecules are highly polar and can incorporate into the sodalite cages, as well as into the supercages, where they interact strongly with intracavity cations. Methanol is also a polar solvent but has a larger molecular diameter than water and thus cannot be incorporated into the sodalite cages.[58,85,91] Hexane was chosen for its non-polar nature. Both methanol and hexane are expected to be located primarily within the supercages. The solvent loading levels were chosen to ensure that the entire range between dry zeolite and complete solvent saturation was investigated.

The pyrene excimer emission rise times as a function of solvent incorporation at 500 nm are given in Tables 3.4, 3.5 and 3.6, and shown graphically in Figures 3.11 to 3.14. In all cases, the addition of co-solvent causes a decrease in the excimer emission rise time. For instance, using NaY, the rise time decreased from 14.1 ps in the absence of methanol to 7.9 ps upon the addition of 20 methanol molecules / cavity. The addition of water also had a dramatic effect by reducing the excimer rise time from 15.8 ps in NaY in the absence of water to 10.6 ps upon the addition of 20 water molecules / cavity. The addition of hexane in NaY caused the smallest change where the rise time decreased from 13.6 ps to 11.7 ps upon the addition of seven hexane molecules / cavity. Similar trends were also observed with the other cation-exchanged zeolites employed in this study, where smaller changes were observed for LiY and KY compared to those observed for NaY samples and the magnitude of changes are comparable between KY and NaX

samples. The addition of hexane to KY and NaX samples did not produce any significant decrease in excimer rise times.

Table 3.4 Pyrene excimer emission rise times, τ (ps), obtained upon 388 nm femtosecond laser irradiation of pyrene within four zeolites under dry conditions and as a function of methanol co-solvent incorporation[a] into the zeolite cavities.

Molecules added / supercage	LiY	NaY	KY	NaX
0	8.5 ps	14.1 ps	11.1 ps	10.5 ps
2	9.6 ps	15.5 ps	13.2 ps	9.1 ps
5	9.9 ps	14.7 ps	9.3 ps	7.4 ps
10	9.6 ps	12.2 ps	10.7 ps	6.4 ps
15	8.9 ps	12.0 ps	9.7 ps	6.9 ps
20	6.8 ps	7.9 ps	9.7 ps	6.8 ps

[a] Molecules added / supercage were calculated from injected amount of solvent.

Table 3.5 Pyrene excimer emission rise times, τ (ps), obtained upon 388 nm femtosecond laser irradiation of pyrene within four zeolites under dry conditions and as a function of hexane co-solvent incorporation[a] into the zeolite cavities.

Molecules added / supercage	LiY	NaY	KY	NaX
0	9.5 ps	13.6 ps	10.7 ps	9.3 ps
1	9.5 ps	13.1 ps	11.0 ps	7.2 ps
3	8.9 ps	12.1 ps	7.9 ps	7.5 ps
5	7.4 ps	12.0 ps	8.1 ps	9.2 ps
7	7.0 ps	11.7 ps	9.6 ps	8.2 ps

[a] Molecules added / supercage were calculated from injected amount of solvent.

Table 3.6 Pyrene excimer emission rise times, τ (ps), obtained upon 388 nm femtosecond laser irradiation of pyrene within four zeolites under dry conditions and as a function of water co-solvent incorporation[a] into the zeolite cavities.

Molecules added / supercage	LiY	NaY	KY	NaX
0	8.7 ps	15.8 ps	11.3 ps	11.8 ps
2	7.7 ps	14.4 ps	9.4 ps	12.0 ps
5	7.6 ps	13.8 ps	7.3 ps	9.4 ps
10	7.6 ps	11.3 ps	6.6 ps	7.7 ps
15	6.9 ps	10.3 ps	7.9 ps	7.0 ps
20	7.0 ps	10.6 ps	7.5 ps	7.9 ps

[a] Molecules added / supercage were calculated from injected amount of solvent.

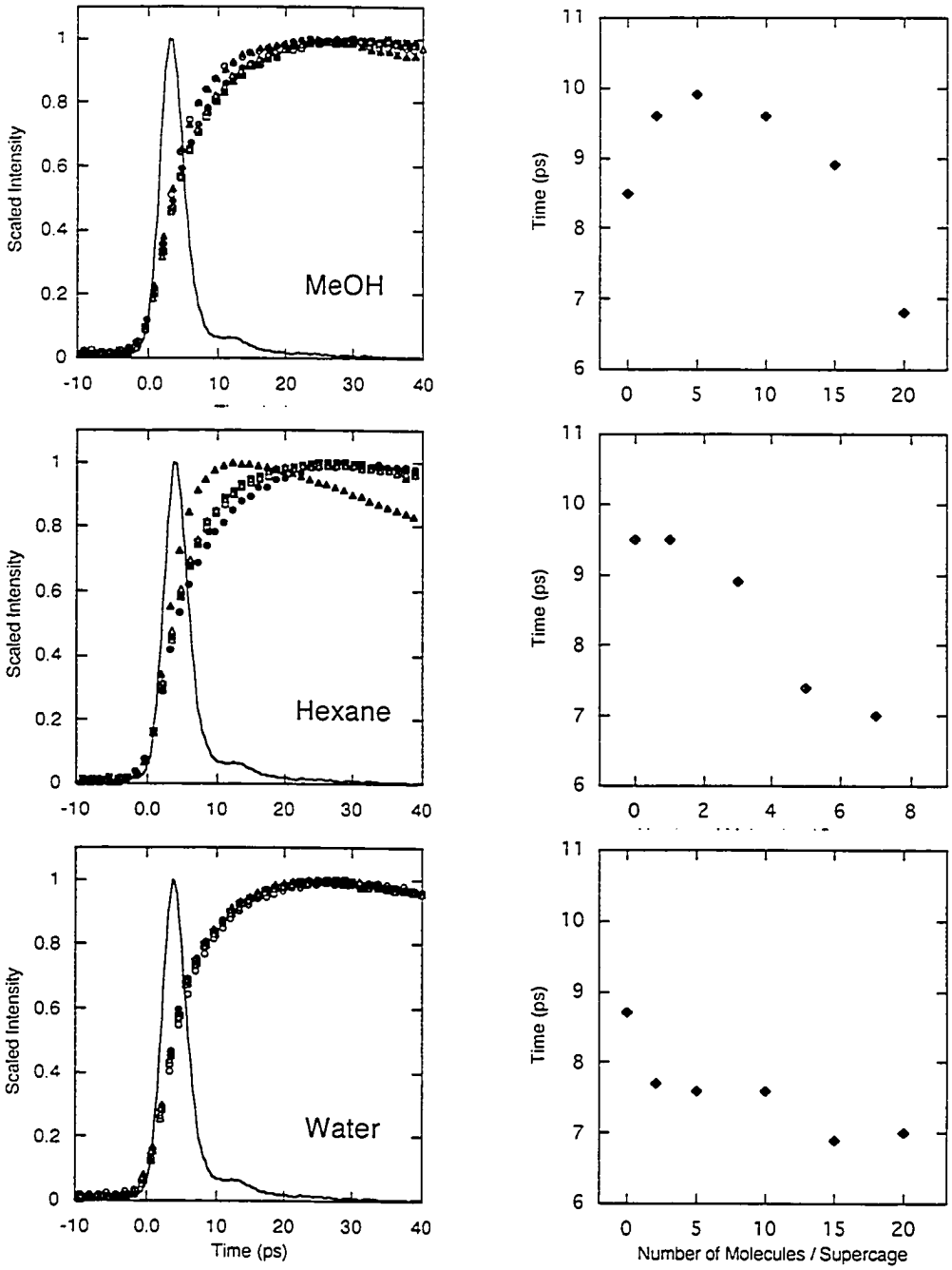

Figure 3.11 Rise-time traces (left column) for pyrene excimer emission at 500 nm obtained upon 388 nm femtosecond laser irradiation of pyrene incorporated into LiY upon the addition of methanol (MeOH), hexane, and water co-solvents under dry nitrogen conditions. Every fourth data point is plotted. Each plot also includes the IRF (—). For methanol and water, 0 (○), 2 (●), 5 (□), 10 (■), 15 (△) and 20 (▲) molecules of co-solvent / supercage were added. For hexane, 0 (○), 1 (●), 2 (□), 3 (■), 5 (△) and 7 (▲) molecules of co-solvent / supercage were added. Corresponding rise times are plotted against the number of molecules per supercage in the right column.

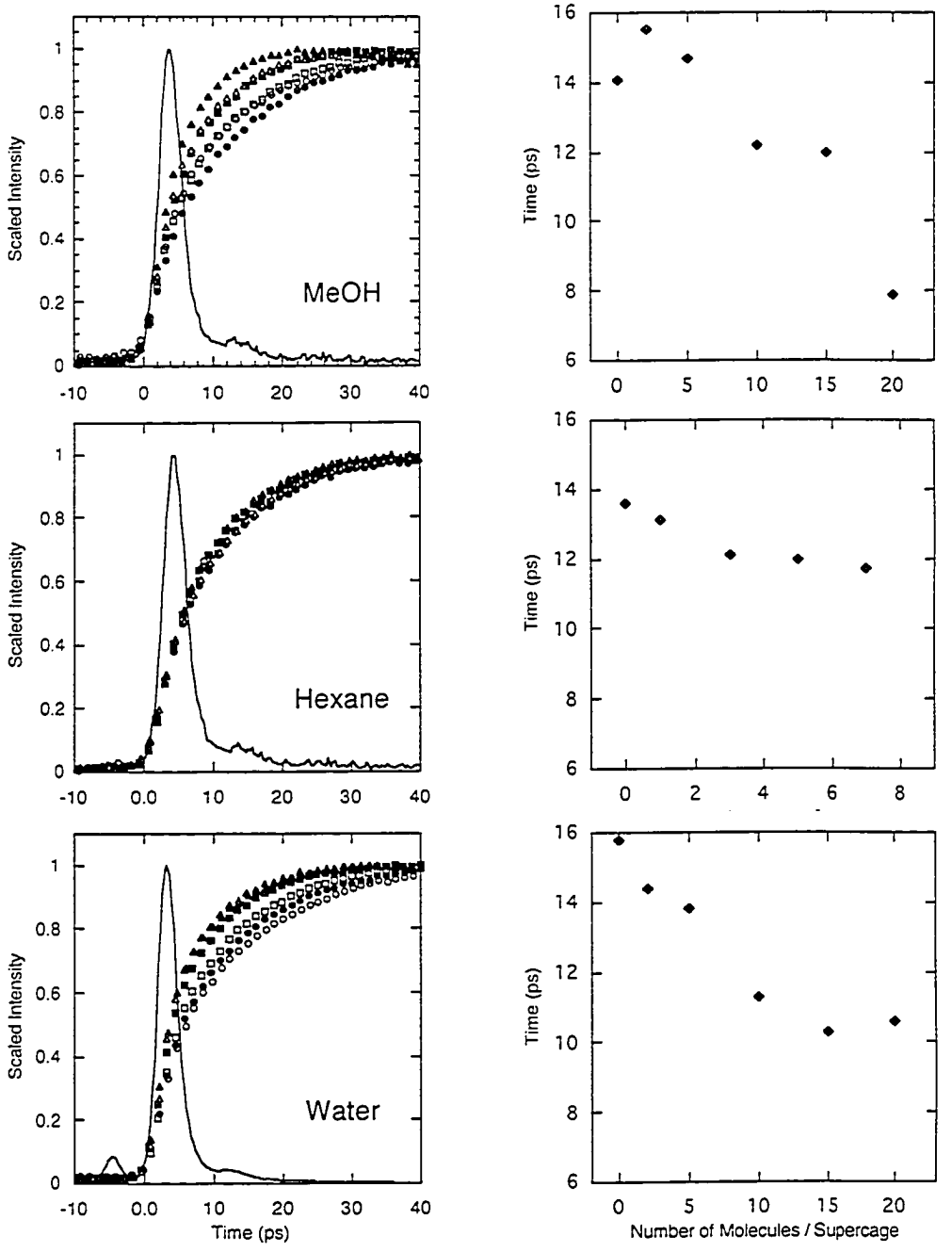

Figure 3.12 Rise time traces (left column) for pyrene excimer emission at 500 nm obtained upon 388 nm femtosecond laser irradiation of pyrene incorporated into NaY upon the addition of methanol (MeOH), hexane, and water co-solvents under dry nitrogen conditions. Every fourth data point is plotted. Each plot also includes the IRF (—). For methanol and water, 0 (○), 2 (●), 5 (□), 10 (■), 15 (△) and 20 (▲) molecules of co-solvent / supercage were added. For hexane, 0 (○), 1 (●), 2 (□), 3 (■), 5 (△) and 7 (▲) molecules of co-solvent / supercage were added. Corresponding rise times are plotted against the number of molecules per supercage in the right column.

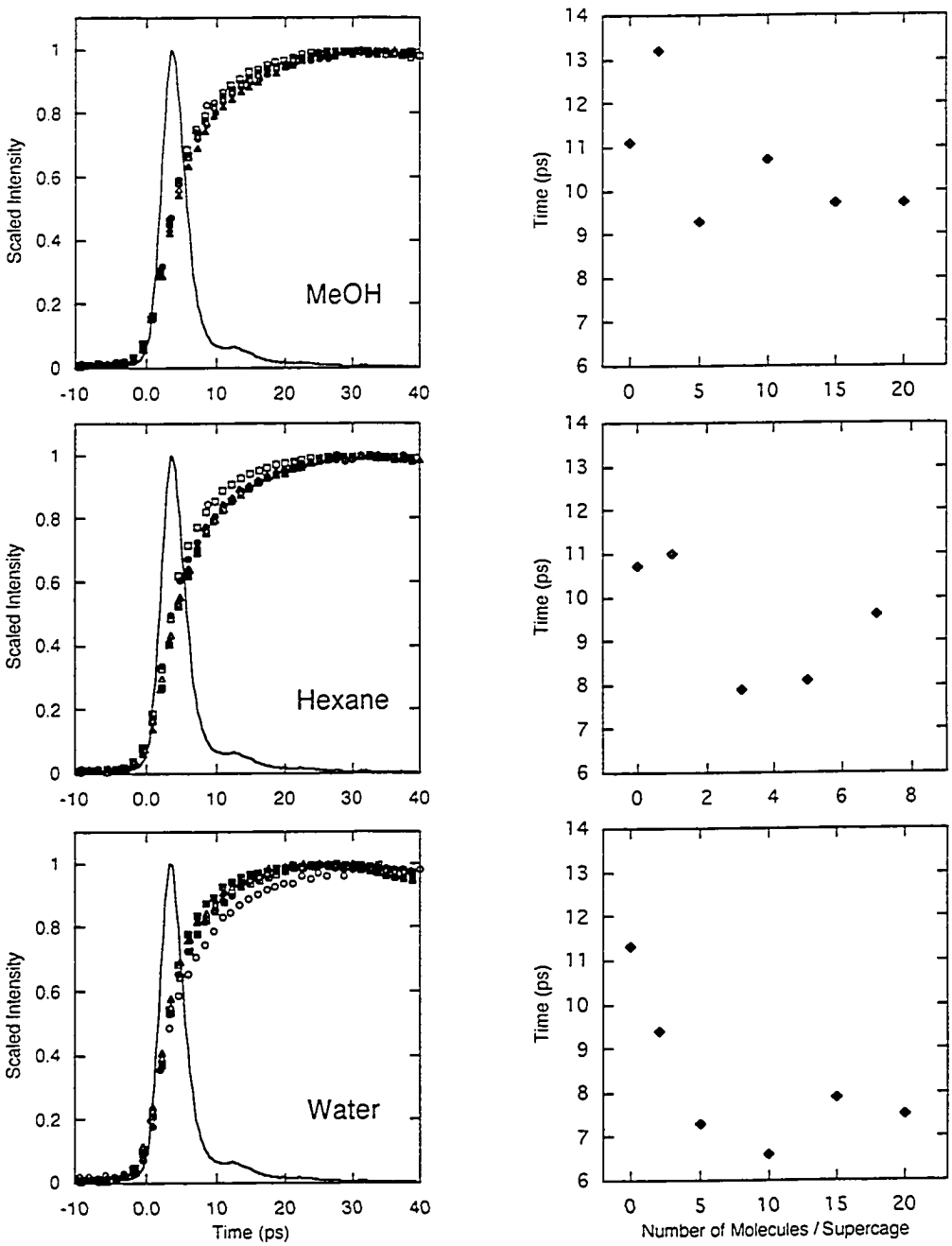

Figure 3.13 Rise time traces (left column) for pyrene excimer emission at 500 nm obtained upon 388 nm femtosecond laser irradiation of pyrene incorporated into KY upon the addition of methanol (MeOH), hexane, and water co-solvents under dry nitrogen conditions. Every fourth data point is plotted. Each plot also includes the IRF (—). For methanol and water, 0 (○), 2 (●), 5 (□), 10 (■), 15 (△) and 20 (▲) molecules of co-solvent / supercage were added. For hexane, 0 (○), 1 (●), 2 (□), 3 (■), 5 (△) and 7 (▲) molecules of co-solvent / supercage were added. Corresponding rise times are plotted against the number of molecules per supercage in the right column.

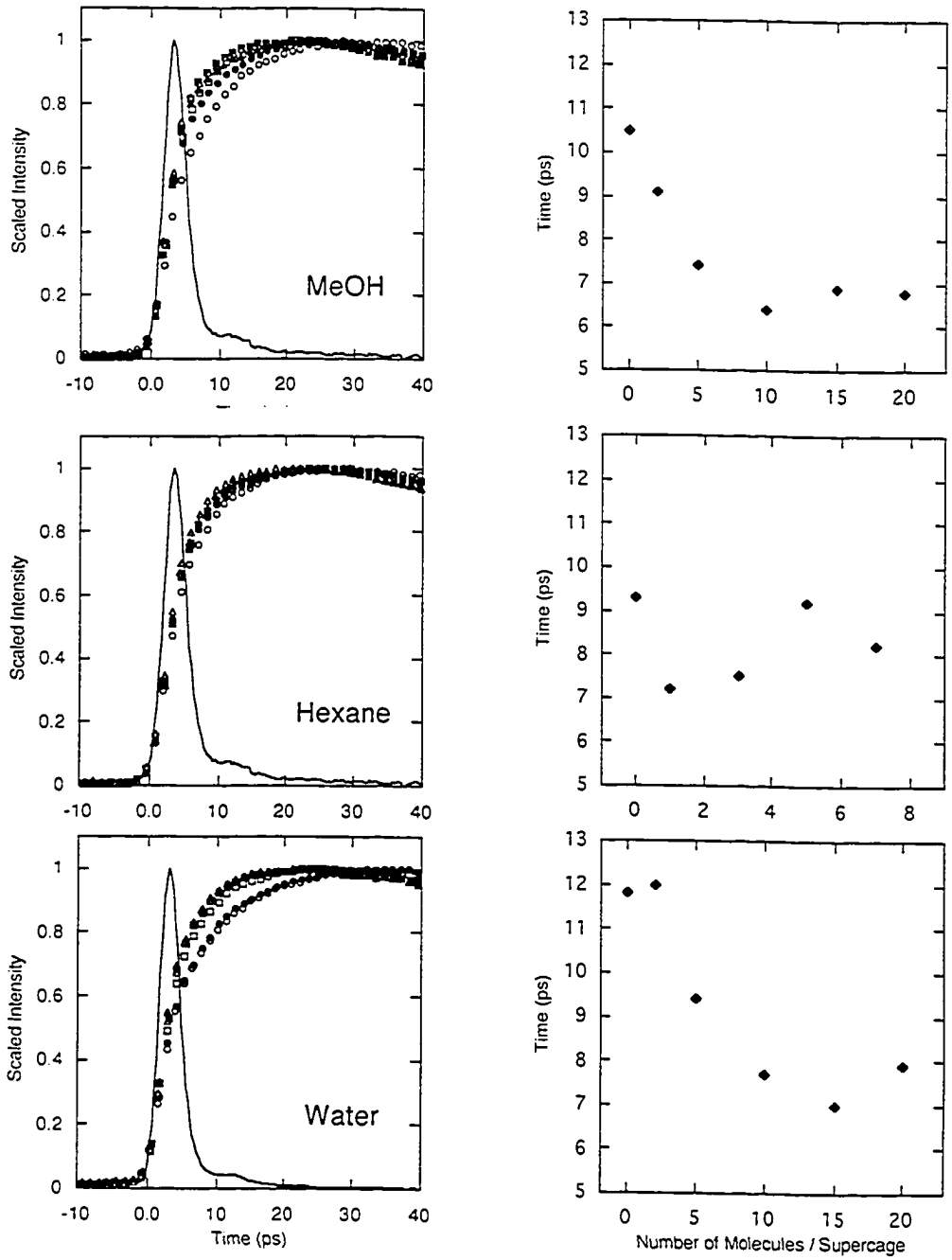

Figure 3.14 Rise-time traces (left column) for pyrene excimer emission at 500 nm obtained upon 388 nm femtosecond laser irradiation of pyrene incorporated into NaX upon the addition of methanol (MeOH), hexane, and water co-solvents under dry nitrogen conditions. Every fourth data point is plotted. Each plot also includes the IRF (—). For methanol and water, 0 (○), 2 (●), 5 (□), 10 (■), 15 (△) and 20 (▲) molecules of co-solvent / supercage were added. For hexane, 0 (○), 1 (●), 2 (□), 3 (■), 5 (△) and 7 (▲) molecules of co-solvent / supercage were added. Corresponding rise times are plotted against the number of molecules per supercage in the right column.

3.2.2.4 Steady-State Data

Steady-state emission spectra confirm that the samples prepared are consistent between trials and with literature results. All steady-state emission spectra in this study were obtained using 315 nm excitation. A typical spectrum of pyrene incorporated into the zeolite will have monomer fluorescence with individual vibrational peaks from 370 to 390 nm, and a wide featureless band at longer wavelengths, typically with a maximum around 470 nm, which is produced by excimer emission. Figure 3.15 shows the steady-state emission spectrum of pyrene upon 315 nm excitation when incorporated into all four zeolites under flame-sealed vacuum and dry nitrogen conditions. Both monomer and excimer fluorescence are most clearly evident for the NaY sample.

Pyrene emission spectra are somewhat dependent upon the zeolite host and sample preparation. In NaY a large excimer band is observed, while in KY a smaller excimer band is observed which is blue-shifted to shorter wavelengths. Under steady-state conditions in zeolites LiY and NaX, the excimer band is very weak and cannot be readily resolved in the steady-state spectra. For NaX, it is well documented[59] that pyrene diffuses more easily from one supercage to another, resulting in much fewer doubly-occupied cavities and a more homogenous distribution of pyrene guest molecules throughout the framework. Thus, in NaX, monomer fluorescence dominates the spectrum. Addition of co-incorporated solvent to the samples changes the relative intensities of the monomer and excimer emission for those samples in which both are observable. Addition of either water or methanol generally results in an increase of monomer intensity at the expensive of the excimer band, Figure 3.16. An increase in monomer resolution is also observed in the addition of these two polar solvents, Figure 3.17. Additions of hexane result in no increased monomer resolution and very small increases in monomer band intensity at the expense of excimer band intensity, Figure 3.18.

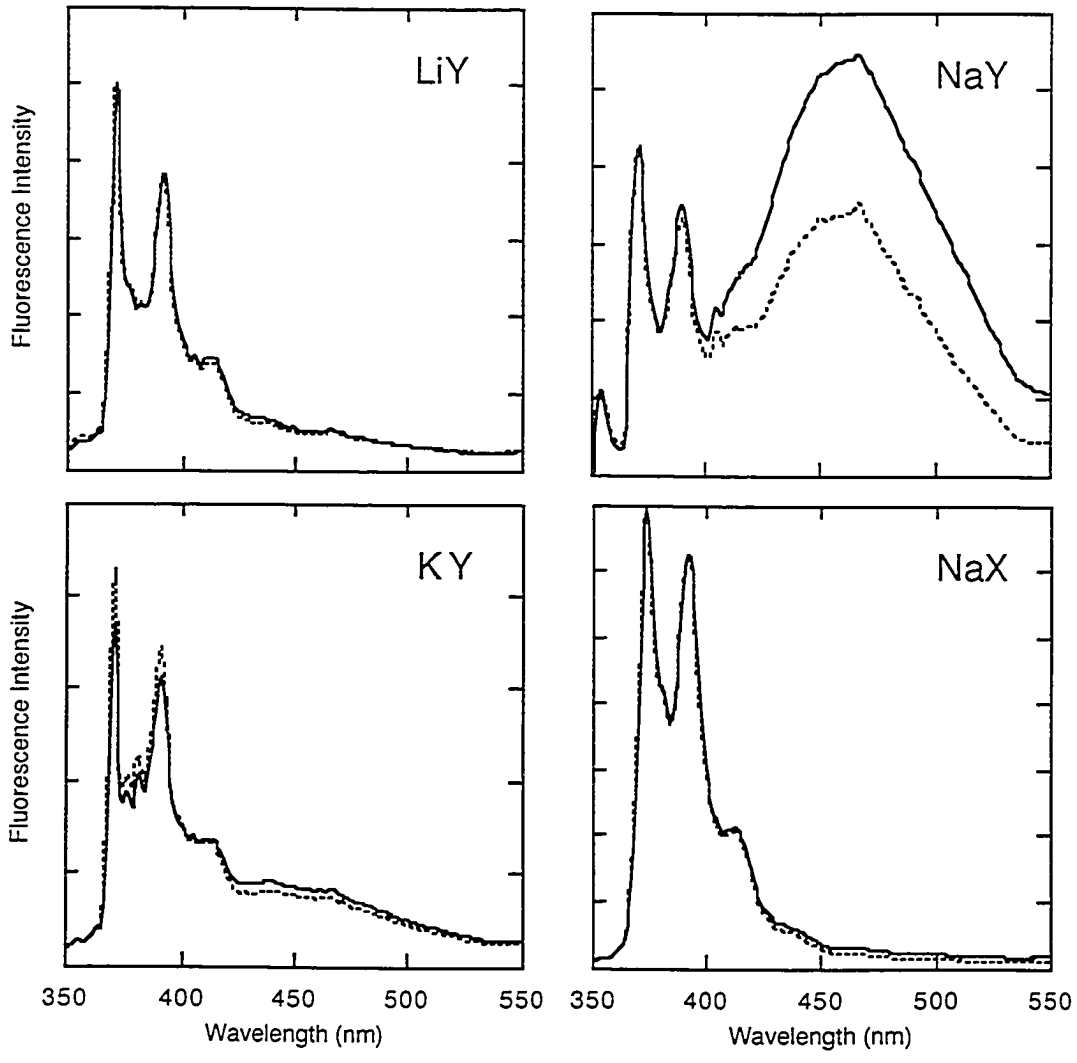

Figure 3.15 Steady-state emission spectra upon 315 nm excitation of pyrene incorporated into zeolites LiY, NaY, KY and NaX under flame-sealed vacuum conditions (—), and dry nitrogen conditions (---).

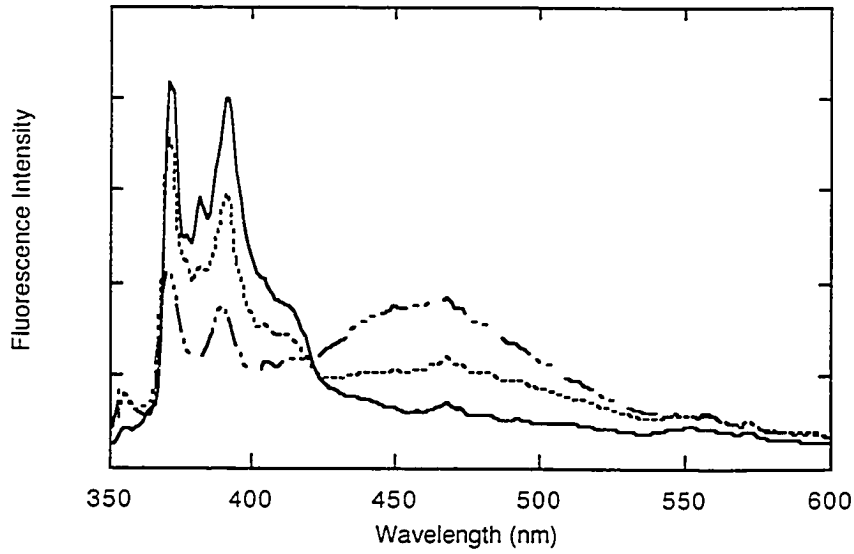

Figure 3.16 Steady-state emission spectra upon 315 nm excitation of pyrene incorporated into zeolite NaY under dry nitrogen conditions (–···–), and after the co-incorporation of 5 (---) and 20 (—) methanol molecules per cavity.

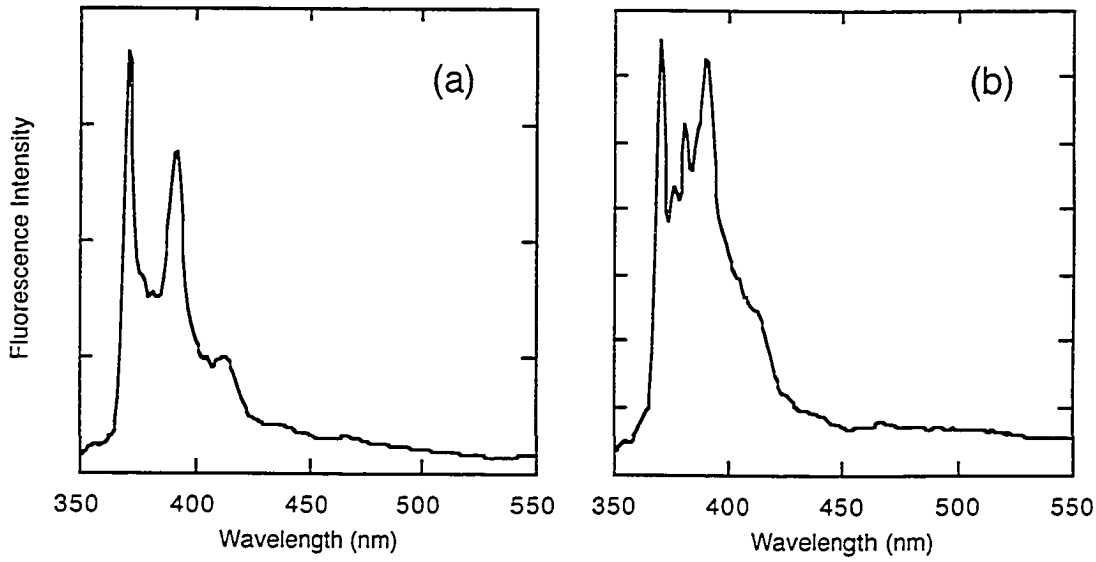

Figure 3.17 Steady-state emission spectra upon 315 nm excitation of pyrene incorporated into zeolite LiY under (a) dry nitrogen conditions, and (b) after the co-incorporation of 20 water molecules per cavity.

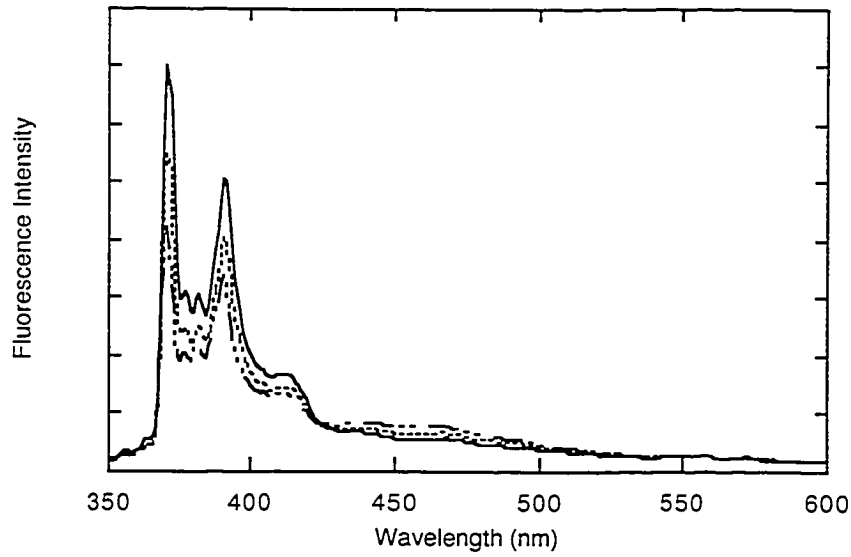

Figure 3.18 Steady-state emission spectra upon 315 nm excitation of pyrene incorporated into zeolite KY under dry nitrogen conditions (–···–), and after the co-incorporation of 5 (---) and 20 (—) hexane molecules per cavity.

While the monomer fluorescence does not shift in wavelength, the intensity and resolution of the individual vibrational peaks change with changing environmental conditions. Pyrene has been well studied as a photophysical probe molecule because its monomer fluorescence peak amplitudes are dependent upon the electric field strength, or polarity, of the surrounding environment. A fully vibrationally free pyrene molecule fluoresces with 5 major discrete bands, where the ratio of any of the third, fourth and fifth peaks to the first peak (371 nm) is an indication of the polarity of the environment.[96] In the monomer fluorescence, only the I and V peaks are consistently visible, making the V/I ratio a more practical choice over the more sensitive III/I ratio. The V/I ratios are reported in Table 3.7. For all zeolites, there was no significant change in the V/I ratio between flame-sealed vacuum and dry nitrogen samples. Conversely, for Y zeolites, the addition of polar co-solvents resulted in a significant increase in the V/I ratio and indicates a decrease in the polarity of the environment immediately surrounding pyrene. The largest increase in the V/I ratio was observed for LiY for the addition of methanol, from 0.75 to 1.00. The addition of methanol to NaY produced a smaller increase of 0.82 to 0.96, while the smallest change in the V/I ratio was noted for KY zeolite with methanol: 0.80 to 0.86.

A similar periodic trend in V/I ratio changes was observed for the addition of water to these three zeolites. For the addition of hexane, the V/I ratio decreased for LiY and KY, while it increased slightly for NaY.

Table 3.7 V/I ratios calculated from steady state emission spectra upon 315 nm excitation of pyrene incorporated into four zeolites under various conditions.

Conditions	LiY	NaY	KY	NaX
flame-sealed vacuum	0.76	0.86	0.84	0.90
dry nitrogen	0.75	0.82	0.80	0.89
methanol[a]	1.00	0.96	0.86	[b]
hexane[a]	0.76	0.90	0.74	[b]
water[a]	0.95	0.93	0.89	0.95

[a]Maximum solvent incorporation reported here. For methanol and water, 20 molecules / supercage. For hexane, 7 molecules / supercage. Molecules / supercage were calculated from injected amount of solvent.
[b]Accurate numbers are not available due to spectral clipping.

Steady state fluorescence for these systems has been well documented in the literature.[56,57,60,79] The steady state fluorescence data collected were in good agreement with published data, and will not be discussed in detail. It was used, rather, as a confirmation of changing intrazeolite environment conditions in light of which the ultrafast time-resolved fluorescence data will be discussed.

3.2.3 Discussion

In the literature, there has been disagreement about the relative placement of two pyrene molecules residing within one zeolite supercage.[52,54,57-60] The previously unresolved rise time of pyrene excimer emission has led to the argument that pyrene exists as a ground state dimer within a doubly occupied supercage. However, if two pyrene molecules in a zeolite supercage were to exist as a ground state dimer with the same structure as the excimer, excimer formation would be complete within the laser pulse. The resulting rise time for the excimer emission would therefore appear to be instantaneous and identical to the prompt rise time for the fluorescence of the pyrene monomer. Two separate time-resolved studies[52,54] on the picosecond time scale have both

commented upon the fast but not instantaneous rise time and have suggested that excimer formation is a dynamic process. Neither study, however, was able to fully resolve this fast growth or study its cation or co-solvent dependence. The ultrafast data measured in this work for pyrene excimer formation upon excitation within a doubly occupied dry NaY cavity clearly shows a fast, but resolvable rise time of 16 ps. This rise time is an order of magnitude slower than the rise time of our streak camera system's IRF of 3.3 ps and is significantly slower than the prompt rise of the monomer emission. Under every experimental condition examined in this work, the pyrene excimer emission rise time is resolvable and varies according to the pyrene-zeolite condition. Our results therefore strongly confirm that some reorientation or movement of the two pyrene molecules is needed after excitation in order for excimer formation and emission to occur, and the time that movement requires is measurable on the early picosecond time scale. The rate of this movement is also highly dependent upon the nature of the zeolite interior. Thus the ground state pyrene molecules in a doubly occupied supercage are not in the same relative position as they are in the excited state.

The interior of the supercage is a highly polar environment,[53,55,57-60,76,116-119] which results in electrostatic interactions between pyrene molecules and the zeolite supercage interior. Previous researchers have postulated different types of sites where the pyrene molecules tend to reside, namely the wall and cation sites.[48,58,79] Our ultrafast fluorescence data support electrostatic interactions with the charge-balancing cation, as changing the nature of the cation results in different excimer emission rise times. Pyrene excimer emission under vacuum conditions exhibits the slowest rise time in NaY, and both LiY and KY have faster rise times, Figure 3.9. Furthermore, there is a correlation between the rise time data and the resolution of the monomer peaks of the steady-state fluorescence emission spectra: the slower the rise time, the lower the resolution of the monomer peaks. Lower monomer peak resolution (broader or unresolved peaks) is an indication of damped vibrational freedom of the pyrene molecule, which indicates a higher degree of interaction with the zeolite framework cation.[58,114] The data suggest that pyrene is interacting with the cations in such a way that pyrene is adsorbed onto the cation, leading to the two observed results: 1. The vibrational freedom of the pyrene molecule is limited by its adherence to the framework cation, and 2. The rise time of the

pyrene excimer is affected by the energy necessary to overcome the binding energy of one or both pyrene molecules to a cation site.

The idea that pyrene and other large aromatic hydrocarbons can interact with a cation is known as the π-cation effect, discussed earlier in the introduction, Section 3.1.2.3. However, previous researchers[101,103-108] have shown that the π-cation effect for polyaromatics follows a periodic trend where the binding energy decreases as the cation changes from Li^+ to Na^+ to K^+, Table 3.2. Although the literature values for the binding energies involve the aromatics benzene, naphthalene, anthracene and phenanthrene, the trend in binding energy is identical for all four aromatic species and thus this trend is anticipated to be similar for pyrene. Therefore, following the trends of the other aromatics, pyrene should have the strongest π-cation interaction with the smallest cation Li^+ and the smallest binding energy with the largest cation K^+. However, the observation that the rise time of excimer emission is slower within NaY than within LiY and KY suggests that pyrene has the largest π-cation interaction with Na^+ and a lesser interaction with both Li^+ and K^+ under our experimental conditions. This trend can be rationalized by taking into account the influence of the distance between the cation and the polyaromatic ring. The optimal distance for the interaction of polyaromatics with cations increases as the cation size increases,[101,103] Table 3.2. In free space, the optimized cation-aromatic distance can be achieved due to the free mobility of both materials. However, in a zeolite, the distance between the cation and the guest molecule is imposed by the supercage structure, where the cation location is dependent upon its size. Li^+ and Na^+ cations are reported to be embedded in the walls of the supercage,[62,70] while K^+ is larger and is located closer to the surface.[71] Thus, there are two main factors acting in opposite directions within the zeolite supercage.[60] The first is the decreased magnitude of the π-cation interaction as a function of cation size and the second is the increase in the cation-pyrene distance as defined by the zeolite for smaller cations. For pyrene in LiY, the distance of pyrene to the Li^+ cation is increased by the small size of Li^+ and its location within the zeolite wall, coupled with the size and planarity of the pyrene, which inhibits the pyrene from approaching the supercage wall more closely. Thus, the strong π-cation interaction is weakened by the geometrical constraint on the system. For pyrene in KY, the distance of pyrene to the K^+ cation is not as critical, as the optimum distance is longer

than for the pyrene-Li^+ system. However, in this case, the periodic trend dictates that the pyrene-K^+ interaction is weaker. Pyrene in NaY thus represents the "optimum case" where both geometric constraints on the pyrene-Na^+ distance and the strength of the π-cation interaction result in the strongest adherence of pyrene to a cation. This results in the observed slowest excimer rise time in the ultrafast streak camera data and lowest monomer peak resolution in the steady state fluorescence data.

3.2.3.1 Sealing Techniques

Table 3.3 lists the measured excimer emission rise times of pyrene incorporated within the four zeolites investigated in this work under vacuum flame-sealed and dry nitrogen conditions. When incorporated in LiY, the pyrene rise times do not show any significant differences under vacuum flame-sealed and dry nitrogen conditions, while with NaY as the host zeolite, a significant decrease in rise time upon going from vacuum conditions to a nitrogen environment is observed. For both KY and NaX zeolites, an increase in rise time is observed upon the addition of dry nitrogen. Overall, a nitrogen environment appears to have a leveling effect of reducing the observed differences in the rise times in the different zeolite hosts. Perhaps the nitrogen molecules interact with the cations to some small but significant amount,[90] decreasing the strength of the π-cation interaction and rendering the zeolite hosts more similar than under vacuum conditions.

3.2.3.2 Co-solvents

The addition of all co-solvents, in all zeolites, results in a faster excimer emission rise time. All zeolites show a larger time reduction for the polar co-solvents, water and methanol, than for the non-polar hexane. It is surprising that hexane shows any rise time influence at all, as its small effect on the steady state spectra indicates that it does not change the pyrene-zeolite environment significantly. Under the condition of co-incorporated solvents, there are likely two factors that influence the excimer formation rise time. One factor is the ability of the incorporated solvent molecules to disrupt the π-

cation effect, which changes the energy necessary for pyrene molecules to rearrange into the excited state dimer, and the second factor is the free volume available in the supercage, which decreases as solvent molecules are incorporated, independent of solvent polarity. Limited free volume decreases the distance that two pyrene molecules have to traverse to form an excimer. All three solvents will limit the free volume available in the supercages; however, the polar solvents will also disrupt the π-cation effect by adhering preferentially to the cations.[60,91,105,120] This is reflected in the time-resolved data as the polar solvents have a larger effect than hexane on the observed excimer emission rise times in all zeolites.

3.2.3.3 Pyrene Placement

Within the doubly occupied supercages, pyrene molecules can either reside as a ground state dimer, with a geometry significantly different than that of the excimer, or they can be dissociated. Both these configurations would require movement to form the excimer and thus produce a resolvable excimer emission rise time upon excitation. However, the co-solvent data suggests that a dissociated ground state is more likely. If the ground state dimer were to exist, the driving force would have to be the π-cation effect, which would sufficiently polarize the first pyrene molecule to attract the second molecule by electrostatic interaction. Disruption of the π-cation effect by the addition of a polar co-solvent would also weaken the pyrene-pyrene association. Thus, by adding the polar co-solvent, an increase in emission rise time would result as the pyrene molecules would have to now come together to form the excimer. However, if the pyrene molecules were dissociated from each other in the ground state but adsorbed to the zeolite cations and framework sites, then disruption of the π-cation interaction would weaken the pyrene-zeolite adherence, enabling pyrene excimer formation with lower activation energies. This would result in a decrease in excimer emission rise time with increased polar solvent incorporation. As the latter explanation matches the experimental results presented here, this study suggests that pyrene molecules in doubly occupied supercages are unassociated from each other in the ground state.

3.3 Placement of 9,10-Dicyanoanthracene Molecules Within Y Zeolites: Loading Level and Cation Dependence

3.3.1 Introduction

Many polyaromatic hydrocarbons have been used as photophysical probe molecules in the study of zeolite / guest composites, including the ubiquitous pyrene,[50-53,59,76,114,115,121] and anthracene.[18,53,86,92,111,116,122] The fluorescence emission of anthracene and its derivatives poses a particularly difficult challenge to study because of their well documented ability to dimerize upon near-UV excitation ($\lambda < 370$ nm) to form the photodimer,[18,123,124] Scheme 3.2. Photochemical cleavage of the photodimer occurs upon absorption of a photon of short UV light ($\lambda = 253$ nm).[18] Chandross and Ferguson[123] were able to characterize the excimer emission of anthracene in 1966 with a series of elegant experiments with the photodimer entrapped in soft glasses. Upon irradiation, the photodimer dissociated into two anthracene molecules that retained their face-to-face conformation within the glassy matrix, essentially forming a trapped "sandwich" dimer. The absorption and emission spectra of these dimers demonstrates the existence of the anthracene excimer, which has been postulated to be a precursor to photodimer formation. In solution, the excimer emission of anthracene is extremely weak, and in chloroform is reported to have a quantum yield (Φ_f) of 0.010.[125] The excimer emission of anthracene has been reported in zeolites NaX and NaY.[86,126]

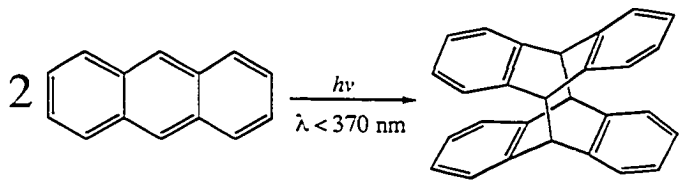

Scheme 3.2

While anthracene is considered to be an electron-rich molecule, the attachment of strongly electron-withdrawing groups, such as cyano moieties, significantly changes the electronic nature of the anthracene rings. When doubly substituted at the 9- and 10-

positions with cyano groups, photodimerization does not occur. The molecule 9,10-dicyanoanthracene, or DCA, is well known for its properties as a sensitizer,[127-129] but has not been extensively used in zeolites in this capacity. There are examples[130,131] of using the sensitization properties of DCA in solution with substrates included in pentasil zeolites because the size and shape of DCA molecules excludes it from the zeolites, thus isolating the sensitizer from the substrate. In preliminary studies in our lab, DCA has been found to absorb well into faujasite zeolites and to exhibit different fluorescent properties in zeolite than in solution. This section presents a systematic study of the placement of DCA molecules incorporated in cation-exchanged Y zeolites using steady-state and nanosecond time-resolved fluorescence spectroscopy as a function of loading level and counterbalancing cation.

3.3.2 Results

Experiments investigating the emission behaviour of DCA molecules in cation exchanged Y zeolites were separated into two categories: cation dependent experiments, and varying loading level experiments. Within the cation dependent work, three loading levels were chosen and DCA molecules were incorporated at each of these loading levels in all five zeolites with identical procedures. This enables the investigation of systematic cation variation as an influence on DCA fluorescence. Loading level was then independently studied in one zeolite, KY, to give a very detailed look at the specific effect of loading level on DCA fluorescence.

3.3.2.1 Highest Loading Level: <S> ~ 0.05

DCA was incorporated into zeolites LiY, NaY, KY, RbY, and CsY with equal ease, and the loading level achieved was $\langle S \rangle = 0.043$. Steady state fluorescence emission spectra of each sample (Figure 3.19) showed dramatically different results as the counterbalancing cation was changed. LiY and NaY samples showed a broad peak centered at 570 nm, while the RbY and CsY samples showed a narrower set of emission

bands with discernable vibrational peaks at about 475 nm. The KY samples showed intermediate behaviour, with both the vibrational peaks and the broad peak being visible. Figure 3.19 also includes an emission spectrum of DCA in dichloromethane solution, which shows vibrational peaks centered about 470 nm that are characteristic of the monomer emission.[132] Comparison of this spectrum to the zeolite spectra demonstrates that assignment of the 470 nm band to monomer emission is reasonable. There is a small but consistent bathochromic shift upon incorporation into zeolite media, and a shift in the relative vibrational peak intensities, both of which are likely due to the change in environment from homogeneous solution to the zeolite interior.[132] The broad emission band at 570 nm is assigned to the DCA excimer. The shift to longer wavelengths, coupled to the lack of resolved vibrational structure, is characteristic of face-to-face excimers.[14] Comparison of the excitation spectra monitored at 570 nm to the monomer excitation spectra (470 nm) shows that both spectra have the same basic shape (Figure 3.20), indicating that the precursor to the species at 570 nm is the excited-state monomer. The DCA excimer spectrum has been observed as the product of triplet-triplet annihilation[132] and in a tethered molecular system,[122] and comparison with these spectra allows us to assign with confidence the 570 nm broad band to DCA excimer emission. The positions of these two bands led to choice of 450 nm and 600 nm as appropriate monitoring wavelengths for the monomer and excimer, respectively. These regions have minimal overlap between the monomer and the excimer bands.

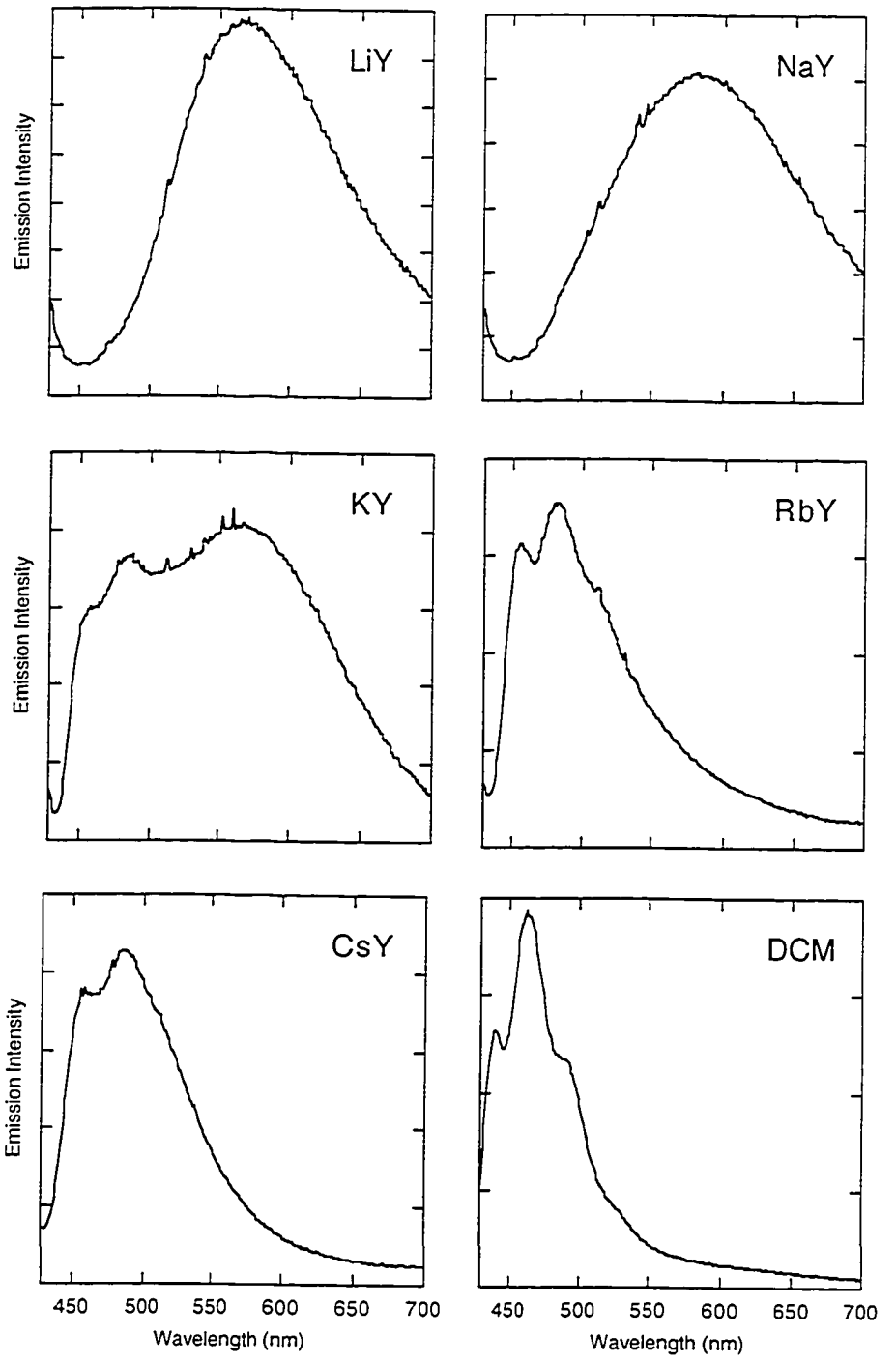

Figure 3.19 Steady state fluorescence spectra of DCA incorporated in Y zeolites, <S> = 0.043, and in dichloromethane (DCM) solution, 8.76×10^{-4} M. The excitation wavelength is 418 nm.

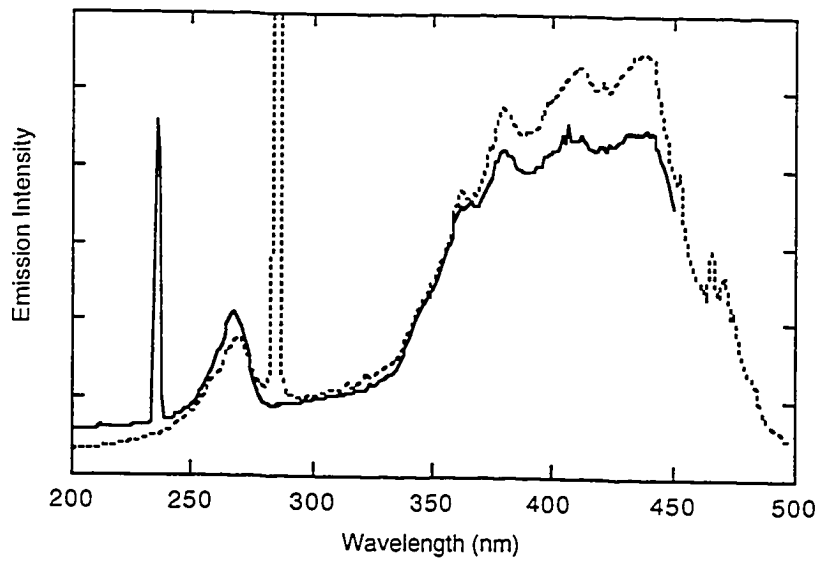

Figure 3.20 Steady-state excitation spectrum of DCA incorporated in KY zeolite, <S> = 0.043. The excitation spectrum monitored at 570 nm (---) matches the shape of the excitation spectrum monitored at 470 nm (—), providing support that the emission band at 570 nm is due to excimer emission. The spikes at 235 and 285 nm are overtones ($\lambda/2$) of 470 and 570 nm, respectively, and are artifacts generated within the monochromator.

Steady-state emission spectra can be fit using a number of Gaussian curves to represent the monomer and excimer emission bands, as shown in Figure 3.21. The excimer band is adequately fit by one broad Gaussian band centered at about 17 500 cm^{-1} (571 nm) while the monomer is fit by three narrow Gaussians, one for each vibrational peak. The monomer Gaussians were allowed to vary in height only, while the excimer Gaussian was allowed to vary in height and center wavelength. Fitting the spectra in this way allowed for the extraction of the central wavelength of the excimer, Table 3.8. As the counterbalancing cation becomes larger, the excimer emission band becomes increasingly blue-shifted. The error in the RbY and CsY spectra is large due to the low intensity of the excimer band; however, the trend is clear despite the uncertainty in the exact values.

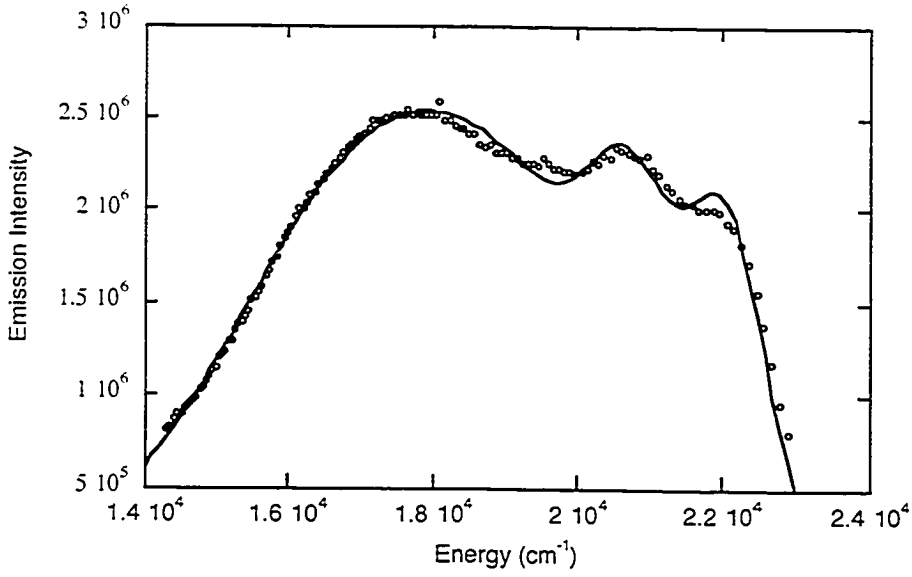

Figure 3.21 Multiple Gaussian fit (—) to the steady state fluorescence spectrum of DCA/KY zeolite composite, <S> = 0.043.

Table 3.8 Central wavelengths of DCA excimer emission bands as a function of cation-exchanged zeolite <S> = 0.043.

Zeolite	Central Wavelength (nm)
LiY	571±1
NaY	579±1
KY	566±2
RbY	524±5
CsY	525±6

Time-resolved emission measurements were carried out using an excitation wavelength of 388 nm and monitored with 450 nm and 600 nm bandpass filters with a bandwidth of 25 nm. For all zeolites, the shape of the kinetic traces collected at 450 nm differs significantly from those collected at 600 nm, confirming that the species being monitored at these two wavelengths are different.

On the nanosecond time scale, the monomer emission is systematically found to be significantly shorter lived than excimer emission, which is similar to the behaviour of pyrene included in NaY zeolite.[54] Figure 3.22 shows the decay traces of monomer compared to excimer emission in all five zeolites. Kinetic fits of both monomer and

excimer decays were performed without deconvolution with three exponentials, which is the minimum number necessary to achieve satisfactory residuals. For the monomer, the three lifetimes (1.3±0.4, 5.9±1.4, and 18.4±4.0 ns, averaged over all five zeolites) are not found to vary much as a function of zeolite; however, their various proportions varied greatly. As the cation mass increases, the shortest lifetime becomes less and less significant while the two longer lifetimes increase in proportion. Figure 3.23 illustrates these trends graphically. In Figure 3.23(a), the three lifetimes extracted from each decay are plotted against the appropriate zeolite, allowing for a quick comparison of lifetimes between zeolites. Each cluster of three bars is plotted from left to right as shortest to longest lifetimes. Figure 3.23(b) plots the relative percentages of each lifetime, calculated from the pre-exponential factors, in the same lifetime order as (a). From Figure 3.23(b) it is clear that the shortest monomer lifetime becomes less and less significant while the longer lifetimes become more prominent as the cation size increases. The excimer emission has much less distinct trends (Figure 3.23(c) and (d)), and there is much more variation in the absolute value of the longest lifetime. This uncertainty is due to the longest lifetime being underrepresented within the longest time window available on the streak camera, 90 ns. However, the lifetimes can still be observed to be roughly constant over all five zeolites and average lifetimes of the excimer emission are 1.3±0.3, 8.7±1.3 and 39.0±9.1 ns. No clear trends can be described for the proportion data of the excimer emission lifetimes. The monomer and excimer lifetimes and lifetime percentages are listed in Tables 3.9 and 3.10.

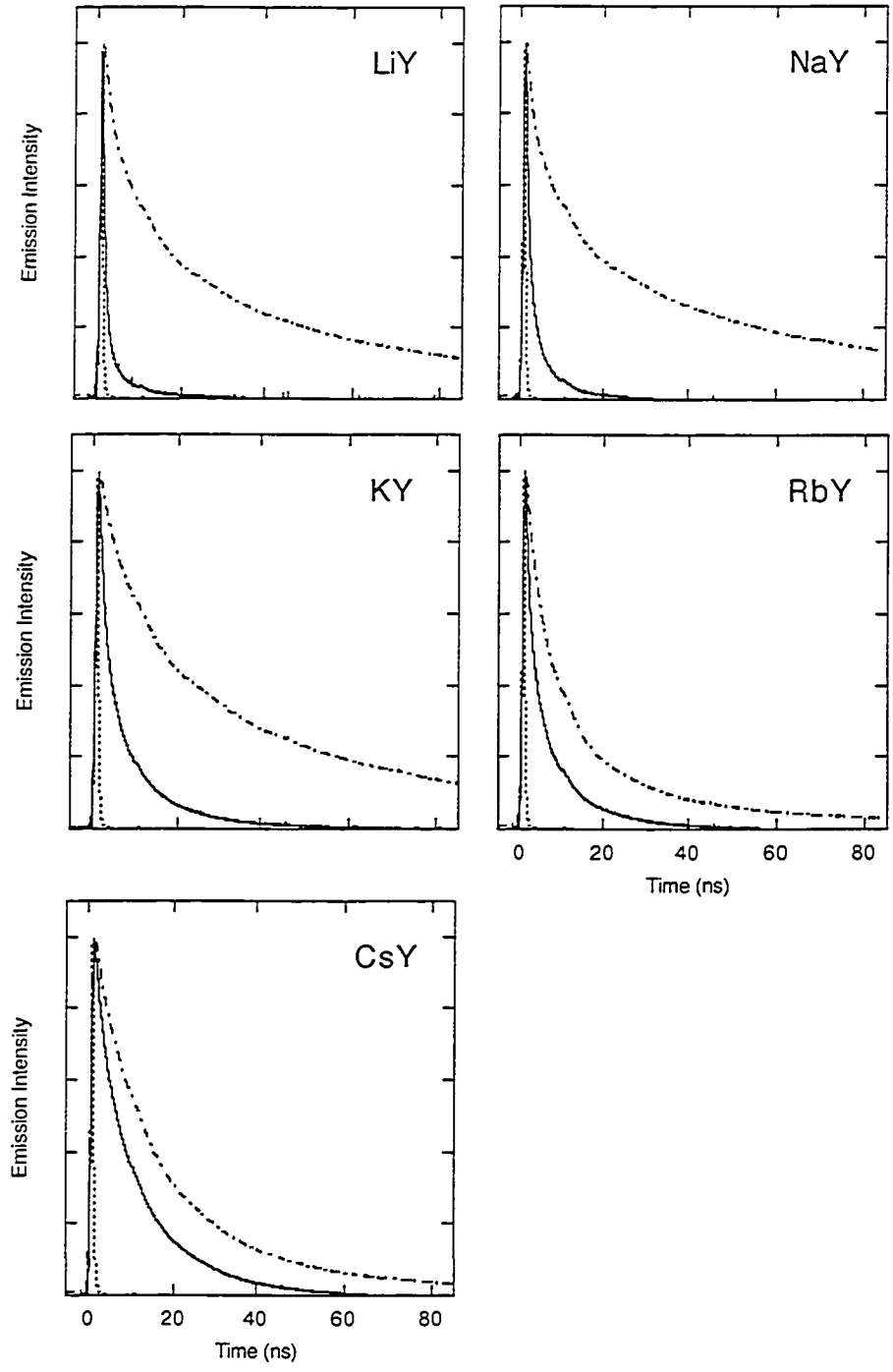

Figure 3.22 Monomer (—) and excimer (–·–) emission decays of DCA included in cation-exchanged Y zeolites, <S> = 0.043. Each plot includes the IRF (---). The excitation wavelength is 388 nm.

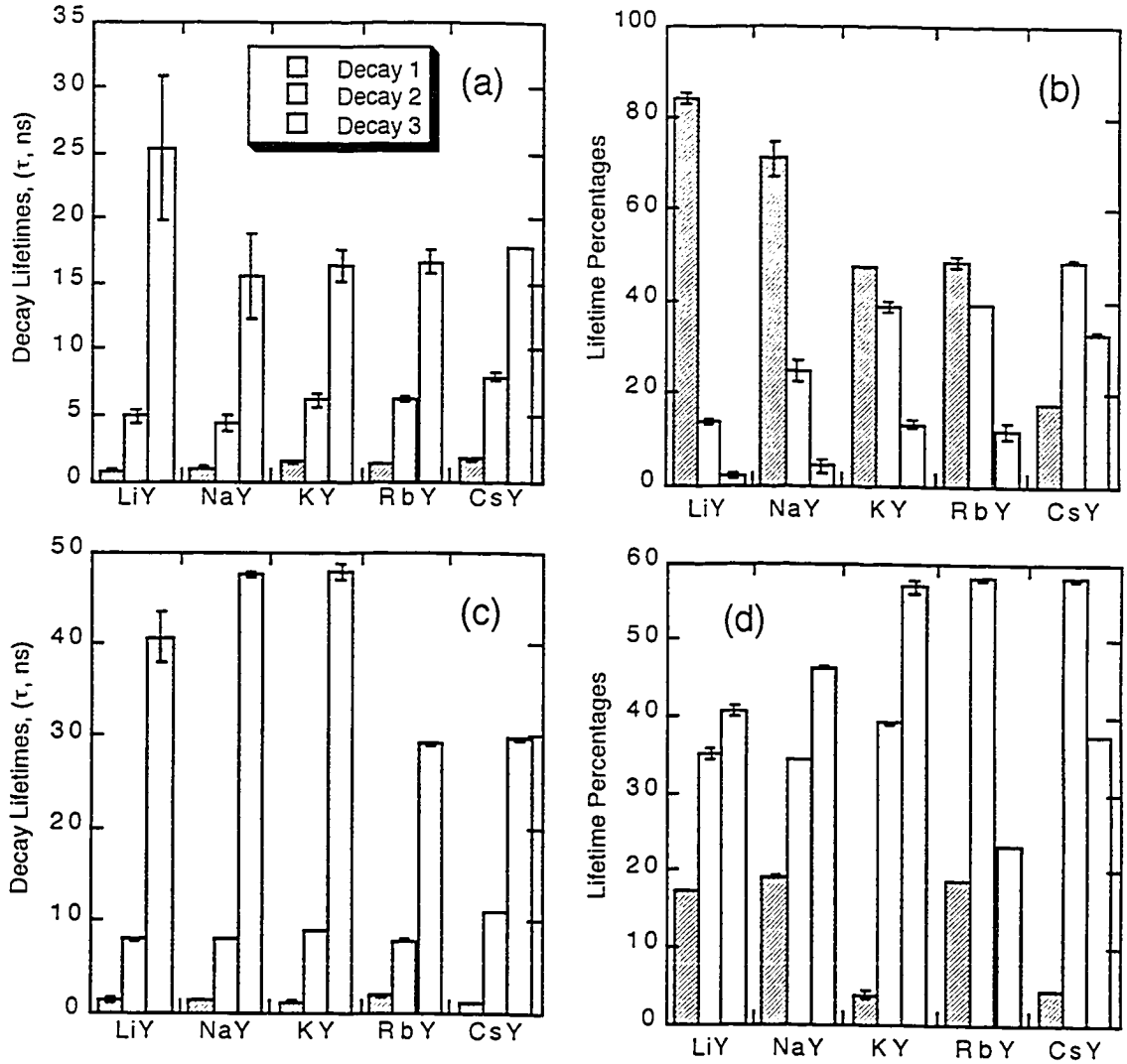

Figure 3.23 Lifetimes and lifetime percentages extracted from emission decay data of DCA/Y zeolite samples at <S> = 0.043. Errors are calculated as standard deviations of calculated lifetimes of sample replicates. (a) Lifetimes of monomer fluorescence decay collected at 450 nm. (b) Percentages of monomer fluorescence decay, calculated from pre-expontial factors of each component. (c) Lifetimes of excimer fluorescence decay collected at 600 nm. (d) Percentages of excimer emission decay, calculated from the pre-exponential factors of each component.

Table 3.9 Lifetimes and lifetime percentages extracted from emission decay data of DCA / zeolite samples collected at 450 nm. The loading level is <S> = 0.043. Decays were put into order of lifetimes, with decay 1 having the shortest lifetime and decay 3 having the longest lifetime.

Zeolite	Decay 1 (ns)	Decay 1 Percentage (%)	Decay 2 (ns)	Decay 2 Percentage (%)	Decay 3 (ns)	Decay 3 Percentage (%)
LiY	0.81±0.04	84.4±1.2	4.92±0.59	13.7±0.7	25.3±5.5	1.9±0.5
NaY	0.97±0.06	71.2±3.9	4.40±0.65	24.7±2.3	15.6±3.3	4.1±1.7
KY	1.45±0.14	47.7±0.0	6.13±0.60	38.8±1.1	16.5±1.2	13.4±1.1
RbY	1.37±0.04	48.7±1.4	6.22±0.23	39.3±0.2	16.7±0.9	12.0±1.6
CsY	1.73±0.10	17.9±0.0	7.94±0.23	48.9±0.3	17.8±0.0	33.1±0.3

Table 3.10 Lifetimes and lifetime percentages extracted from emission decay data of DCA / zeolite samples collected at 600 nm. The loading level is <S> = 0.043. Decays were put into order of lifetimes, with decay 1 having the shortest lifetime and decay 3 having the longest lifetime.

Zeolite	Decay 1 (ns)	Decay 1 Percentage (%)	Decay 2 (ns)	Decay 2 Percentage (%)	Decay 3 (ns)	Decay 3 Percentage (%)
LiY	1.32±0.18	17.3±0.1	7.94±0.17	35.0±0.7	40.7±2.7	40.7±0.7
NaY	1.22±0.01	19.2±0.2	8.07±0.04	34.4±0.0	47.5±0.3	46.5±0.2
KY	1.13±0.04	3.8±0.6	8.88±0.11	39.3±0.2	47.9±0.9	57.0±0.8
RbY	1.80±0.06	18.7±0.0	7.87±0.08	58.1±0.1	29.2±0.2	23.3±0.1
CsY	1.07±0.04	4.3±0.1	10.94±012	58.1±0.2	29.8±0.2	37.6±0.2

3.3.2.2 Lower Loading Levels: <S> ~ 0.005, <S> ~ 0.002

At the higher loading level of <S> ~ 0.005, the LiY and NaY samples showed excimer emission; however, the other samples were dominated by monomer emission, Figure 3.24. A decrease in loading level to <S> ~ 0.002 produced samples that gave monomer fluorescence only, Figure 3.27. Excitation spectra monitored at 570 nm shows that the weak but characteristic excitation spectrum of the excimer was still measurable, Figure 3.29. From this, it can be concluded that excimer emission is still present but is

very low in intensity. The comparably high intensity of the monomer band makes the extraction of the excimer band's central wavelength with any certainty impossible.

The lower loading levels did not see a uniform adsorption of guest molecules across the cation-exchanged zeolites, despite the fact that the same stock solution and procedure was used for all the samples. For the samples of <S> ~ 0.005, the measured loading level varied from <S> = 5.3 × 10^{-3} for LiY and NaY to <S> = 2.4 × 10^{-3} for CsY, while the <S> ~ 0.002 samples varies from <S> = 2.2 × 10^{-3} for LiY, NaY and KY to <S> = 1.2 × 10^{-3} for CsY, with the achieved loading level becoming lower as the atomic number of the counterbalancing cation increased. Actual loading levels are listed in Table 3.11. This suggests that incorporation of DCA is hindered by the size of the cation and by its location within each zeolite supercage, as all other factors are held constant.

The decays of the monomer and excimer emission exhibit similar behaviour to that observed in the higher loading level, Figures 3.25 and 3.28. The same approach to data analysis was undertaken for these data, and it is found that for the excimer decays, the short lifetime component disappeared and the data are adequately fit to a kinetic model with only two lifetimes. The shortest lifetime also disappears completely for the monomer emission for the CsY samples at the lowest loading level. In general, the lifetimes do not vary much as a function of zeolite or loading level and are listed in Tables 3.14 and 3.15. However, at both of these low loading levels, the proportions exhibit behaviour which is echoed in both monomer and excimer emission. There is a distinct split between the excited state behaviours in the light cation zeolites, LiY and NaY, versus the heavier cation zeolites KY, RbY and CsY, Figures 3.26 and 3.30. For the monomer, the light cations show a greater contribution from the short lifetimes while the heavy cations show the opposite effect. The excimer demonstrates exactly the opposite behaviour from that of the monomer, showing a greater contribution from the longer lifetimes for the light cations while the heavier cations are dominated by the shorter lifetimes. In all cases, the change in behaviour happens precisely between the NaY and KY zeolite hosts.

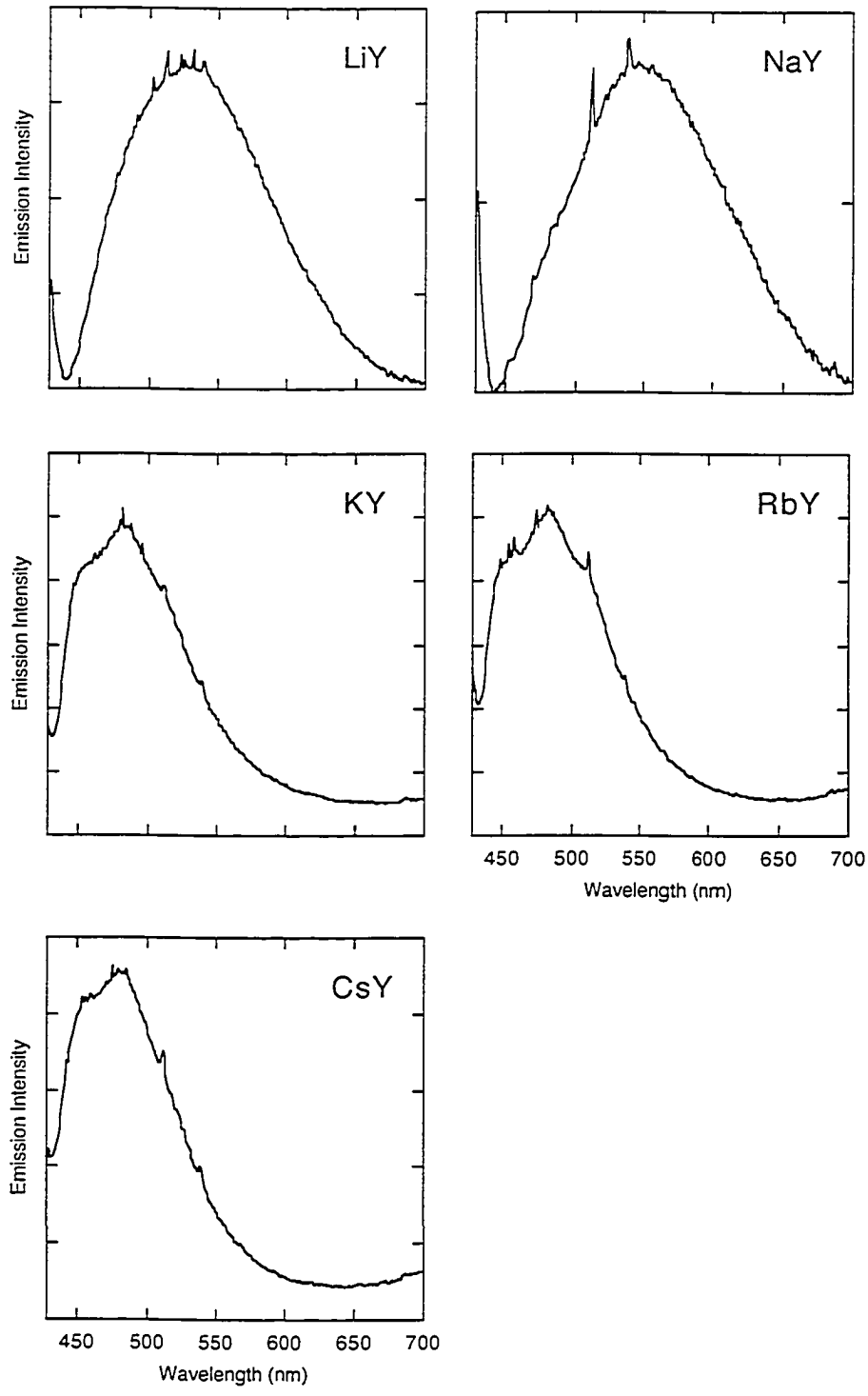

Figure 3.24 Steady state fluorescence spectra of DCA incorporated in Y zeolites, <S> ~ 0.005. The excitation wavelength is 418 nm.

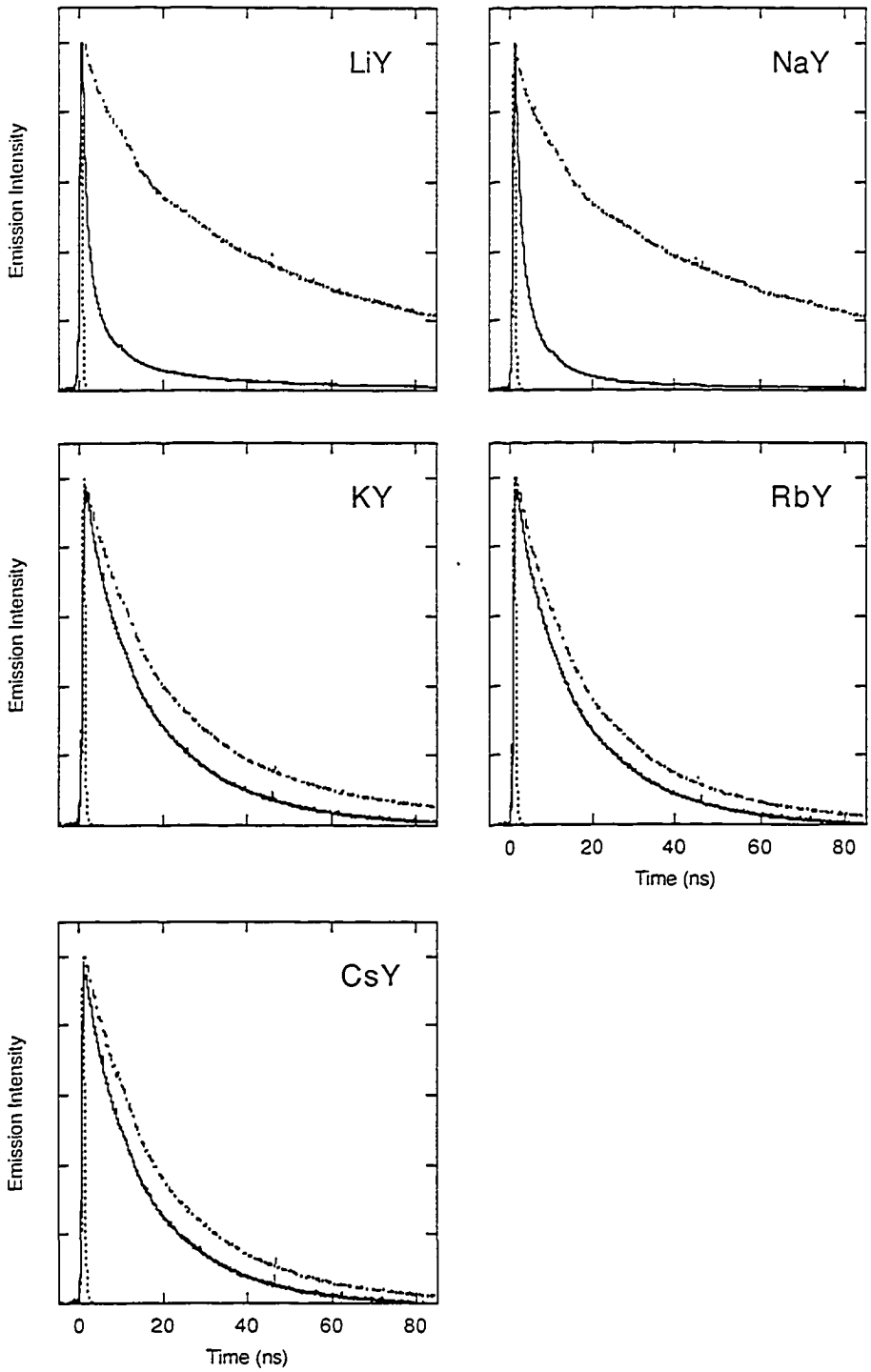

Figure 3.25 Monomer (—) and excimer (-·-) emission decays of DCA included in cation-exchanged Y zeolites, <S> ~ 0.005. Each plot includes the IRF (---).

Table 3.11 Actual loading levels <S> achieved for DCA in cation-exchanged zeolites.

Zeolite	<S> ~ 0.05	<S> ~ 0.005	<S> ~ 0.002
LiY	0.043	5.3×10^{-3}	2.2×10^{-3}
NaY	0.043	5.3×10^{-3}	2.2×10^{-3}
KY	0.043	4.8×10^{-3}	2.2×10^{-3}
RbY	0.043	3.9×10^{-3}	1.7×10^{-3}
CsY	0.043	2.4×10^{-3}	1.2×10^{-3}

Table 3.12 Lifetimes and lifetime percentages extracted from monomer emission decay data of DCA / zeolite samples collected at 450 nm. The loading level achieved is <S> ~ 0.005. Decays were put into order of lifetimes, with decay 1 having the shortest lifetime and decay 3 having the longest lifetime.

Zeolite	Decay 1 (ns)	Decay 1 Percentage (%)	Decay 2 (ns)	Decay 2 Percentage (%)	Decay 3 (ns)	Decay 3 Percentage (%)
LiY	1.10±0.03	57.2±3.2	4.89±0.07	31.9±2.1	22.0±0.5	10.6±1.0
NaY	1.23±0.04	59.6±0.9	5.21±0.20	34.2±0.2	18.6±1.2	6.1±0.8
KY	1.81±0.11	3.2±0.6	8.45±0.04	40.0±1.5	21.4±0.2	56.8±2.1
RbY	1.03±0.01	2.4±0.3	9.08±0.08	46.1±1.2	21.9±0.0	51.5±0.9
CsY		0.5±0.8	10.0±0.1	57.3±2.3	22.8±0.2	42.2±1.6

Table 3.13 Lifetimes and lifetime percentages extracted from excimer emission decay data of DCA / zeolite samples collected at 600 nm. The loading level is <S> ~ 0.005. Decays were put into order of lifetimes, with decay 1 having the shortest lifetime and decay 3 having the longest lifetime.

Zeolite	Decay 1 (ns)	Decay 1 Percentage (%)	Decay 2 (ns)	Decay 2 Percentage (%)	Decay 3 (ns)	Decay 3 Percentage (%)
LiY	0.62±0.24	2.4±0.7	10.7±0.1	31.1±0.6	57.8±1.5	66.5±0.1
NaY			8.9±0.2	30.9±0.2	58.2±1.3	69.1±0.2
KY			16.8±0.1	76.8±0.2	112±12	23.2±0.2
RbY			14.1±0.2	70.3±0.3	38.1±1.0	29.7±1.3
CsY			16.4±0.0	82.9±1.3	165±25	17.1±1.3

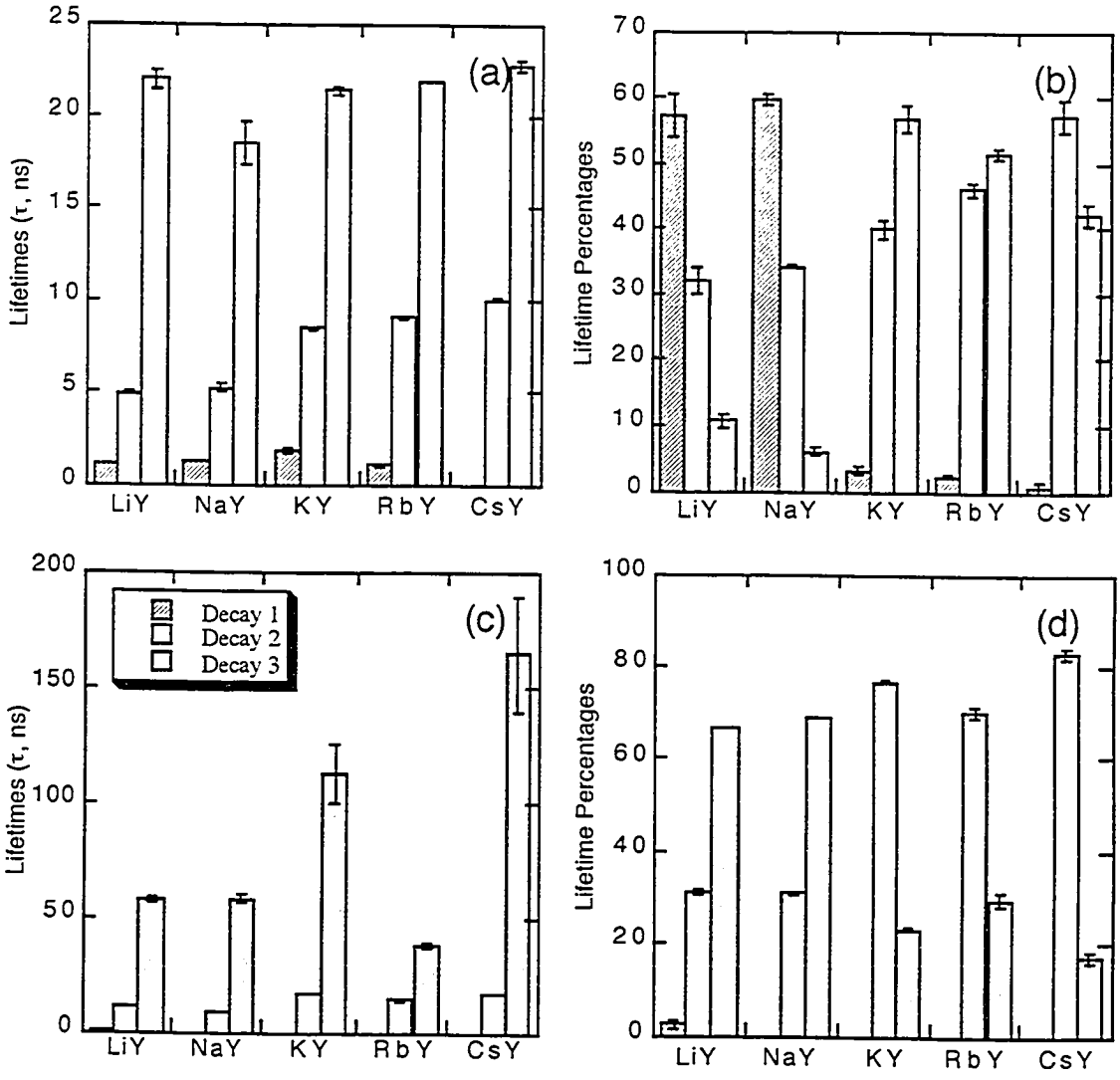

Figure 3.26 Lifetimes and lifetime percentages extracted from emission decay data of DCA/Y zeolite samples at <S> ~ 0.005. Errors are calculated as standard deviations of calculated lifetimes of sample replicates. (a) Lifetimes of monomer fluorescence decay collected at 450 nm. (b) Percentages of monomer fluorescence decay, calculated from pre-exponential factors of each component. (c) Lifetimes of excimer fluorescence decay collected at 600 nm. (d) Percentages of excimer emission decay, calculated from pre-exponential factors of each component.

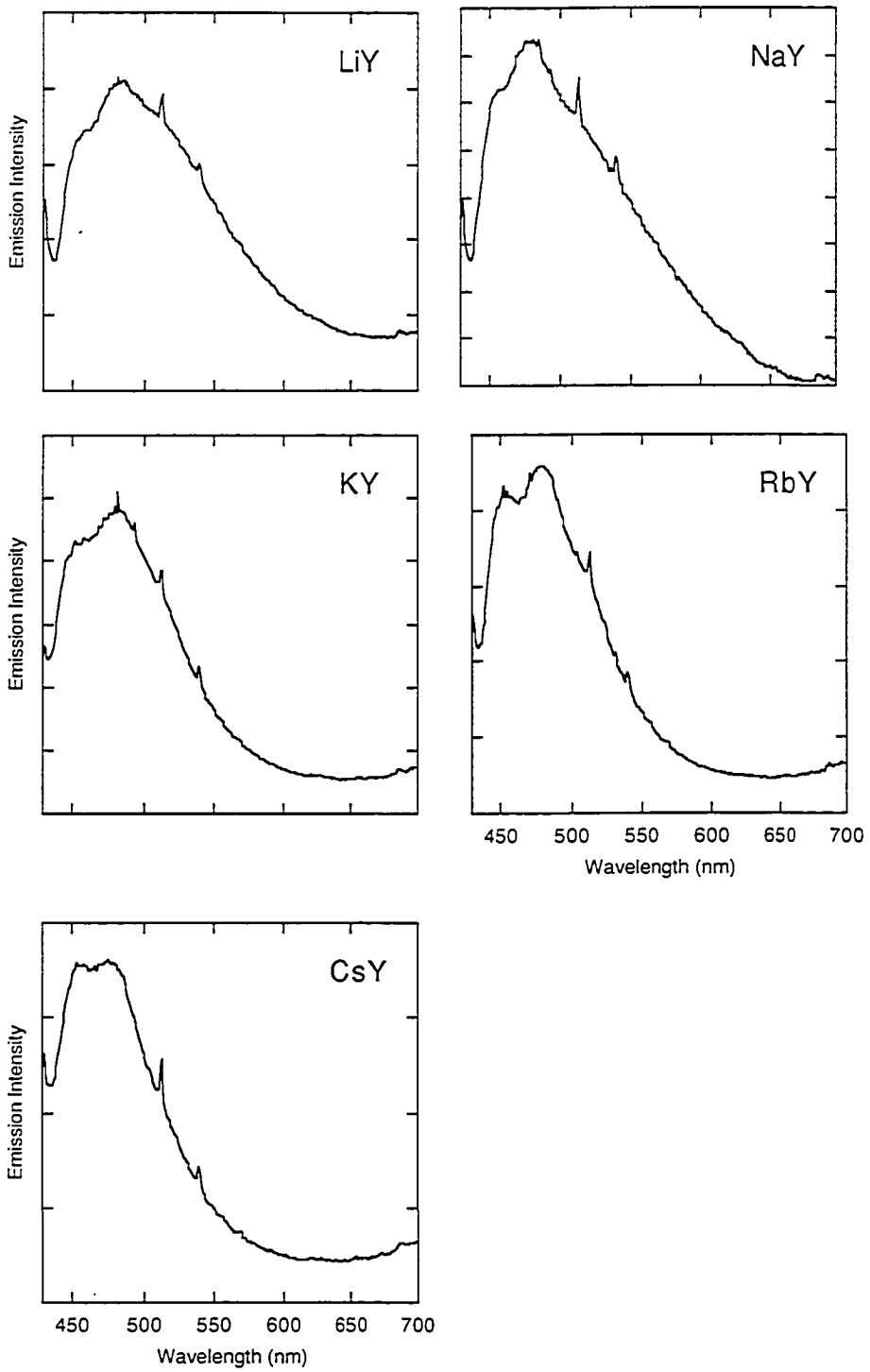

Figure 3.27 Steady state fluorescence spectra of DCA incorporated in Y zeolites, <S> ~ 0.002. The excitation wavelength is 418 nm.

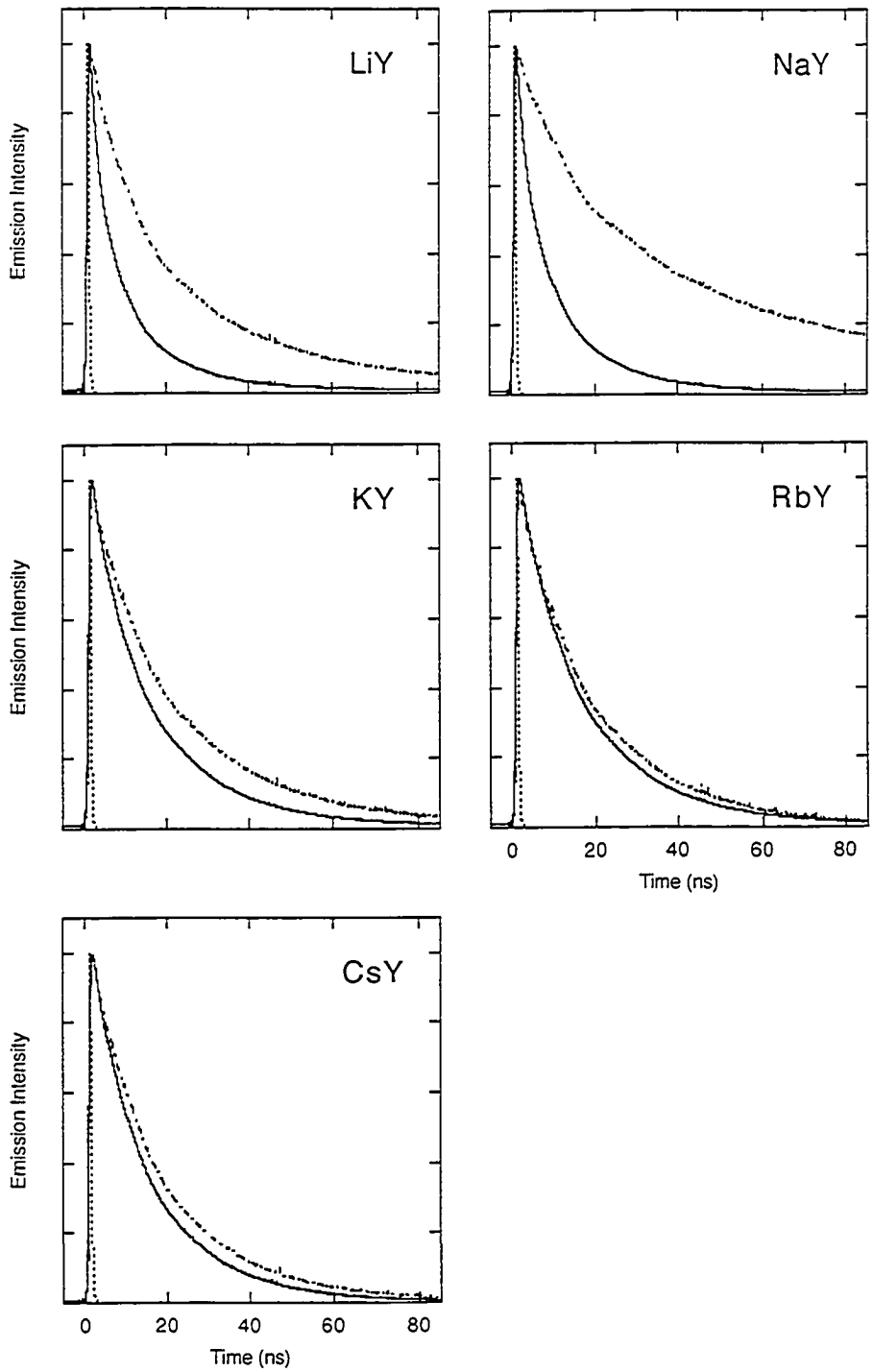

Figure 3.28 Monomer (—) and excimer (–·–) emission decays of DCA included in cation-exchanged Y zeolites, <S> ~ 0.002. Each plot includes the IRF (---). The excitation wavelength is 388 nm.

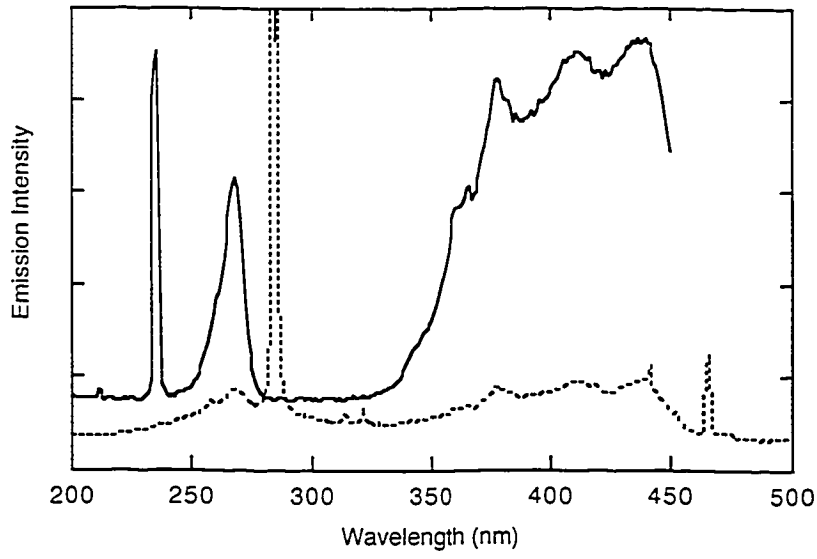

Figure 3.29 Steady state excitation spectrum of DCA incorporated in RbY zeolite, <S> ~ 0.002. The excitation spectrum of the excimer band monitored at 570 nm (---) still has the shape of the excitation spectrum monitored at 470 nm (—), indicating that some excimer is still being formed at these low loading levels. The spikes at 235 and 285 nm are overtones ($\lambda/2$) of 470 and 570 nm, respectively, and are artifacts generated within the monochromator.

Table 3.14 Lifetimes and lifetime percentages extracted from monomer emission decay data of DCA / zeolite samples collected at 450 nm. The loading level is <S> ~ 0.002. Decays were put into order of lifetimes, with decay 1 having the shortest lifetime and decay 3 having the longest lifetime.

Zeolite	Decay 1 (ns)	Decay 1 Percentage (%)	Decay 2 (ns)	Decay 2 Percentage (%)	Decay 3 (ns)	Decay 3 Percentage (%)
LiY	1.58±0.11	23.8±2.5	6.91±0.21	52.9±0.1	17.4±0.4	23.3±2.4
NaY	1.70±0.09	23.5±0.8	7.09±0.16	49.2±0.2	16.7±0.2	27.3±0.9
KY	1.42±0.05	2.3±0.2	8.49±0.23	35.0±3.2	18.6±0.1	62.7±3.4
RbY			8.45±0.32	32.0±1.9	18.6±0.3	68.0±1.9
CsY			9.49±0.30	47.7±3.1	18.9±0.4	52.3±3.1

Table 3.15 Lifetimes and lifetime percentages extracted from excimer emission decay data of DCA / zeolite samples collected at 450 nm. The loading level is <S> ~ 0.002. Decays were put into order of lifetimes, with decay 2 having the shortest lifetime and decay 3 having the longest lifetime.

Zeolite	Decay 1[a] (ns)	Decay 1 Percentage[a] (%)	Decay 2 (ns)	Decay 2 Percentage (%)	Decay 3 (ns)	Decay 3 Percentage (%)
LiY			10.1±0.2	50.2±1.4	33.9±1.0	49.8±1.4
NaY			12.1±0.1	37.3±0.1	55.8±1.7	62.7±0.1
KY			1.91±0.1	75.3±1.0	46.3±9.3	24.7±1.0
RbY			13.6±0.0	66.3±0.3	32.4±0.4	33.7±0.3
CsY			14.3±0.1	81.4±0.6	39.0±1.8	18.6±0.6

[a] Decay 1, although insignificant in these samples, was kept to facilitate comparision between these and previous samples.

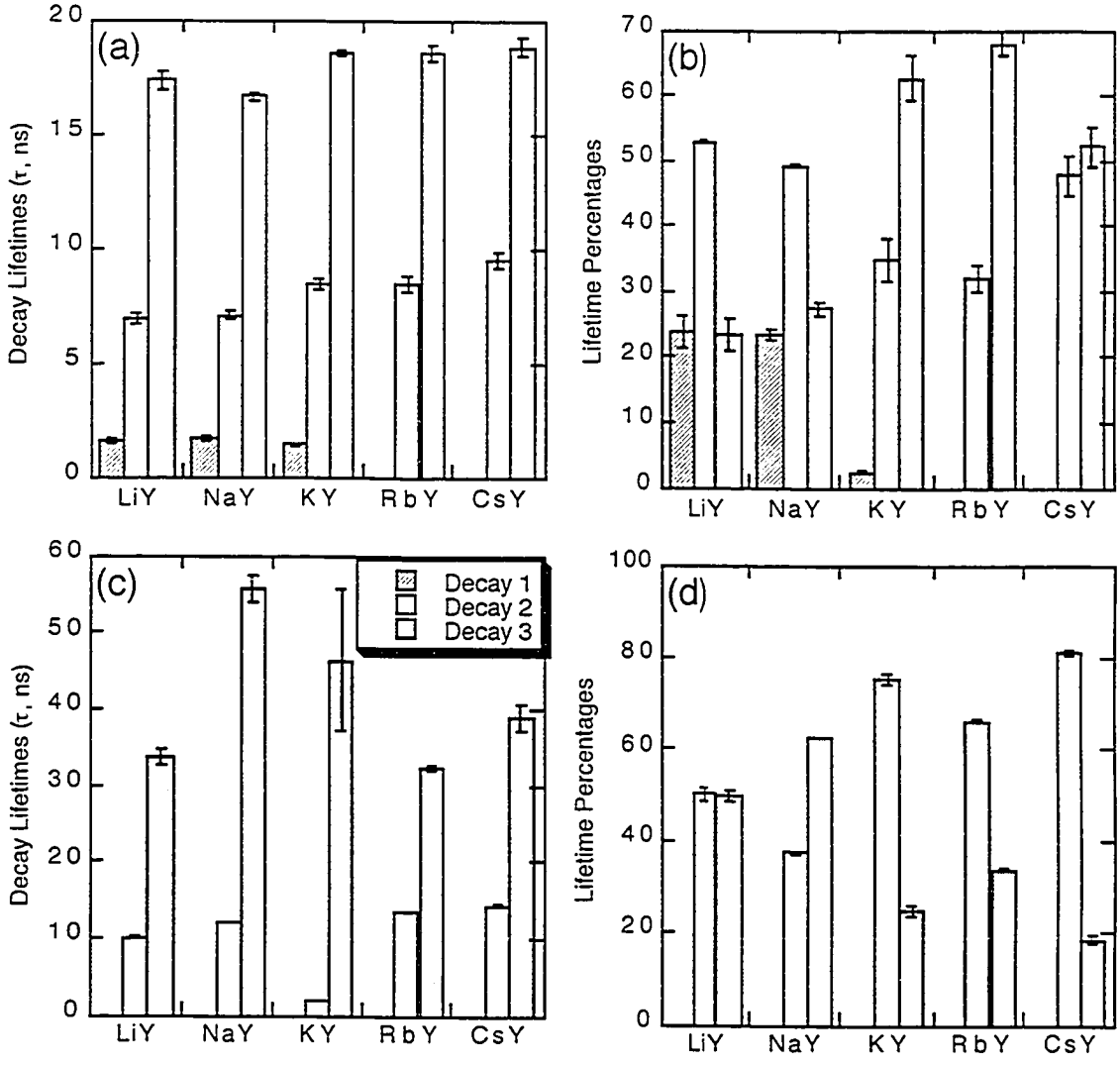

Figure 3.30 Lifetimes and lifetime percentages extracted from emission decay data of DCA/Y zeolite samples at <S> ~ 0.002. Errors are calculated as standard deviations of calculated lifetimes of sample replicates. (a) Lifetimes of monomer fluorescence decay collected at 450 nm. (b) Percentages of monomer fluorescence decay, calculated as initial intensity percentages of each component. (c) Lifetimes of excimer fluorescence decay collected at 600 nm. (d) Percentages of excimer emission decay, calculated as initial intensity percentages of each component.

3.3.2.3 Loading Level Experiment, DCA in KY

In order to further study the influence of loading level on the fluorescence decay, a new experiment was carried out to vary the loading level in one zeolite only. KY was chosen because of its ability to show the existence of both the monomeric and excimeric species in the steady state spectra. Preparations of all five KY samples were carried out simultaneously to keep all other conditions constant, with only the amount of added DCA stock solution changing between samples. Loading levels achieved were <S> = 0.042, 0.013, 5.0×10^{-3}, 2.9×10^{-3}, and 2.0×10^{-3}.

Steady state spectra were collected for samples at all loading levels and are depicted in Figure 3.31. At the highest loading level, the fluorescence spectra are identical in shape to those observed previously at comparable loading levels. From <S> = 0.042 to 0.013, a dramatic drop in the excimer emission band intensity is accompanied by an increase in the monomer signal, rather than an overall decrease in intensity. This suggests that even though the overall loading levels decreased, the ratio of monomeric to excimeric species formed are influenced heavily by the loading level, with a preference towards excimer formation at higher loading levels. This preference implies an inhomogeneous loading of KY at high loading levels, where aggregation is favoured. Loading levels lower than <S> = 0.013 show subsequent decreases in intensity without significant differences in the shape of the spectra. Analysis of the steady state spectra by Gaussian curve fitting revealed that the excimer band becomes increasingly red-shifted as the loading level increases. These numbers are reported in Table 3.16.

Time-resolved emission on the nanosecond time scale, shown in Figure 3.32, gave clear loading level dependences of lifetime trends. Lifetimes for the data are given in Tables 3.17 and 3.18. The monomer fluorescence data show the most distinctive trends. Like the previous experiments, a kinetic model with three exponential decays adequately fits the decay of the monomer fluorescence. The plot of the monomer lifetimes (Figure 3.33(a)) shows that the three lifetimes 2.0±0.3 ns, 8.4±0.9 ns, and 18.4±0.6 ns do not change as a function of loading level. However, in stark contrast to the unchanging lifetimes, the percentages of DCA lifetimes (Figure 3.33(b)) show that as the loading

level decreases, the shortest lifetime becomes less significant and the longer lifetimes become more significant.

The excimer emission data show less distinctive trends. The decay lifetimes of the excimer can be said to show little trend as a function of loading level, and the percentages also do not show much difference as a function of loading level. This suggests that the excimer is much less sensitive to the loading level than the monomer, which implies that the excimers, once formed, are not interacting with the contents of neighbouring supercages. Plots of the monomer and excimer decay lifetimes and percentages are given in Figure 3.33.

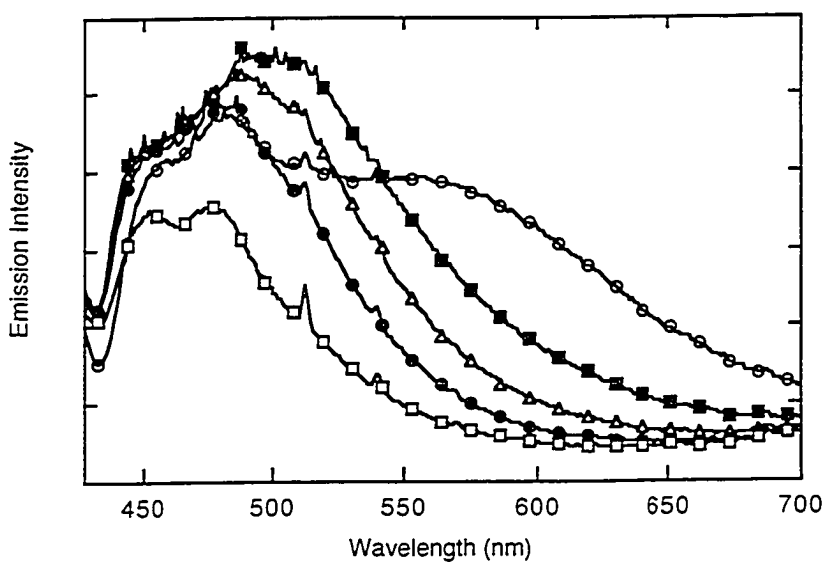

Figure 3.31 Steady state emission spectra of DCA incorporated in KY zeolite at various loading levels. Excitation wavelength is 418 nm. Loading levels: <S> = 0.042 (○), <S> = 0.013 (■), <S> = 5.0×10^{-3} (△), <S> = 2.9×10^{-3} (●), and <S> = 2.0×10^{-3} (□).

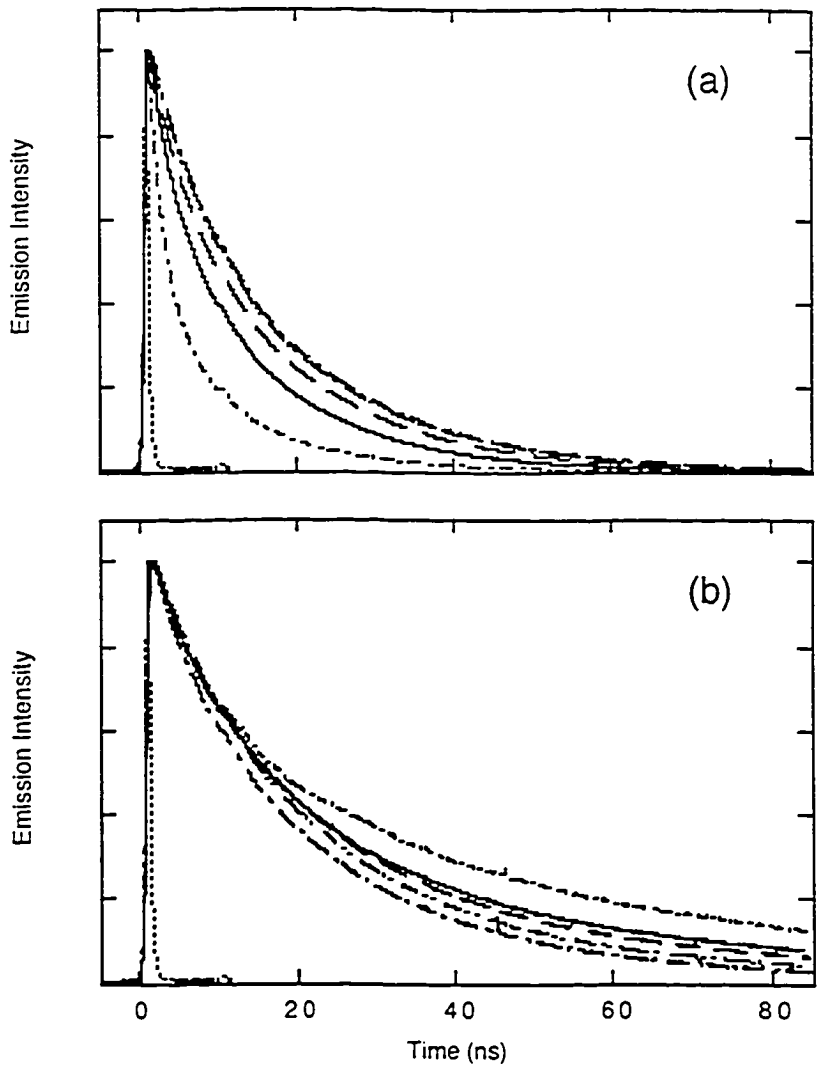

Figure 3.32 Monomer (a) and excimer (b) emission decays of DCA included in KY zeolites with varying loading levels: <S> = 0.042 (—·—), <S> = 0.013 (—), <S> = 5.0×10^{-4} (— —), <S> = 2.9×10^{-3} (—···—), <S> = 2.0×10^{-3} (—·—). Plots include the IRF (---).

Table 3.16 Central wavelengths of DCA excimer emission bands as a function of loading level in KY zeolite.

Loading Level <S>	Central Wavelength (nm)
0.042	564±2
0.013	554±5
5.0×10^{-3}	503±6
2.9×10^{-3}	491±6
2.0×10^{-3}	[a]

[a]The error in this number is very large (± 20 nm) due to the low intensity of the excimer emission band in the collected spectrum.

Table 3.17 Lifetimes and lifetime percentages extracted from monomer emission decay data of DCA / KY zeolite samples collected at 450 nm as a function of loading level. Decays were put into order of lifetimes, with decay 1 having the shortest lifetime and decay 3 having the longest lifetime.

Loading Level <S>	Decay 1 (ns)	Decay 1 Percentage (%)	Decay 2 (ns)	Decay 2 Percentage (%)	Decay 3 (ns)	Decay 3 Percentage (%)
0.042	1.61±0.04	49.3±1.2	7.53±0.42	39.4±1.0	17.9±1.3	11.3±2.2
0.013	2.24±0.15	21.8±0.6	9.98±0.21	51.0±1.2	18.8±0.0	27.2±0.6
5.0×10^{-3}	2.31±0.09	11.2±0.0	8.45±0.06	28.1±0.7	17.8±0.2	60.6±0.7
2.9×10^{-3}	1.81±0.03	4.08±0.56	7.84±0.13	25.7±0.3	18.5±0.2	70.3±0.8
2.0×10^{-3}	1.84±0.40	2.29±0.56	8.42±0.10	28.1±0.4	19.2±0.0	69.6±0.1

Table 3.18 Lifetimes and lifetime percentages extracted from excimer emission decay data of DCA / KY zeolite samples collected at 450 nm as a function of loading level. Decays were put into order of lifetimes, with decay 1 having the shortest lifetime and decay 3 having the longest lifetime.

Loading Level <S>	Decay 1 (ns)	Decay 1 Percentage (%)	Decay 2 (ns)	Decay 2 Percentage (%)	Decay 3 (ns)	Decay 3 Percentage (%)
0.042	1.27±0.02	3.6±0.6	8.77±0.11	35.0±0.4	44.1±0.8	61.4±0.2
0.013	2.54±0.32	5.6±0.3	14.5±1.0	53.7±5.21	44.6±6.0	40.7±4.8
5.0×10^{-3}	3.12±1.12	3.7±0.4	15.6±0.1	59.5±0.7	40.0±0.7	36.8±0.3
2.9×10^{-3}	1.68±0.01	1.1±0.2	12.2±0.2	37.0±2.7	26.7±0.4	61.9±2.5
2.0×10^{-3}	2.40±0.26	5.3±0.6	11.3±0.4	34.7±0.8	25.3±0.2	60.0±1.3

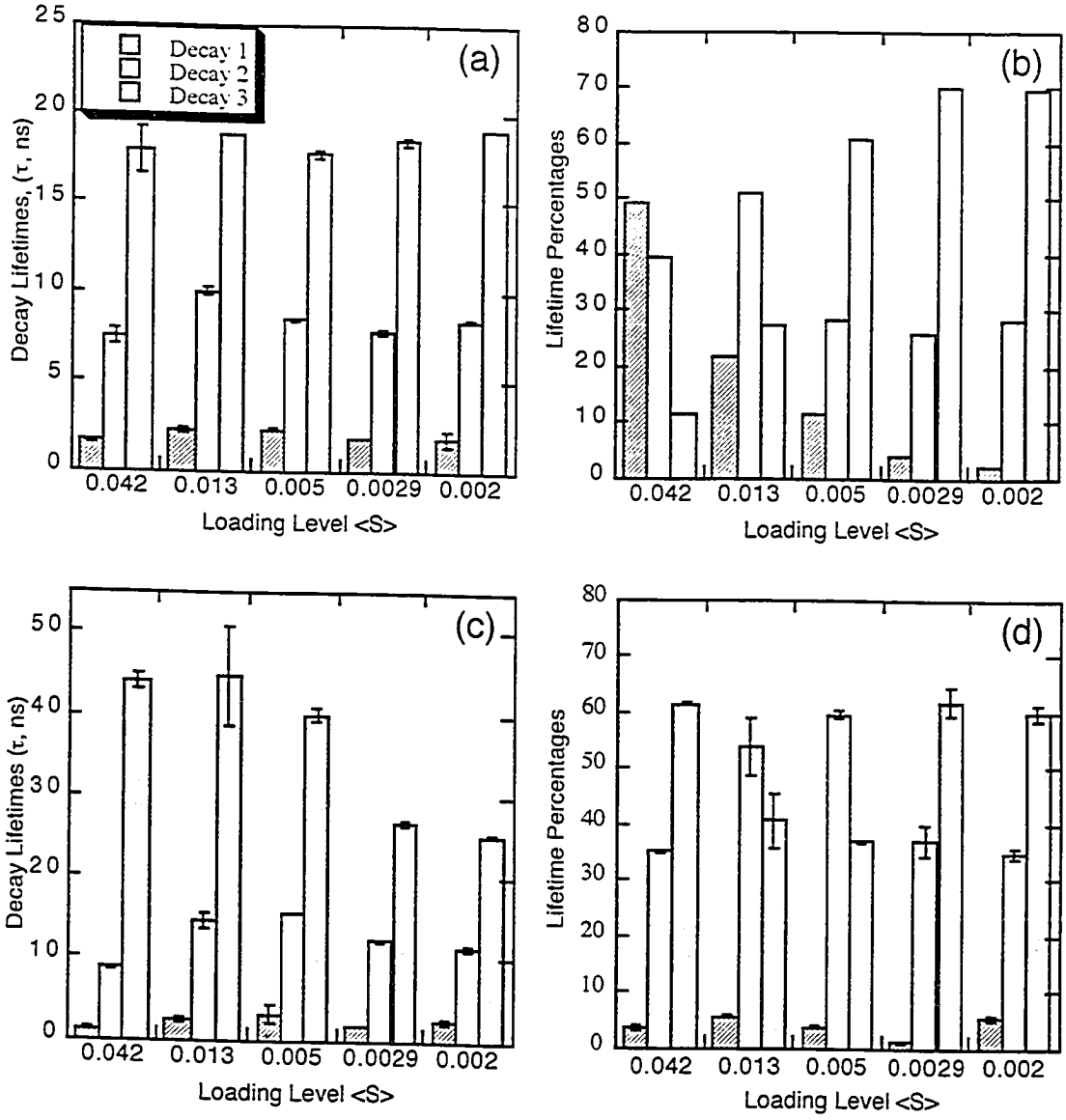

Figure 3.33 Lifetimes and lifetime percentages extracted from emission decay data of DCA/KY zeolite samples as a function of loading level. Loading levels are plotted such that lower loading levels are towards the right. Errors are calculated as standard deviations of calculated lifetimes of sample replicates. (a) Lifetimes of monomer fluorescence decay collected at 450 nm. (b) Percentages of monomer fluorescence decay, calculated from pre-exponential factors of each component. (c) Lifetimes of excimer fluorescence decay collected at 600 nm. (d) Percentages of excimer emission decay, calculated as pre-exponential factors of each component.

3.3.3 Discussion

The DCA molecule, while well studied in solution[132,133] and often used as a sensitizer,[127-129] has not been used extensively as a probe molecule in zeolite host systems. More popular probe molecules are related polyaromatic hydrocarbons, such as pyrene and anthracene. The dimensions of DCA are comparable to those of pyrene and anthracene molecules. Both pyrene and anthracene are able to fit into Y zeolite supercages by incorporation through the pores, and up to two molecules can fit into one zeolite supercage.[54,57,111] By inference, up to two DCA molecules should also be able to fit into one Y supercage. With these spatial characteristics, the observed monomer and excimer emission from the DCA/zeolite system can arise from the origins outlined in Scheme 3.3:

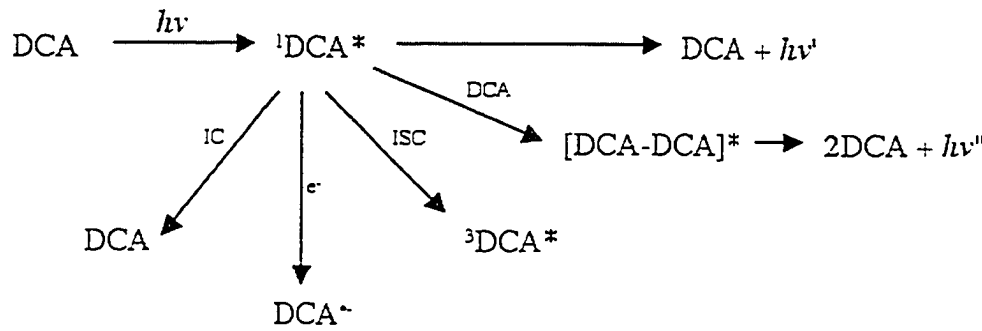

Scheme 3.3

Upon laser irradiation of the incorporated DCA molecule, the singlet state of DCA is generated in a one-photon process. ^{1}DCA* can then deactivate via the five pathways outlined in Scheme 3.3. Two pathways, fluorescence and internal conversion, lead back to the ground state DCA molecule. Coupling of ^{1}DCA* with a nearby ground state DCA molecule leads to the formation of an excimer [DCA-DCA]* and subsequent excimer emission also results in two ground state DCA molecules. ^{1}DCA* is an excellent electron acceptor[132] and can scavenge an electron to form $DCA^{\bullet-}$. The electron is most likely taken from the zeolite framework, which can act as either an electron donor or an electron acceptor,[134] rather than from another DCA or ^{1}DCA* molecule, both of which are electron deficient species. Finally, the excited singlet species can undergo intersystem crossing to

form the ^{3}DCA* species, which has been reported to have quantum yields (Φ_T) between 0.01 to 0.12 in solutions where the solvent does not possess a heavy atom.[132] From the solution data, it is expected that some intersystem crossing will occur when DCA is incorporated into the zeolite environment. The last two processes, electron transfer and intersystem crossing, can lead to new pathways of interaction and reaction. Of particular interest to this study are the emissive pathways, and the information that can be gleaned about the microenvironment surrounding the DCA molecules, and their placement and movement within the zeolite interior.

3.3.3.1 Inhomogeneous Distribution of DCA Guest Molecules

At the highest loading level achieved in this study, <S> = 0.043, a purely homogeneous distribution of DCA molecules throughout the zeolite framework would result in essentially every molecule being housed individually, with empty adjacent cages. These circumstances would result in little or no excimer formation, and thus no observable excimer emission. However, Figure 3.19 clearly shows that even at the loading level of <S> = 0.043 the predominant luminescence is excimer emission for the LiY, NaY and KY samples, indicating that the distribution of DCA guest molecules is inhomogeneous in these zeolites. Even at a dramatically lower loading level of <S> = 5.3×10^{-3}, the LiY and NaY emission spectra are dominated by the excimer band. The inhomogeneous nature of the loading is characteristic of related polyaromatic guest molecules, such as pyrene[54] and anthracene.[111,112] For anthracene, it has been suggested the preferential aggregation is due to loading of doubly occupied cavities in a concerted manner.[111] A similar mechanism may be responsible for the preferred aggregation of DCA molecules in Y zeolites.

Inhomogeneous distribution of samples results in an inaccurate representation of molecular density by the calculation of loading levels. All loading levels reported in this study are calculated assuming statistical distributions. A loading level gradient is much more representative of the actual distribution. It can be inferred that the guest molecules are aggregated in cavities near the surface of the zeolite particles because the molecules must load from the outside of the particle into the inside *via* supercage hopping. Thus,

high loading levels would be expected near the surface and low loading levels near the center of the zeolite particles.

3.3.3.2 Location of DCA Within Supercages

From the sample preparation procedure, which ensured that surface molecules were removed, and the knowledge of the zeolite framework dimensions, which limits where the DCA molecules can fit, it is known that the DCA molecules being studied reside within the Y zeolite supercages. However, within these supercages, there is some variability as to where the DCA molecules (or ^{1}DCA* molecules) can reside. It is known for other aromatic species that there are preferred adsorption locations, the most popular of these being the cation site and the wall site.[58] The cation site is defined as a site in which the guest molecule is close to and interacts with the cation through such stabilization mechanisms as the π-cation interaction. Wall sites are sites where the guest molecule can adsorb onto the walls of supercages through electrostatic interaction and dispersion forces. Additional sites are possible depending upon the size and shape of the guest molecules.[55] Previous studies[52,54,58] have shown that these different preferred sites result in several localized microenvironments that manifest as multiple lifetimes in the fluorescence decay traces.

The fluorescence decay traces for all DCA / zeolite systems were fit with multiexponential decays, indicating that ^{1}DCA* is present in a minimum of two or three different environments when it relaxes by fluorescence. Having two or three different lifetimes indicates that the kinetic stability of the ^{1}DCA* molecule is different depending upon the absorption site. The shorter the lifetime, the more pathways are readily available for relaxation in that particular microenvironment for the ^{1}DCA* molecule. A quick comparison of the lifetimes in cation-exchanged Y zeolite at $\langle S \rangle = 0.043$ (1.3, 5.9 and 18.4 ns) with the fluorescence lifetimes of DCA in solution[132] (12.0 ns for cyclohexane, to 16.3 ns for p-xylene) indicates that the zeolite interior has two local sites that are much less kinetically stable for ^{1}DCA* and one that is similar in stability to a homogeneous non-polar solvent environment.

In all the cation-exchanged zeolites, the lifetimes of the monomer do not vary as a function of loading level or cation. This is consistent with the rigid framework structure of the zeolite, which does not change structure as a function of cation or amount of incorporated guest molecule. Therefore, the same adsorption sites are available to ^{1}DCA* regardless of the counterbalancing cation or loading level.

Here it is important to make the distinction between lifetimes, which are indicative of the type of adsorption site, and the lifetime percentages, which are interpreted as the probability of site occupancy.[58] Lifetime percentages of monomer emission are plotted in Figures 3.23, 3.26, 3.30 and 3.33. Similar trends are noted as a function of cation size across all loading levels: as the charge-balancing cation increases in size, the kinetically destabilized sites become less and less populated and the longer lifetime sites increase proportionally. There are two possible reasons for this change in relative populations. Firstly, as the cation gets larger, the free volume within the supercage decreases, and the size of the cation could prevent the monomer from residing in a potential adsorption site. The cation location within a Y zeolite is dependent upon its size. The smaller cations are reported to be embedded within the supercage walls, while the larger cations reside within the supercage cavity itself,[71] taking up space. Thus, any guest molecules in the supercages will have to distribute themselves differently around the larger cations than around the smaller cations, and the population distributions will change. This is consistent with the observation that at lower loading levels, the site occupancy proportions of the smaller (Li^+, Na^+) are exactly opposite of those of the larger (K^+, Rb^+, Cs^+) cations.

A second possible explanation concerns changing electrostatic conditions. As the cation size increases, the charge density on the cation decreases, which changes the polarity of the supercage interior.[119] As the cations become more diffuse, their ability to withdraw electrons from the neighbouring framework decreases and their ability to stabilize an aromatic compound by π-cation interactions also decreases.[101,103-108] Thus, the relative attraction and stabilization of the ground state DCA molecule to a particular site can be altered by changing the charge-balancing cation, thereby changing the site occupancy proportion. While the site occupancy would change, it would be expected that the lifetimes would also show a change because the nature of the sites have changed.

Because the data do not reflect this difference, this contribution to the change in site occupancy proportion is probably less dominant than the space considerations outlined above.

Examination of Figure 3.33 shows an interesting factor influencing the location of monomers, namely, a loading level dependence. Figure 3.33(a) shows the decay lifetimes of DCA monomer fluorescence as a function of loading level in KY zeolite. As expected, there is no loading level dependence on lifetime, indicating that the adsorption sites of the zeolite are independent of guest molecule occupancy. However, the site with the shortest lifetime becomes less and less populated while the more kinetically stable sites become more populated as the loading level decreases, Figure 3.33(b). Similar results have been noted for pyrene / NaX systems,[52] leading to some interesting inferences. The first inference is that the most thermodynamically stable sites for the ground state DCA molecules, as well as the most kinetically stabilizing sites for ^{1}DCA*, are more easily occupied at low loading levels. The second inference is the actual location of the absorption sites. Ramamurthy and coworkers[58] have proposed that there are families of sites where guest molecules reside, namely the cation site, and the wall site. These sites stabilize the aromatic guest molecules by electrostatic interactions between the zeolite framework or cation with the electron-rich π orbitals of the molecule. Given the electron-withdrawing effects of the cyano group, the π orbitals of DCA are much less electron-rich than an unsubstituted aromatic compound and would be less attracted to these sites. A third site is suggested by the lifetime data: a "near-window" site, where the ^{1}DCA* molecule resides not entirely within one supercage, but rather can interact with the contents of two adjoining supercages. This site would become less populated as the loading level is increased because space considerations would force the ^{1}DCA* molecule more into the confines of one supercage.

3.3.3.3 Location of Excimers in Supercages

Although the decay lifetimes of excimers showed multiexponential decays, the comparisons of lifetime and lifetime percentage data had less distinct trends than those observed for the monomer. The time window of the nanosecond emission data was

insufficient to capture the full decay of the excimer emission and thus the variability in the long lifetime data can be in part attributed to this. In general, the lack of clear trends in the lifetime and percentage data indicate that the excimer, once formed, is much less sensitive to the effects of loading level and the counterbalancing cation than the monomer. Insensitivity to the loading level indicates that the excimers do not interact with other monomers or excimers outside of the supercage and thus are likely fully contained within one supercage. Geometric constraints dictate that the face-to-face geometry demanded to form an excimer[14] would make the excimer too wide to be located halfway through the 7.4 Å windows, and confirms that excimers must be fully contained within a supercage.

3.3.3.4 Excimer Band Movement

Tables 3.8 and 3.16 provide evidence that the excimer band has a variable energy that is dependent on both the counterbalancing cation and the loading level of the DCA within the zeolite supercages. It is difficult to correlate the emission energy to the stability of the excimer, as a decrease in emission energy is due to a decreased energy difference between the excimer potential energy surface and the ground state dissociative state surface. This movement of the two surfaces closer together could either be due to the lowering of the upper energy surface (excimer), or an increase in the energy of the dissociative ground state. The former is an increase in the stability of the excimer, while a destabilizing force causing the excimers to be too close together could produce the latter. Due to the inability of the present measurements to distinguish between the two, a discussion of emission frequency trends is pursued instead.

The emission frequency of excimers, unlike that of exciplexes, is generally not very solvent dependent due to the smaller amount of charge-transfer interactions between the monomer units of the excimer.[14] Thus, the variable emission frequency of the DCA excimer in different Y zeolites suggests a substantial charge-transfer character in the DCA excimer which is likely induced by the highly ionizing nature of the Y zeolite interior. The presence of strong electrostatic fields produced by the cations polarizes the DCA monomers, and it has been postulated that dimers of aromatic species could be

induced by polarization.[105] While these excimers are measurably dynamic, the strongly polar nature of the zeolite interior[116,135] could induce charge-transfer character in the DCA excimer. The smaller the cation, the stronger the electric fields and hence the stronger the charge-transfer character introduced into the excimer. For a series of exciplexes in the same solvent, the excimer emission frequency is proportional to either the ionization potential of the donor (IP_D) or the electron affinity of the acceptor (EA_A) provided that the other is held constant. In this case, it is the ionization potential of the solvent, *i.e.* the Y zeolite, that is changing. Ionizing ability is represented by the Y scale, and Y scale values for cation exchanged Y zeolites have been determined experimentally.[119] A plot of the DCA excimer emission frequency versus the Y scale gives a roughly linear correlation, Figure 3.34, suggesting that indeed the charge-transfer character of the DCA excimer is induced by the ionizing nature of the zeolite host.

A second variable, which may affect the movement of the excimer emission frequency, is space considerations. In the KY loading level experiment, at high loading levels, the central frequency of the excimer band is comparable to the more ionizing zeolites, LiY and NaY, while as the loading level decreases, the trend towards higher excimer band energies is comparable to the charge balancing cations moving down the periodic table, despite the fact that the KY zeolite host is held constant. A possible explanation for this observation is the increase in density of excimers throughout the zeolite particle. From the size of the DCA molecule, it is inferred that a maximum of two molecules can fit into one supercage, and thus, there is a maximum possibility of one excimer per supercage. The similarity in trend to the periodic trend suggests that as the loading level increases, the increase in excimer density forces the excimers more into the interior of the supercages, to decrease interactions between excimers in adjacent cavities. These excimers are thus closer to the K^+ cations and feel greater effective ionization ability, which from the argument above, would change the charge-transfer character of the excimer and shift the excimer emission energy accordingly.

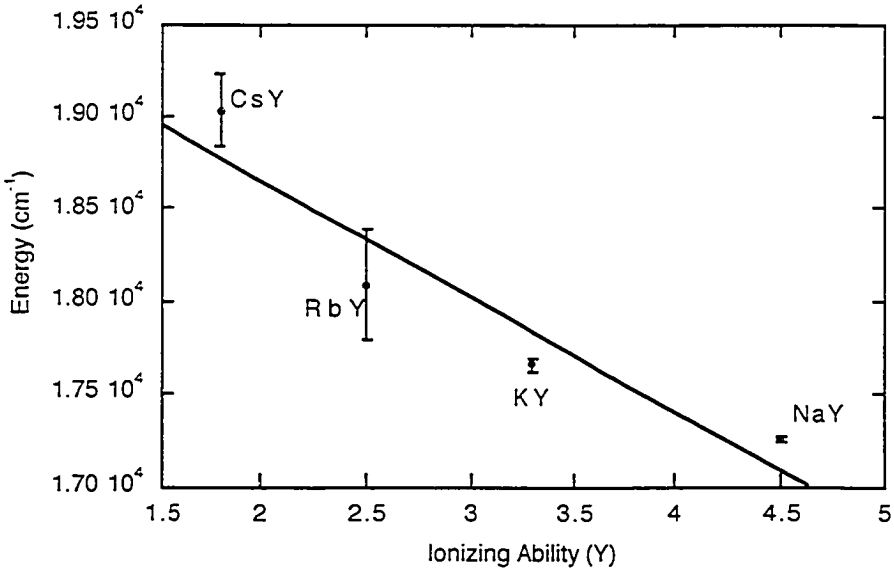

Figure 3.34 DCA excimer emission frequency compared to the ionizing ability (Y scale) of the zeolite host. LiY has been omitted because its Y value has only been estimated. Values for ionizing ability were taken from reference 119.

3.4 Observation and Modelling of the Ultrafast Movement of Excited State 9,10-Dicyanoanthracene in Y Zeolites

3.4.1 Introduction

Intercavity migration rates of guest molecules and counterbalancing cations through the rigid zeolite framework has been the subject of much investigation.[54,87,88,105,136-139] The interaction of the zeolite interior, acting as a solid solvent, with the guest molecules incorporated within, produces very different rates of movement from those observed in conventional solutions. As a result, understanding the zeolite-guest interactions and their influence on guest mobility is of great importance in being able to design systems that have the desired properties of intercavity movement. This is of vital significance as zeolites are widely used in industrial applications as catalysts, molecular sieves, chemical absorbants, and ion exchange materials.[65] All of these applications require the movement of materials through the porous framework of zeolites. This

section describes a unique guest-zeolite system that exhibits the first observation of the intercavity movement of guest molecules on the ultrafast time scale.

The open nature of the rigid framework of Y zeolites is comprised of nanosized supercages which can incorporate guest molecules. Supercages are connected to each other tetrahedrally *via* 7.4 Å pores. Guest molecules can be incorporated by either "ship in a bottle" synthesis, producing guests that are too large to move between supercages through the pores, or by diffusion into the supercages through the pores.[67] As long as the guest molecule is small enough to fit through a pore, intercavity movement of the guest species is possible.

Polyaromatic hydrocarbons and their derivatives are molecules that can be readily incorporated into faujasite zeolites, and hence they have been extensively studied in zeolites. The intercavity mobility of benzene[87,88,137] in X and Y zeolites has been investigated using ^{2}H NMR spectroscopy and modeling, and has revealed that benzene diffusion is slow compared to solution due to the adsorption of benzene molecules at specific framework and cation sites. Larger molecules, such as pyrene and anthracene, are known to aggregate in the outer cavities of the zeolite particles when incorporated. Upon aging over hours and days, pyrene redistributes throughout the zeolite particles to effect a homogeneous loading level.[54] Anthracene redistributes randomly when subjected to high temperatures (570 K),[111] but very little over two months at room temperature.[112] A more dramatic demonstration of guest molecule mobility is the motion of aromatic molecules incorporated within one zeolite particle to another zeolite particle through contact interactions and through-space migration at elevated temperatures.[112] These motions were observable over time periods of up to one hour. All of these examples involve the motion of guest molecules through the zeolite framework while in their ground electronic states.

There have been many studies in the literature of the diffusion of singlet and triplet excited state molecules. Two very popular techniques are the measurement of fluorescence quenching[92,140,141] and triplet-triplet quenching rates.[56,116,138] Time scales of dynamic quenching in these studies range from the ultrafast[92] (< 0.3 ns) to scales of microseconds and longer.[138] One of the factors that influences the rate of movement are coadsorbed solvents, which can affect the strength of adsorption between aromatic

molecules and the cations or the framework structure.[56,116] Small amounts of solvent can greatly increase the rate of diffusion, while large amounts of coadsorbed solvents serve to fill up the cavity spaces and inhibit guest molecule movement. Analyses of these systems frequently use random walk models[2] to fit the decay curves of time-resolved fluorescence emission or triplet absorption data. The random walk model has been successfully applied not only to the movement of excited state molecules through the zeolite framework, but also to radicals.[139]

This study was conducted simultaneously with the research presented in section 3.2 but has been presented separately for clarity. Here, both rise time and decay kinetics are used to explore the intercavity hopping of 9,10-dicyanoanthracene (DCA) molecules in cation-exchanged Y zeolites on the low picosecond time scale. Specifically, the rate of formation of excimer is explored as a function of counterbalancing cation and loading level. A dynamic hopping model based upon distribution probabilities is proposed to describe the dependence of excimer formation time upon loading levels. There is no literature precedent for dynamic excimer formation in zeolites involving intercavity movement, which is generally considered too slow to be possible on an picosecond time scale. The results of this study suggest that ultrafast intercavity movement is necessary to account for the photophysical behaviour of DCA in Y zeolites.

3.4.2 Results

3.4.2.1 Highest Loading Level: <S> ~ 0.05

The actual loading level achieved for these samples was <S> = 0.043, regardless of the zeolite used. In all the zeolites at this high loading level, the DCA excimer emission collected at 600 nm exhibits an ultrafast rise time which is resolvable on our streak camera, Figure 3.35. Rise times vary as a function of cation, and range from 8.0 ps to 9.7 ps, as listed in Table 3.19. There is a small trend as one moves down the periodic table that the rise times become progressively slower. Figure 3.36 shows a typical trace and convoluted fit with residuals for the rise time of DCA excimer emission at 600 nm in

NaY. The error in rise times due to sample reproducibility is estimated to be ±1 ps by comparing data from repeated trials (see Section 3.2.2.2).

In contrast to the resolvable rise times collected at 600 nm, the rise times collected 450 nm are all within the resolution of the instrument response function and rise times could not be extracted. As well, the behaviour of the DCA monomer emission showed pronounced differences between the LiY and NaY samples and the heavier cation zeolites. Both the LiY and NaY samples showed an instantaneous rise time and almost complete decay over the short 300 ps time window, while the KY, RbY, and CsY samples show a slower rise time and very small amounts of decay over the same time period (Figure 3.35). The stark difference between the results obtained in zeolites with the small cations, Li^+ and Na^+, and zeolites with the larger cations, K^+, Rb^+ and Cs^+, suggests that at this loading level, the DCA excited state is less stable in the low molar mass zeolites, while it is much more stabilized in the remaining zeolites.

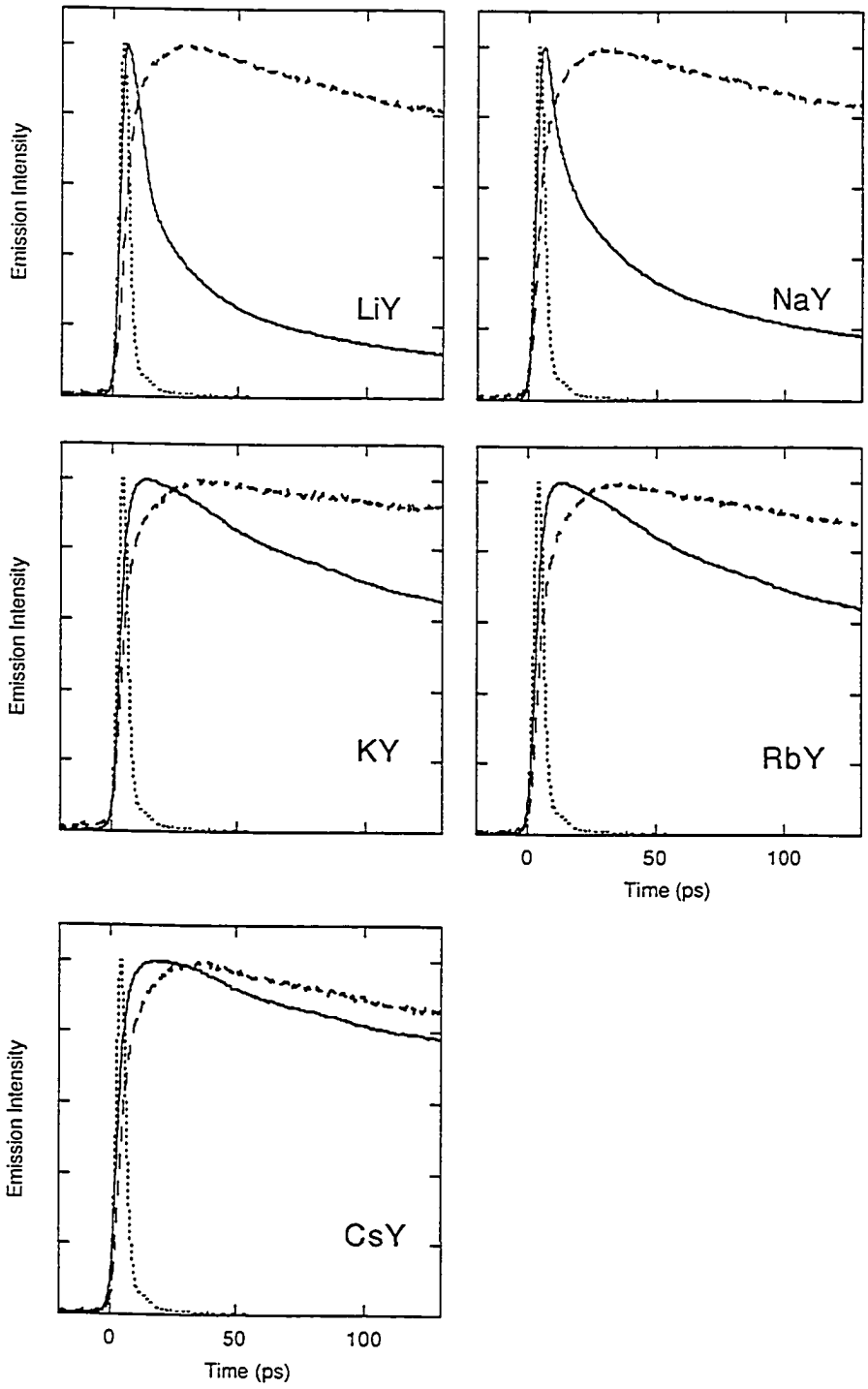

Figure 3.35 Ultrafast traces of DCA monomer emission at 450 nm (—) and excimer emission at 600 nm (— —), in cation-exchanged Y zeolites, <S> = 0.043. Each plot includes the IRF (---). The excitation wavelength is 388 nm.

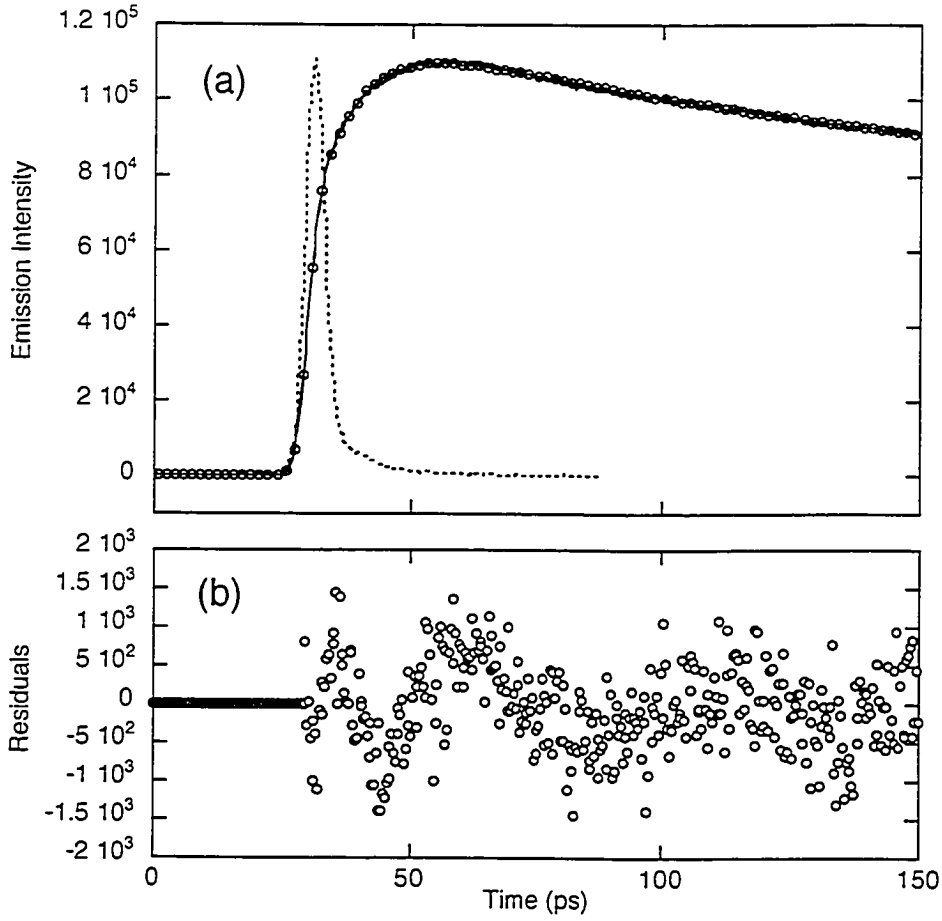

Figure 3.36 Excimer rise time extraction from collected time-resolved fluorescence data using the Levenberg-Marquardt algorithm with convolution. (a) Rise-time trace for DCA excimer emission at 600 nm (○) (every 5th data point plotted for clarity) obtained upon 388 nm femtosecond laser irradiation of DCA incorporated in NaY, <S> = 0.043. Figure shows best fit line (—) and the IRF (---). (b) Residuals of best fit line from (a).

Table 3.19 Rise times of DCA excimer emission as a function of loading level and zeolite.

Zeolite	<S> ~ 0.05		<S> ~ 0.005		<S> ~ 0.002	
	Measured <S>	Rise Time (ps)[a]	Measured <S>	Rise Time (ps)[a]	Measured <S>	Rise Time (ps)[a]
LiY	0.043	8.0	5.3×10^{-3}	9.1	2.2×10^{-3}	12.2
NaY	0.043	8.6	5.3×10^{-3}	10.1	2.2×10^{-3}	12.3
KY	0.043	9.6	4.8×10^{-3}	10.0	2.2×10^{-3}	14.1
RbY	0.043	9.5	3.9×10^{-3}	11.7	1.7×10^{-3}	13.3
CsY	0.043	9.7	2.4×10^{-3}	14.5	1.2×10^{-3}	15.4

[a] The error in rise times is estimated to be 1 ps by comparison between sample replicates and fit replicates.

Table 3.20 Rise times of DCA monomer emission as a function of loading level and zeolite.

Zeolite	<S> ~ 0.05		<S> ~ 0.005		<S> ~ 0.002	
	Measured <S>	Rise Time (ps)[a]	Measured <S>	Rise Time (ps)[a]	Measured <S>	Rise Time (ps)[a]
LiY	0.043	fast	5.3×10^{-3}	fast	2.2×10^{-3}	6.3
NaY	0.043	fast	5.3×10^{-3}	fast	2.2×10^{-3}	6.4
KY	0.043	fast	4.8×10^{-3}	5.9	2.2×10^{-3}	8.7
RbY	0.043	fast	3.9×10^{-3}	5.8	1.7×10^{-3}	8.0
CsY	0.043	fast	2.4×10^{-3}	8.5	1.2×10^{-3}	10.0

[a] The error in rise times is estimated to be 1 ps by comparison between sample replicates and fit replicates.

3.4.2.2 Lower Loading Levels: <S> ~ 0.005, <S> ~ 0.002

The ultrafast time-resolved data at lower loading levels showed dramatic differences in rise times compared to those described earlier for the <S> ~ 0.05 loading level. The rise times for the monomer emission become slower and resolvable as the loading level decreases (Table 3.20), but are still distinct from those of the excimer emission. In general, the rise times for the excimer emission increase as a function of decreasing loading level, Table 3.19. For the <S> ~ 0.005 loading levels, the excimer emission rise times range from 9.1 ps (LiY) to 14.5 ps (CsY), while at the lowest loading

level of <S> ~ 0.002, the rise times range from 12.2 (LiY) to 15.4 ps (CsY). Table 3.19 also shows that the rise time differences across zeolites at the lower loading levels are larger compared to the high loading level of <S> ~ 0.05. Part of this difference must be attributed to the larger variation in loading levels within these sets compared to the <S> ~ 0.05. However, this cannot account for all the differences, as comparison of different samples with similar loading levels do not exhibit the same rise times. For example, the comparison of NaY at $<S> = 2.2 \times 10^{-3}$ with CsY at $<S> = 2.4 \times 10^{-3}$ shows a rise time of 12.3 ps for the former and 14.5 ps for the latter, a difference that is significant compared to experimental uncertainty. A second factor affects the excimer emission rise time variability, and this factor is the size of the counter-ion. Just as in the higher loading level case of <S> ~ 0.05 described previously, as the cation size increases, the excimer emission rise times are observed to increase as well. For example, for LiY, the rise times change from 8.0 to 9.1 to 12.2 ps as the loading level varies from <S> ~ 0.05 to 0.005 to 0.002, while these same loading levels in CsY have longer rise times of 9.7 to 14.5 to 15.4 ps. This illustrates that zeolite cations play an important role in directing the excimer emission rise times. The increases in measured rise times are clearly due both to decreases in loading level and increases in cation size. The kinetic profiles used to obtain these rise times are plotted in Figures 3.38 and 3.39.

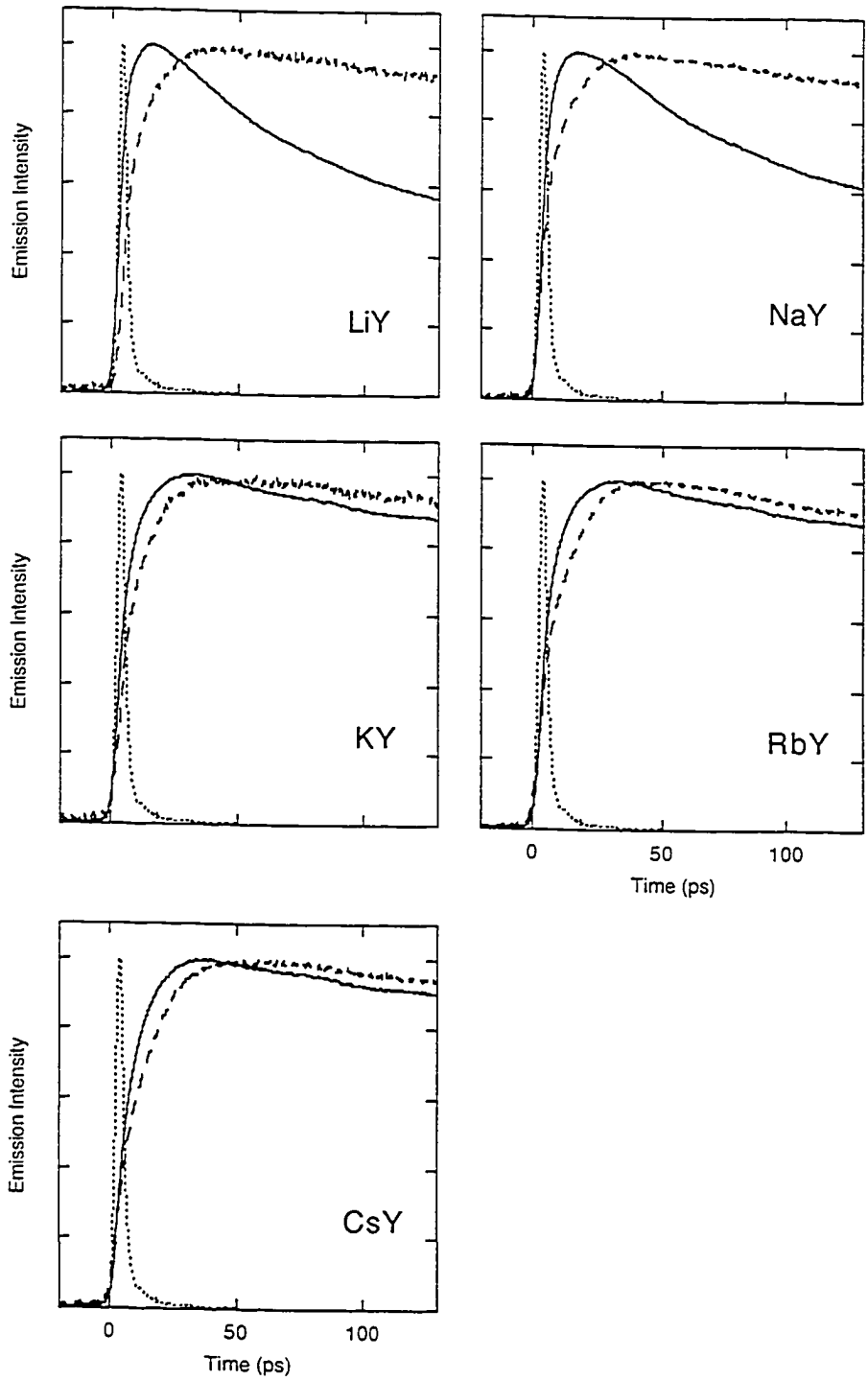

Figure 3.37 Ultrafast traces of DCA monomer emission at 450 nm (—) and excimer emission at 600 nm (— —), in cation-exchanged Y zeolites, <S> ~ 0.005. Each plot includes the IRF (---). The excitation wavelength is 388 nm.

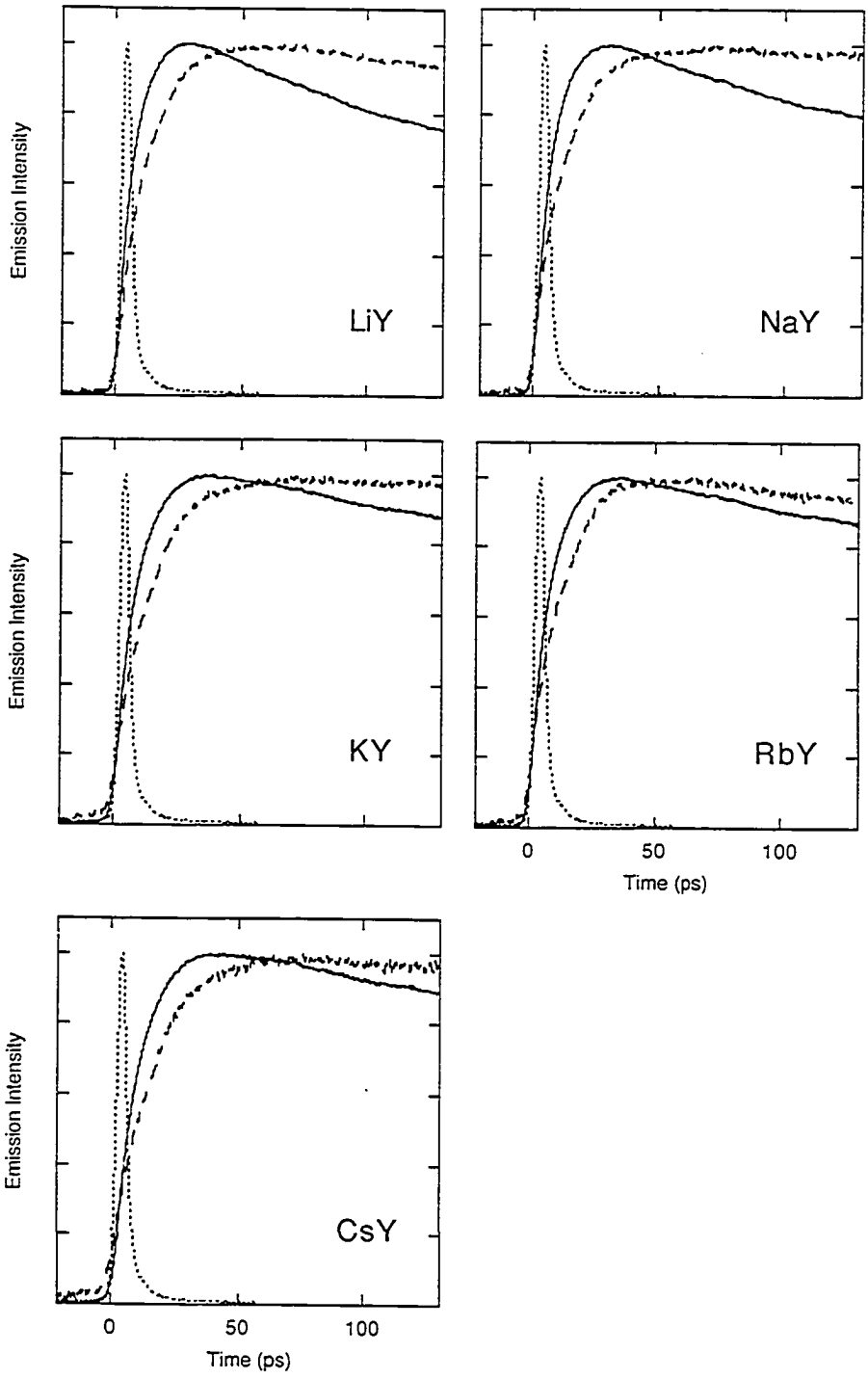

Figure 3.38 Ultrafast traces of DCA monomer emission at 450 nm (—) and excimer emission at 600 nm (— —), in cation-exchanged Y zeolites, <S> ~ 0.002. Each plot includes the IRF (---). The excitation wavelength is 388 nm.

3.4.2.3 Loading Level Experiment, DCA in KY

In order to further study the excimer emission rise times as a function of guest molecule concentration, a loading level experiment was carried out while keeping the zeolite cation constant. KY was chosen because of its ability to show the existence of both the monomeric and excimeric species in the steady state spectra, and for the large difference in excimer emission rise times from the highest to lowest loading levels. All five samples were produced under identical conditions, varying only the amount of DCA stock solution added. Loading levels achieved were <S> = 0.042, 0.013, 5.0×10^{-3}, 2.9×10^{-3}, and 2.0×10^{-3}.

As expected, the rise time dependence on loading level was manifested in the results of the time-resolved ultrafast data. The excimer emission rise times at 600 nm varied from 9.0 ps to 15.8 ps as the loading levels achieved varied from <S> = 0.042 to <S> = 2.0×10^{-3}. This change in rise times is clearly observed in Figure 3.39(b), and the rise times are recorded in Table 3.21. Figure 3.40 also plots the rise times as a function of loading level, on a reverse loading level axis. The reverse axis was chosen to facilitate comparisons to model calculations in the discussion. The plot of rise times against loading level demonstrates a "plateau" effect at high loading levels. A smaller loading level dependence was manifested in the delayed fluorescence data for the DCA monomer, although the trend is not as distinct as for the excimer emission rise times. These numbers are also recorded in Table 3.21 and the kinetic traces are plotted in Figure 3.39(a).

Table 3.21 Rise times of monomer and excimer emission data as a function of loading level in zeolite KY.

Loading Level <S>	Monomer Rise Time[a] (ps)	Excimer Rise Time[a] (ps)
0.042	fast	9.0
0.013	7.6	9.7
5.0×10^{-3}	7.3	10.6
2.9×10^{-3}	7.9	13.3
2.0×10^{-3}	10.8	15.8

[a] The error in rise times is estimated to be 1 ps by comparison between sample replicates and fit replicates.

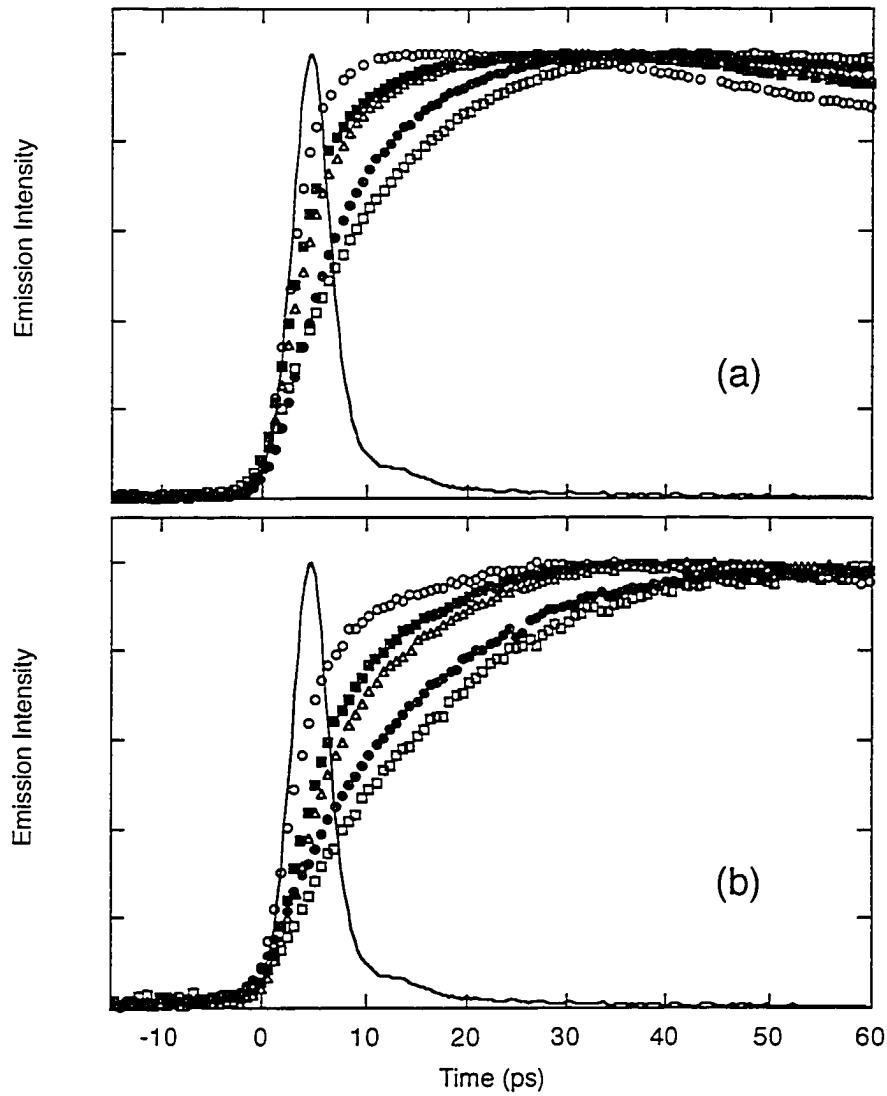

Figure 3.39 Monomer (450 nm) (a) and excimer (600 nm) (b) emission kinetic profiles of DCA included in zeolite KY as a function of loading level. Loading levels: <S> = 0.042 (○), <S> = 0.013 (■), <S> = 5.0×10^{-3} (△), <S> = 2.9×10^{-3} (●), and <S> = 2.0×10^{-3} (□). Each plot includes the IRF (—). Every second data point is plotted for clarity. The excitation wavelength is 388 nm.

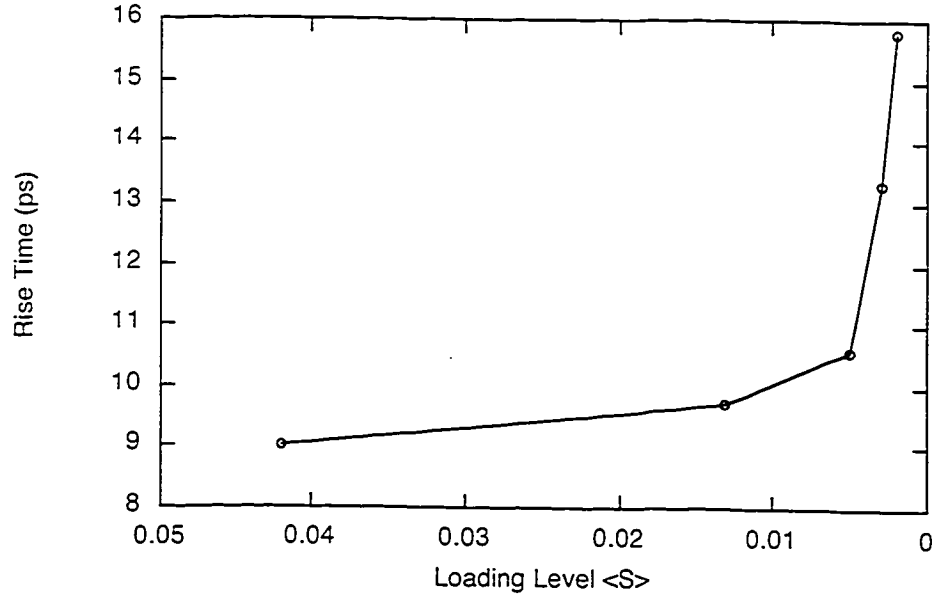

Figure 3.40 Rise times of DCA excimer emission at 600 nm as a function of loading level <S>. The loading level scale is plotted in reverse, *i.e.* decreasing loading levels are towards the right.

3.4.2.4 Aging Experiments

Thus far, it has been observed that the growth of excimer emission has been a loading level dependent phenomenon, where the rise time increases as the loading level decreases. From the steady state fluorescence spectra, it is observed that DCA molecules incorporate non-homogeneously in Y zeolites and form aggregates (excimers) even at loading levels as low as <S> ~ 0.005. Thus, knowing that some other non-homogeneously loading zeolite / guest systems such as NaY / pyrene show redistribution of guest molecules upon aging[54] to form homogeneously loaded zeolites, an aging study of DCA in NaY and RbY was undertaken. Non-homogeneously loaded zeolites show a great deal of aggregation, and the local loading level in the doubly occupied cavities is much higher than the calculated loading level, which assumes homogeneous loading. As the sample ages and the DCA redistributes throughout the zeolite particle, the local loading level would change and approach the calculated loading level. Thus as the sample ages, the local loading level would be expected to become lower and the excimer emission rise times which vary as a function of loading level should reflect this

difference. It was hypothesized that over a time period of several days to a month, the DCA excimer emission rise times would become slower in an aging sample.

These samples were designed such that the original loading level was at the bend of the curve shown in Figure 3.40. In the NaY case, the loading level was <S> = 0.012, while the RbY case had a calculated loading level of <S> = 0.010. Both samples were flame-sealed under vacuum to ensure that the environment about the zeolite would not change over the duration of the experiment. When not being used, the samples were stored at room temperature in ambient light.

Both samples were followed closely by steady state fluorescence measurements and were expected to show a significant change from predominantly excimer emission to only monomer emission, a change that is very dramatic upon the aging of pyrene in NaY.[54] However, for DCA / NaY, only a small increase in the intensity was noted in the monomer region while the excimer emission intensity was almost unchanged, Figure 3.41. It is also important to note that there is an isosbestic point at 590 nm, indicating that one species is being converted into another species. In this case, the isosbestic point supports the following equation:

$$M_2(2DCA) \rightarrow 2M(DCA) \qquad (3.1)$$

For every molecule of DCA from a doubly occupied cavity (M_2) moving into an empty supercage, two singly occupied supercages of DCA (M) are formed. This phenomenon can be detected by fluorescence, assuming that the doubly occupied cavity will produce an excimer upon excitation while a singly occupied cavity will produce a monomer upon excitation. Combining this doubling of monomer for every doubly occupied supercage that dissociates with the quantum yield / extinction coefficient of fluorescence of monomer being much larger than that of excimer, the plot of increasing monomer fluorescence with little degradation of the excimer emission is very reasonable.

However, the expected dramatic decrease in excimer emission and increase in monomer emission to reflect a change from a mainly aggregated distribution to a homogeneous disctribution was not observed, and hence it can be concluded that the DCA did not redistribute to any significant amount over 30 days in the NaY zeolite. The DCA / RbY sample showed no variation in the shape of fluorescence emission spectra at

all over 30 days, Figure 3.42, but this is not unexpected as the steady state spectra did not vary as a function of loading level (Figures 3.19, 3.24, and 3.27).

Both samples showed no variation in rise times that were outside the error margin of the experiment. The DCA / NaY sample had an excimer emission rise time of 8.5 ps that remained unchanged over the entire 30 day period, and the DCA / RbY sample had an excimer emission rise time of 10.5 ps over the same time period. The lack of variation in excimer rise time clearly illustrates the complete independence of excimer emission rise times from sample aging. The DCA molecules do not appear to redistribute over 30 days.

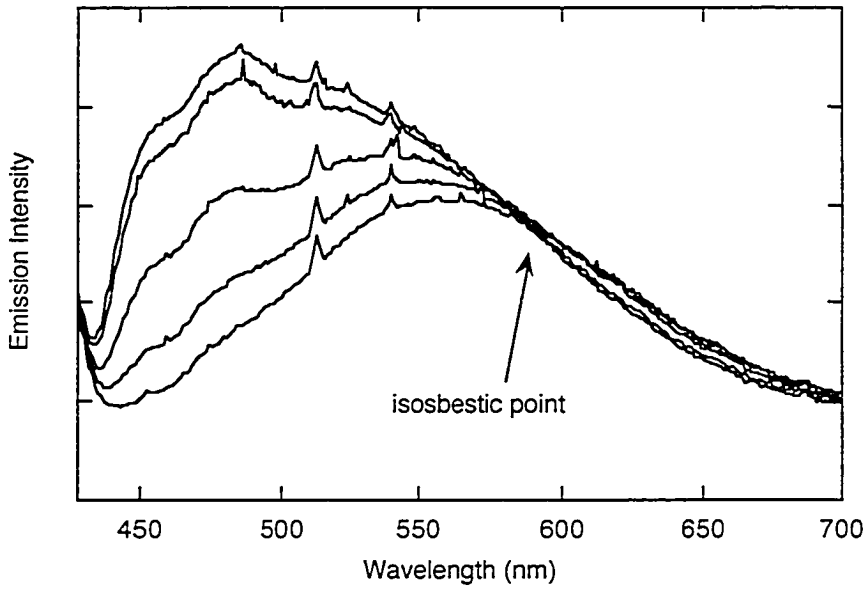

Figure 3.41 Steady state fluorescence spectra of DCA in NaY (<S> = 0.012) over the first 20 days of a 30 day aging experiment. From bottom to top at 500 nm, Day 1, 2, 5, 14, 20. Note the presence of an isosbestic point at 590 nm. The excitation wavelength is 418 nm.

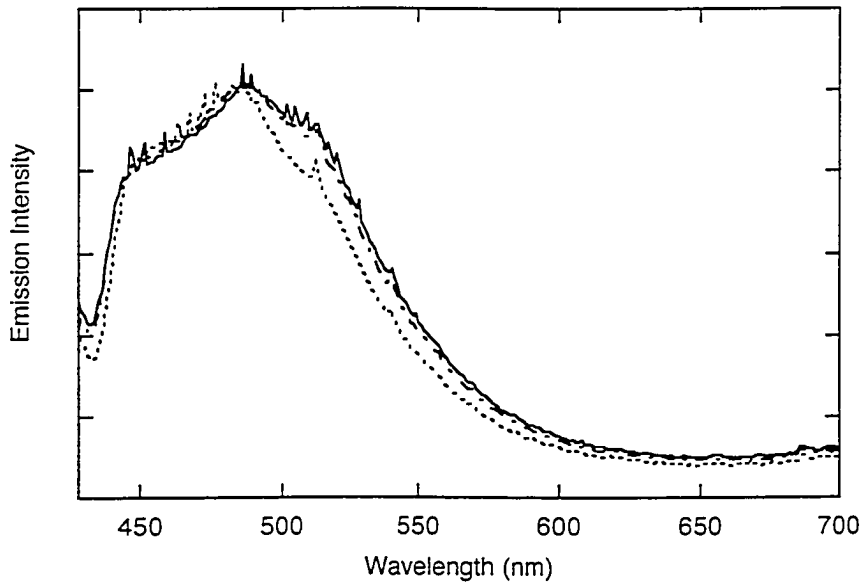

Figure 3.42 Steady state fluorescence spectra of DCA in RbY (<S> = 0.010) over the first 22 days of a 30 day aging experiment: Day 1 (---), Day 15 (—) and Day 22 (–·–).

3.4.3 Discussion

As discussed in Section 3.3.3, the DCA / Y zeolite system is excited into the ^{1}DCA* state upon absorption of a photon and can deactivate by a number of pathways. Two pathways are emissive, namely monomer fluorescence from ^{1}DCA*, and excimer emission, produced by the coupling of ^{1}DCA* with a ground state DCA molecule to form an excimer, and its subsequent relaxation by emission of a photon. Monomers are formed by excitation of a single DCA molecule into its singlet state. However, excimers require the presence of two molecules in close proximity in order to form.

The DCA / Y zeolite system facilitates the formation of excimers even at low loading levels because DCA molecules are inhomogeneously distributed within the zeolite matrix. Because the guest molecules are loaded from the outside of each zeolite particle to the inside *via* supercage hopping, high loading levels would be expected near the surface and progressively lower loading levels as one approaches the center.

In contrast to the predominant excimer emission of DCA at high loading levels and in the lighter cation-exchanged zeolites, the steady-state spectra show mainly

monomer emission at lower loading levels and in zeolites with heavier cations. In these zeolites, the dominance of monomer could be due to a more homogeneous loading, or a preference of singly occupied cavities over doubly occupied cavities. Doubly occupied cages may be more difficult to form due to the reduced amount of free space in the zeolite supercage when large cations are present. This would result in singly occupied cavities but a non-homogeneous distribution would have a high density of these singly occupied cavities at the outer edge of the particle. Due to the continued observation of excimer *via* excitation spectra and streak camera measurements, it is more likely that the loading is still non-homogeneous but that aggregates are disfavoured.

3.4.3.1 Observable Rise Times of Monomer Fluorescence

Monomer fluorescence is a phenomenon that should not have a rise time, as the singlet excited state is formed directly upon absorption of a photon. Even more puzzling is the dependence of the rise times upon loading levels and cation (Tables 3.20 and 3.21). The observed monomer rise time is not an artifact inherent in the instrumentation. This is most clearly illustrated by results from experiments with pyrene described above in Section 3.1, and from other experiments with substrates not discussed here, that show that monomer emission, as expected, has an unresolvable rise time.

One possible source of time-resolved monomer growth is a time-resolved shift in the fluorescence maximum of the DCA monomer. It is possible that the ground state DCA is located in environments different from those preferred by excited state DCA. Thus, ^{1}DCA*, when initially generated, may be located at a site with an environment that is less stabilizing than the preferred location of excited DCA, but then rapidly migrates to a site that better "solvates" the excited DCA. The emission maximum for the initially generated ^{1}DCA* would likely reflect the lack of environmental stabilization; the emission from ^{1}DCA* immediately after the laser pulse might therefore be at higher energies (lower wavelengths) then the stabilized DCA*. Under these conditions, monitoring fluorescence at the maximum wavelength for stabilized DCA* could show a growth.

Such time-resolved Stokes shifts have been observed in organized media, including zeolites.[142,143] In particular, Das and co-workers have shown[142] that the dye, coumarin 480, initially has a fluorescence maximum at 470 nm which shifts over time to 515 nm as the excited dye migrates to a more "solvated" environment with the zeolite cavity. When fluorescence emission is monitored at 515 nm, emission growth is observed due to the time-resolved Stokes shift.

A reasonable explanation for the effect of cation and loading level on the time-resolved emission can be offered on the basis of the assumption that the time-resolved monomer emission is caused by migration of ^{1}DCA* from its original location to a more "solvated" location. At low loading levels, a greater proportion of ground state DCA molecules may have better access to preferred sites within cavities, while at high loading levels, ground state DCA molecules may be distributed less homogeneously and forced to occupy higher energy sites. Thus, at low loading levels, the majority of initially formed ^{1}DCA* molecules would be generated in sites that accommodate the ground-state DCA, but not ^{1}DCA*. These ^{1}DCA* molecules would then migrate to their preferred sites that provide a more solvated environment. At high loading levels, a significant fraction of the ^{1}DCA* molecules are created in sites that are more suitable for ^{1}DCA*; the magnitude of the Stokes shift will be diminished, and the dynamics of the Stokes shift will be more rapid. These arguments are consistent with the effect of loading level on the lifetime of the monomer emission discussed above. As discussed in Section 3.3.3.2, monomer emission at low loading levels is generally slower than at high loading levels. It was argued that at low loading levels, both ground state and excited state DCA are more homogeneously distributed in stabilized sites. If these sites are different for the two states, and if the emission from the ^{1}DCA* molecule generated in a ground state site is different from the emission of ^{1}DCA* molecule in stabilized sites, one would observe a substantial time-resolved shift. At high loading levels, ^{1}DCA* exists in a range of sites that lead to a range of emission lifetimes. This suggests an inhomogeneous distribution of both the ground-state and the excited state, which would produce a less distinctive shift in emission wavelength.

Similarly, large cations like Cs^+ would likely hinder the movement of $^1DCA^*$ molecules from their initial site to their more solvated site. Thus, the rise times associated with the Stokes shift should be longer in Cs^+ as compared to Na^+ or Li^+.

A test for the presence of a time-resolved Stokes shift for DCA in the zeolites is to monitor emission decay or growth at wavelengths less than 450 nm. Since the focus in this section was on time-resolved excimer growth, such testing for time-resolved Stokes shift for monomer emission was not carried out. Thus, while a time-resolved Stokes shift does provide an adequate explanation for the growth of monomer emission at 450 nm, more experiments must be carried out in the future to explore this postulate.

3.4.3.2 Excimer Formation: Loading Level and Cation Dependence

In principle, a time-resolved shift in excimer emission might also be invoked to explain the growth in excimer emission at 600 nm. However, such a process is more difficult to envision for an excimer as compared to a monomer due to the bimolecular nature of an excimer. In particular, given the relatively weak interaction that holds an excimer together, it is improbable that an excimer formed at one site within the constrained space of a zeolite could migrate to another site without an accompanying rearrangement or reorientation of the two DCA molecules with respect to each other. Thus, at the very least, the time resolved excimer formation should involve some kind of reorientation of molecules similar to that described earlier for pyrene.

In addition, unlike pyrene excimer formation discussed previously which only arises from doubly occupied cavities, any discussion of time-resolved DCA excimer growth must also consider the possibility of intercavity migration of the ground-state DCA to another cavity containing $^1DCA^*$, or $^1DCA^*$ to a cavity containing ground-state DCA. Thus, the following discussion concerning the effect of loading level and cation is based on the reasonable assumption that time-resolved excimer growth involves either intracavity reorientation of the two participating DCA molecules with respect to each other or intercavity migration of one DCA (or $^1DCA^*$) molecule from one cavity to another cavity containing a $^1DCA^*$ (or DCA) molecule, or that both processes are present.

The data presented in Table 3.21 show that the rise times are loading level dependent. In the case of pyrene / zeolite systems, where it is known that excimers arise only from doubly occupied cavities, the rise times of excimer emission are loading level independent.[121] This is consistent with the notion that the zeolite cavity imposes a maximum distance that the molecules need to move or reorient. However, in this case where a decrease in loading level results in a increase in the rise time of the emission, a basic concentration effect is observed. As the concentration of DCA molecules becomes lower, the average distance between molecules becomes larger and the longer it takes for the molecules to come together to form an excimer. In the context of a zeolite host material where the monomers are in supercages, an explanation for an observed loading level dependence must include the possibility that monomers can move from one supercage to another in order to form the excimer.

Table 3.19 shows that the increase in cation size results in increases in measured rise times. As was previously discussed, the observation of predominant monomer fluorescence in the steady-state spectra of heavier cations suggests that aggregates are harder to form because of the lesser void space available in a supercage when large cations are present. Thus, the distribution model in these zeolites near the particle surface is a high density of singly occupied supercages with some doubly occupied supercages. The larger the counterbalancing cation, the higher the number of singly occupied supercages versus doubly occupied supercages. In order for an excimer to form, two monomers must come together, either from the same supercage or from nearby supercages. Assuming that it takes longer for two monomers to come together if intercavity movement is necessary than if the two monomers are already in the same cage, it is obvious that distributions that favour singly occupied cavities should have slower rise times. Thus, the slower rise times observed as a function of increasing cation size are a direct result of decreasing void spaces available to the guest DCA molecules in the zeolite supercages.

3.4.3.3 Dynamic Excimer Model

In order to better understand the intercavity movement of DCA molecules within zeolites, a model of DCA excimer formation within Y zeolites has been developed. The Y zeolite is modeled as a series of tetrahedrally linked cavities, and each cavity is allowed to contain zero, one or two molecules of DCA. Excimers are allowed to form between monomers within the same cavity, or monomers in singly occupied cavities that are close together, where one or more jumps between supercages are required. The minimum amount of time required for excimer formation is the intracavity rearrangement time, *i.e.* the amount of time required to form an excimer if both monomers reside in the same cavity. For monomers that reside in singly occupied cavities, the time for excimer formation is related to the number of jumps necessary for the two monomers to form a doubly occupied cavity, where the larger the number of jumps, the longer the excimer formation time. Every distribution of DCA molecules throughout a zeolite matrix will therefore have excimer formation from doubly occupied cavities as well as singly occupied cavities that require multiple numbers of jumps. An average excimer formation time can be calculated by the weighted average of these individual formation times, where the weights are calculated by the relative probabilities of each excimer formation pathway. Thus, it is possible to calculate the dependence of the average excimer emission rise times on loading level. This model also allows for the examination of the influence of different maximum allowed jumps and rise time models.

3.4.3.4 Structural Model

This structural model is based upon the shell model developed by Sykora et al.[113] for use in describing through-space quenching of excited state $Ru(bpy)_3^{2+}$ complexes entrapped in Y zeolites, and has been extended to measuring electron and hole migration distances in Y zeolites.[80] The application of this distribution model can be used to describe the distribution of DCA molecules in Y zeolite supercages; however, it must be modified to consider the number of supercage "jumps" rather than a through-space distance model.

Consider first a model where one central supercage **A** is connected tetrahedrally to four adjacent supercages, denoted **B**. In order for a DCA molecule in the **B** supercage to form an excimer with the DCA molecule in supercage **A**, the molecule must jump once between supercages. Each supercage in shell **B** is surrounded by 3 more supercages, producing a total of 12 supercages in set **C**. A molecule in shell **C** must jump twice between supercages to form an excimer with a molecule in supercage **A**. Likewise, there are 24 supercages in shell **D**, which are three jumps away from the central supercage, and 42 supercages in shell **E**, which require four jumps to reach the center. These shells are defined differently from those given in the Sykora model where shells *d* through *h* have lower numbers of supercages. Shells in the Sykora model are defined by distance from the central supercage; past shell *c* not all adjacent supercages are equidistant from the center. However, in this model, it is only the number of jumps from the central supercage that is of interest rather than variations within the shells of supercage distance from the center. The structural model is summarized in Table 3.22.

Table 3.22 Structural model of Y zeolite.

Shell	Jumps to A	No. Cages/Shell
A	0	1
B	1	4
C	2	12
D	3	24
E	4	42

3.4.3.5 Probabilities of Supercage and Shell Occupancy

The probabilities of supercage occupancy can be calculated assuming homogeneous distributions of molecules throughout the supercage network. Probabilities are calculated for unoccupied, singly occupied, and doubly occupied supercages: P(0), P(1) and P(2). These probabilities are listed in Table 3.23, and a discussion of the probability calculation is found in the Appendix.

Table 3.23 Calculated probabilities of supercage occupancy as a function of loading level.

Loading Level <S>	P(0)	P(1)	P(2)
1	0.3332	0.3336	0.3332
0.5	0.6161	0.2678	0.1161
0.2	0.8262	0.1476	2.624×10^{-2}
0.1	0.9078	8.439×10^{-2}	7.808×10^{-3}
0.05	0.9522	4.562×10^{-2}	2.176×10^{-3}
0.013	0.9868	1.303×10^{-2}	1.698×10^{-4}
5.0×10^{-3}	0.9950	4.976×10^{-2}	2.441×10^{-5}
2.9×10^{-3}	0.9972	2.792×10^{-3}	8.014×10^{-6}
2.0×10^{-3}	0.9980	1.996×10^{-3}	3.932×10^{-6}

The objective of calculating shell occupancy is to produce an estimate of the probability of excimer formation. In order for an excimer to be formed, it is necessary that two molecules are found in close proximity to each other. If both molecules occupy the same supercage, then they will form excimers with each other. If the supercage is singly occupied, then there must exist another singly occupied supercage in order for an excimer to form from the two molecules. This calculation assumes that an excimer will not form between a molecule from a doubly occupied supercage and a molecule from a singly occupied supercage. Singly and doubly occupied supercages are equally likely to form an excimer, and if an excimer can form between two molecules, it will.

Consider one arbitrary molecule incorporated within one zeolite supercage **A**. The probability that there is a second molecule within the same supercage is given by P(2). The probability that this arbitrary molecule is alone within the supercage is defined as:

$$P_{alone} = \frac{P(1)}{P(1) + P(2)}. \tag{3.2}$$

The reason $P_{alone} \neq P(1)$ is because the focus is on the molecule, not upon the supercage in question. The probability that a singly occupied supercage exists in shell **B** (the four supercages directly surrounding **A**) is calculated by the complement of doubly and non-occupied supercages,

$$P_B(1) = 1-(P(0)+P(2))^4. \quad (3.3)$$

However, an excimer will only form if supercage **A** is singly occupied, and so the probability of the **A** being singly occupied *and* **B** being singly occupied is:

$$P_{AB} = \frac{P(1)}{P(1)+P(2)}\left[1-(P(0)+P(2))^4\right] \quad (3.4)$$

Notice that as the loading level decreases, P_{alone} approaches 1 and equation 3.4 simplifies to:

$$P_{AB}(1) = 1-(P(0)+P(2))^4, \quad (3.5)$$

which matches the method of calculation used in previous papers[80,113] that only take into account single occupancy of supercages.

To calculate the probability of single occupancy in shell **C**, a similar method to (3.3) and (3.4) are used. There are a total of 12 supercages in shell **C**, and thus there are 16 supercages in shells **B** + **C**. The probability of occupancy in shells **B** + **C** is defined in equation (3.6):

$$P_{B+C}(1) = 1-(P(0)+P(2))^{16}. \quad (3.6)$$

In order to determine $P_C(1)$, it is necessary to subtract the probability of occupancy of the inner shell **B**:

$$P_C(1) = P_{B+C}(1) - P_B(1). \quad (3.7)$$

Finally, the probability of a singly occupied supercage in both **A** and **C** is:

$$P_{AC}(1) = (1-P(2))P_C(1). \quad (3.8)$$

This calculation can be carried forth for as many shells are as desired in the model. Table 3.24 gives the probabilities of $P_{AX}(1)$ for the shells **A** through **E**.

Table 3.24 Probabilities of singly occupied cages in Y zeolite about a singly occupied center cage.

Loading Level <S>	$P_{AA}(1)$	$P_{AB}(1)$	$P_{AC}(1)$	$P_{AD}(1)$	$P_{AE}(1)$	Total
1	3.33×10^{-1}	4.02×10^{-1}	9.79×10^{-2}	7.57×10^{-4}	4.45×10^{-8}	8.34×10^{-1}
0.5	1.16×10^{-1}	4.97×10^{-1}	1.96×10^{-1}	4.76×10^{-3}	2.68×10^{-6}	8.14×10^{-1}
0.2	2.62×10^{-2}	4.01×10^{-1}	3.82×10^{-1}	6.46×10^{-2}	1.43×10^{-3}	8.75×10^{-1}
0.1	7.81×10^{-3}	2.72×10^{-1}	4.20×10^{-1}	1.96×10^{-1}	2.63×10^{-2}	9.23×10^{-1}
0.05	2.18×10^{-3}	1.63×10^{-1}	3.98×10^{-1}	3.05×10^{-1}	1.27×10^{-1}	9.36×10^{-1}
0.013	1.70×10^{-4}	5.05×10^{-2}	1.36×10^{-1}	2.16×10^{-1}	2.47×10^{-1}	6.51×10^{-1}
5.0×10^{-3}	2.44×10^{-5}	1.97×10^{-2}	5.67×10^{-2}	1.04×10^{-1}	1.54×10^{-1}	3.34×10^{-1}
2.9×10^{-3}	8.01×10^{-6}	1.11×10^{-2}	3.25×10^{-2}	6.19×10^{-2}	9.88×10^{-2}	2.04×10^{-1}
2.0×10^{-3}	3.93×10^{-6}	7.95×10^{-3}	2.35×10^{-2}	4.53×10^{-2}	7.42×10^{-2}	1.51×10^{-1}

3.4.3.6 Calculation of Excimer Rise Times from Probability Data

The distribution of singly occupied cages in a zeolite can be used to calculate trends of excimer emission rise times given a specified number of allowed inter-supercage jumps. In order to do this, the model for inter-supercage movement must be defined precisely.

As specified previously, excimer emission can either arise from two molecules in a doubly occupied cavity or two molecules each in one singly occupied cavity. The latter case always requires one of the molecules to travel, or jump, from one supercage to another. It is reasonable to assume that the number of allowed jumps is limited. The larger the number of allowed jumps, the longer the time it will take for the excimer to form, and the more likely that the molecule will deactivate by another pathway before excimer formation can take place. Thus, past a certain number of jumps, formation of excimer becomes highly improbable. One can define different models based on the maximum number of allowed jumps.

If an estimate of the average time of each jump can be determined, then the probabilities calculated in Table 3.24 can be used to calculate an average time of excimer formation. For example, for a loading level of 1/1, allowing for up to 1 jump, the allowed pathways for excimer formation are $P_{AA}(1)$ (formation from a doubly occupied

supercage) and $P_{AB}(1)$ (formation from two adjacent singly occupied cavities). Because no other shells contribute to excimer formation, the percentage of $P_{AA}(1)$ contribution to excimer formation is 38.4% while $P_{AB}(1)$ contribution is 61.6%. If intracavity movement requires 8 ps and one jump requires 16 ps, the average time of excimer formation is 12.9 ps.

It is difficult to estimate the average time for intracavity movement and intercage jumping. If it takes 8 ps for two molecules to rearrange within the supercage into a configuration appropriate to form the excimer, should rearrangement plus an intercage hop take twice as long? Should it take three times as long? And if the number of intercage hops increase, should the estimated time increase linearly or exponentially? Because the only reasonable assumption is that increasing the number of jumps should result in an increase in the excimer formation time, four models were selected with rearrangement times beginning at 5 and 6 ps. These values were chosen because they approximated the fastest rise times for pyrene excimer formation in zeolites (Section 3.2.2). The first is a linear model. The subsequent models increase by larger factors, by doubling, tripling and by factors of ten. The models and their estimates for jump times are given in Table 3.25.

Table 3.25 Estimates of excimer formation times (ps) for four different jump time models.

No. of Jumps	Linear Model	Doubling Model	Tripling Model	Factors of Ten Model
0	6	6	6	5
1	12	12	18	50
2	18	24	54	500
3	24	48	162	5000
4	30	98	486	50000

Using these estimates for jump times, and the procedure described above, the average excimer emission rise times can be calculated for any given number of allowed jumps. Tables 3.26 to 3.29 show the calculated rise times for no allowed jumps through

to a maximum of four allowed jumps, for each of the four time models. The predicted rise times are displayed graphically in Figure 3.43.

Table 3.26 Predicted excimer emission rise times for the linear jump time model versus maximum number of jumps allowed.

Loading Level <S>	0 Jumps	1 Jump	2 Jumps	3 Jumps	4 Jumps
1.0	6.0	9.28	10.3	10.3	10.3
0.50	6.0	10.9	12.6	12.6	12.7
0.20	6.0	11.6	14.6	15.3	15.4
0.10	6.0	11.8	15.5	17.4	17.7
0.050	6.0	11.9	16.0	19.0	20.5
0.013	6.0	12.0	16.4	20.5	24.1
0.0050	6.0	12.0	16.5	20.8	25.0
0.0029	6.0	12.0	16.5	20.9	25.3

Table 3.27 Predicted excimer emission rise times for the doubling jump time model versus maximum number of jumps allowed.

Loading Level <S>	0 Jumps	1 Jump	2 Jumps	3 Jumps	4 Jumps
1.0	6.0	9.28	11.0	11.0	11.0
0.50	6.0	10.9	14.0	14.2	14.2
0.20	6.0	11.6	17.5	19.7	19.9
0.10	6.0	11.8	19.1	25.5	27.5
0.050	6.0	11.9	20.1	30.6	39.7
0.013	6.0	12.0	20.7	35.4	59.2
0.0050	6.0	12.0	20.9	36.5	64.9
0.0029	6.0	12.0	20.9	36.8	66.4

Table 3.28 Predicted excimer emission rise times for the tripling jump time model versus maximum number of jumps allowed.

Loading Level <S>	0 Jumps	1 Jump	2 Jumps	3 Jumps	4 Jumps
1.0	6.0	12.6	17.4	17.6	17.6
0.50	6.0	15.7	25.0	25.8	25.8
0.20	6.0	17.3	34.6	44.0	44.8
0.10	6.0	17.7	39.5	66.3	78.3
0.050	6.0	17.8	42.2	87.3	141
0.013	6.0	18.0	44.2	107	251
0.0050	6.0	18.0	44.7	112	285
0.0029	6.0	18.0	44.8	114	294

Table 3.29 Predicted excimer emission rise times for the factor of ten jump time model versus maximum number of jumps allowed.

Loading Level <S>	0 Jumps	1 Jump	2 Jumps	3 Jumps	4 Jumps
1.0	5.0	29.6	84.9	89.4	89.4
0.50	5.0	41.5	152	181	181
0.20	5.0	47.2	261	611	692
0.10	5.0	48.7	320	1345	2730
0.050	5.0	49.4	353	2103	8586
0.013	5.0	49.8	378	2856	20785
0.0050	5.0	49.9	384	3042	24697
0.0029	5.0	50.0	386	3092	25774

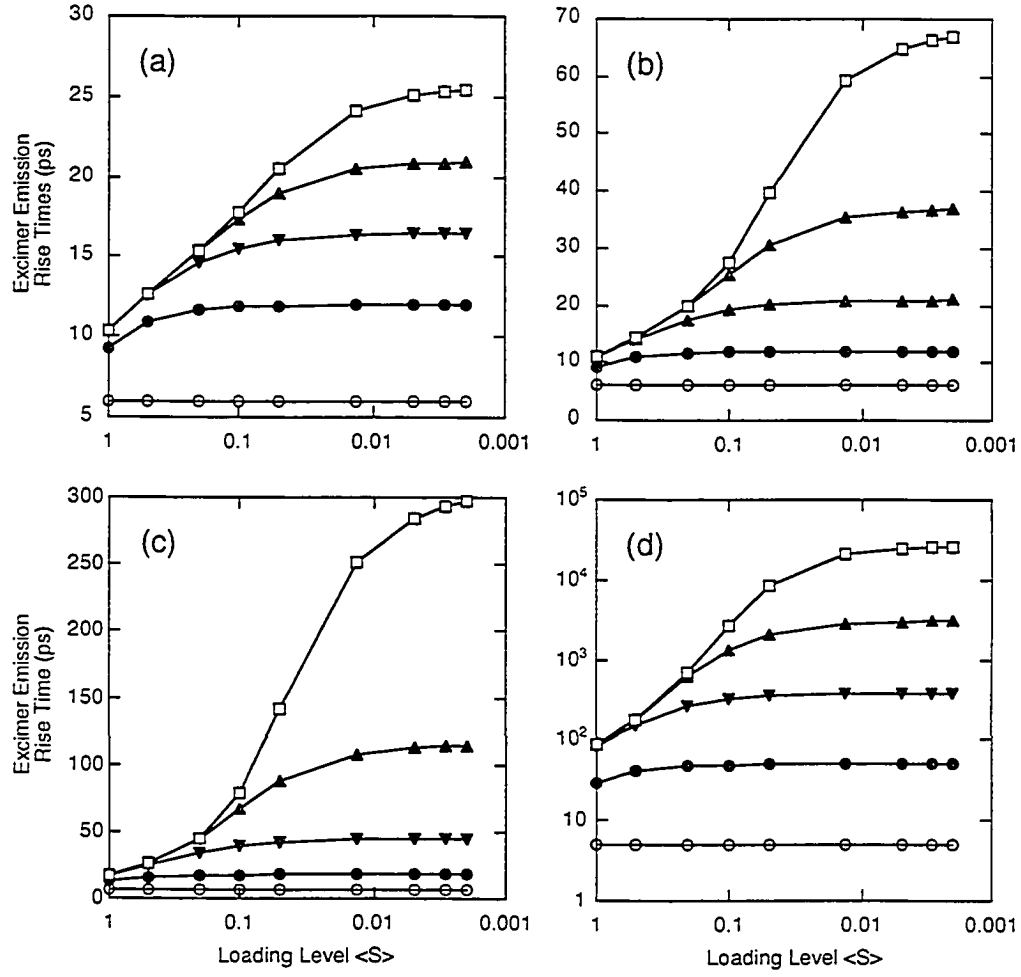

Figure 3.43 Predicted average excimer rise times as a function of loading level, jump models, and time models. Jump models: no jumps (○), up to 1 jump (●), up to 2 jumps (▼), up to 3 jumps (▲), and up to 4 jumps (□). Time models: (a) linear model, (b) doubling model, (c) tripling model, and (d) factor of 10 model.

Although the increases in rise times vary greatly between the time models, all four models show the same basic patterns. First of all, the rise times show a loading level dependence for the models that allow at least one jump, while the model that allows only intracavity movement shows no loading level dependence. This is expected because the formation of excimers *via* intercavity movement would depend on the distribution of excimers to determine the average rise time, while in the no jump model, excimers only arise from doubly occupied cavities. As the loading level decreases, the probability of doubly occupied cavities decreases, resulting in the loss of excimer emission intensity, but the time it takes for the excimers to form does not vary because the pairs of molecules are all still moving only the distance within one supercage to form the excimer.

While the loading level dependence is observed in all the jump models, the rise times all reach a plateau at low loading levels. The greater the number of allowed jumps, the lower the loading level must be for the rise times to reach the plateau. The estimated rise time stops showing variation when the changing loading levels no longer affect the ratios of shell probabilities. Higher numbers of allowed jumps show a dependence on loading level for larger ranges because the distribution of molecules in the outer shells are still changing at these low loading levels, while the inner shells have reached a constant probability of occupancy relative to one another.

A plateau at high loading levels is also expected and observed in the models by the sigmoidal shape of the curves. At very high loading levels, such as $\langle S \rangle > 1$, the proportion of doubly occupied supercages is so much larger than singly occupied supercages that excimer formation is predominantly from intracavity movement. The highest loading level possible, of $\langle S \rangle = 2$, would result in the predicted excimer rise time equal to that of zero jumps for all jump models in question.

3.4.3.7 Comparison of Model Estimates to Experimental Rise Times

The range of estimated rise times is significantly greater than that observed experimentally (from 9 to 16 ps for the KY loading level study). Given that the DCA molecules do not redistribute much within the zeolite over a month, it is assumed that

intercavity hopping of ground state DCA molecules is extremely slow or does not happen at all without the carrier solvent. Excited state DCA molecules may have different hopping abilities; however, the excited singlet state of a molecule is generally more polar than the ground state and this enhanced polarity within the polar supercages of the zeolite framework make it unlikely that the supercage hopping is faster for ^{1}DCA*. The loading level dependence observed in the experimental work suggests that there is intercavity movement in excimer formation but that intercavity hopping is likely only possible for a maximum of one or two jumps (*vide infra*). Because the time models are all very similar for one or two jumps, the linear and doubling models were chosen to compare with the KY loading level data (Figure 3.44). The striking difference between the predicted and experimental data is the difference in shape. In the experimental data, there is a plateau at the higher loading levels, while at the low loading levels the rise times continue to increase without evidence of a plateau. In the model, a plateau is seen at both the upper and lower levels of guest molecule concentration. The major cause of this difference is the assumption in the model of homogeneous distribution of guest molecules throughout the zeolite framework. Because the DCA molecules are not loaded homogeneously into the Y zeolites, the loading levels calculated for these samples are not representative of the loading level surrounding a typical DCA molecule within the zeolite framework. The immediate environment has a much higher loading level than calculated, perhaps as high as $\langle S \rangle = 2$. At these extremely highly aggregated levels, the plateau to the fastest rise time of zero jumps is evident in the KY loading level data. Conversely, the upper plateau of the rise times at low loading levels is not observed because the actual loading level may not be low enough to reach the plateau. Experimentally, it becomes more and more difficult to observe the plateau because the lower the loading level, the lower the intensity of the excimer emission and the harder the emission is to measure. Thus, in order to observe the longest rise time plateau, it would be necessary to work with a different guest molecule that loads homogeneously and still exhibits excimer emission, or to use a different incorporation technique that will promote the homogeneous distribution of DCA in the Y zeolite framework. One possible technique is described by Kwon *et. al.* and incorporates anthracene into Y zeolites by vacuum sublimation at high temperatures.[111]

Because the upper plateau is not observed, it is difficult to conclude which of the jump models is a likely model to describe the maximum movement of DCA in the Y zeolites. It has been stated previously (*vide supra*) that intercavity movement is unlikely to exceed one or two jumps. Comparing the experimental data to the models, the relatively small increase in rise time places the data neatly between the zero and two jump models, confirming that the intracavity movement is unlikely to exceed two jumps. One jump seems probable, especially if both guest molecules reside near the pore interconnecting their cavities. If one is excited, then movement through the pore to form the lower energy excimer seems likely. Two jumps may also be possible, either by one molecule jumping twice or both molecules jumping once into the same cavity. However, the latter is highly improbable because the DCA ground state molecule does not move between cavities readily. Thus excimers formed by jumps greater than one are the result of excited DCA molecules moving through multiple pores. Multiple jumps incur the difficulty of random motion that may or may not result in excimer emission, assuming that motion of excited state molecules is independent of each other. As the number of jumps gets larger, the number of excimers actually formed between monomers that are several jumps apart is no longer equal to the occupancy probability because the monomers may move randomly apart rather than together. Thus, at high numbers of jumps, the model begins to overestimate the proportion of multiple jumps compared to smaller numbers of jumps. A random walk model,[139] where the ground state molecule is stationary and the excited state molecule is permitted to jump, would then provide a more accurate model of movement.

None of the reported intercavity movements[92,116,138,140,141] of excited state polyaromatic hydrocarbons expresses the intercavity movement as a number of possible jumps. However, their studies leave little doubt that intercavity hopping does occur. This, combined with the experimental and model results reported herein, supports the suggestion that DCA excimer formation by intercavity movement is the result of one or two jumps.

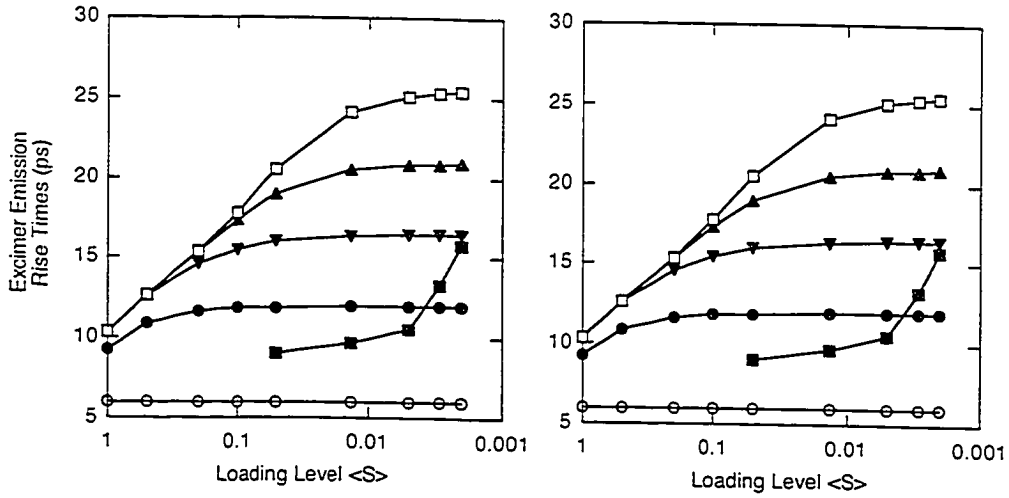

Figure 3.44 Comparison of experimental KY loading level data (■) with calculated excimer emission rise times for (A) linear time models, and (B) doubling time models. Jump models: no jumps (○), up to 1 jump (●), up to 2 jumps (▼), up to 3 jumps (▲), and up to 4 jumps (□).

3.5 Synopsis of Results

Chapter 3 used steady-state and time-resolved fluorescence spectroscopy to study the placement and movement of pyrene and DCA molecules incorporated into cation-exchanged X and Y zeolites. The ultrafast movement of pyrene in doubly occupied supercages has been shown to be resolvable and in all cases, slower than the instrument response function of the streak camera system. This non-instantaneous rise time shows that rearrangement of two pyrene molecules within a supercage must take place in order for the excimer to form.

The rise times of the excimer emission are found to be cation dependent, with the slowest rise time found in NaY compared to both LiY and KY. Adsorption of polar co-solvents into impregnated zeolite samples lowered the rise times in all cases, indicating that adsorption of the pyrene molecule to the zeolite cations by the π-cation effect retards excimer formation. The accelerating effect of polar co-solvent adsorption also suggests that two pyrene molecules within the same supercage are not in a ground state dimer formation as previously postulated in the literature.

The study of fluorescence spectroscopy of DCA incorporated into cation-exchanged Y zeolites has been used to demonstrate that DCA exhibits very different behaviour in zeolites than in solution. The observation of a readily formed excimer demonstrates the tethering effect of a rigid supercage upon molecules in doubly occupied cavities. Time-resolved emission decays illustrate that two or three adsorption sites were present within the zeolite. As the cation was exchanged, the adsorption sites available to DCA monomers do not change but the relative populations of DCA molecules at these sites are affected by size considerations and to a lesser extent by electronic effects. As well, a clear loading level dependence upon the site occupancy distributions is observed: as the loading level increases, the shortest lifetime sites increase in relative population. This leads to the inference that increasing intercage interactions causes the DCA molecules to be pushed further into the cage to more kinetically unstable sites. Finally, DCA excimers are less sensitive to the effects of the cation and loading level, although the strong polar nature of the zeolite interior induced a charge transfer character in the excimer, which is dependent on the nature of the charge-balancing cation.

The observation of a resolvable excimer emission rise time for DCA indicates that the formation of DCA excimer is dynamic. In all five zeolites, at all loading levels studied, there is at least some rearrangement that is necessary in order for DCA to achieve the configuration to produce an excimer. It was observed that the rise times measured varied with the size of the counterbalancing cation. As the cation increased in size, the rise times were slower, reflecting a size effect in the void space of the supercages. However, unlike the pyrene / zeolite samples studied in the earlier part of the chapter, a dramatic loading level effect on excimer rise time was also observed, indicating that the dynamic formation of DCA excimers is possible not only within doubly occupied supercages, but by intercage hopping by DCA monomers to come together.

In order to further study the movement of DCA monomers between supercages, a dynamic excimer model was developed based upon inter-shell hopping probabilities. This model predicted that for a maximum allowed number of supercage hops, the excimer rise time would be loading level dependent, confirming that the observed data was indicative of intercavity movement. A plateau at both the lowest and highest loading levels was also suggested. In comparison to the data, only one plateau was observed due

to the inhomogeneous distribution of DCA within the zeolite particles. From the model and rise time data, it is concluded that DCA excimer formation is a dynamic process involving intercavity movement, and that the probable maximum number of supercage jumps does not exceed two.

Chapter 4: Ultrafast Studies of Tris-(2,2'-bipyridine)ruthenium(II) Derivatives

4.1 Introduction

The need to harness renewable energy resources has prompted the development of technology that efficiently coverts solar energy into electric energy. Conversion of solar energy involves the photovoltaic effect, where photon energy is used to excite an electron from the ground state to a higher energy level. Subsequent charge separation is crucial in order to prevent the energy wasting process of recombination and as a result the solar energy is stored as electrical energy *via* the potential difference between separated electrons and holes. One solar cell design being developed is a dye-sensitized nanocrystalline solar cell.[144] Briefly, this device uses nanocrystals of titanium dioxide, an inexpensive, non-toxic semiconductor, that have been sintered together to form a mesoporous layer. Sensitizer dye molecules are adsorbed onto the surface of the crystals. Upon photoexcitation, these dye molecules undergo photoinduced charge transfer to inject electrons into the conduction band of the semiconductor substrate. Electron donation from the electrolyte bathing the mesoporous layer regenerates the ground state sensitizer and also reduces back electron transfer between the dye molecule and the titanium dioxide. Generally, the electrolyte is an iodide/triiode redox system in an organic solvent, and it is regenerated at the counter electrode to complete the circuit. Overall efficiencies for dye-sensitized solar cells are currently over 10 %.[144]

Light absorbing sensitizers facilitate endoergonic electron transfer reactions (4.1) by harnessing light energy to make the process thermodynamically allowed. Upon absorption of light, the sensitizer (S) is excited into its excited state, which is able to reduce (or oxidize) one of the reactant species. The redox reaction is completed when the oxidized (or reduced) sensitizer reduces (or oxidizes) the other reactant and regenerates the sensitizer. Equations 4.2 to 4.4 outline the sensitization process with S* as an oxidant.

$$A + B \rightarrow A^{+} + B^{-} \quad (\Delta G < 0) \tag{4.1}$$

$$S + h\nu \rightarrow S^{*} \tag{4.2}$$

$$A + S^* \rightarrow A^- + S^+ \quad (4.3)$$

$$B + S^- \rightarrow B^- + S \quad (4.4)$$

Ruthenium(II) metal complexes are attractive as sensitizers because their redox and excited state properties satisfy the requirements necessary for efficient sensitization, which include suitable ground and excited state potentials, reversible redox behaviour, and a suitable lifetime of the reactive excited state.[145] Additionally, the complexes can be synthetically tailored to control various photophysical properties. The standard sensitizer being used in these cells is $Ru(dcbpy)_2(NCS)_2$ (dcbpy = 4,4'-dicarboxylic-2,2'-bipyridine, NCS = isothiocyanato), or "RuN_3," due to a high efficiency of electron injection and the ease of attachment to the nanocrystalline surface.[146] The efficiency has been attributed to the fast electron injection from the sensitizer dye to the semiconductor,[33] with < 100 fs electron injection rates reported for RuN_3 to nanocrystalline TiO_2,[147,148] and reports as fast as < 25 fs for RuN_3 dye to a colloidal anatase TiO_2 film.[149] Due to the success of RuN_3 dye, much interest has been directed toward understanding the photophysical behaviour of ruthenium metal complexes, especially non-thermalized states involved in the electron injection process. One complex in particular, tris-(2,2'-bipyridine)ruthenium(II), or $Ru(bpy)_3^{2+}$, has been considered the prototype for understanding transition metal photophysics.

$Ru(bpy)_3Cl_2$ crystals are deeply coloured and solutions of $Ru(bpy)_3Cl_2$ have a bright red-orange hue, even at low concentrations. Figure 4.1 shows the absorption spectrum for $Ru(bpy)_3^{2+}$ at ambient temperature. The absorption band at 450 nm gives rise to the bright colour of the complex, and this band, along with the bands at 238 and 250 nm, are attributed to the metal-to-ligand charge transfer (MLCT) transition ($d\pi \rightarrow \pi^*$). The long wavelength tail of the MLCT band has been assigned to the lowest lying ^{3}MLCT absorption. Ligand centered (LC) $\pi \rightarrow \pi^*$ transitions are sharp bands at 208 and 285 nm, while Laporte forbidden metal centered (MC) transitions are thought to lie near 395 nm. The molecular orbitals giving rise to these transitions are shown in Figure 4.2.

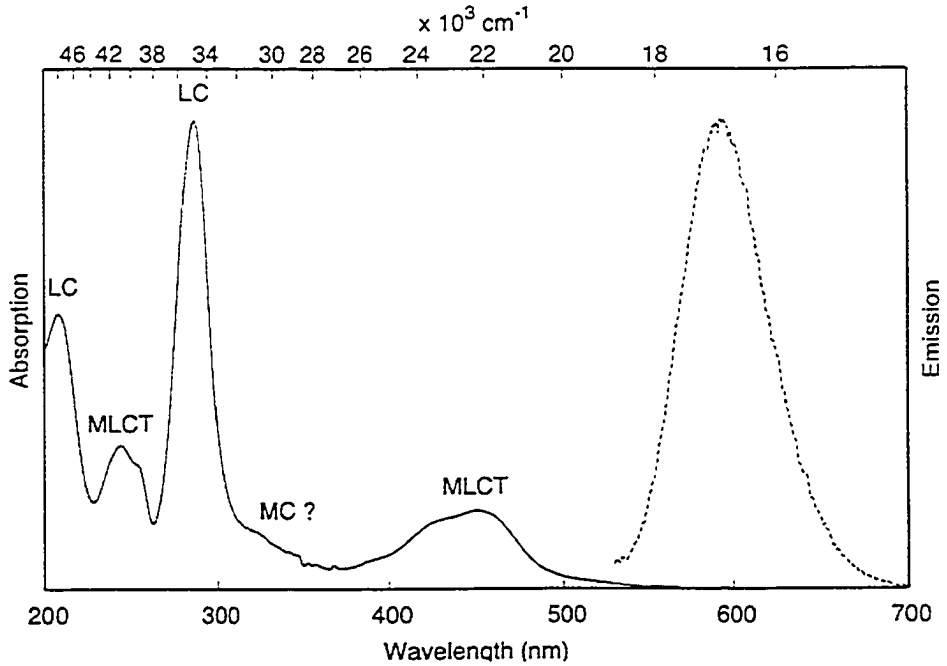

Figure 4.1 The absorption (—) and emission (---) spectra for $Ru(bpy)_3^{2+}$ in acetonitrile at 298K. Figure reproduced from reference 15.

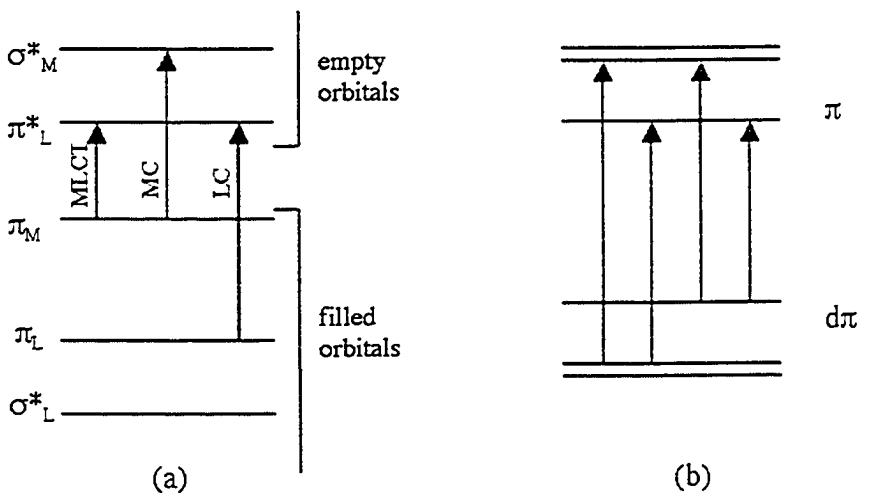

Figure 4.2 (a) A simplified molecular orbital diagram[15] showing the three types of electron transitions giving rise to the UV-visible absorption spectrum of $Ru(bpy)_3^{2+}$. (b) Further splitting of the orbitals involved in the MLCT transition in D_3 symmetry.

Luminescence from $Ru(bpy)_3^{2+}$ was first detected in 1959.[150] Absorption into any of the absorption bands produces luminescence at 600 nm. At ambient temperature, the emission spectrum is a broad, featureless band; however, at 77K in a glass matrix, the emission spectrum is well-resolved. The luminescence has been shown to originate from the lowest lying ^{3}MLCT state and has a reported quantum yield of 0.029 to 0.071 in various solvents.[151] The steady state luminescence of $Ru(bpy)_3^{2+}$ is also shown in Figure 4.1.

The lowest lying ^{3}MLCT state of $Ru(bpy)_3^{2+}$ is no longer of D_3 symmetry due to electron localization of the photoexcited electron upon a single ligand, giving rise to $[Ru(III)(bpy)_2(bpy^{\cdot-})]^{2+}$. This species is sufficiently long-lived to encounter other solute molecules and can act as an energy donor, electron donor or an electron acceptor. The energy available to $^3[Ru(bpy)_3^{2+}]$ for energy transfer processes is 2.12 eV while the reduction and oxidation potentials are +0.84 and -0.86 V in aqueous solution.[145] These three processes result in quenching of the excited state of $Ru(bpy)_3^{2+}$:

$$^3[Ru(bpy)_3^{2+}] + Q \rightarrow Ru(bpy)_3^{2+} + Q^* \text{ (energy transfer)} \quad (4.5)$$

$$^3[Ru(bpy)_3^{2+}] + Q \rightarrow Ru(bpy)_3^{3+} + Q^- \text{ (oxidative quenching)} \quad (4.6)$$

$$^3[Ru(bpy)_3^{2+}] + Q \rightarrow Ru(bpy)_3^{+} + Q^+ \text{ (reductive quenching)} \quad (4.7)$$

Much of the initial, non-thermalized excited state behaviour of $Ru(bpy)_3^{2+}$ leading to ^{3}MLCT formation has been determined by transient absorption experiments reported by the McCusker group.[26,39,45,152-154] At λ_{ex} = 480 nm, comparison of nanosecond and femtosecond transient absorption experiments of $Ru(bpy)_3^{2+}$ indicated that the formation of the long-lived (1 μs) ^{3}MLCT state was complete in 300 fs with a half-life of 100 fs for the formation of the triplet state.[26] Typically, for organic chromophores, intramolecular vibrational relaxation (IVR) has rates on the femtosecond to low picosecond time scale, while rates of the processes of internal conversion (IC) and intersystem crossing (ISC) are slower (10^{11}-10^{13} s^{-1} for IC, 10^6-10^{10} s^{-1} for ISC). Compounds containing transition metals do not necessarily follow simple cascade relaxation dynamics ($k_{IVR} > k_{IC} > k_{ISC}$) because spin orbit coupling provides a mechanism for allowing singlet to triplet transitions. The rapid formation of the ^{3}MLCT state suggests that upon excitation, evolution of the

wavepacket does not occur on the ^{1}MLCT surface; rather, crossing to the ^{3}MLCT surface happens almost instantaneously. However, it is difficult to interpret the dynamics within the first 300 fs due to a significant ground state bleach superimposed on the excited state absorptions.

Bhasikuttan and co-workers investigated the weak fluorescence from the short-lived ^{1}MLCT state of $Ru(bpy)_3^{2+}$ by up-conversion fluorescence spectroscopy.[33] Fluorescence up-conversion is able to probe ultrafast fluorescence without interference from triplet state emission because the radiative flux from the ^{3}MLCT state is insufficient to generate the up-converted signal. Steady state fluorescence measurements revealed a weak emission band centered at 500 nm, which was assigned to fluorescence from the Franck-Condon (FC) state. The lifetime of the FC state was been estimated to be 40 ± 15 fs, and this value has been interpreted as the time constant for ISC. Thus, any photophysical process occurring with a time constant longer than 40 fs represents dynamics on the triplet surface. Emission profiles at wavelengths longer than 500 nm were found to be wavelength dependent and yielded slower kinetics. Emission at 620 nm had a decay constant of 600 ± 50 fs, and accordingly, this has been assigned to vibrational cooling in the triplet manifolds.

The photophysics of transition metal complexes are known to exhibit excitation wavelength dependence due to a large number of spin orbit coupled states. Increased excitation energy changes the state being initially accessed, and these states may couple to lower energy states differently. The excitation of $Ru(bpy)_3^{2+}$ and its derivative $Ru(dmb)_3^{2+}$ (dmb = 4,4'-dimethyl-2,2'-bipyridine) at λ_{ex} = 400 nm produces very different dynamics than those described for $Ru(bpy)_3^{2+}$ at λ_{ex} = 480 nm.[45] Formation of the ^{3}MLCT state was monitored at 532 nm, where absorption of dmb radical anion occurs and thus is indicative of the intraligand delocalized, thermalized triplet state. An instantaneous bleach formation is observed for both molecules at 450 nm, as expected, but for $Ru(dmb)_3^{2+}$ decay kinetics at 532 nm are observed out to 15 ps, consisting of a fast component (τ_1 = 120 ± 40 fs) and a slow component (τ_2 = 5 ± 0.5 ps).[45] The same paper also mentions that similar kinetics are observed for $Ru(bpy)_3^{2+}$ when excited at 400 nm, in contrast with excitation at 480 nm where all spectral evolution is complete in 300 fs. The picosecond dynamics are attributed to vibrational cooling of the lowest energy ^{3}MLCT,[154]

as the lack of large changes in the transient absorption spectrum indicates that there are no large changes in the electronic structure of the excited state over this time. The 120 fs lifetime indicates that the process giving rise to the observed kinetics is happening on the triplet state surface and is likely a combination of processes including solvent dynamics, ISC, and some vibrational cooling.[154]

A recent report[155] indicated that the fluorescence originating from the ^{1}MLCT state of $Ru(bpy)_3^{2+}$ was observable as an instrument response limited signal on an instrument with 3 ps resolution. In contrast to this, the perdeuterated form of $Ru(bpy)_3^{2+}$ was reported to fluoresce with a lifetime over 200 ps. It is this observation that led our group to investigate the emission of $Ru(bpy)_3^{2+}$, its deuterated analgoue $Ru(bpy\text{-}d_8)_3^{2+}$, and $Ru(bpy)_3^{2+}$ derivatives using the streak camera system, as it was not immediately obvious to us that ISC should exhibit an isotope effect. This explanation has since been retracted[156] and the observation attributed to impurities in the $Ru(bpy\text{-}d_8)_3^{2+}$ sample. While emission at 500 nm from both $Ru(bpy)_3^{2+}$ and $Ru(bpy\text{-}d_8)_3^{2+}$ have been found to decay within the IRF of the streak camera system in our lab, some $Ru(bpy)_3^{2+}$ derivatives have been found to fluoresce with both an IRF-limited fluorescence (τ_3) and a longer-lived emission ($\tau_{4,5} > 50$ ps).[157] Four of these complexes, along with $Ru(bpy)_3^{2+}$, are the subject of this Chapter. All four compounds are homoleptic (*i.e.* all three ligands are the same species) and involve substitution at the 4,4' positions of 2,2'-bipyridine with $-CH_3$, $-CF_3$, $-OCH_3$, and $-C(CH_3)_3$. These substituents are chosen to provide a range of electron withdrawing ($-CF_3$) to electron donating ($-OCH_3$) effects. Herein is reported the fluorescence and transient absorption spectroscopy of these five complexes in an effort to shed light on the origin of $\tau_{4,5}$, to increase the number of $Ru(bpy)_3^{2+}$-based complexes being investigated on the ultrafast time scale, and to study the effect of higher energy excitation wavelengths ($\lambda_{ex} = 388$ nm) upon the excited state dynamics.

The work in this chapter is a collaborative effort between Felix Lee, Sherri McFarland and the author. Felix Lee is responsible for the synthesis, purification and characterization of all the complexes used.[158] Sherri McFarland is responsible for the observations on the streak camera with $\lambda_{ex} = 388$ nm and synthesis of the PF_6^- salts, and the author has collected the remainder of the data.

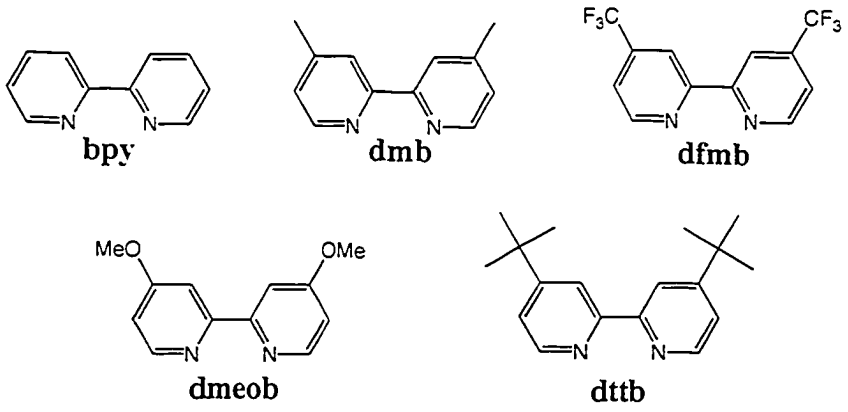

Figure 4.3 Bipyridyl ligands used in this study: bpy = 2,2'-bipyridine, dmb = 4,4'-dimethyl-2,2'-bipyridine, dfmb = 4,4'-di(trifluoromethyl)-2,2'-bipyridine, dmeob = 4,4'-dimethoxy-2,2'-bipyridine, and dttb = 4,4'-di(*tert*-butyl)-2,2'-bipyridine.

4.2 Results

4.2.1 Steady State Spectra

The chloride salts of all five ruthenium complexes dissolved readily in water to form bright red-orange solutions. Steady state absorption and emission spectra of the complexes are shown in Figure 4.4. Most notable about the five spectra are the similarities between $Ru(bpy)_3^{2+}$, $Ru(dmb)_3^{2+}$, $Ru(dfmb)_3^{2+}$, and $Ru(dttb)_3^{2+}$. These four spectra show very small shifting of the ligand centered transitions and the MLCT bands do not show much difference in shape or position. In contrast to these spectra, the absorption and emission spectra for $Ru(dmeob)_3^{2+}$ shows the MLCT band becoming much broader and red-shifted, as well as significant shape and wavelength changes of the UV absorption bands. The $Ru(dmeob)_3^{2+}$ compound also exhibited very weak fluorescence compared to the other compounds. Excitation of the compounds at 450 nm and at 388 nm yielded similar fluorescence spectra in both shape and fluorescence intensity.

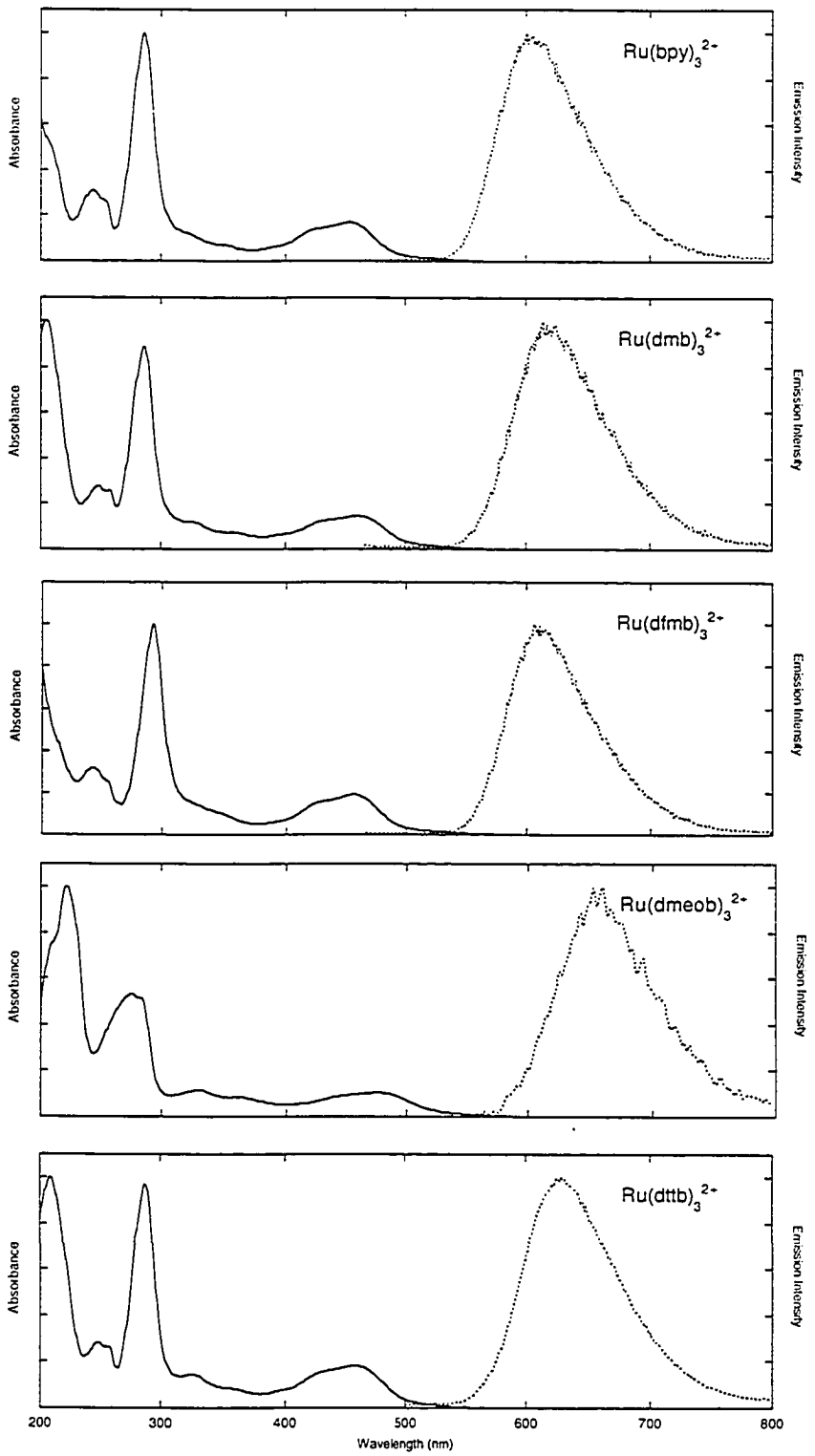

Figure 4.4 Steady state absorption and emission spectra for ruthenium complexes with ligands listed in Figure 4.3. All complexes were dissolved in water and studied at 298 K. The excitation wavelength for the emission spectra is 450 nm.

4.2.2 Time-Resolved Fluorescence Studies

All five compounds were studied by both nanosecond and picosecond time-resolved fluorescence spectroscopy using the streak camera system. Following excitation at 388 nm, the luminescence of $Ru(bpy)_3Cl_2$ collected at 500 nm decayed within the instrument response time (3-5 ps). The top panel in Figure 4.5 plots the first 250 ps of $Ru(bpy)_3Cl_2$ luminescence along with the IRF. Extending the time window to ~100 ns confirmed that there was no long-lived luminescence present, Figure 4.6. In contrast to $Ru(bpy)_3Cl_2$, all the derivatives exhibited a second, longer lived emission in addition to the instrument response limited luminescence upon excitation at 388 nm. Due to the longer lifetime of the second emission, its intensity was very low when the first 250 ps were observed, Figure 4.5. However, when studied on the nanosecond time scale, the instrument resolution decreases from 3-5 ps to 64-180 ps, resulting in attenuation of the IRF-limited peak compared to the intensity of the longer-lived emission, Figure 4.6. For two species, $Ru(dfmb)_3Cl_2$ and $Ru(dmeob)_3Cl_2$, the traces on the nanosecond time scale do not show any evidence for the instrument limited luminescence signal. In contrast, the picosecond trace for $Ru(dttb)_3Cl_2$ does not appear to exhibit the long lived tail, but upon examination of the nanosecond trace it is evident that the tail does exist, albeit very weakly. Both the picosecond and nanosecond data are necessary to completely capture the luminescence of these ruthenium complexes.

While resolution of the short lived signal was not possible, the longer lifetimes were extracted by iterative convoluted fitting to double exponential functions and evaluated by visual examination of residuals. Table 4.1 lists the lifetimes that were calculated and highlights the lifetimes that are within the instrument response time. The lifetimes that were distinctly different from the IRF range from 0.7 to 6 ns, with the longest lifetimes observed for $Ru(dfmb)_3Cl_2$. Interestingly, it was only $Ru(dfmb)_3Cl_2$ that exhibited two resolvable lifetimes.

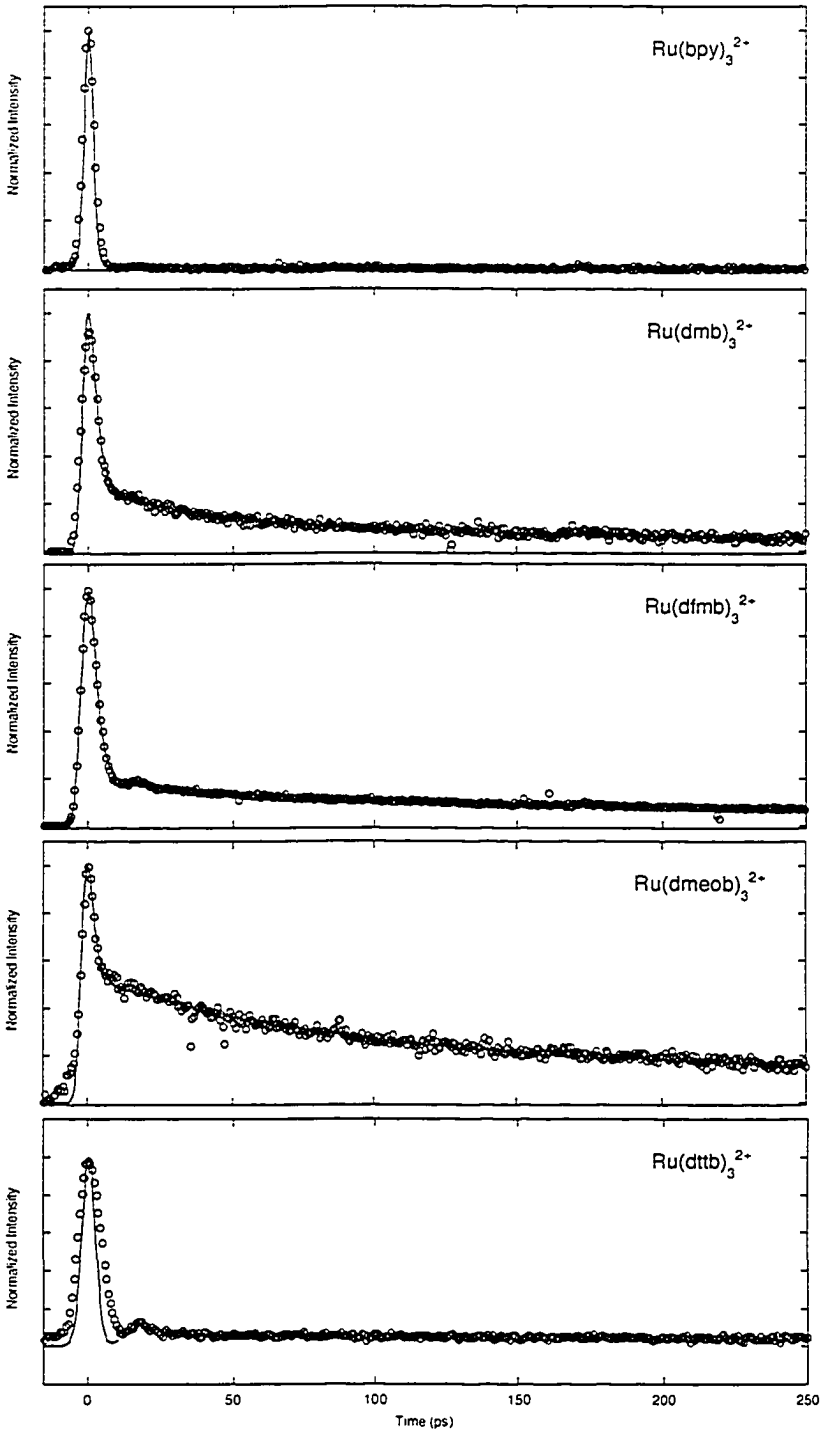

Figure 4.5 Picosecond time-resolved luminescence at 500 nm of the five $Ru(bpy)_3^{2+}$ derivatives. The excitation wavelength is 388 nm.

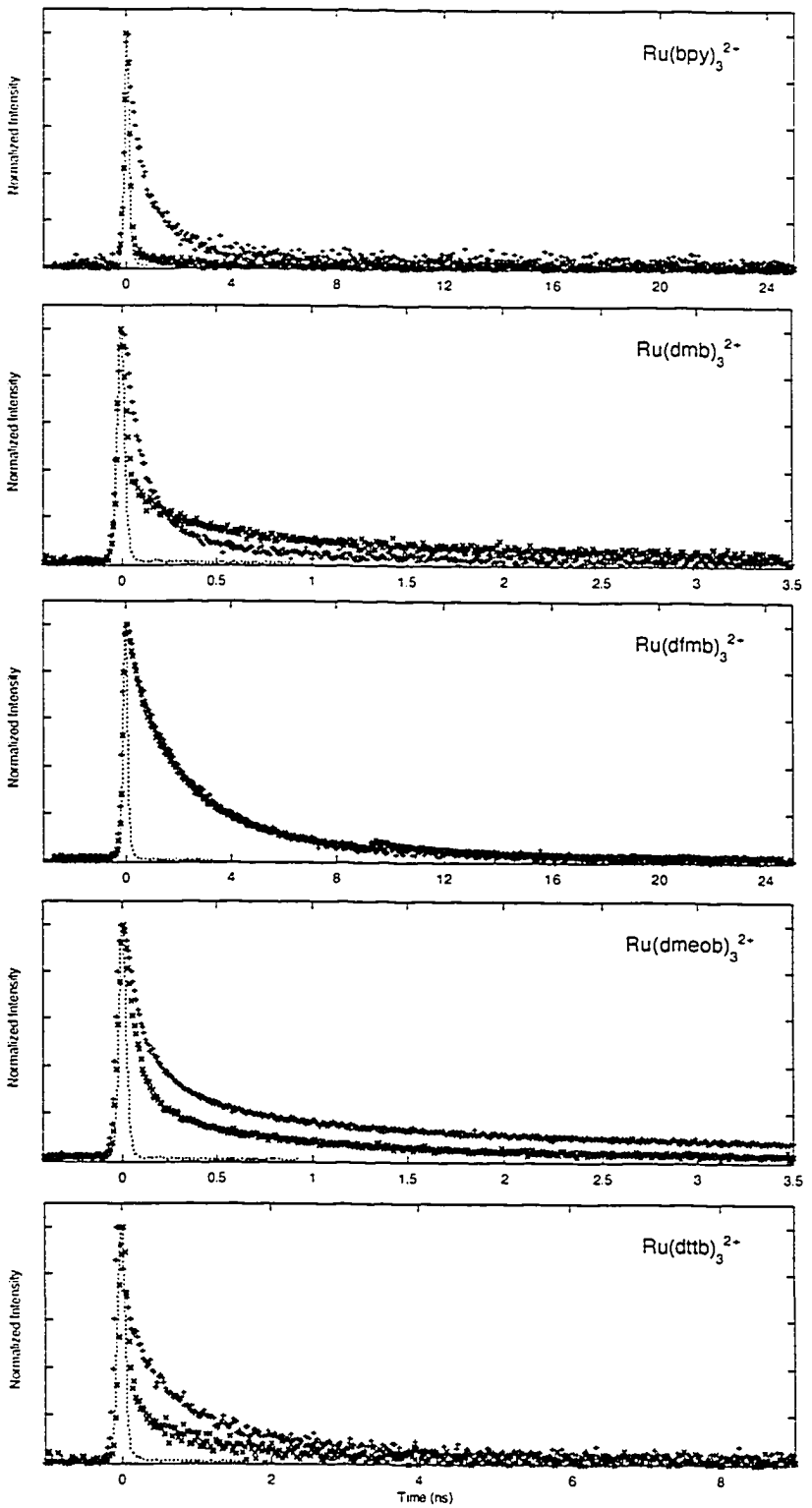

Figure 4.6 Nanosecond time-resolved luminescence traces collected at 500 nm of the five $Ru(bpy)_3^{2+}$ derivatives. The excitation wavelengths are 258 nm (+) and 388 nm (×). Each plot includes the IRF (---). Every second data point is plotted for clarity.

Table 4.1 Lifetimes[a] of the long lived emission at 500 nm upon high energy excitation of five $Ru(bpy)_3^{2+}$ derivatives. Highlighted numbers represent lifetimes that are within the instrument response limit.[b]

Complex	388 nm excitation		258 nm excitation	
	τ_4 (ns)	τ_5 (ns)	τ_4 (ns)	τ_5 (ns)
$Ru(bpy)_3^{2+}$			1.0 ± 0.4	4 ± 2
$Ru(dmb)_3^{2+}$	0.11 ± 0.05	1.4 ± 0.1	0.11 ± 0.02	0.62 ± 0.02
$Ru(dfmb)_3^{2+}$	1.6 ± 0.2	6 ± 2	1.7 ± 0.1	4.7 ± 0.5
$Ru(dmeob)_3^{2+}$	0.05 ± 0.02	0.70 ± 0.02	0.22 ± 0.05	2.0 ± 0.1
$Ru(dttb)_3^{2+}$	0.07 ± 0.04	1.3 ± 0.3	0.41 ± 0.06	1.6 ± 0.1

[a] Error estimates are based upon comparison between fits of multiple emissions collected from the same sample.
[b]The instrument response limit varied from 64 to 750 ps, depending on the time window used to collect the data.

In order to determine whether the observation of $\tau_{4,5}$ is a result of the short excitation wavelength or due to the electronic nature of the substituents, the excitation wavelength was tuned. Unfortunately, when tuning the wavelength to 450 or 480 nm, the photon flux in the excitation pulse became so low the luminescence was undetectable using the streak camera. To get some sense of the wavelength dependence of the nanosecond lifetimes, the fundamental beam was frequency tripled to produce 258 nm pulses. Exciting at 258 nm produced very low intensity emission, rendering the signal to noise ratio of the streak camera data (when triggered using the G2 jitter-free unit) too low to discern whether picosecond luminescence was present. However, the weak signals were detectable on the nanosecond time scale and are shown in Figure 4.6. Interestingly, exciting at such high excitation energies produced secondary emission for all the complexes, including $Ru(bpy)_3^{2+}$. Again, their lifetimes were determined by convoluted fitting and are also listed in Table 4.1. While there is no discernable trend relating the length of the lifetime to the excitation wavelength, it appears that for the five complexes studied, τ_4 in the 388 nm experiments becomes resolvable from the IRF at $\lambda_{ex} = 258$ nm.

When researching the initial dynamics of excited state ruthenium metal complexes, it is useful to compare the findings from different laboratories in order to take advantage of the different excitation wavelengths and capabilities of various ultrafast instruments. The disadvantage of this is the inability to do experiments under exactly the same conditions. Most of the ruthenium complexes studied by the McCusker group use

PF_6^- as the counter-ion and are studied with acetonitrile as the solvent, in contrast to our compounds, which are chloride salts and studied in aqueous solution. In order to confirm that the counter-ion and solvent are not the source of $\tau_{1,5}$, the PF_6^- salts of the five compounds were produced and the nanosecond fluorescence experiments were repeated in acetonitrile solution. All the PF_6^- salts produced results similar to those obtained for the chloride salts in aqueous solution although the lifetimes of the long-lived emission varied slightly. Figure 4.7 illustrates the similarity between the decay profiles collected for $Ru(dfmb)_3Cl_2$ versus $Ru(dfmb)_3(PF_6)_2$.

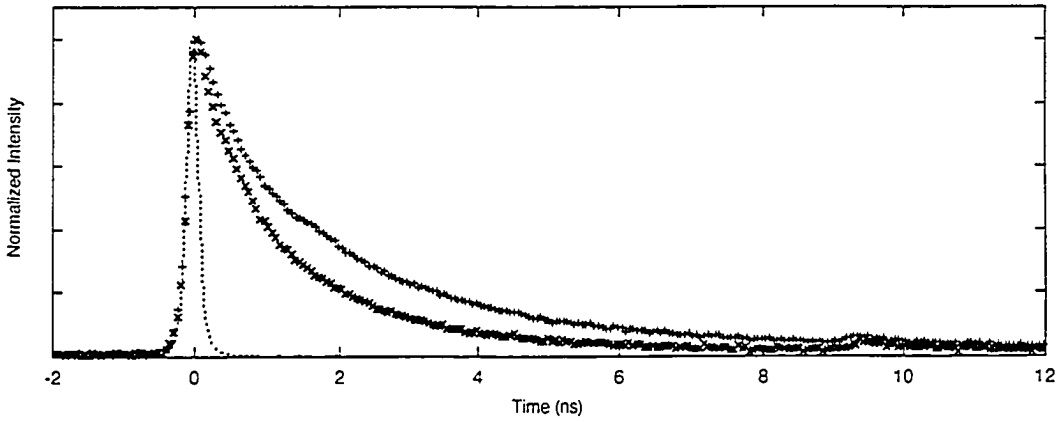

Figure 4.7 A comparison of nanosecond time-resolved luminescence traces collected at 500 nm of $Ru(dfmb)_3Cl_2$ in H_2O (+) versus $Ru(dfmb)_3(PF_6)_2$ in acetonitrile (×). Each plot includes the IRF (---). Every second data point is plotted for clarity.

4.2.3 Transient Absorption Spectroscopy

One of the great advantages of the femtosecond laser system setup is the capability to do both time-resolved luminescence and transient absorption spectroscopy, allowing the absorption and emission of samples to be studied under virtually identical conditions. In particular, the ruthenium complexes of interest can be studied by transient absorption spectroscopy at exactly the same excitation wavelength as used in the emission studies. As well, the transient absorption spectrometer has a time resolution of 305 fs,

allowing the initial dynamics of these complexes to be investigated with a resolution that is not accessible with the streak camera.

Figures 4.8 to 4.12 show the full spectrum transient absorption data for all five complexes collected over the first 15 ps after excitation with 388 nm radiation. These figures show that excitation at 388 nm of each of the complexes in aqueous solution produced a bleach signal corresponding to the position of the MLCT absorption band and is attributed to the loss of the ground-state population. The formation of this bleach signal was not instantaneous because the bleach signal overlapped with an intense, broad absorption band that extended throughout the bleach region (~ 475-650 nm). The intense absorption band decayed away within the IRF to form a broad, low level absorption that extended from 500 to 650 nm. Spectrochemical measurements[45] of $Ru(dmb)_3(PF_6)_2$ and $Ru(dpb)_3(PF_6)_2$ (the ligand is 4,4'-diphenyl-2,2'-bipyridine) in acetonitile after oxidation and reduction show that the broad, low level absorption consists of two overlapping absorption bands. Absorption of the reduced complex results in a broad band with a peak between 500 and 530 nm attributed to absorption by the reduced ligand species. Oxidation of the ruthenium metal complexes results in a broad absorption at ~640 nm; this has been assigned to ligand-to-metal charge transfer (LMCT) transitions between one of the neutral ligand π-orbitals and the oxidized metal center.[45,159] The LMCT transition for the species $Ru(dmeob)_3^{2+}$ has been reported[159] to have a peak at 730 nm after oxidation. Based on the similarity between the ligand structures investigated herein and those reported in the literature, the long-lived low level absorption band observed after excitation of the ruthenium complexes is assigned to absorption by the reduced ligand species in the 530 nm region and a LMCT transition in the red wavelengths (575-665 nm). The one exception is $Ru(dfmb)_3^{2+}$, which does not show any absorption in the 530 nm region (Figure 4.10).

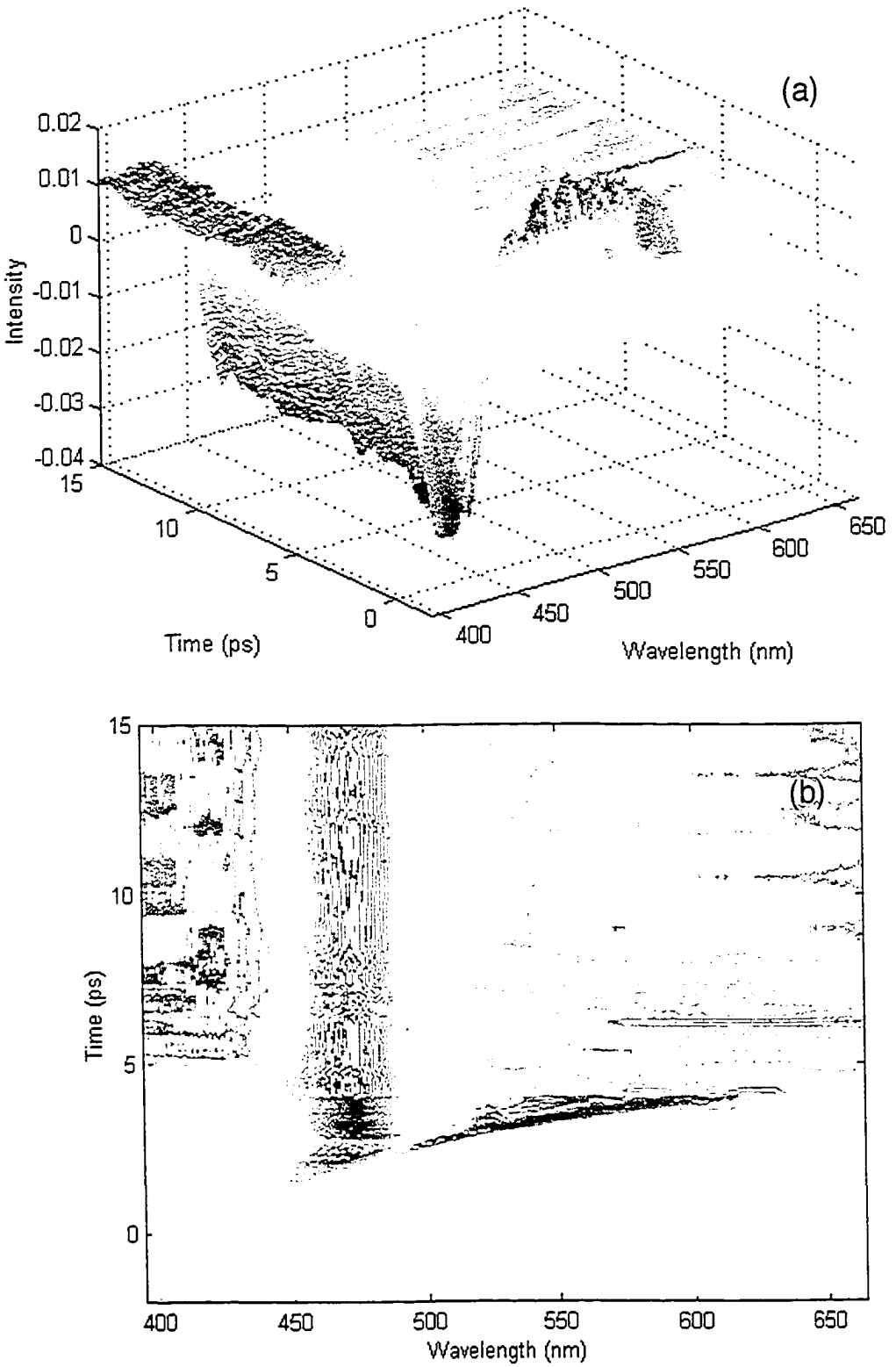

Figure 4.8 Full spectrum transient absorption data of $Ru(bpy)_3^{2+}$ after 388 nm excitation, investigating the first 12 ps. The colour scale is from blue to red, with blue representing the lowest intensities (bleach) and red representing the highest intensities (absorption). (a) A 3-dimensional plot. (b) The corresponding contour plot to (a).

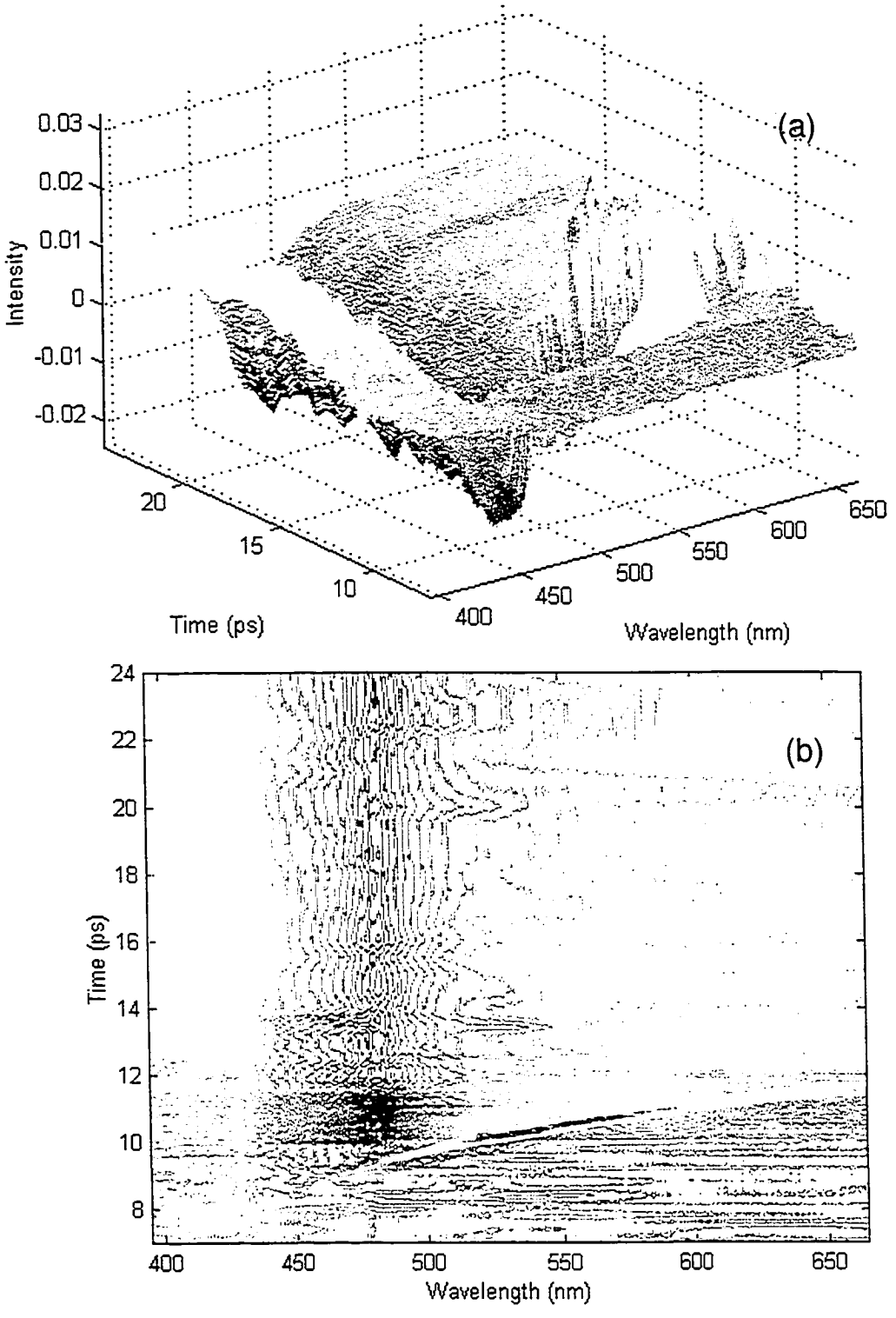

Figure 4.9 Full spectrum transient absorption data of $Ru(dmb)_3^{2+}$ after 388 nm excitation, investigating the first 12 ps. The colour scale is from blue to red, with blue representing the lowest intensities (bleach) and red representing the highest intensities (absorption). (a) A 3-dimensional plot. (b) The corresponding contour plot to (a).

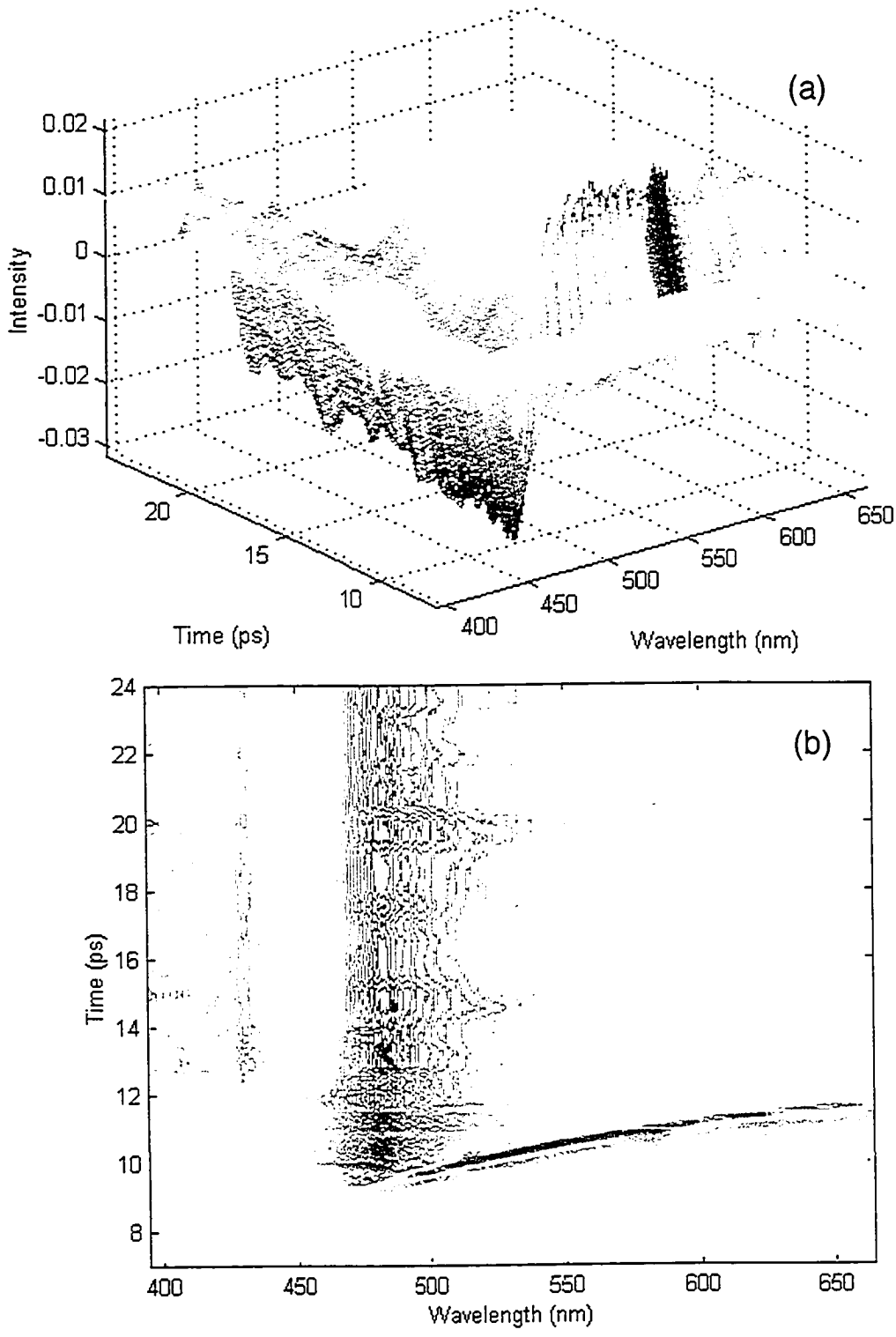

Figure 4.10 Full spectrum transient absorption data of $Ru(dfmb)_3^{2+}$ after 388 nm excitation, investigating the first 12 ps. The colour scale is from blue to red, with blue representing the lowest intensities (bleach) and red representing the highest intensities (absorption). (a) A 3-dimensional plot. (b) The corresponding contour plot to (a).

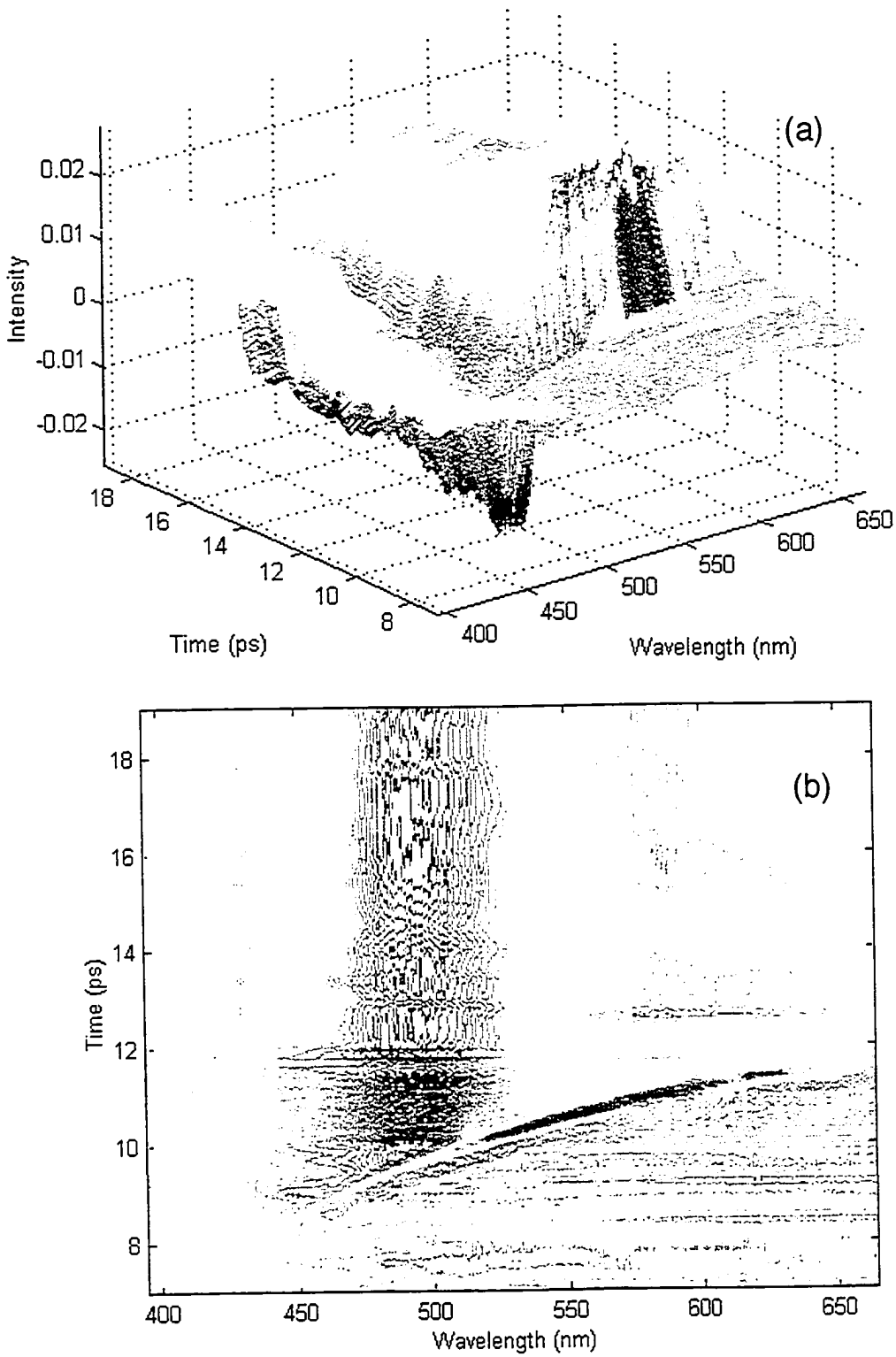

Figure 4.11 Full spectrum transient absorption data of $Ru(dmeob)_3^{2+}$ after 388 nm excitation, investigating the first 12 ps. The colour scale is from blue to red, with blue representing the lowest intensities (bleach) and red representing the highest intensities (absorption). (a) A 3-dimensional plot. (b) The corresponding contour plot to (a).

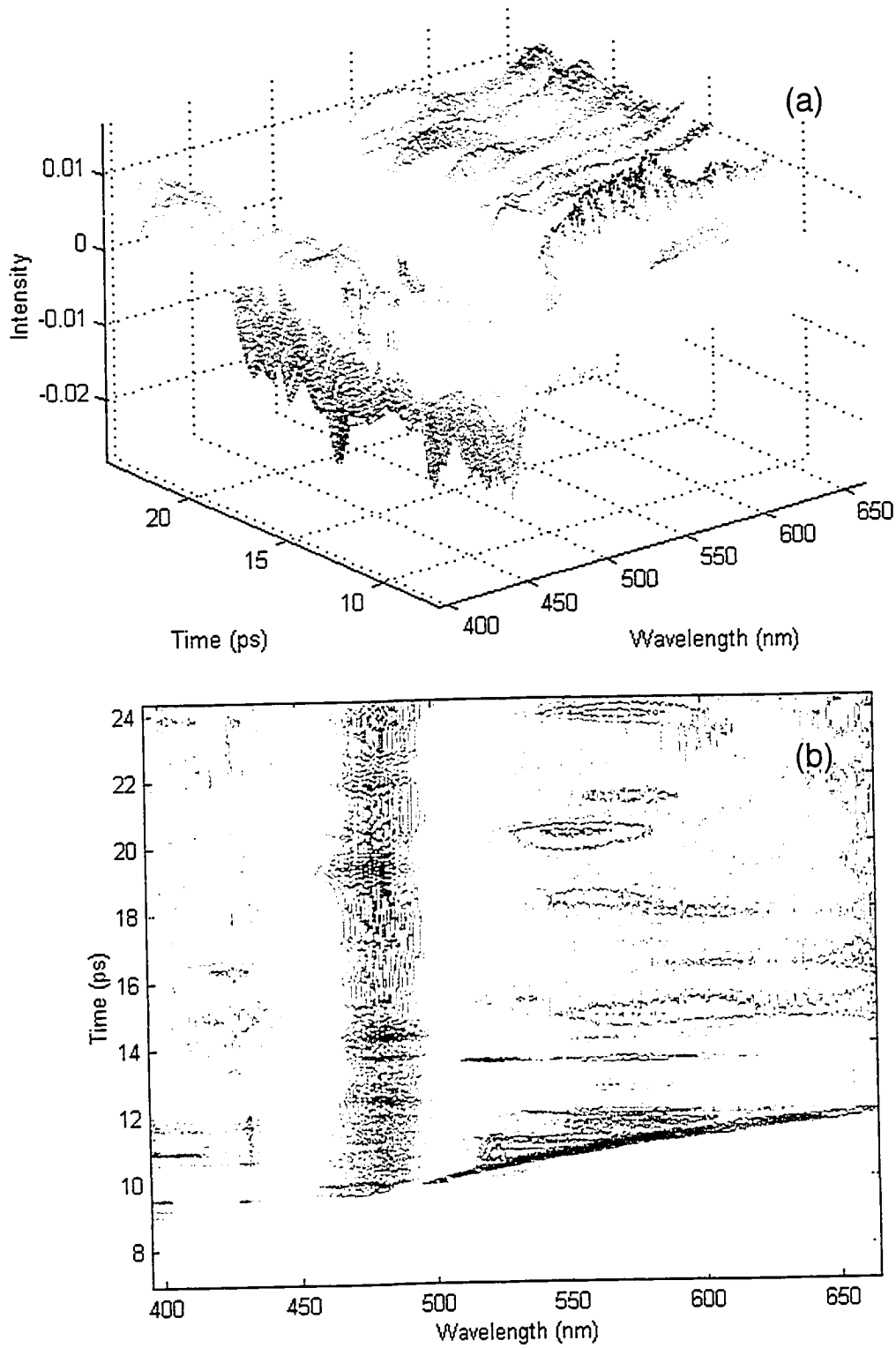

Figure 4.12 Full spectrum transient absorption data of $Ru(dttb)_3^{2+}$ after 388 nm excitation, investigating the first 12 ps. The colour scale is from blue to red, with blue representing the lowest intensities (bleach) and red representing the highest intensities (absorption). (a) A 3-dimensional plot. (b) The corresponding contour plot to (a).

Each of the full spectrum plots shows clearly the spectral shape of the fast transient absorption band. The contour plots not only highlight the chirp in the data, but also the short lifetime of the band, which is instrument response limited in all cases. Unchirped reconstruction of the data was accomplished using the USRP program (Chapter 2, section 2.2.4.2), producing unchirped spectra with zero time defined as the peak of the fast transient. The spectra at 0 and 1 ps for each of the five complexes are shown in Figure 4.13. In each of the spectra at zero time, the bleach signal is not clearly formed; however, this is likely due to the overlap of the strong bleach signal with the broad transient absorption band. Due to this overlap and cancellation effect, it is difficult to determine the exact shape of the broad absorption band.

The short-lived absorption band decayed away, producing the characteristic ground state bleach and the low intensity absorption band. After 1 ps, the shape of the spectrum was constant out to 15 ps. The position of the bleach signal was dependent upon the ligand complex: the more electron donating the substituent on the ligand, the lower energy the MLCT transition and thus the longer wavelength of the bleach signal. In all cases except for the $Ru(dmeob)_3^{2+}$ complex, the shape of the bleach signal is strangely V-shaped. This is due to the low spectral intensity of the probe beam wavelengths shorter than 450 nm produced by the sapphire plate, rendering the absorption spectrum inaccurate below 470 nm. A similar problem has been noted with other femtosecond spectrometers employing a sapphire plate.[26] For $Ru(dmeob)_3^{2+}$, the shape of the bleach signal is as predicted due to the MLCT transition being shifted to lower energy (500 nm).

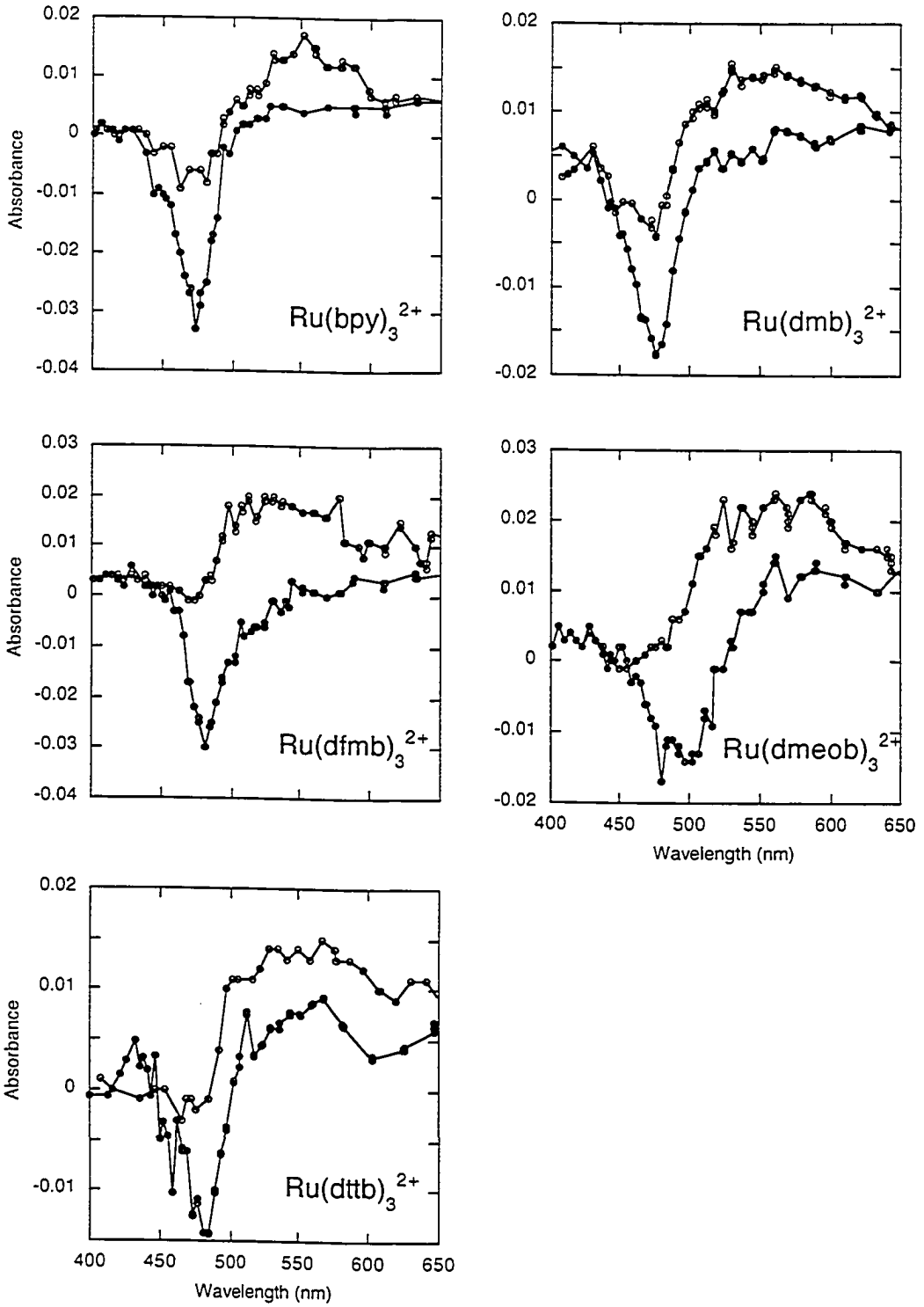

Figure 4.13 Unchirped, reconstructed spectra of all five ruthenium complexes at 0 ps (○) and 1 ps (●) after excitation at 388 nm.

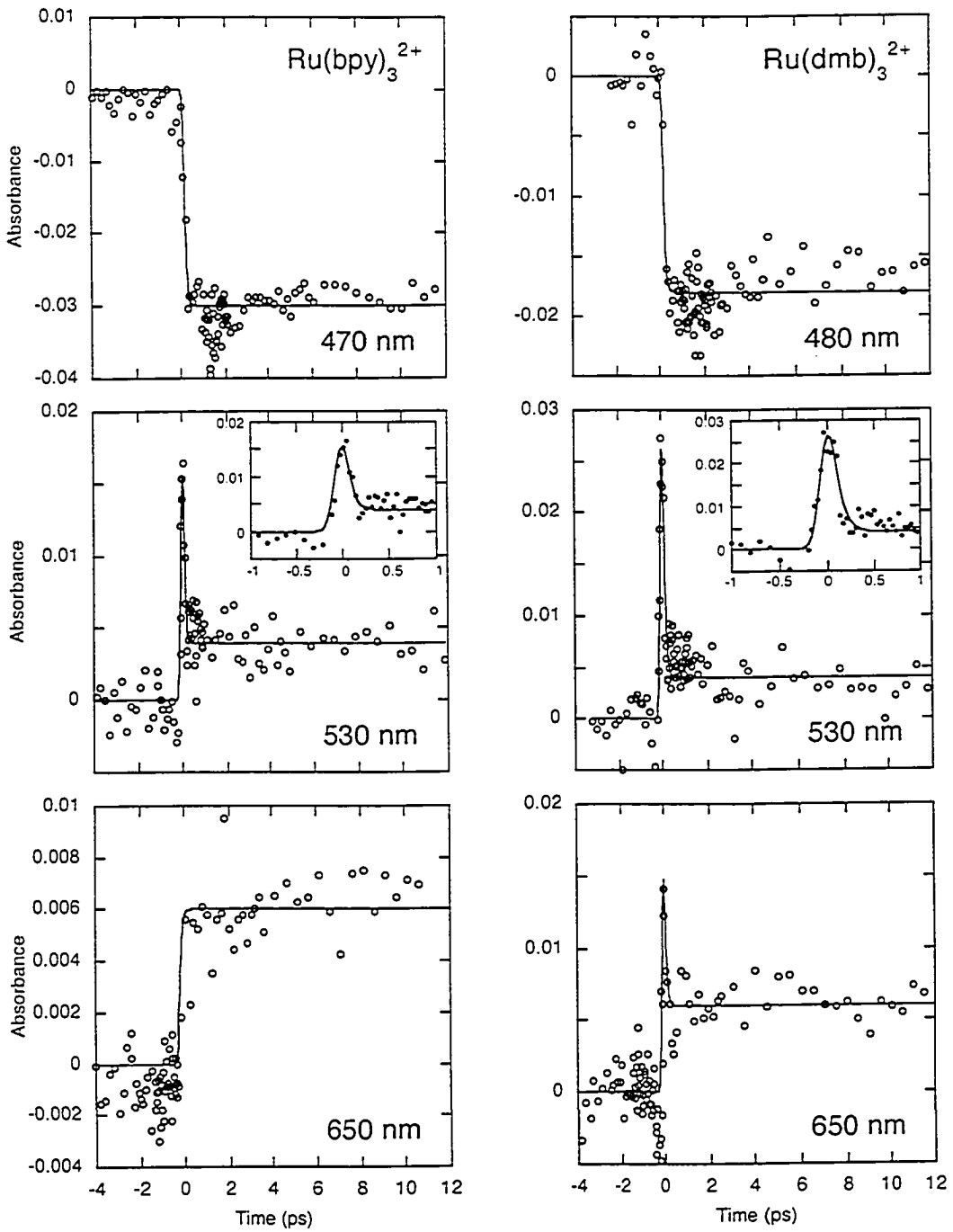

Figure 4.14 Kinetic profiles extracted from the full spectrum data at the bottom of the bleach signal (470, 480 nm), and at 530 nm and 650 nm of $Ru(bpy)_3^{2+}$ (left column) and $Ru(dmb)_3^{2+}$ (right column). For 530 nm, the inset is an expansion of the region -1 to 1 ps. The excitation wavelength is 388 nm. Solid lines are meant to be a guide for the eye.

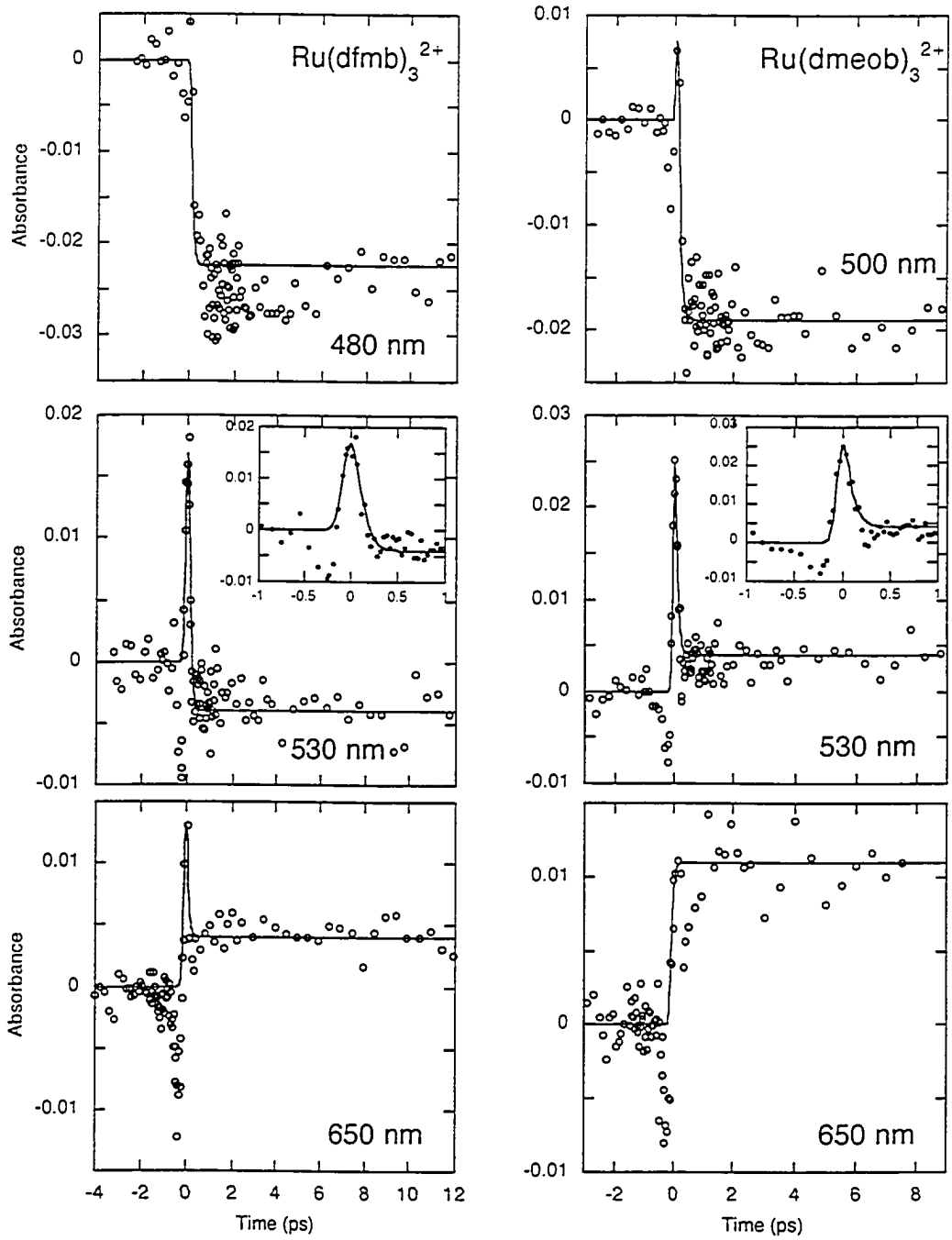

Figure 4.15 Kinetic profiles extracted from the full spectrum data at the bottom of the bleach signal (480, 500 nm), and at 530 nm and 650 nm of $Ru(dfmb)_3^{2+}$ (left column) and $Ru(dmeob)_3^{2+}$ (right column). For 530 nm, the inset is an expansion of the region -1 to 1 ps. The excitation wavelength is 388 nm. Solid lines are meant to be a guide for the eye.

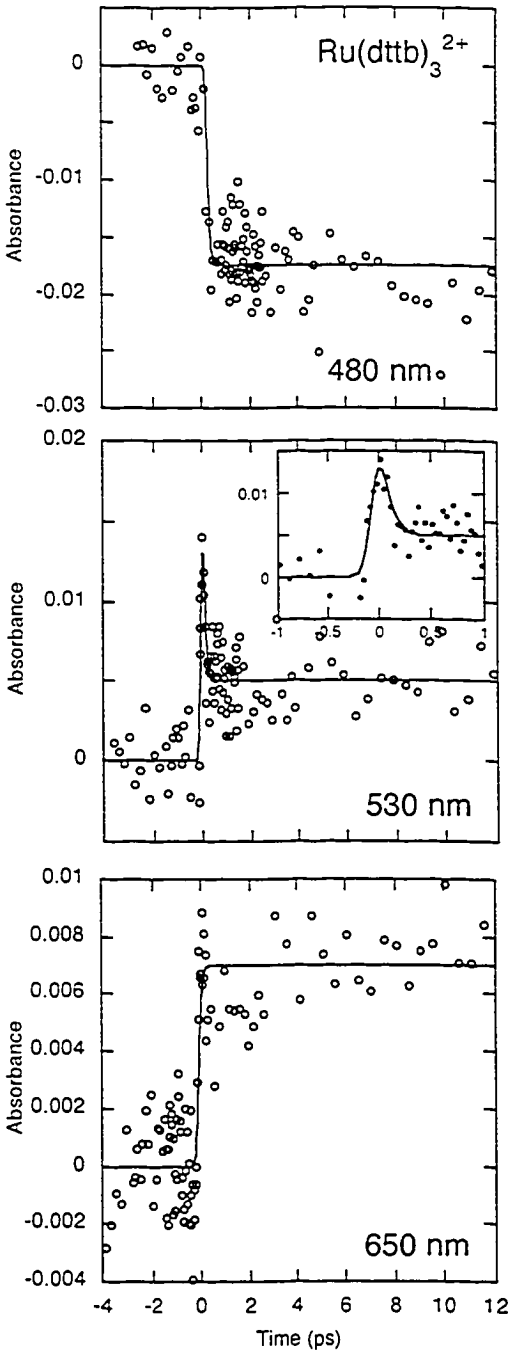

Figure 4.16 Kinetic profiles extracted from the full spectrum data at the bottom of the bleach signal at 480 nm, and at 530 nm and 650 nm of $Ru(dttb)_3^{2+}$. For 530 nm, the inset is an expansion of the region -1 to 1 ps. The excitation wavelength is 388 nm. Solid lines are meant to be a guide for the eye.

Kinetic profiles can be extracted from the full spectrum data at wavelengths of interest. In order to monitor evolution of the bleach signal, the reduced ligand, and the LMCT absorption, kinetic traces were extracted at 470 to 500 nm (bleach region), 530 nm (reduced ligand) and 650 nm (LMCT). These traces are shown in Figure 4.14 to Figure 4.16 with solid lines drawn in to guide the eye. Most striking about these plots are the traces at 530 nm showing the fast rise and decay of the short-lived absorption. In all cases, the rise and decay of this band was well within the instrument response limit of the spectrometer, Figure 4.17. The fast band was mainly seen in the traces at 530 nm, with very small hints of its presence out in the red wavelengths ($Ru(dmb)_3^{2+}$ and $Ru(dfmb)_3^{2+}$) or in the bleach region ($Ru(dmeob)_3^{2+}$). The lack of intensity of the fast band in the bleach region is likely in part due to the strong bleach signal masking the absorption signal.

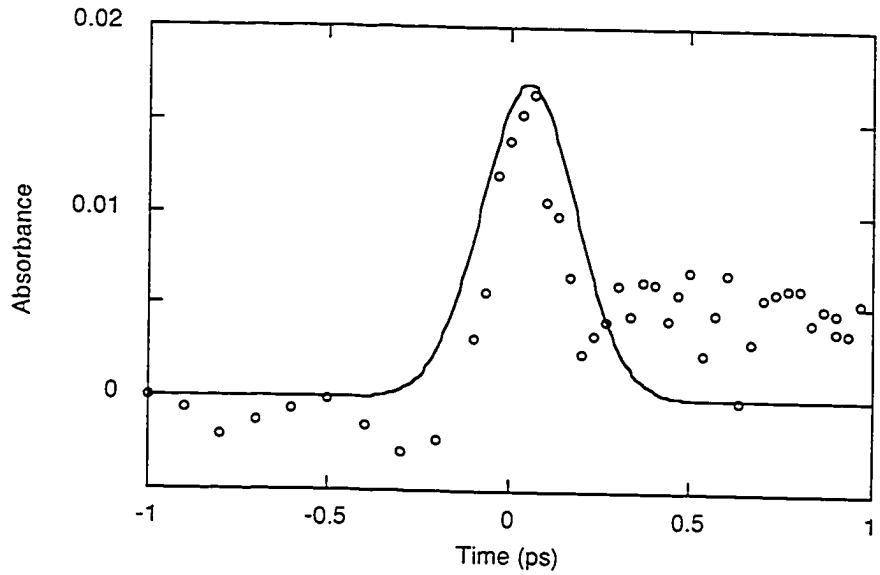

Figure 4.17 A comparison of the fast decay data of $Ru(bpy)_3^{2+}$ at 530 nm (○) with the IRF function (—), FWHM = 305 fs.

The presence of significant noise in the data rendered determination of decay rate constants with any reasonable certainty impossible. While previous researchers[45] have determined decay kinetics for $Ru(dmb)_3^{2+}$ in acetonitrile solution after 400 nm excitation to be biexponential ($\tau_1 = 120 \pm 40$ fs, $\tau_2 = 5 \pm 0.5$ ps), similar quantification of these data

is not possible due to the lower resolution of our instrument (305 fs *vs.* 220 fs, FWHMs of the IRF) and the presence of noise. However, several qualitative observations can be made. First of all, τ_1 is not observed at long wavelength excitation (λ_{ex} = 480 nm) for $Ru(bpy)_3(PF_6)_2$,[26] but is observed for both $Ru(bpy)_3(PF_6)_2$ and $Ru(dmb)_3(PF_6)_2$ at λ_{ex} = 400 nm.[45] We have now also observed τ_1 for $Ru(bpy)_3Cl_2$ and $Ru(dmb)_3Cl_2$ as well as for three more chloride salts of the same basic ligand structure with shorter wavelength excitation (λ_{ex} = 388 nm). Moreover, comparing the trace of the $Ru(dmb)_3(PF_6)_2$ complex with the kinetic trace in Figure 4.14 for $Ru(dmb)_3Cl_2$ shows that the intensity of the fast component absorption compared to the long lived component is much greater as the excitation wavelength is shortened from 400 to 388 nm.

The fluorescence studies described in the previous section displayed a long-lived fluorescence emission that had a lifetime in the low nanoseconds. In order to help identify the source of this luminescence, transient absorption spectroscopy was used to monitor the excited state evolution out to 5 ns on all five compounds using the water cell as a broadband source with the anticipation that spectral changes over this time period would yield similar kinetic data to that observed in the emission studies. Full spectral data plots are shown in Figures 4.18 to 4.22.

Observations every 100 ps from -0.5 ns to 5 ns produced spectra identical in shape, if not intensity, to the spectra recorded at 1 ps in Figure 4.13. All spectra appeared to remain unchanged over the time period investigated. The spectra collected at 100 ps and at 5 ns for each compound are plotted in Figure 4.23. Although the absolute intensity varies somewhat due to noise, no discernable kinetics were observed at any wavelength.

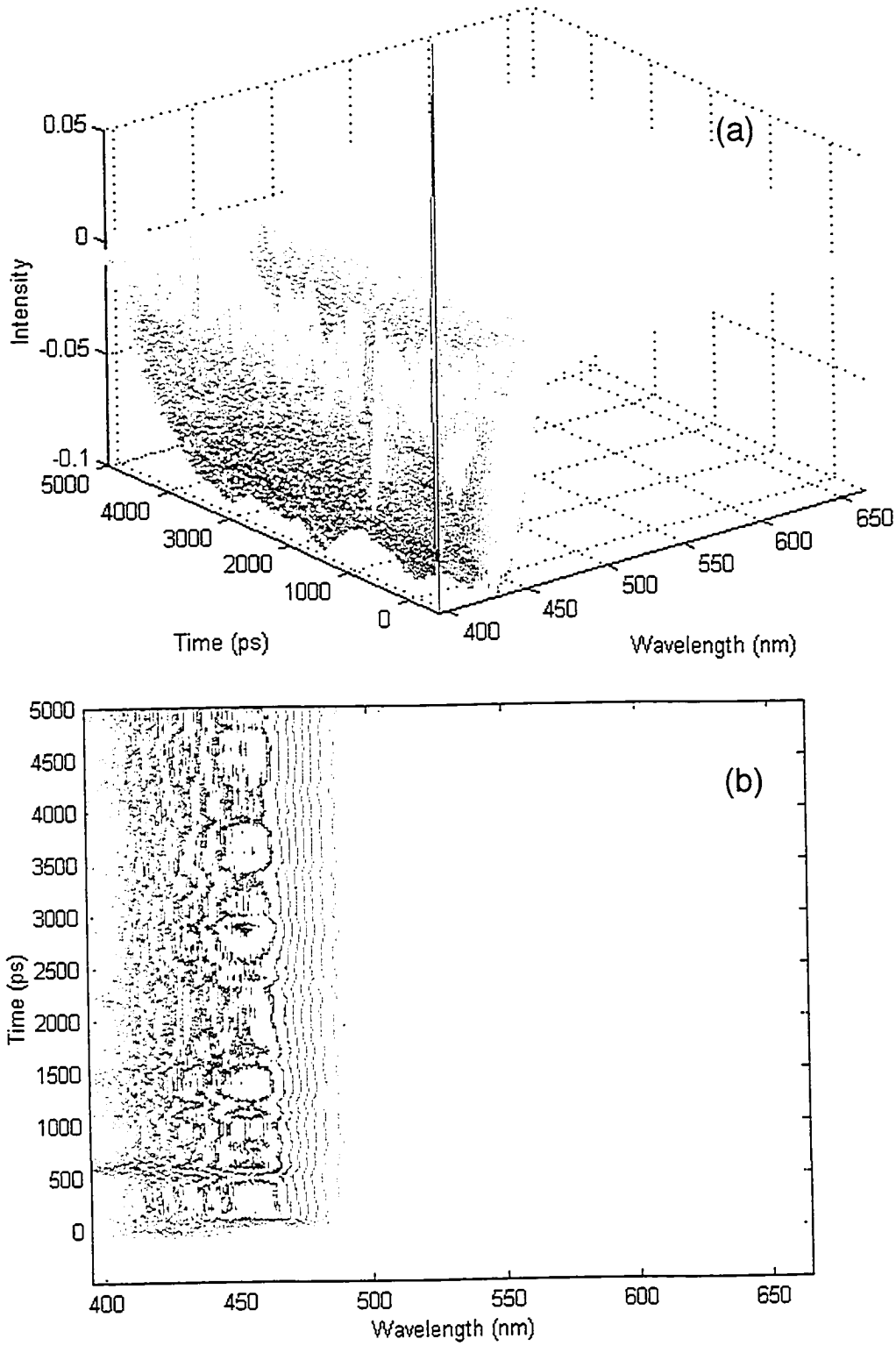

Figure 4.18 Full spectrum transient absorption data of $Ru(bpy)_3^{2+}$ after 388 nm excitation, from -0.5 to 5 ns. The colour scale is from blue to red, with blue representing the lowest intensities (bleach) and red representing the highest intensities (absorption). (a) A 3-dimensional plot. (b) The corresponding contour plot to (a).

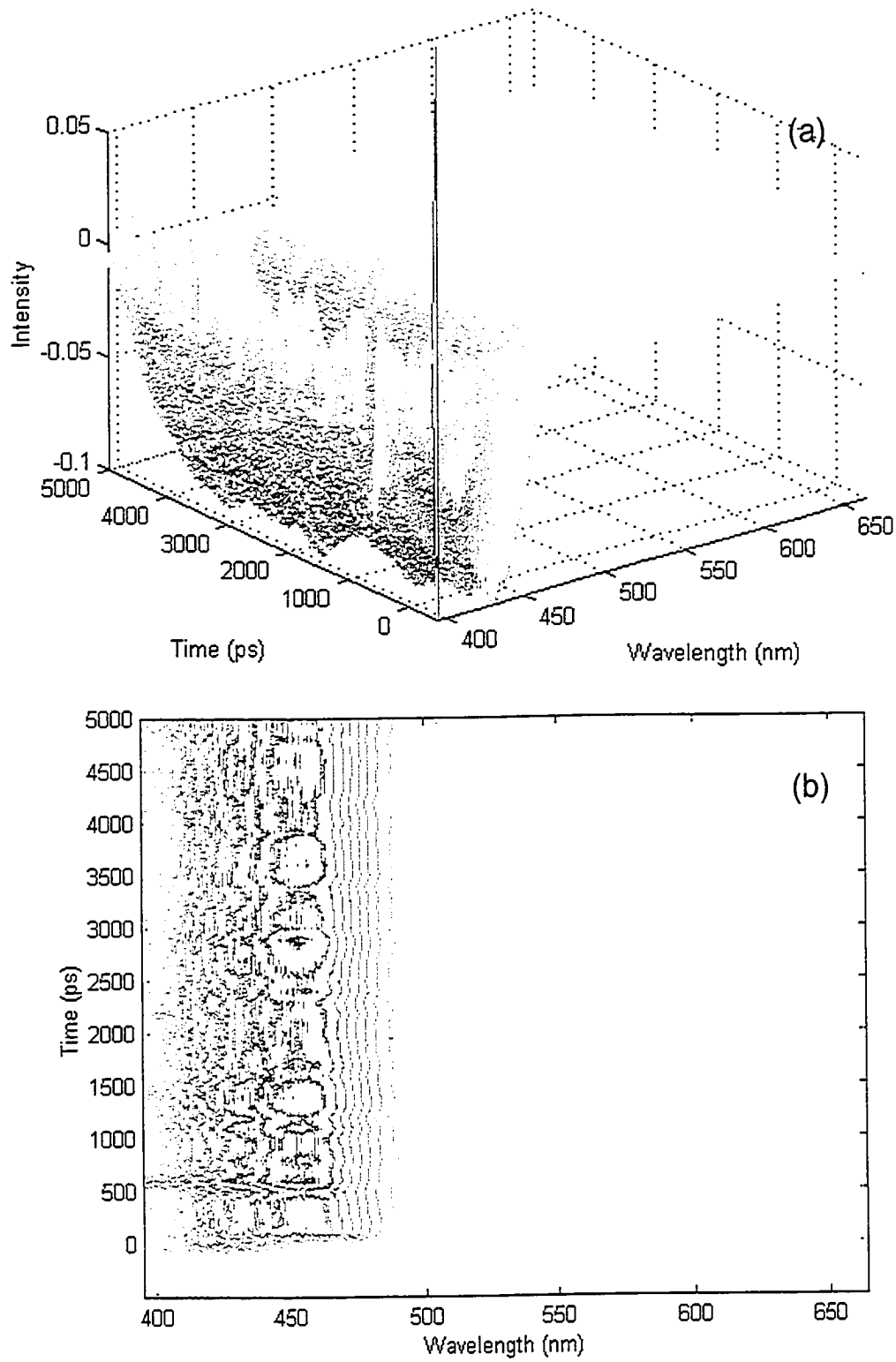

Figure 4.19 Full spectrum transient absorption data of $Ru(dmb)_3^{2+}$ after 388 nm excitation, from -0.5 to 5 ns. The colour scale is from blue to red, with blue representing the lowest intensities (bleach) and red representing the highest intensities (absorption). (a) A 3-dimensional plot. (b) The corresponding contour plot to (a).

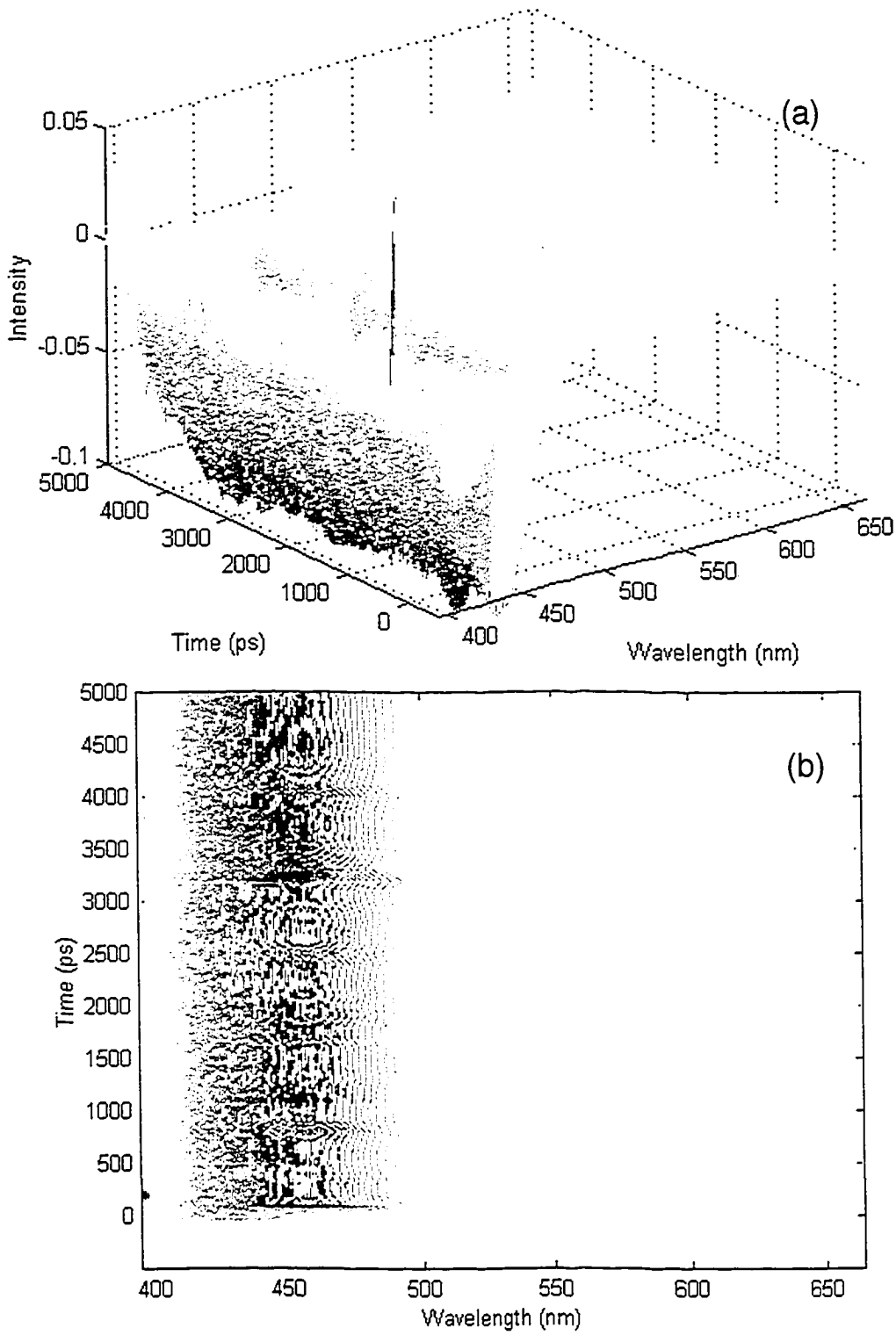

Figure 4.20 Full spectrum transient absorption data of $Ru(dfmb)_3^{2+}$ after 388 nm excitation, from -0.5 to 5 ns. The colour scale is from blue to red, with blue representing the lowest intensities (bleach) and red representing the highest intensities (absorption). (a) A 3-dimensional plot. (b) The corresponding contour plot to (a).

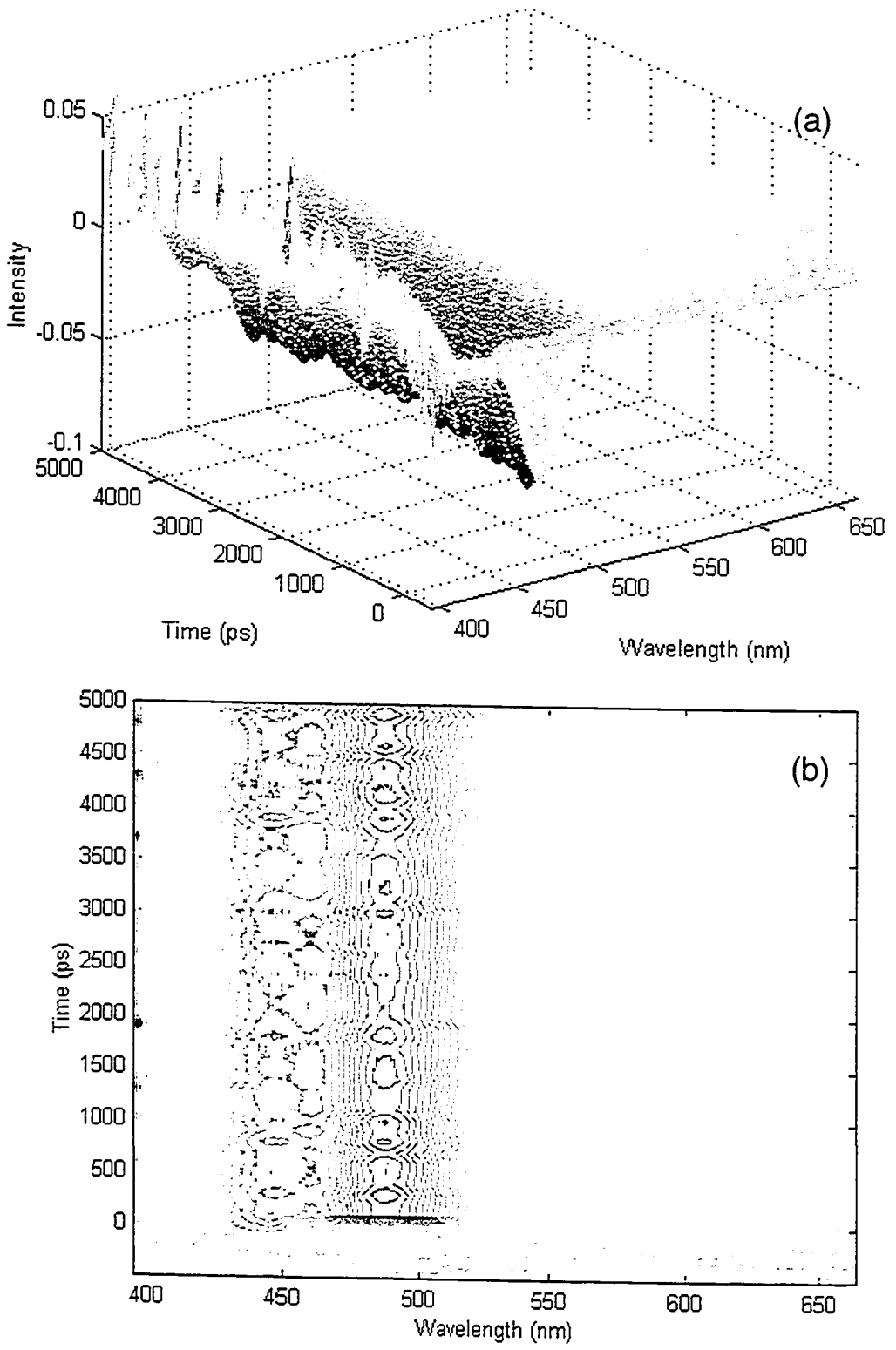

Figure 4.21 Full spectrum transient absorption data of $Ru(dmeob)_3^{2+}$ after 388 nm excitation, from -0.5 to 5 ns. The colour scale is from blue to red, with blue representing the lowest intensities (bleach) and red representing the highest intensities (absorption). (a) A 3-dimensional plot. (b) The corresponding contour plot to (a).

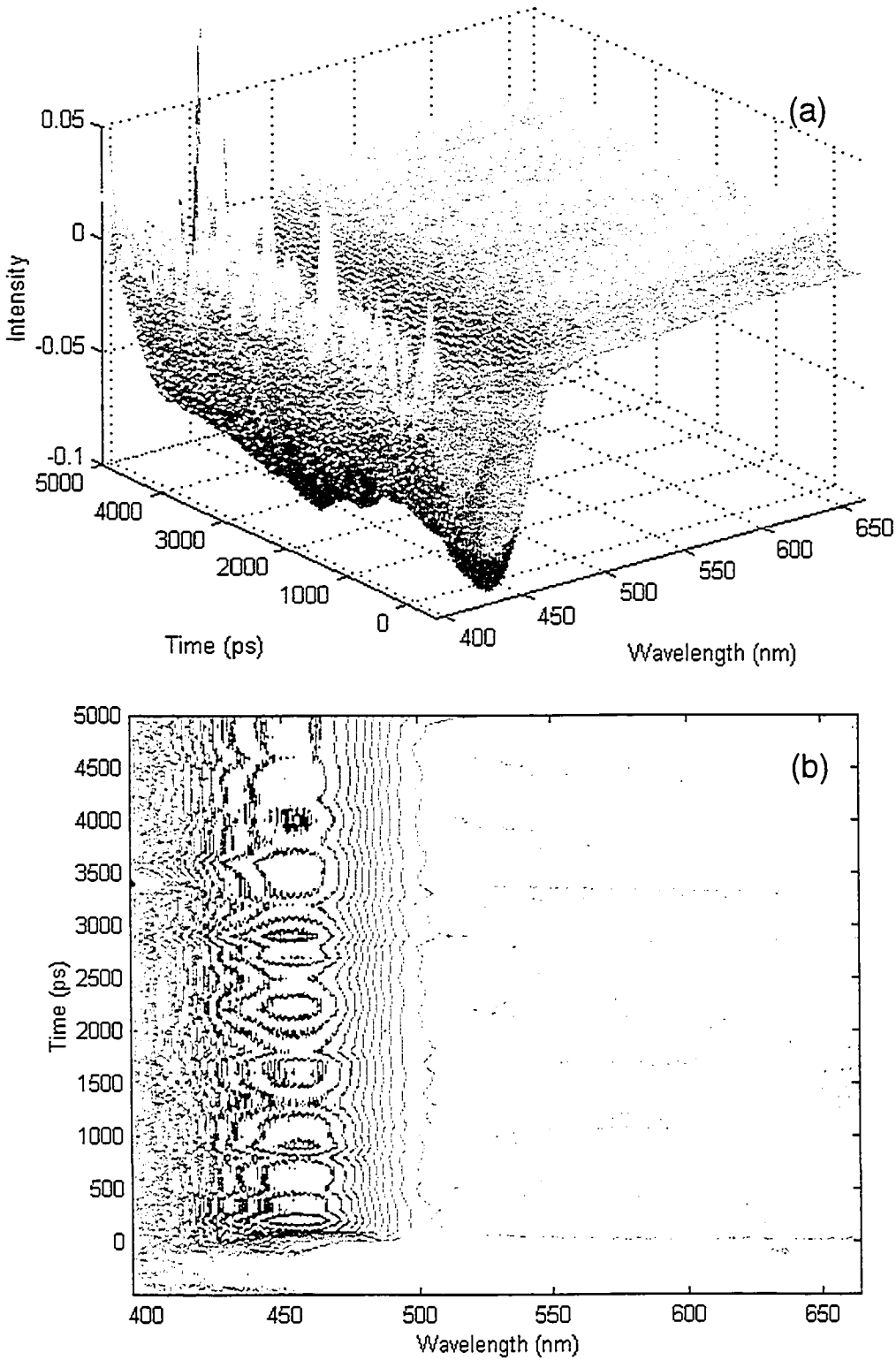

Figure 4.22 Full spectrum transient absorption data of $Ru(dttb)_3^{2+}$ after 388 nm excitation, from -0.5 to 5 ns. The colour scale is from blue to red, with blue representing the lowest intensities (bleach) and red representing the highest intensities (absorption). (a) A 3-dimensional plot. (b) The corresponding contour plot to (a).

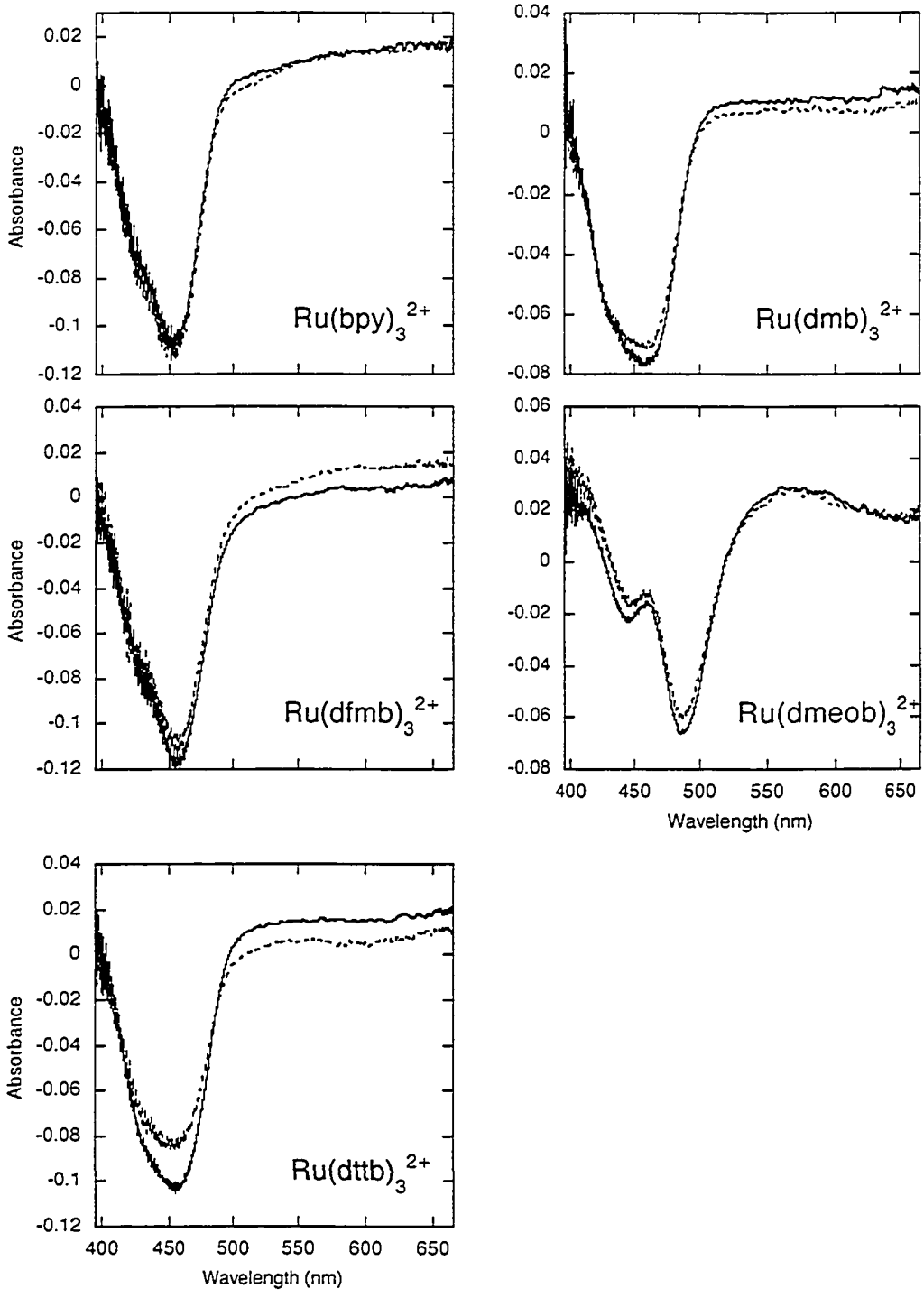

Figure 4.23 Transient absorption spectra of all five ruthenium metal complexes, 0.1 ns (—) and 5 ns (---) after excitation with 388 nm radiation.

The shapes of the bleach signal varied greatly from the ultrafast transient data to the nanosecond data. Figure 4.24 compares the unchirped spectrum of $Ru(dmb)_3^{2+}$ taken 1 ps after excitation with the spectrum taken 100 ps after excitation; the probe beam of the former was generated by a sapphire plate while the probe beam of the latter was generated by the water cell. As discussed earlier, the dramatic difference in the shape of the bleach signal is due to low probe beam intensity at short wavelengths produced by the sapphire plate. The shape of the bleach signal recorded using the water cell for broadband production is the negative of the MLCT bands observed in Figure 4.4, confirming that the bleach signal is indeed due to loss of the ground state MLCT band.

In order to produce Figure 4.24, the unchirped spectrum of $Ru(dmb)_3^{2+}$ had to be scaled by a factor of two to match the absorbance values recorded on the 100 ps spectrum. Because the transient absorption spectrometer has not been characterized by actinometry, the absorbance values reported in the plots shown are not absolute values. However, within each data set the relative absorption intensities are consistent and the kinetics observed are valid.

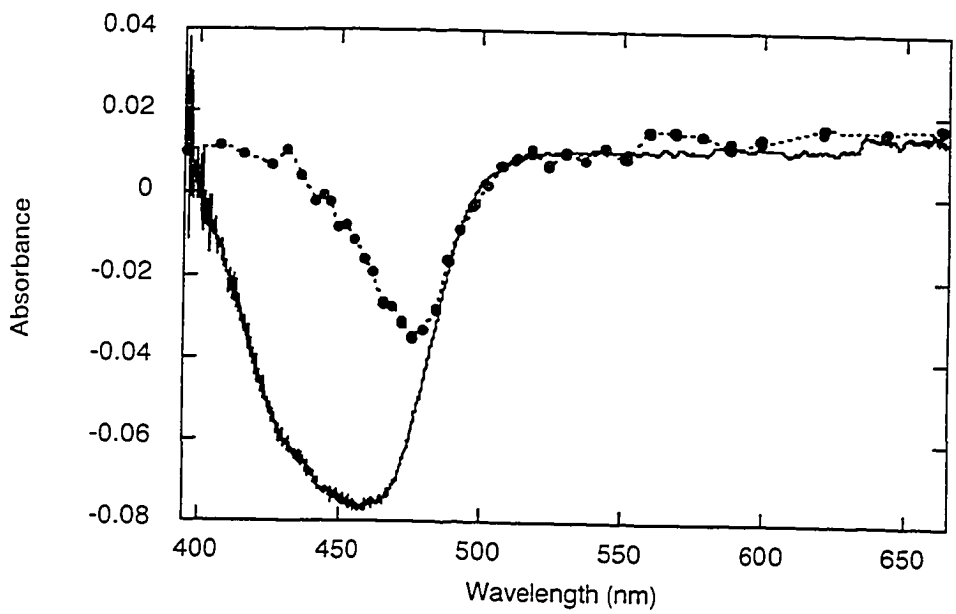

Figure 4.24 A comparison of the shape of the transient absorption spectrum of $Ru(dmb)_3^{2+}$ taken 1 ps (●) and 100 ps (—) after excitation with 388 nm radiation. The probe pulse for the spectrum at 1 ps is generated using the sapphire plate while the probe pulse for the latter spectrum is generated using the water cell. The sapphire plate generates insufficient intensity of light of wavelengths shorter than 470 nm to accurately detect a signal.

4.3 Discussion

The observations presented above add to a growing amount of ultrafast experimental data measured for ruthenium(II) metal complexes that have 4,4'-bipyridine based ligands. These transition metal complexes do not exhibit the photophysical behaviour associated with organic chromophores: namely, that $\tau_{IVR} << \tau_{IC} << \tau_{ISC}$. This is presumably due to a large amount of singlet-triplet surface mixing in transition metal complexes, which allows very rapid ISC (*i.e.* 40 fs). In essence, these experiments aim to investigate complex photophysics and describe them using simplified models. Between the literature data and the data presented in the results section, there are multiple lifetimes measured. Table 4.2 summarizes the notation used for this discussion.

Table 4.2 Summary of the notation used to describe various lifetimes measured for $Ru(bpy)_3^{2+}$ derivatives.

Label	Description	Measured Lifetime
τ_1	transient absorption kinetics; fast component at 532 nm	120 ± 40 fs[45]
τ_2	transient absorption kinetics; slow component at 532 nm	5 ± 0.5 ps[45]
τ_3	emission decay; fast component at 500 nm	< 3-5 ps
$\tau_{4,5}$	emission decay; long-lived component at 500 nm	0.7 - 6 ns

Most of the data presented in the results section used 388 nm radiation as the excitation wavelength. The primary assumption is that 388 nm, though on the blue side of the MLCT band, is primarily exciting the MLCT transition.[157] Varying the excitation wavelength of the steady state fluorescence spectra of the ruthenium complexes studied from 450 nm to 388 nm did not yield a significant difference in the shape or intensity of the resulting ^{3}MLCT emission, lending evidence to the validity of this assumption. 258 nm excitation, although also into an MLCT transition, is close to a LC transition and is not likely to be exciting into the same manifold.

The model put forth by the Okada and McCusker groups[33,154] to describe the photophysical behaviour of $Ru(bpy)_3^{2+}$ is pictured in Figure 4.25. Excitation into the MLCT band results in ultrafast fluorescence and intersystem crossing from a non-

thermalized ^{1}MLCT state, with the time constant of 40 fs. Although the streak camera data reported here does not have the resolution of fluorescence up-conversion experiments used to obtain the value of 40 fs, it is likely that the instrument response limited fluorescence at 500 nm encompasses the 40 fs time constant and thus reflects ^{1}MLCT-^{3}MLCT surface crossings and vibrational cooling.[157] The observation of the second luminescence component $\tau_{4,5}$, however, for $Ru(bpy)_3^{2+}$ derivatives with a lifetime of 0.7 to 6 ns has not been reported previously, and no transient absorption or fluorescence up-conversion lifetimes have been reported that are on the same time scale. Probing the photophysics with the transient absorption spectrometer out to 5 ns reveals no transient absorption kinetic or spectral information that may indicate the origin of this emission. In essence, the state giving rise to the second luminescence component is not obvious in transient absorption experiments.

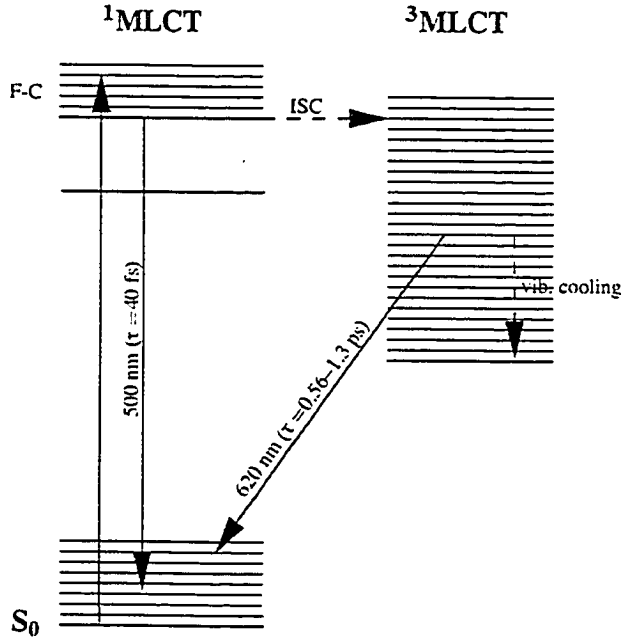

Figure 4.25 Proposed model for non-thermalized excited state decay in $Ru(bpy)_3^{2+}$. Figure reproduced from reference 157.

Because the lifetime of the second fluorescence component ($\tau_{4,5}$) is significantly slower than the 40 fs time constant for ISC, we assume that $\tau_{4,5}$ does not reflect singlet surface dynamics. However, $\tau_{4,5}$ likely does not originate from upper vibrational states of the ^{3}MLCT manifold either because vibrational cooling takes place on the order of 0.5 to

5 ps, and hot band-to-hot band fluorescence has been observed[33] with a lifetime of 620 fs at 600 nm, a wavelength that cannot be observed on the streak camera due to interference from ^{3}MLCT emission. Thus, $\tau_{4,5}$ has been assigned to emission from State C, where State A corresponds to the ^{1}MLCT manifold and State B corresponds to the ^{3}MLCT manifold (Figure 4.26).[157] State C could either be a local minimum on the potential energy surface of State B or a distinct state altogether. Excitation to a sufficiently high level within State A produces emission from a non-thermalized state and ISC to both States B and C, which is reflected in the instrument response limited component of fluorescence observed with 388 nm excitation (τ_3). $\tau_{4,5}$ describes emission from State C and other radiationless deactivation pathways. It is unclear at this point as to why State C is not accessible to $Ru(bpy)_3^{2+}$ at λ_{ex} = 388 nm, when all the derivatives do exhibit $\tau_{4,5}$ whether their substituents are electron donating or withdrawing. One possible explanation is that the presence of the substituent itself introduces large amplitude motions that couple State A to otherwise inaccessible states.

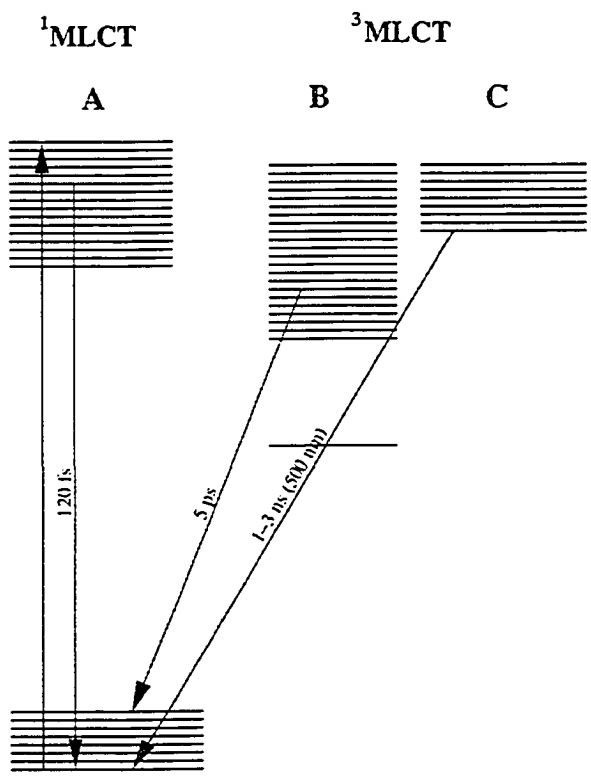

Figure 4.26 Jablonski diagram for $Ru(bpy)_3^{2+}$ derivatives modified to include $\tau_{4,5}$. Figure reproduced from reference 157.

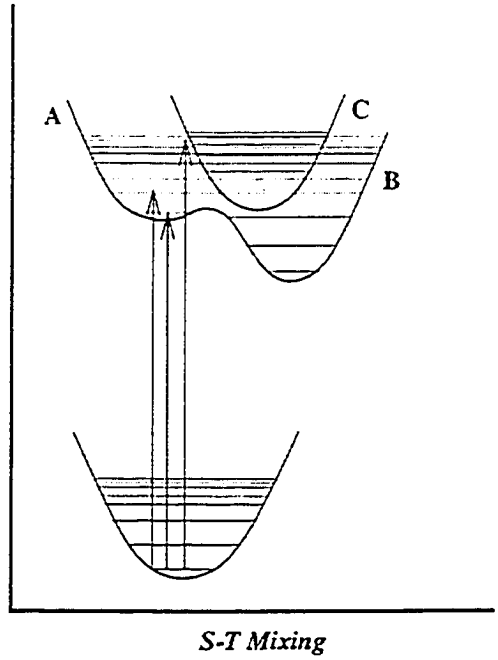

Figure 4.27 Potential energy surface diagram depicting the influence of excitation energy on population dynamics where the abscissa indicates the degree of singlet-triplet mixing. Figure reproduced from reference 157.

Figure 4.27 emphasizes the influence of excitation wavelength on the observed emission behaviour. Excitation to the lowest levels of ^{1}MLCT prevents access to State C and higher levels of State B, and should affect the kinetics observed in transient absorption data. Wavelength dependent kinetic behaviour is observed in the femtosecond and picosecond transient absorption data reported for $Ru(bpy)_3^{2+}$ and $Ru(dmb)_3^{2+}$ at 532 nm.[26,45] When excited at 480 nm, no further spectral changes are observed after the first 300 fs; however, after 400 nm excitation, biexponential kinetics are observed consisting of a fast decay (τ_1 = 120 fs) and a slower component (τ_2 = 5 ps). The ultrafast transient absorption data at 530 nm reported in the results section also show a fast decay component within the IRF of the instrument (305 fs) followed by a longer plateau which may or may not encompass a decay that is masked by a poor signal to noise ratio. From comparison of the $Ru(dmb)_3^{2+}$ data excited at 388 nm with the reported data with 400 nm excitation, it is likely that the fast decay τ_1 measured by Damrauer *et al.* is contained within by the instrument response limited decay observed after 388 nm excitation. Both $Ru(dmb)_3^{2+}$ and $Ru(bpy)_3^{2+}$ are reported to exhibit τ_1 with 400 nm excitation although a

value has not been reported for τ_1 for the latter. Even so, the lack of τ_1 after 450 nm excitation, followed by the presence of τ_1 with 400 nm excitation as well as now 388 nm excitation, indicates that τ_1 is due to some process within the higher vibrational levels of the triplet manifold which can only be accessed by higher energy excitation. Moreover, the observation that the relative size of the fast component versus the long-lived plateau height increased as a function of increasing excitation energy also suggests that these higher energy states either have increased oscillator strength with respect to the thermalized ^{3}MLCT state, or are more easily populated and thus more of these higher energy states are being accessed. Unfortunately, our instrument does not have the resolution necessary to determine whether increasing the excitation energy also affects the magnitude of τ_1.

By comparison of the ultrafast transient absorption data for $Ru(dmb)_3^{2+}$ and $Ru(bpy)_3^{2+}$ complexes with the remainder of the complexes, very similar behaviour is seen. τ_1 exists for all three of the other compounds after 388 nm excitation. Thus, τ_1 for these complexes also likely represents evolution within ^{3}MLCT. It is curious that the electronic effects of the substituent do not appear to have an influence on the initial behaviour of these compounds. However, this may be due to the inability of the transient absorption spectrometer to resolve τ_1. The electronic effect of the substituent would affect the energy of the ligand orbitals, perhaps changing the coupling between the initially accessed levels and the thermalized ^{3}MLCT state and thus affecting τ_1.

The four τ values that have been discussed represent the dynamics observed in emission and absorption measurements on the same complexes with the same excitation wavelengths. Therefore τ_1 and τ_2 of the transient absorption data should be related to the luminesence lifetimes τ_3 and $\tau_{4,5}$. It is not immediately obvious where $\tau_{4,5}$ is represented in the transient absorption data. The state giving rise to $\tau_{4,5}$ either does not absorb in the wavelength window used in the transient absorption experiment, or the amplitude change giving rise to $\tau_{4,5}$ is so subtle that it is not apparent with the current signal to noise ratio of the instrument. Comparisons between the magnitude of τ_3 (the short luminescence component), and the transient absorption decay values of τ_1 and τ_2 indicate that the instrument response limited τ_3 encompasses both τ_1 and τ_2. This comparison is severely limited by the resolution limitations of the current femtosecond spectrometer setup.

4.4 Concluding Comments

In summary, time-resolved fluorescence and transient absorption spectroscopy has been used to study the initial photophysics of $Ru(bpy)_3^{2+}$, $Ru(dmb)_3^{2+}$, $Ru(dfmb)_3^{2+}$, $Ru(dmeob)_3^{2+}$, and $Ru(dttb)_3^{2+}$ using high energy excitation at 388 nm. These studies have revealed that for the compounds other than $Ru(bpy)_3^{2+}$, at 500 nm, a fluorescence decay component ($\tau_{4,5}$ = 0.7 to 6 ns) has been observed in addition to the instrument response limited decay. This suggests that there exists a higher lying emissive state, which is not accessed when longer excitation wavelengths are being used. Transient absorption data on the nanosecond time scale have failed to produce any obvious spectral changes that correspond to $\tau_{4,5}$ observed by fluorescence.

Ultrafast transient absorption spectroscopy has shown that fast decay kinetics similar to τ_3 that has been observed previously for $Ru(bpy)_3^{2+}$ and $Ru(dmb)_3^{2+}$ are also observed at shorter wavelength excitation for all five compounds. Relative absorption intensities indicates that exciting at shorter wavelengths results in an increase in the relative amount of higher energy states being accessed within ^{3}MLCT. While quantitative kinetic data cannot be extracted from the full spectrum data recorded for these compounds, the observation of the fast decay component indicates that there is a large wavelength dependence of the initial dynamics after excitation, and that this is an area that requires further study to fully understand the early photophysics of ruthenium(II) metal complexes.

Chapter 5: Experimental

5.1 Characterization of the Transient Absorption Spectrometer

5.1.1 Materials

Chloranil (Aldrich) was recrystallized from ethanol to yield pale yellow crystals. Solutions of chloranil (5 mM) were made with spectrophotometric grade dichloromethane (EM Science). 1-Methylnaphthalene (Aldrich, 99%) was used as received. Solutions of 1-methylnaphthalene were prepared in spectroscopic grade acetonitrile (99%; Aldrich).

5.2 Zeolite Samples

5.2.1 Materials

Pyrene (Aldrich, 99+%) was recrystallized from ethanol prior to use and 9,10-dicyanoanthracene (9,10-anthracenedicarbonitrile, Aldrich) was used as received. Stock solutions of pyrene were prepared in hexane (99%; BDH, Omnisolv™) while stock solutions of DCA were prepared in dichloromethane (99%; Omnisolv™). Both solvents were of spectroscopic grade (<0.02% water) and were used as received. Spectroscopic grade hexane was also used for the zeolite sample preparation and co-solvent incorporation. Nanopure water used for solvent co-incorporation was produced in house by distillation followed by deionization. Methanol was also used as a co-solvent; it was HPLC grade (VWR) and used as received.

NaY (LZY52 molecular seives, Si/Al = 2.4) and NaX (Si/Al = 1.2) were obtained from Aldrich and used as received. Cation-exchanged Y zeolites used in this thesis project were prepared by the standard aqueous cation exchange method.[160] 15 g of NaY were stirred with 1M aqueous solutions of the corresponding chloride salt at 80 °C for one hour, followed by rinsing of the zeolite with nanopure water until no chlorides were found in the rinse water by testing with silver nitrate. The procedure was repeated twice more with calcination of the zeolite at 450 °C between exchanges. Cation exchange is less than 100% due to the inaccessibility of the innermost type I cations for exchange.[64]

Typical cation exchanges are 45% for LiY, 85% for KY, 73% for RbY and 62% for CsY.[161]

5.2.2 Sample Preparation

Each sample of zeolite was baked at 500 °C overnight (16 - 20 h) to facilitate water removal. Pyrene samples were made in batches, requiring 1.3 g of zeolite, while DCA samples were made in single sample quantities and required 300-450 mg of zeolite. The activated zeolite was transferred in air and allowed to cool for one minute before 20 mL of hexane (carrier solvent) and the stock solution of pyrene or DCA was added. This zeolite slurry was stirred magnetically for 2 h, after which time the suspension was centrifuged and decanted. A further aliquot of 20 mL hexane was added to the pyrene/zeolite and stirred for an additional 20 minutes. The supernatant was removed after centrifugation and both decants were analyzed to determine loading levels by UV-visible spectroscopy. Typical loading levels for pyrene samples <S> were 1 pyrene per 32 cavities for NaY, 61 cavities for LiY, 22 cavities for KY, and 9 cavities for NaX.

The impregnated zeolites were placed into a vacuum desiccator and evacuated for 4 h. Batch samples were then split into four solvent incorporation quartz cells under a dry nitrogen atmosphere in a glovebag, while single samples were transferred in their entirety into regular quartz cells. The quartz cells consisted of a flat chamber at the bottom to house the zeolite sample, glass tubing extending upwards from the chamber to allow for attachment to a vacuum line. Solvent incorporation quartz cells had a small arm fused onto the glass tubing of a regular quartz cell to allow for solvent incorporation. The samples were then placed on a vacuum line and evacuated with a diffusion pump at a pressure of 10^{-4} torr for a minimum of 12 h. One sample was flame sealed on the vacuum line and the remaining three samples, used for solvent incorporation studies, were sealed with rubber septa and parafilm under dry nitrogen in the glovebag. During the sample preparation the utmost care was taken to keep the zeolite samples dry.

Pyrene samples were always studied the day directly following sample preparation with all solvent incorporation studies complete within 12 hours, in order to avoid significant redistribution of the incorporated molecules within the zeolite by intercavity

diffusion.[54] Over the course of an experiment of 12 hours, the amount of excimer emission in the control sample is decreased only slightly and monomer emission is not significantly increased, indicating that redistribution was not signficiant over this time period.

DCA samples were kept under vacuum for the duration of experiments. In order to maintain constant vacuum conditions for the duration of the aging experiment, those samples were flame sealed under vacuum and stored at room temperature. Samples ranged from white to pale yellow, depending upon the loading level of DCA in the zeolite.

Comparison between samples made on different days comfirmed that batch-to-batch reproducibility in loading levels achieved and observed photophysical behaviour was consistent. Under identical preparation procedures, the loading levels achieved did not vary by more than 3-5%. Excimer emission rise times varied by ±1 ps between batches.

5.2.3 Determination of Time Constants of Rise and Decay Kinetics

All luminescence decay traces collected on the picosecond time scale required convoluted fitting to extract the rate constants and were fit using the Deconfit program described in Section 2.3.3.2. The kinetic model used was a double exponential fit:

$$f(t) = A_1 e^{-k_1 t} + A_2 e^{-k_2 t} + M, \qquad (5.1)$$

where A_1 and A_2 represent pre-exponential factors, k_1 and k_2 are the rate constants and M is a constant to approximate all the remaining terms that are invariant over the short time window being studied. All five terms are determined by the Deconfit program. When A_n is negative, then the corresponding rate constant k_n is the rate constant for the rise of the decay trace, whereas when A_n is positive, then the corresponding rate constant k_n is the rate constant describing the decay of the decay trace. All fits were evaluated using the χ^2 value (goodness of fit), the R^2 value, and visual inspection of the residuals. Residuals that showed only stochastic noise about zero indicated that the model used and the fit parameters calculated adequately described the data.

The time constant τ was calculated from rate constants:

$$\tau = k^{-1}. \tag{5.2}$$

Luminescence decays on the nanosecond time scale did not require convoluted fitting. Kinetic parameters were extracted by iterative fitting using the commercially available Kaleidagraph package. The following two kinetic models were used:

$$f(t) = A_1 e^{-k_1 t} + A_2 e^{-k_2 t} + M \tag{5.1}$$

$$f(t) = A_1 e^{-k_1 t} + A_2 e^{-k_2 t} + A_3 e^{-k_3 t} + M \tag{5.3}$$

Determination of which model to use required the visual evaluation of residuals of each model after fitting. Residuals that showed only stochastic noise about zero indicated that the model used and the fit parameters calculated adequately described the data.

Errors in the time constants reported are discussed in Section 5.5.

5.2.4 Determination of Adsorbate Concentrations

The loading level <S> of guest molecules in the zeolite is defined as:

<S> = moles of guest molecules / moles of zeolite cavities (5.4)

<S> = number of guest molecules / zeolite cavity. (5.5)

<S> is a statistical average, assuming a homogeneous distribution of guest molecules through the zeolite matrix, and also assuming that the guest molecules reside only within the supercages. In order to calculate <S>, equation 5.4, together with the fact that the faujasite zeolite unit cell has 8 cavities, becomes:

<S> = (moles of guest molecules × unit cell mass) / (8 × mass zeolite) (5.6)

Table 5.1 gives the typical unit cell formula and molecular masses of the faujasite zeolites used in this thesis.

Table 5.1 Typical unit cell formula and molecular mass of alkali metal cation faujasites.[62]

Zeolite	Typical Unit Cell Formula	Molecular Mass (g/unit cell)
LiY	$Li_{26}Na_{30}Al_{56}Si_{136}O_{384}$	12344
NaY	$Na_{56}Al_{56}Si_{136}O_{384}$	12762
KY	$K_{54}Na_{2}Al_{56}Si_{136}O_{384}$	13362
RbY	$Rb_{25}Na_{31}Al_{56}Si_{136}O_{384}$	14324
CsY	$Cs_{26}Na_{30}Al_{56}Si_{136}O_{384}$	15620
NaX	$Na_{86}Al_{86}Si_{106}O_{384}$	13418

5.2.5 Solvent Incorporation

Zeolite samples used in the solvent incorporation experiments were prepared by vapor phase adsorption of the solvent into the dry pyrene / zeolite composite. The samples for each experiment were made in batches to ensure that the pyrene loading level was identical for a set of four samples, where one was flame sealed, and a different solvent was added to each of the remaining three samples. The solvent incorporation procedure was as follows: a syringe was used to add the appropriate amount of solvent through the septa into the glass arm on the side of the sample cell. A heat gun was used to heat the entire cell to ensure the solvent did not condense onto the glass. The solvent in the arm was then vapourized with the heat gun to ensure the solvent incorporation in the gas phase in an effort to get an even distribution of solvent throughout the zeolite sample. Thorough shaking of the zeolite sample within the cell combined with further heating ensured the incorporation of solvent into the zeolite. The sample was then allowed to cool, placed on the dry nitrogen line and purged for 20 minutes before fluorescence data was collected.

The quantity molecules / supercage was calculated for each solvent based upon the quantity of cosolvent injected into the sample and the cosolvent density using equation (5.6). This calculation assumed that all the cosolvent injected was adsorbed into the zeolite. However, the reported molecules / supercage is the maximum solvent that was coincorporated into each sample, and was calculated cumulatively. The actual molecules / supercage is likely lower.

After all solvent incorporation experiments were complete, the samples were washed with hexane and the hexane decants analyzed by UV-visible spectroscopy to determine whether the pyrene was still incorporated within the zeolites or had moved to the surface. In all cases, the pyrene contained in the hexane decant was negligible (<0.1%) compared to the amount of pyrene impregnated originally in the sample.

5.3 Ruthenium Complexes

5.3.1 Materials

All chloride salts of the ruthenium complexes were prepared, purified and characterized by Felix S. Lee[158] and used as received. Sherri A. McFarland prepared, purified and characterized the PF_6 salts of the ruthenium complexes. These were also used as received.

Solutions of the chloride salts were prepared in nanopure water, which was produced in house by distillation followed by deionization. Solutions of the PF_6 salts were prepared in spectroscopic grade acetonitrile (99%; Omnisolv™) and used as received.

5.3.2 Sample Preparation for Time-Resolved Fluorescence Spectroscopy

5 mM solutions of the complex being studied were placed into a 1 mm Hellma quartz cell and capped with a teflon lid. Each fluorescence experiment consisted of a background collection, and a minimum of two emission collections. Between collections, the sample was shaken to ensure that possible sample degradation by repeated laser excitation was diluted. Collection times ranged from 3 to 12 minutes. All collections using 258 nm excitation or picosecond fluorescence using 388 nm required 12 minute exposures; the remainder required 3 minute exposures. New solutions were generally used for each fluorescence experiment. All fluorescence experiments were done by front face excitation. No noticeable change in sample composition was detected by UV-visible spectroscopy after laser irradiation.

5.3.3 Sample Preparation for Transient Absorption Spectroscopy

50 mL of 1 mM solutions of the complex being studied were prepared and adjusted by the addition of solvent until the absorbance of the solution was between 0.4 and 0.6 at 388 nm. These solutions were recycled by a varistaltic pump through a 1 mm quartz flow cell (Hellma) until it was evident that sample degradation was significant by inconsistent spectral features between shots. The same solution was used for an entire data set and the collection process was randomized to ensure that no kinetic effects seen were due to systematic sample degradation. For the ultrafast data, each raw spectrum consisted of 2500 accumulated shots while each raw nanosecond spectrum was produced by averaging three spectra, each consisting of 5000 shots. Each raw spectrum was corrected for fluorescence and dark counts. Three of these raw spectra were averaged to produce the experimental spectrum recorded. Each one of the raw spectra was manually approved to eliminate faulty shots and to guard against outliers.

5.3.4 Determination of Kinetic Rate and Time Constants

All the luminescence decays collected required convoluted fitting procedures to extract kinetic rate constants (k). These were accomplished using the Deconfit program (Section 2.3.3.2). The kinetic model employed for these decays was equation (5.1) (Section 5.2.3):

$$f(t) = A_1 e^{-k_1 t} + A_2 e^{-k_2 t} + M \qquad (5.1)$$

All fits were evaluated using the χ^2 value (goodness of fit), the R^2 value, and visual inspection of the residuals. Residuals that showed only stochastic noise about zero indicated that the model used and the fit parameters calculated adequately described the data. Time constants (τ) were calculated from the k values by the relation

$$\tau = k^{-1}. \qquad (5.2)$$

The major source of error for the time constants reported in Chapter 4 was variations between multiple collections of the same sample. The errors reported were the standard deviations of the time constants.

5.4 Instrumentation

All time-resolved fluorescence instrumentation and software were described in Chapter 2. Steady-state fluorescence studies were performed using a PTI fluorimeter with front face excitation, and UV-visible spectroscopy was facilitated by a Varian-Cary 100 UV-VIS spectrometer.

5.5 Uncertainties in Reported Quantities

Because the rise times, decays, and wavelengths reported in this thesis work were all derived by numerical fitting of collected data, the uncertainties had to be carefully evaluated to determine whether they reflected the error in the mathematical fit, the error between multiple fits of the same data, differences between multiple collections using the same sample, or differences between samples made on different days. In all cases, the largest source of error was reported as the uncertainty.

For the zeolite samples, the largest source of variation was between samples made on different days. Excimer emission rise times were estimated to vary by ±1 ps by comparison between different zeolite / guest molecule batches. Smaller sources of error include variations between multiple data collections performed using the same sample with sample shaking between data collections. These errors were estimated to be ±0.5 ps. The fitting algorithm itself reported much smaller uncertainties (±0.1 ps) and the error from multiple fits to the same data is estimated to be (±0.2 ps). Because the largest source of uncertainty arose from variations between repeated trials, the error in all the rise times reported is estimated to be ±1 ps.

Lifetimes and lifetime percentages derived from nanosecond decay traces were found to vary most in the actual values produced by fits to multiple data collections. The

errors reported are calculated as standard deviations of calculated lifetimes of sample replicates.

In the cases where the errors in the calculated fit parameters needed to be compared to the variation between lifetimes, the errors in lifetimes ($d\tau$) were calculated from the calculated rate decay constant (k) and its calculated error (dk) by the following formula:

$$d\tau = -\frac{dk}{k^2} \tag{5.7}$$

Chapter 6: Conclusions and Future Work

6.1 Conclusions

Three major projects were pursued as part of this thesis project. The first project was the development of a femtosecond laser spectrometer to study kinetic processes on the femtosecond, picosecond and nanosecond time scales. This spectrometer is composed of two sections: a transient absorption spectrometer and a streak camera system. The transient absorption spectrometer uses the pump-probe technique to study solution samples by absorption measurements. Full absorption spectra are collected at specific times after excitation, and by collecting spectra over a time window, changes in absorption intensity as a function of time can be analyzed to give kinetic information about the system being studied. Two white light generation sources are available to the transient absorption spectrometer. The first source is a sapphire plate. Under the sapphire plate setup, the transient absorption spectrometer has a resolution of 305 fs and a spectral window of 450 to 750 nm. The second white light generator is a water cell that facilitates a spectral window of 395 to 700 nm with a resolution of 800 fs. The transient absorption spectrometer offers two excitation wavelengths of 388 nm and 258 nm, and facilitates the collection of transient absorption data through the femtosecond and picosecond time scales, with 5 ns as the longest time available for observation.

The streak camera system is a complementary instrument to the transient absorption spectrometer, and uses streak camera technology to capture time-resolved luminescence. Samples studied by the streak camera system can be excited by 258 nm, 388 nm and 480 - 750 nm excitation wavelengths. Two methods are available for triggering the streak camera system: the G2 jitter-free unit, and the slow sweep unit. With the G2 jitter-free unit, the resolution of the streak camera system is 3 to 5 ps, while the slow sweep unit allows for the capture of luminescence with a maximum time window of 90 ns. Samples studied by the streak camera system can be either solid or solution samples, and bandpass filters facilitate the study of luminescence at specific wavelengths.

Both these systems have required software to be written in-house to facilitate data collection and analysis. Because the data collected on these systems are convoluted by the instrument response function (IRF), iterative fitting of the time-resolved data required a convolution step to account for the IRF. Several programs have been written that facilitate convoluted fitting, including the Deconfit program, for streak camera data, the Convoluted Fitting of Non-Regularly Spaced Data program (CFnP), and the ManCon program, all of which offer specialized fitting capabilities for the specific needs of the data collected using the femtosecond laser spectrometer.

The femtosecond laser spectrometer was used to study the placement and ultrafast movement of pyrene and 9,10-dicyanoanthracene (DCA) in faujasite zeolites. Both molecules exhibited a resolvable excimer emission rise time, indicating that excimer formation within X and Y zeolites is a dynamic process. For pyrene, the excimer emission rise times ranged from 7 to 16 ps, and was found to be slowest in dry pyrene / NaY samples. The variation in rise times was in part due to the strength of the π-cation interaction between the charge balancing cations of the zeolite and the delocalized π cloud of the pyrene molecule. The introduction of co-solvents into the pyrene / zeolite samples produced a decrease in the excimer emission rise times, and this effect is attributed to the disruption of the π-cation interaction. While the pyrene excimer emission rise times were independent of loading level, and thus reflected excimer formation from doubly occupied supercages alone, the excimer emission rise times of DCA were found to vary as a function of loading level. The counterbalancing cation also played a role in the rise time variation: as the cation size increased, the rise time increased. These observations, along with luminescence data on the nanosecond time scale, were used to determine that DCA adsorbs to a number of different sites within the zeolite supercage, and that excited state DCA molecules are capable of intercavity movement to form an excimer. This movement was modelled using probabilities to estimate the excimer emission rise times of DCA as a function of loading level, and the model predicted that intercavity hopping to form an excimer does not exceed one or two jumps.

The final system investigated in this thesis project was the ultrafast dynamics of tris-(2,2'-bipyridine)ruthenium(II) ($Ru(bpy)_3^{2+}$) derivatives at short excitation

wavelengths. For all the derivatives, a second fluorescence decay component ($\tau_{4,5}$ = 0.7 to 6 ns) was observed at 500 nm upon 388 nm excitation, while the parent compound $Ru(bpy)_3^{2+}$ showed only the one component, an instrument response limited decay. This suggests that a higher lying emissive state exists for these compounds which can only be accessed by the use of these short excitation wavelengths. While studies using the transient absorption spectrometer on these complexes did not add insight as to the nature of this higher emissive state, ultrafast studies revealed that fast decay kinetics similar to those observed in the literature for excitation at 400 nm are also observed at 388 nm excitation. The higher state decays too quickly to be time-resolved on the transient absorption spectrometer. Qualitatively, an increase in intensity of the fast decay component is observed as the excitation wavelength decreases from 400 to 388 nm.

6.2 Future Work

6.2.1 Transient Absorption Spectrometer

There are three main improvements that can be made to the transient absorption spectrometer: 1. increased time resolution, 2. decreased spectral chirp, and 3. a major increase in the signal to noise ratio. The first improvement, increased time resolution, requires the pump and probe pulses to be shortened prior to their incidence on the sample cell. The best way to do this is to use a pulse compressor; however, the use of a pulse compressor also requires the use of an auto-correlator to determine the extent of pulse compression, making this an expensive venture. Collimating and focusing the white light produced by the sapphire plate using off-axis parabolic mirrors can accomplish the improvement of spectral chirp. These mirrors minimize the amount of distance that the white light travels through lenses and other materials that can introduce chirp. Unfortunately, the major source of chirp when broadband radiation is produced using the water cell is the water cell itself. However, a reduction in chirp can be achieved by decreasing the length of the water cell. When the water cell was reduced from 10 cm to 3 cm, a three-fold decrease in chirp was evidenced. Shortening the water cell again would

improve the chirp while retaining the large spectral bandwidth of the white light produced.

While the first two improvements to the transient absorption spectrometer are desired, they are not essential improvements. Conversely, it is absolutely essential that the signal to noise ratio of the spectrometer be improved; otherwise it will be impossible to extract kinetic data from the spectrometer. This situation was demonstrated in Chapter 4. The main introduction of noise is shot-to-shot instability, which can be introduced by instability in the laser, and further compounded by instability in white light production, particularly with the finicky alignment of the sapphire plate. There are two ways of increasing the signal to noise ratio: the first involves referencing the probe beam and the second involves referencing the pump beam. To reference the probe beam, one of the options would be to introduce a chopper such that the raw data spectrum (both pump and probe beams on) and the continuum spectrum (just the probe beam) are collected with fast alternation, with ideally every other shot being collected for the raw data spectrum. Even alternating every 20 shots would decrease the signal to noise ratio greatly because slow undulations of the laser power would be accounted for. This is a difficult solution to introduce logistically, because it would involve the synchronization of the chopper to the detection unit, and currently the system is only set up such that the detection unit collects on an independent timer while the laser shots run freely. A more practical solution for the spectrometer would be to collect the raw data spectrum and the continuum truly simultaneously by introducing a beam splitter between the probe pulse and the sample. The beam splitter would redirect part of each pulse so that it could be collected for the continuum spectrum. Ideally, this portion would also be sent through the sample cell, but it is not absolutely essential as theoretically this can be adjusted mathematically.

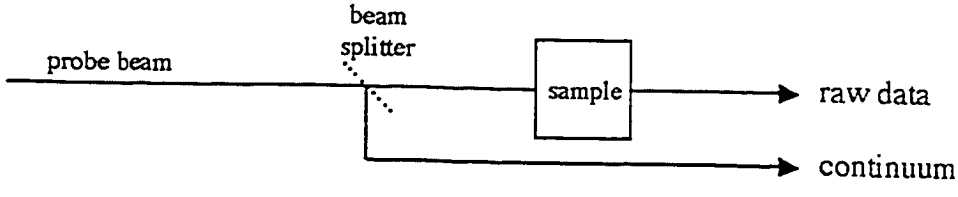

Figure 6.1 A schematic demonstrating the simultaneous collection of the raw data and continuum spectrum.

In order to implement this solution into the current setup, the photodiode array would need to be replaced by a CCD camera and the single fibre optic cable would be replaced by two fibre optic cables, one for collecting the raw data and the other for collecting the continuum. These two cables would be vertically aligned into the imaging spectrograph (one on top of the other), and the CCD camera would then collect both spectra simultaneously. Vertical summation of the portions of the CCD camera corresponding to each spectrum yields the raw data and continuum spectra. Each experiment would be performed twice: the first time, the pump beam would be exciting the sample, generating the raw data and continuum spectra, and the second time, the pump beam would be turned off, generating two continuum spectra. These latter two spectra allows for the calculation of a scaling factor for each pixel in the CCD camera so that differences in intensity between the two beams can be accounted for. The major differences can arise from uneven splitting of the beam by the beamsplitter and differences in path direction, such as travel through the sample cell. After this scaling factor is used in the calculation of the absorbance spectrum, the only intensity variations should be due to the absorption by transients produced by the incidence of the probe beam. The absorbance spectrum is calculated by:

$$A(\lambda) = \log\left(\frac{C_P(\lambda)}{R_P(\lambda)} \times \frac{R_N(\lambda)}{C_N(\lambda)}\right), \tag{6.1}$$

where $C_P(\lambda)$ and $R_P(\lambda)$ represent the continuum and raw data spectra with the pump beam on, and $C_N(\lambda)$ and $R_N(\lambda)$ represent the continuum and raw data spectra in the absence of pump beam. Under perfect circumstances, the $C_P(\lambda)$ and $C_N(\lambda)$ spectra should be identical and cancel out, leaving the standard absorption equation:

$$A(\lambda) = \log\left(\frac{R_N(\lambda)}{R_P(\lambda)}\right). \tag{6.2}$$

This method minimizes baseline noise and will decrease the data collection time immensely, as most of the spectra that are manually discarded are due to poor baselines. If successful, this method could even minimize the need for manual inspection of every spectrum, allowing for truly non-biased collection of data. The ultimate goal would be

fully automatic data collection, although the need to ensure good pump-probe overlap over longer time scales would still require the user's presence at all times.

A second way of improving the overall signal to noise ratio is to reference the pump beam. Currently, it is assumed that there is no variation in pump beam intensity as a function of time. Although these intensity variations are a smaller noise contributor than baseline fluctuation, referencing the pump beam in a similar way to the absorption spectrum would eliminate this source of noise. A beam splitter inserted before the sample cell is necessary to extract a small amount of the pump beam, which is then collected by a photodiode to measure fluctuations in the pump beam intensity. Undulations of pump beam intensity could then be corrected for.

The implementation of all these recommendations would significantly increase the quality of the data collected by the transient absorption spectrometer, as well as improve user ease for more widespread use of this instrument.

6.2.2 Single Wavelength Kinetics

Single wavelength transient absorption kinetics, while extractable from full spectrum data, would also be easily implemented with the referencing system described above. Just prior to the beam splitter in Figure 6.1, the introduction of a narrow bandpass filter would selectively choose the wavelength of interest. A pair of matched fast photodiodes would replace the two fibre optic cables, and these two photodiodes would be linked to a dual boxcar integrator, which is electronically synchronized to the laser pulse. The boxcar integrator would integrate the signal of both photodiodes for a specified number of pulses, generating the single wavelength equivalent of $C_P(\lambda)$ and $R_P(\lambda)$ described above. The second collection in the absence of the pump beam would also be corrected and the absorbance at the selected wavelength would be calculated using equation (6.1). Single wavelength kinetics is used for a further increase in signal to noise ratio over the full spectrum data. This decrease in noise is attributed to the photodiode / boxcar combination, which has significantly less dark count noise than the CCD camera.

6.2.3 The Streak Camera System

In order to facilitate the detection of very low intensity emissions, either due to low quantum yields of emission or low intensity excitation radiation, the following is suggested. Currently, the sample cell is about 40 cm away from the photocathode of the streak camera. Emission from the sample cell must travel through a collimation lens and then a focusing lens before incident of the streak camera. By eliminating one of the these lenses and moving the sample cell closer to the streak camera entrance, losses in emission intensity can be decreased, which should help with the intensity of the emission collected.

6.2.4 Polyaromatic Compounds in Zeolites

In order to complete the DCA studies that have been presented in this thesis, the increasingly slow rise of the DCA monomer emission at 450 nm as a function of decreasing loading level requires investigation. The proposal outlined in Section 3.4.3.1 hypothesizes that a time-resolved Stokes shift is being observed as a result of the movement of excited state DCA molecules into more thermodynamically favoured adsorption sites. To test this hypothesis, the monomer emission of DCA / Y zeolite samples would need to be studied at wavelengths shorter than 450 nm. If a Stokes shift is present, then as the wavelength being monitored becomes shorter (higher energy), the monomer emission rise time would become progressively faster and faster until it matched the rise time of the IRF. This shift would also be cation and loading level dependent. Large cations such as Cs^+ would inhibit the movement of the ^{1}DCA* molecules, causing a larger difference in rise time for the same wavelength shift than would be seen for the smaller cations of Li^+ and Na^+. At high loading levels, the aggregation of ground state DCA molecules within the zeolite framework would result in a higher percentage of ^{1}DCA* molecules being formed in the stabilized sites, and thus the magnitude of the Stokes shift will be more rapid.

One aspect of the pyrene and DCA studies in zeolites that require further investigation is the variables that control excited state intercavity motion. A possible way of increasing knowledge in this area is to expand the number of related polyaromatic

compounds that have been inserted into X and Y zeolites. By a systematic study of excited state movement as a function of molecular electronic and steric features, the specific attributes that allow for intracavity hopping could be identified. As well, theoretical studies on the intracavity movement energy barriers for pyrene and DCA could prove helpful.

6.2.5 Ultrafast Photophysical Behaviour of Ruthenium(II) Complexes

Chapter 4 represents a very small sampling of the experiments possible with these ruthenium(II) complexes. First of all, these experiments need to be redone after the improvements suggested in 6.1 are implemented in order to be able to quantitatively describe the ultrafast transient absorption behaviour being observed. The transient absorption experiments also need to be repeated for the PF_6 salts of the complexes studied in Chapter 4 in order to be able to compare the decay kinetics between our data and the data obtained by the McCusker group.[45] Studying the PF_6 salts in acetonitrile solution would eliminate two of the variables (namely, the solvent and the counterion) that could be contributing to the different kinetic behaviour observed under our experimental conditions, and identify precisely the role of the excitation wavelength on the initial photophysical behaviour.

In order to fully investigate the effect of excitation energy upon the initial dynamics of $Ru(bpy)_3^{2+}$ derivatives, systematic changes in the pump beam wavelength need to be employed. Ideally, if the wavelengths between 388 nm and 480 nm could be used for excitation under identical conditions, then changes in the absorption data can be correlated with changes in the excitation wavelength. However, this would require a well-working OPA or even a NOPA (an OPA that produces near IR wavelengths) with output wavelengths that could be efficiently frequency doubled to produce the necessary wavelengths. Even this solution may not be feasible as both the OPA and NOPA outputs diminish significantly as the output wavelength approaches the fundamental beam frequency, 775 nm. The frequencies that need to be doubled to form these excitation wavelengths are all near to 775 nm, and thus the stability and intensity of the output beam may be too low to study this region between 388 and 480 nm well.

Further experiments need to be carried out to identify the nature of State C proposed as the emitting state of the nanosecond fluorescence at 500 nm. Ideally, these experiments need to be carried on an up-conversion instrument for the femtosecond time resolution that it offers; however, the flux of the long-lived nanosecond fluorescence may be too low to generate the up-conversion signal. If it were detectable, then the spin of the emitting state could be determined as radiative coupling with the ground state to produce the upconversion signal is strongly dependent upon a change of spin in the excited state.[154] Repetition of the transient absorption experiments out to 5 ns could also be informative as long as the signal to noise ratio were high enough to detect kinetics that could be compared to the nanosecond fluorescence lifetimes.

All the complexes studied were homoleptic complexes of the type $Ru(LL)_3^{2+}$, where LL denotes the bidentate ligand. A natural extension of the work would be to study heteroleptic complexes of the type $Ru(LL)_2(LL')^{2+}$ using the same ligands. Some fluorescence work on these complexes has already been carried out but further experimentation needs to take place in order to draw any conclusions.

Appendix A: Supercage Occupancy Probability Calculations

The probability of supercage occupancy can be calculated assuming a completely random distribution of molecules within the supercage network. Because each supercage can be unoccupied, singly or doubly occupied, the calculation of occupancy probabilities must reflect all three possibilities. In the literature, the probability of supercage occupancy is generally calculated using a Poisson distribution where the probability of finding a supercage occupied by j molecules is defined as

$$P(j) = \frac{\lambda^j e^{-\lambda}}{j!}, \tag{A.1}$$

where λ is the loading level, <S>. While the Poisson distribution is valid for low loading levels, it cannot be restricted to a maximum of two molecules within one supercage. At loading levels approaching <S> = 1, the probability of three or more molecules becomes significant and a different method of calculating cage occupancy probabilities must be developed.

This calculation assumes that molecules distribute in supercages independently, so that a molecule has equal probability of entering either an empty supercage or one that is already occupied. Given N molecules and k supercages, the number of all possible configurations of molecules in supercages is given by:

$$\sum_{l_2} \Omega(k) = \sum_{l_2} \frac{k!}{l_o! l_1! l_2!}, \qquad 0 \le l_2 \le l_2^{\max}, \quad l_2^{\max} \begin{cases} \dfrac{N}{2} & \text{for even } N \\ 1 - \dfrac{N}{2} & \text{for odd } N \end{cases} \tag{A.2}$$

$$l_1 = N - 2l_2 \tag{A.3}$$

$$l_0 = k - l_1 - l_2 \tag{A.4}$$

The quantities l_0, l_1, and l_2 represent the number of supercages that are unoccupied, singly occupied and doubly occupied, respectively. Each quantity $\Omega(k)$ to be summed in equation (1) is the number of possible combinations of configurations for a given l_0, l_1, and l_2. It is then summed over all allowed variations of l_0, l_1, and l_2.

The probability of a given supercage being unoccupied, *P(0)*, is defined as:

$$P(0) = \frac{\sum_{l_2} \left(\frac{l_0}{k}\right) \Omega(k)}{\sum_{l_2} \Omega(k)}. \tag{A.5}$$

Likewise, the probability of a given supercage being singly and doubly occupied are:

$$P(1) = \frac{\sum_{l_2} \left(\frac{l_1}{k}\right) \Omega(k)}{\sum_{l_2} \Omega(k)} \tag{A.6}$$

$$P(2) = \frac{\sum_{l_2} \left(\frac{l_2}{k}\right) \Omega(k)}{\sum_{l_2} \Omega(k)} \tag{A.7}$$

Satisfying the rules of probabilities, the following must be true:

$$P(O) + P(1) + P(2) = 1. \tag{A.8}$$

For any regular array of supercages in a zeolite framework, the number of supercages, k, must be approximated by infinity. However, the only quantity that is known when applying these equations to molecules in supercages is the loading level <S> = N/k, and if k is extrapolated to infinity, then it follows that N must also be extrapolated to infinity. Therefore, for a given <S>, it is very difficult to calculate P(0), P(1) and P(2) by an analytical solution. Furthermore, analytical techniques may result in the use of complex numbers or other solutions that do not have physical meaning. The following describes the numerical approach used to compute the probabilities.

In order to calculate P(0), P(1) and P(2) for a given loading level, it is possible to approximate an infinite k by a large number. By systematically increasing k, and increasing N accordingly, the values of P(0), P(1) and P(2) can be calculated until these values plateau and become constant. However, evaluating these probabilities involves the evaluation of very large factorials which becomes very difficult. The largest factorial that can be evaluated directly is 170! = 7.25742e306. This corresponds to a maximum k value of 170, which is not large enough to calculate probabilities for N/k values smaller than 1/10. In order to dramatically increase the size of the factorials that can be computed, logarithms were employed. The logarithm of a factorial is defined as:

$$\log N! = \sum_{i=1}^{N} \log i. \qquad \text{(A.9)}$$

Likewise, log $\Omega(k)$ can now be evaluated as:

$$\log \Omega(k) = \log(k!) - \log(l_0!) - \log(l_1!) - \log(l_2!). \qquad \text{(A.10)}$$

Because $\Omega(k)$ is a much smaller number than the factorials needed to calculate it, the evaluation of equation (10) allows $\Omega(k)$ to be calculated for much larger numbers of k. For N/k = 1/500, N = 90 and k = 45 000 are the largest values that can be computed. Incorporation of equation (10) into equations (5), (6) and (7) permits the calculation of P(0), P(1) and P(2). All probabilities reached a plateau before the maximum N and k values were reached. These probabilities are listed in Table A1 below. A comparison of this calculation to the conventional Poisson calculation is shown in Table A2.

Table A1 Calculated probabilities of supercage occupancy.

Loading Level $\langle S \rangle = N/k$	Maximum N	Maximum k	P(0)	P(1)	P(2)
1/1	500	500	0.3332	0.3336	0.3332
1/2	350	700	0.6161	0.2678	0.1161
1/5	250	1250	0.8262	0.1476	2.624e-2
1/10	210	2100	0.9078	8.439×10^{-2}	7.808×10^{-3}
1/20	175	3500	0.9522	4.562×10^{-2}	2.176×10^{-3}
1/75	130	9750	0.9868	1.303×10^{-2}	1.698×10^{-4}
1/200	110	22000	0.9950	4.976×10^{-2}	2.441×10^{-5}
1/350	100	35000	0.9972	2.792×10^{-3}	8.014×10^{-6}
1/500	90	45000	0.9980	1.996×10^{-3}	3.932×10^{-6}

Table A2 Comparison of Poisson distribution to calculated probabilities.

Loading Level $\langle S \rangle = N/k$	Unoccupied Cage		Singly Occupied		Doubly Occupied	
	Poisson	P(0)	Poisson	P(1)	Poisson	P(2)
1/1	0.368	0.3332	0.368	0.3336	0.184	0.3332
1/2	0.607	0.6161	0.303	0.2678	0.076	0.1161
1/5	0.819	0.8262	0.164	0.1476	0.016	2.624×10^{-2}
1/10	0.905	0.9078	0.090	8.439×10^{-2}	0.005	7.808×10^{-3}
1/20	0.951	0.9522	0.048	4.562×10^{-2}	0.001	2.176×10^{-3}
1/75	0.987	0.9868	0.013	1.303×10^{-2}	0.000	1.698×10^{-4}
1/200	0.995	0.9950	0.005	4.976×10^{-2}	0.000	2.441×10^{-5}
1/350	0.997	0.9972	0.003	2.792×10^{-3}	0.000	8.014×10^{-6}
1/500	0.998	0.9980	0.002	1.996×10^{-3}	0.000	3.932×10^{-6}

References

(1) Atkins, P. W. *Physical Chemistry*, 5th ed.; W. H. Freeman and Company: New York, 1994.

(2) Press, W. H.; Teukolsky, S. A.; Vetterling, W. T.; Flannery, B. P. *Numerical Recipes in Fortran 77: The Art of Scientific Computing*, 2nd ed.; Cambridge University Press: New York, 2001; Vol. 1.

(3) Laidler, K. J. *Chemical Kinetics*, 3rd ed.; HarperCollinsPublishers, Inc.: New York, 1987.

(4) Hartridge, H.; Roughton, F. J. W. *Nature* **1923**, *111*, 325.

(5) Chance, B. *J. Franklin Inst.* **1940**, *229*, 613.

(6) Chance, B. *J. Franklin Inst.* **1940**, *229*, 455.

(7) Eigen, M. *Discuss. Faraday Soc.* **1954**, *17*, 194.

(8) Eigen, M. Immeasurable Fast Reactions. In *Nobel lectures: Chemistry,1963-1970*; Elsevier Publishing Co.: New York, 1972.

(9) Norrish, R. G.; Porter, G. *Nature* **1949**, *164*, 658.

(10) Maiman, T. H. *Nature* **1960**, *187*, 493.

(11) DeMaria, A. J.; Stetser, D. A.; Heynau, H. *Appl. Phys. Lett.* **1966**, *8*, 174.

(12) Shank, C. V.; Ippen, E. P. *Appl. Phys. Lett.* **1974**, *24*, 373.

(13) Spence, D. E.; Kean, P. N.; Sibbett, W. *Opt. Lett.* **1991**, *16*, 42.

(14) Turro, N. J. *Modern Molecular Photochemistry*; University Science Books: Sausalito, 1991.

(15) McFarland, S. A. Modulating Luminescence via Conformational Control of Nonradiative Processes: A New Approach to Chemosensor Design. Doctoral Thesis, University of California, San Diego, 2003.

(16) Birks, J. B.; Dyson, D. J.; Munro, I. H. *Proc. Roy. Soc. (London)* **1963**, *275 (Ser. A; 1363)*, 575.

(17) Yoshihara, K.; Kasuya, T.; Inoue, A.; Nagakura, S. *Chem. Phys. Lett.* **1971**, *9*, 469.

(18) Ferguson, J.; Mau, A. W.-H.; Morris, J. M. *Aust. J. Chem.* **1973**, *26*, 91.

(19) Diels, J.-C.; Rudolph, W. *Ultrashort Laser Pulse Phenomena: Fundamentals, Techniques, and Applications on a Femtosecond Time Scale*; Academic Press, Inc.: San Diego, 1996.

(20) Rosker, M. J.; Dantus, M.; Zewail, A. H. *J. Chem. Phys.* **1988**, *89*, 6113.

(21) Schmidt, J. A.; Hilinski, E. F. *Rev. Sci. Instrum.* **1989**, *60*, 2902.

(22) Dantus, M.; Rosker, M. J.; Zewail, A. H. *J. Chem. Phys.* **1988**, *89*, 6128.

(23) Rose, T. S.; Rosker, M. J.; Zewail, A. H. *J. Chem. Phys.* **1989**, *91*, 7415.

(24) Scherer, N. F.; Sipes, C.; Bernstein, R. B.; Zewail, A. H. *J. Chem. Phys.* **1990**, *92*, 5239.

(25) Zewail, A. H. *J. Phys. Chem. A* **2000**, *104*, 5660.

(26) Damrauer, N. H.; Cerullo, G.; Yeh, A.; Roussie, T. R.; Shank, C. V.; McCusker, J. K. *Science* **1997**, *275*, 54.

(27) Hubig, S. M.; Bockman, T. M.; Kochi, J. K. *J. Am. Chem. Soc.* **1997**, *119*, 2926.

(28) Cartwright, M. *Fourier Methods: For Mathematicians, Scientists and Engineers*; Ellis Horwood Ltd.: Toronto, 1990.

(29) James, J. F. *A Student's Guide to Fourier Transforms: With Applications in Physics and Engineering*; Cambridge University Press: New York, 1995.

(30) Jennison, R. C. *Fourier Transforms: Convolutions for the Experimentalist*; Pergamon Press: New York, 1961.

(31) Smith, S. W. *The Scientist and Engineer's Guide to Digital Signal Processing*; California Technical Publishing: San Diego, 1998.

(32) Wentzell, P. D.; Brown, C. D. Signal Processing in Analytical Chemistry. In *Encyclopedia of Analytical Chemistry*; Meyers, R. A., Ed.; John Wiley and Sons Ltd.: Chichester, 2000; Vol. 11; pp 9764.

(33) Bhasikuttan, A. C.; Suzuki, M.; Nakashima, S.; Okada, T. *J. Am. Chem. Soc.* **2002**, *124*, 8398.

(34) Backus, S.; Durfee, C. G.; Murmane, M. M.; Kapteyn, H. C. *Rev. Sci. Instrum.* **1998**, *69*, 1207.

(35) White, M. A. *Properties of Materials*; Oxford University Press: New York, 1999.

(36) Garito, A.; Shi, R. F.; Wu, M. *Physics Today* **1994**, *47*, 51.

(37) Fejer, M. *Physics Today* **1994**, *47*, 25.

(38) Brodeur, A.; Chin, S. L. *J. Opt. Soc. Am. B* **1999**, *16*, 637.

(39) Yeh, A.; Shank, C. V.; McCusker, J. K. *Science* **2000**, *289*, 935.

(40) Gordon, R. G. *J. Chem. Phys.* **1966**, *45*, 1643.

(41) Fleming, G. R. *Chemical Applications of Ultrafast Spectroscopy*; Oxford University Press: New York, 1986.

(42) Kobashi, H.; Gyoda, H.; Morita, T. *Bull. Chem. Soc. Jpn.* **1977**, *50*, 1731.

(43) Porter, G. *Proc. Roy. Soc. (London)* **1970**, *A315*, 163.

(44) Gschwind, R.; Haselbach, E. *Helv. Chim. Acta* **1979**, *62*, 941.

(45) Damrauer, N. H.; McCusker, J. K. *J. Phys. Chem. A* **1999**, *103*, 8440.

(46) Klimov, V. I.; McBranch, D. W. *Opt. Lett.* **1998**, *23*, 277.

(47) Dick, B.; Gonska, H.; Hohlneicher, G. *Ber. Bunsenges. Phys. Chem.* **1981**, *85*, 746.

(48) Thomas, J. K. *Chem. Rev.* **1993**, *93*, 301.

(49) Yoon, K. B. *Chem. Rev.* **1993**, *93*, 321.

(50) Liu, X.; Iu, K.-K.; Thomas, J. K. *J. Phys. Chem.* **1994**, *98*, 7877.

(51) Liu, X.; Iu, K. K.; Thomas, J. K. *Chem. Phys. Lett.* **1993**, *204*, 163.

(52) Hashimoto, S. *Chem. Phys. Lett.* **1996**, *252*, 236.

(53) Iu, K.-K.; Thomas, J. K. *J. Phys. Chem.* **1991**, *95*, 506.

(54) Cozens, F. L.; Regimbald, M.; Garcia, H.; Scaiano, J. C. *J. Phys. Chem.* **1996**, *100*, 18165.

(55) Ramamurthy, V.; Sanderson, D. R.; Eaton, D. F. *Photochem. and Photobiol.* **1992**, *56*, 297.

(56) Ellison, E. H. *J. Phys. Chem. B* **1999**, *103*, 9314.

(57) Liu, X.; Thomas, J. K. *Langmuir* **1993**, *9*, 727.

(58) Ramamurthy, V.; Sanderson, D. R.; Eaton, D. F. *J. Phys. Chem.* **1993**, *97*, 13380.

(59) Liu, X.; Iu, K.-K.; Thomas, J. K. *J. Phys. Chem.* **1989**, *93*, 4120.

(60) Thomas, K. J.; Sunoj, R. B.; Chandrasekhar, J.; Ramamurthy, V. *Langmuir* **2000**, *16*, 4912.

(61) Breck, D. W. *J. Chem. Educ.* **1964**, *41*, 678.

(62) Breck, D. W. *Zeolite Molecular Sieves: Structure, Chemistry and Use*; John Wiley and Sons: New York, 1974.

(63) Dyer, A. *An Introduction to Zeolite Molecular Sieves*; John Wiley and Sons: Bath, 1988.

(64) van Bekkum, H.; Flanigen, E. M.; Jansen, J. C. *Introduction to Zeolite Science and Practice*; Elsevier: Amsterdam and New York, 1991.

(65) Auerbach, S. M.; Carrado, K. A.; Dutta, P. K. *Handbook of Zeolite Science and Technology*; Marchel Dekker, Inc.: New York, 2003.

(66) Jobic, H.; Fitch, A. N.; Combet, J. *J. Phys. Chem. B* **2000**, *104*, 8491.

(67) Scaiano, J. C.; Garcia, H. *Acc. Chem. Res.* **1999**, *32*, 783.

(68) Ramamurthy, V.; Turro, N. J. *Inclusion Phenom. Mol. Recognit. Chem.* **1995**, *21*, 239.

(69) Ward, J. W. *J. Catalysis* **1968**, *10*, 34.

(70) Forano, C.; Slade, R. C. T.; Andersen, E. K.; Andersen, I. G. K.; Prince, E. *J.Solid State Chem.* **1989**, *82*, 95.

(71) Godber, J.; Baker, M. D.; Ozin, G. A. *J. Phys. Chem.* **1989**, *93*, 1409.

(72) Ramamurthy, V.; Eaton, D. F.; Caspar, J. V. *Acc. Chem. Res.* **1992**, *25*, 299.

(73) Hallett, G. L. A Laser Flash Photolysis Study of Carbocation Formation in Non-Acidic Y Zeolites. Master's Thesis, Dalhousie University, 2004.

(74) Chretien, M. N.; Shen, B.; Garcia, H.; English, A. M.; Scaiano, J. C. *Photochem. and Photobiol.* **2004**, *80*, 434.

(75) Alvaro, M.; Carbonell, E.; Garcia, H.; Lamaza, C.; Pillai, M. N. *Photochem. Photobiol. Sci.* **2004**, *3*, 189.

(76) Suib, S. L.; Kostapapas, A. *J. Am. Chem. Soc.* **1984**, *106*, 7705.

(77) Stamires, D. N.; Turkevich, J. *J. Am. Chem. Soc.* **1964**, *86*, 749.

(78) Baretz, B. H.; Turro, N. J. *J. Photochem.* **1984**, *24*, 201.

(79) Ramamurthy, V. *J. Am. Chem. Soc.* **1994**, *116*, 1345.

(80) O'Neill, M. A.; Cozens, F. L.; Schepp, N. P. *J. Phys. Chem. B* **2001**, *105*, 12746.

(81) O'Neill, M. A. Nanosecond Time-Resolved Diffuse Reflectance Studies of Reactive Carbocations and Charge Migration in Non-Acidic Zeolites. Doctoral Thesis, Dalhousie University, 2001.

(82) Gedeon, A.; Bonardet, J. L.; Ito, T.; Fraissard, J. *J. Phys. Chem.* **1989**, *93*, 2563.

(83) Gedeon, A.; Ito, T.; Fraissard, J. *Zeolites* **1988**, *8*, 376.

(84) Kasai, P. H.; Bishop, R. J. *J. Am. Chem. Soc.* **1972**, *94*, 5560.

(85) Kogelbauer, A.; Goodwin, J. J. G.; Lercher, J. A. *J. Phys. Chem.* **1995**, *99*, 8777.

(86) Hashimoto, S.; Ikuta, S.; Asahi, T.; Masuhara, H. *Langmuir* **1998**, *14*, 4284.

(87) Auerbach, S. M.; Bull, L. M.; Henson, N. J.; Metiu, H. I.; Cheetham, A. K. *J.Phys. Chem.* **1996**, *100*, 5923.

(88) Bull, L. M.; Henson, N. J.; Cheetham, A. K.; Newsam, J. M.; Heyes, S. J. *J. Phys. Chem.* **1993**, *97*, 11776.

(89) Lunsford, J. H.; Tutunjian, P. N.; Chu, P.; Yeh, E. B.; Zalewski, D. J. *J. Phys. Chem.* **1989**, *93*, 2590.

(90) Larin, A. V.; Vercauteren, D. P.; Lamberti, C.; Bordiga, S.; Zecchina, A. *Phys. Chem. Chem. Phys.* **2002**, *4*, 2424.

(91) Rep, M.; Palomares, A. E.; Eder-Mirth, G.; van Ommen, J. G.; Rosch, N.; Lercher, J. A. *J. Phys. Chem. B* **2000**, *104*, 8624.

(92) Ellison, E. H.; Thomas, J. K. *Langmuir* **2001**, *17*, 2446.

(93) Eckert, J.; Draznieks, C. M.; Cheetham, A. K. *J. Am. Chem. Soc.* **2002**, *124*, 170.

(94) Fitch, A. N.; Jobic, H.; Renouprez, A. *J. Phys. Chem.* **1986**, *90*, 1311.

(95) Nakajima, A. *Bull. Chem. Soc. Jpn.* **1971**, *44*, 3272.

(96) Kalyanasundaram, K.; Thomas, J. K. *J. Am. Chem. Soc.* **1977**, *99*, 2039.

(97) Alvaro, M.; Facey, G. A.; Garcia, H.; Garcia, S.; Scaiano, J. C. *J. Phys. Chem.* **1996**, *100*, 18173.

(98) Hicks, J.; Vandersall, M.; Babarogic, Z.; Eisenthal, K. B. *Chem. Phys. Lett.* **1985**, *116*, 18.

(99) Hicks, J. M.; Vandersall, M. T.; Sitzmann, E. V.; Eisenthal, K. B. *Chem. Phys. Lett.* **1987**, *135*, 413.

(100) Unland, M. L.; Freeman, J. J. *J. Phys. Chem.* **1978**, *82*, 1036.

(101) Kim, D.; Hu, S.; Tarakeshwar, P.; Kim, K. S. *J. Phys. Chem. A* **2003**, *107*, 1228.

(102) Gokel, G. W.; DeWall, S. L.; Meadows, E. S. *Eur. J. Org. Chem.* **2000**, 2967.

(103) Ikuta, S. *Theochem* **2000**, *530*, 201.

(104) Tsuzuki, S.; Yoshida, M.; Uchimaru, T.; Mikami, M. *J. Phys. Chem. A* **2001**, *105*, 769.

(105) Hashimoto, S.; Ikuta, S. *Theochem* **1999**, *468*, 85.

(106) Taft, R. W.; Anvia, F.; Gal, J.-F.; Walsh, S.; Capon, M.; Holmes, M. C.; Hosn, K.; Oloumi, G.; Vasanwala, R.; Yazdani, S. *Pure Appl. Chem.* **1990**, *62*, 17.

(107) Sunner, J.; Nishizawa, K.; Kebarle, P. *J. Phys. Chem.* **1981**, *85*, 1814.

(108) Guo, B. C.; Purnell, J. W.; Castleman Jr., A. W. *Chem. Phys. Lett.* **1990**, *168*, 155.

(109) Kumpf, R. A.; Dougherty, D. A. *Science* **1993**, *261*, 1708.

(110) Ma, J. C.; Dougherty, D. A. *Chem. Rev.* **1997**, *97*, 1303.

(111) Kwon, O.-H.; Yu, H.; Jang, D.-J. *J. Phys. Chem. B* **2004**, *108*, 3970.

(112) Hashimoto, S.; Kiuchi, J. *J. Phys. Chem. B* **2003**, *107*, 9763.

(113) Sykora, M.; Kincaid, J. R.; Dutta, P. K.; Castagnola, N. B. *J. Phys. Chem. B* **1999**, *103*, 309.

(114) Iu, K.-K.; Thomas, J. K. *Langmuir* **1990**, *6*, 471.

(115) Liu, X.; Thomas, J. K. *Chem. Mater.* **1994**, *6*, 2303.

(116) Hashimoto, S.; Miyashita, T.; Hagiri, M. *J. Phys. Chem. B* **1999**, *103*, 9149.

(117) Yoon, K. B.; Kochi, J. K. *J. Am. Chem. Soc.* **1988**, *110*, 6586.

(118) Sarkar, N.; Das, K.; Nath, D. N.; Bhattacharyya, K. *Langmuir* **1994**, *10*, 326.

(119) Ortiz, W.; Cozens, F. L.; Schepp, N. P. *Org. Lett.* **1999**, *1*, 531.

(120) Vayssilov, G. N.; Lercher, J. A.; Rosch, N. *J. Phys. Chem. B* **2000**, *104*, 8614.

(121) Cheng, K. A. W. Y.; Schepp, N. P.; Cozens, F. L. *J. Phys. Chem. A* **2004**, *108*, 7132.

(122) Hayashi, Y.; Kawada, Y.; Ichimura, K. *Langmuir* **1995**, *11*, 2077.

(123) Chandross, E. A.; Ferguson, J. *J. Chem. Phys.* **1966**, *45*, 3564.

(124) Hoshi, T.; Okubo, J.; Imaizumi, F.; Ono, I.; Kobayashi, M.; Inoue, H. *Bull. Chem. Soc. Jpn.* **1992**, *65*, 692.

(125) McVey, J.; Schold, D. M.; Yang, N. C. *J. Chem. Phys.* **1976**, *65*, 3375.

(126) Hashimoto, S.; Fukazawa, N.; Fukumura, H.; Masuhara, H. *Chem. Phys. Lett.* **1994**, *219*, 445.

(127) Ikeda, H.; Akiyama, K.; Takahashi, Y.; Nakamura, T.; Ishizaki, S.; Shiratori, Y.; Ohaku, H.; Goodman, J. L.; Houmam, A.; Wayner, D. D. M.; Tero-Kubota, S.; Miyashi, T. *J. Am. Chem. Soc.* **2003**, *125*, 9147.

(128) Darmanyan, A. P. *Chem. Phys. Lett.* **1984**, *110*, 89.

(129) Wilkinson, F.; McGarvey, D. J.; Olea, A. F. *J. Am. Chem. Soc.* **1993**, *115*, 12144.

(130) Tung, C.-H.; Wang, H.; Ying, Y.-M. *J. Am. Chem. Soc.* **1998**, *120*, 5179.

(131) Tong, Z.; Tung, C.-H.; Wang, H. *Ganguang Kexue Yu Guang Huaxue* **1997**, *15*, 289.

(132) Olea, A. F.; Worrall, D. R.; Wilkinson, F.; Williams, S. L.; Abdel-Shafi, A. A. *Phys. Chem. Chem. Phys.* **2002**, *4*, 161.

(133) Hirayama, S.; Lampert, R. A.; Phillips, D. *J. Chem. Soc., Faraday Trans.* **1985**, *81*, 371.

(134) Liu, X.; Iu, K.-K.; Thomas, J. K. *Chem. Phys. Lett.* **1993**, *204*, 163.

(135) Uppilli, S.; Thomas, K. J.; Crompton, E. M.; Ramamurthy, V. *Langmuir* **2000**, *16*, 265.

(136) Jaramillo, E.; Grey, C. P.; Auerbach, S. M. *J. Phys. Chem. B* **2001**, *105*, 12319.

(137) Sousa Goncalves, J. A.; Portsmouth, R. L.; Alexander, P.; Gladden, L. F. *J. Phys. Chem.* **1995**, *99*, 3317.

(138) Hashimoto, S.; Hagiri, M.; Barzykin, A. V. *J. Phys. Chem. B* **2002**, *106*, 844.

(139) Johnston, L. J.; Scaiano, J. C.; Shi, J.-L.; Siebrand, W.; Zerbetto, F. *J. Phys. Chem.* **1991**, *95*, 10018.

(140) Ellison, E. H.; Thomas, J. K. *J. Phys. Chem. B* **2001**, *105*, 2757.

(141) Ellison, E. H.; Thomas, J. K. *Microporous and Mesoporous Materials* **2001**, *49*, 15.

(142) Das, K.; Sarkar, N.; Das, S.; Datta, A.; Bhattacharyya, K. *Chem. Phys. Lett.* **1996**, *249*, 323.

(143) Datta, A.; Pal, S. K.; Mandal, D.; Bhattacharyya, K. *J. Phys. Chem. B* **1998**, *102*, 6114.

(144) Hagfeldt, A.; Gratzel, M. *Acc. Chem. Res.* **2000**, *33*, 269.

(145) Juris, A.; Balzani, V.; Barigelletti, F.; Campagna, S.; Belser, P.; von Zelewsky, A. *Coord. Chem. Rev.* **1988**, *84*, 85.

(146) Nazeerruddin, M. K.; Kay, A.; Rodicio, I.; Humphry-Baker, R.; Muller, E.; Liska, P.; Vlachopoulos, N.; Gratzel, M. *J. Am. Chem. Soc.* **1993**, *115*, 6382.

(147) Asbury, J. B.; Ellingson, R. J.; Ghosh, H. N.; Ferrere, S.; Nozik, A. J.; Lian, T. *J. Phys. Chem. B* **1999**, *103*, 3110.

(148) Ellingson, R. J.; Asbury, J. B.; Ferrere, S.; Ghosh, H. N.; Sprague, J. R.; Lian, T.; Nozik, A. J. *J. Phys. Chem. B* **1998**, *102*.

(149) Hannappel, T.; Burfeindt, B.; Storck, W.; Willig, F. *J. Phys. Chem. B* **1997**, *101*, 6799.

(150) Paris, J. P.; Brandt, W. W. *J. Am. Chem. Soc.* **1959**, *81*, 5001.

(151) Caspar, J. V.; Meyer, T. J. *J. Am. Chem. Soc.* **1983**, *105*.

(152) Damrauer, N. H.; Weldon, B. T.; McCusker, J. K. *J. Phys. Chem. A* **1998**, *102*, 3382.

(153) Damrauer, N. H.; Boussie, T. R.; Devenney, M.; McCusker, J. K. *J. Am. Chem. Soc.* **1997**, *119*, 8253.

(154) McCusker, J. K. *Acc. Chem. Res.* **2003**, *36*, 876.

(155) Browne, W. R.; Coates, C. G.; Brady, C.; Matousek, P.; Towrie, M.; Botchway, S. W.; Parker, A. W.; Vos, J. G.; McGarvey, J. J. *J. Am. Chem. Soc.* **2003**, *125*, 1706.

(156) Browne, W. R.; Coates, C. G.; Brady, C.; Matousek, P.; Towrie, M.; Botchway, S. W.; Parker, A. W.; Vos, J. G.; McGarvey, D. J. *J. Am. Chem. Soc.* **2004**, *126*, 10190.

(157) McFarland, S. A.; Lee, F. S.; Cheng, K. A. W. Y.; Cozens, F. L.; Schepp, N., *J. Am. Chem. Soc.* **2005**, in press.

(158) Lee, F. S. Generation of Radical Cations and Carbocations by Tris(bipyridyl)ruthenium Photosensitization. Doctoral Thesis, Dalhousie University, 2004.

(159) Nazeerruddin, M. K.; Zakeeruddin, S. M.; Kalyanasundaram, K. *J. Phys. Chem.* **1993**, *97*, 9607.

(160) Cozens, F. L.; Cano, M. L.; Garcia, H.; Schepp, N. P. *J. Am. Chem. Soc.* **1998**, *120*, 5667.

(161) Alvaro, M.; Garcia, H.; Garcia, S.; Marquez, F.; Scaiano, J. C. *J. Phys. Chem. B* **1997**, *101*, 3043.